



The Mechanical Stability of Instrumentation for Gravitational Wave
Detection

by

George Dixon

A thesis submitted to
The University of Birmingham
for the degree of
DOCTOR OF PHILOSOPHY

School of Physics and Astronomy
College of Engineering and Physical Sciences
The University of Birmingham
October 2010

UNIVERSITY OF
BIRMINGHAM

University of Birmingham Research Archive

e-theses repository

This unpublished thesis/dissertation is copyright of the author and/or third parties. The intellectual property rights of the author or third parties in respect of this work are as defined by The Copyright Designs and Patents Act 1988 or as modified by any successor legislation.

Any use made of information contained in this thesis/dissertation must be in accordance with that legislation and must be properly acknowledged. Further distribution or reproduction in any format is prohibited without the permission of the copyright holder.

ABSTRACT

This thesis opens with a brief review of the aspects of gravitational waves which are relevant for detector design and engineering, and an introduction to the LISA and LISA Pathfinder missions.

The thesis describes original work carried out to support the LISA Pathfinder mission at the University of Birmingham. The salient space mission quality requirements and mission specific technical and documentation requirements are set out.

The classical and computer based mechanical analysis, birefringence optical inspections, and linear elastic fracture mechanics and fracture control engineering which were applied to support flight acceptance of the brittle glass-ceramic optical bench interferometer structure are presented.

The design of a new photodiode mount is shown and justified, while the mechanical, optical, and electrical analysis, electrical and optical testing and, finally, the installation and alignment of the photodiodes are presented.

This thesis is dedicated for my family,
for the sacrifices they have made,
and for the memory of my father.

ACKNOWLEDGEMENTS

My work has been carried out within the LISA Pathfinder project, and as such has been influenced and guided by many scientists and engineers from ESTEC and Astrium Friedrichshafen (ASD). I would like to thank them for their professional approach, their care and wisdom in dealing with some difficult situations during the development of these technically challenging designs, in particular, I would like to thank Bengt Johlander of ESTEC, and Rüdiger Gerndt, Hermann Abele, Markus Bode, and Dieter Lebherz of ASD.

For their funding of the UK's contribution to the LISA Pathfinder mission, and therefore, to the funding of my position at The University of Birmingham, (UBI), I thank PPARC and STFC.

The LISA Pathfinder team in the Institute for Gravitational Research at the University of Glasgow, (UGL), were consistently helpful, keen, and professional throughout my participation in the project, and I owe a debt of gratitude to Harry Ward, David Robertson, Christian Killow, Michael Perreur-Lloyd, and Ewan Fitzsimons; not least for their diligent kindness in introducing me to the curry restaurants and public houses of Glasgow's West End!

Among the very many things which I should thank him for, my supervisor, Mike Cruise has been absolutely constant in offering me help and support. This stability and Mike's confidence in me has provided the best foundation for my work I could ever hope for. Thank you.

I would like to thank the technical staff in the department of Physics and Astronomy at the University of Birmingham; particularly, David Hoyland, David Smith, John Bryant, and Anthony Page. Their sense of fun, enthusiasm, professionalism, and skill were critical in making our designs make the transition from paper to reality, and then in making the designs actually work properly – critical in a much more direct and meaningful way than the forests of trees which have been felled to provide the mission's “quality” documents!

For sharing his office with an always messy and disorganised, sometimes grumpy, and sometimes slightly less than gracious colleague, while keeping smiling throughout, I offer my apologies and express my gratitude to Stuart Aston.

To Paul Booth, for his kind “final” proof read of my thesis, and his unfailing ability to present a contentious topic for debate between us, I offer my thanks.

Without the help and forbearance of my family, it would not have been possible for me to take up my position at Birmingham. For coping with the seemingly always urgent demands of the project with good grace, and for sharing my life, I owe much more than my thanks to Anne and George Hartley Dixon.

TABLE OF CONTENTS

1	PREFACE.....	1
2	REVIEW.....	2
2.1	Newton's Law of Gravitation	2
2.2	Tidal Gravitational Force.....	3
2.3	Gravitational Wave Properties.....	5
2.4	Gravitational Wave Sources.....	8
2.4.1	<i>Earth-Bound Sources.....</i>	<i>8</i>
2.4.2	<i>Astrophysical Sources.....</i>	<i>10</i>
2.5	Gravitational Wave Detectors.....	12
2.5.1	<i>Ground Based Detectors.....</i>	<i>15</i>
2.5.1.1	Resonant Bar Detectors.....	15
2.5.1.2	Interferometric Detectors.....	15
2.5.2	<i>Space-Borne Detectors.....</i>	<i>18</i>
2.5.2.1	LISA.....	18
2.5.2.2	The Need for LISA Pathfinder.....	22
3	LISA PATHFINDER.....	24
3.1	Charge Management System.....	25
3.2	Optical Bench Interferometer.....	26
3.3	Photodiodes.....	33
3.4	Phasemeter.....	33
4	PROJECT ENGINEERING CONTROL.....	35
4.1	My Responsibilities.....	35
4.2	Document Management.....	37

4.2.1	<i>Document Numbering System</i>	37
4.2.2	<i>Documentation Creation and Management</i>	39
4.3	Review Preparation	39
4.3.1	<i>Preliminary Design Review</i>	40
4.3.2	<i>Critical Design Review</i>	43
4.3.3	<i>Oversight Committee</i>	43
4.4	Project Reporting and Progress Meetings	44
4.5	Product Assurance	46
4.5.1	<i>Product Assurance Planning</i>	46
4.5.2	<i>Non Conformance Reporting</i>	47
5	OPTICAL BENCH STRUCTURAL INTEGRITY	48
5.1	Mechanical Modelling	49
5.1.1	<i>Introduction and Configuration</i>	50
5.1.2	<i>Scoping Calculations</i>	54
5.2	Finite Element Analysis	57
5.2.1	<i>Initial Model</i>	57
5.2.2	<i>Insert Analysis</i>	63
5.2.3	<i>Revised Shape Baseplate Analysis</i>	71
5.2.4	<i>Baseplate Modelling</i>	72
5.2.4.1	<i>Simply Supported Model</i>	72
5.2.4.2	<i>Built-in Model</i>	77
5.2.4.3	<i>Insert Interaction and Local Zerodur® Modelling</i>	83
5.3	Optical Bench Fracture Control	90
5.3.1	<i>Linear Elastic Fracture Mechanics</i>	90
5.3.2	<i>Fracture Control Methodology</i>	93
5.3.3	<i>Fracture Mechanics Analysis</i>	97

5.3.3.1	Edge crack at thin section between insert bore and baseplate upper surface	98
5.3.3.2	Derivation of Factors of Safety	100
5.3.4	<i>Optical Bench Inspection</i>	105
5.3.4.1	Inspection Method	106
5.3.4.2	Birefringence Measurement	108
5.3.4.3	Birefringence Measurement – Theoretical Example	114
5.3.4.4	Inspection Apparatus	116
5.3.4.5	Optical Bench First Inspection	118
5.3.4.6	Optical Bench Inspection Records	130
5.3.4.7	Optical Bench Re-Inspection	130
5.3.4.8	Inspection Verification	136
5.3.4.9	Fibre Injector Sample Inspection	146
5.3.4.10	Conclusion	147
6	PHOTODIODE DESIGN	149
6.1	Photodiode Mount Design	149
6.1.1	<i>Photodiode Bond Design and Verification</i>	151
6.1.2	<i>Photodiode Bond Testing</i>	164
6.2	Photodiode Design Summary	170
6.2.1	<i>Photodiode Design Description</i>	170
6.2.2	<i>Photodiode Mechanical and Thermal Summary</i>	174
6.2.2.1	<i>Harness Clamping</i>	179
6.3	Photodiode Procurement	180
6.3.1	<i>EEE Requirements and Qualification</i>	181
6.3.2	<i>Photodiode Status</i>	183
6.4	Photodiode Assembly Integration and Verification	183
6.4.1	<i>Photodiode Inspection</i>	183

6.4.2	<i>Selection of Photodiodes</i>	193
6.4.3	<i>Photodiode Inspection and Test Summary</i>	197
6.5	The Possible Use of QPDs as SEPDs	197
6.5.1	<i>The Use of QPD as SEPD</i>	197
6.5.1.1	QPD & SEPD Electrical Connections and Cable	198
6.5.1.2	Possible “QPD as SEPD” Configurations	199
6.6	Photodiode 202 Failure Investigation	203
6.6.1	<i>PD 202 Test and Integration History</i>	207
6.6.2	<i>PD 202 Investigation Method</i>	209
6.6.3	<i>ESTEC Scanning Electron Microscope Inspection</i>	216
6.6.4	<i>PD 202 Summary</i>	218
6.7	Photodiode Mechanical Testing	219
6.7.1	<i>Shock Response Spectrum Analysis</i>	224
6.7.2	<i>Mechanical Testing Summary</i>	229
6.8	Photodiode Installation	229
6.8.1	<i>Photodiode Installation</i>	229
6.9	Photodiode Summary	238
7	THESIS SUMMARY	240
8	INDEX OF TABLES	244
9	INDEX OF FIGURES	247
10	REFERENCES	257
11	APPENDICES	266
	APPENDIX A Strain As Applied to Gravitational Waves	266
	APPENDIX B Optical Bench Serial Number 03, Inspection II Images	268

<u>APPENDIX C Fibre Injector Failure.....</u>	<u>272</u>
<u>APPENDIX D Theory - Beam on an Elastic Foundation.....</u>	<u>283</u>
<u>APPENDIX E Photodiode 202 Inspection Results.....</u>	<u>286</u>
<u>APPENDIX F Photodiode 203 Inspection Results.....</u>	<u>288</u>
<u>APPENDIX G Photodiode 205 Inspection Results.....</u>	<u>290</u>
<u>APPENDIX H Photodiode 206 Inspection Results.....</u>	<u>292</u>
<u>APPENDIX I Photodiode 208 Inspection Results.....</u>	<u>294</u>
<u>APPENDIX J Photodiode 209 Inspection Results.....</u>	<u>296</u>
<u>APPENDIX K Photodiode 211 Inspection Results.....</u>	<u>298</u>
<u>APPENDIX L Photodiode 213 Inspection Results.....</u>	<u>300</u>
<u>APPENDIX M Photodiode 217 Inspection Results.....</u>	<u>302</u>
<u>APPENDIX N Photodiode 218 Inspection Results.....</u>	<u>304</u>
<u>APPENDIX O Photodiode 219 Inspection Results.....</u>	<u>306</u>
<u>APPENDIX P Photodiode 221 Inspection Results.....</u>	<u>308</u>
<u>APPENDIX Q Photodiode 222 Inspection Results.....</u>	<u>310</u>
<u>APPENDIX R Photodiode 232 Inspection Results.....</u>	<u>312</u>
<u>APPENDIX S Photodiode 233 Inspection Results.....</u>	<u>314</u>
<u>APPENDIX T Photodiode 236 Inspection Results.....</u>	<u>315</u>
<u>APPENDIX U Photodiode 238 Inspection Results.....</u>	<u>317</u>
<u>APPENDIX V Photodiode 239 Inspection Results.....</u>	<u>319</u>
<u>APPENDIX W Photodiode 241 Inspection Results.....</u>	<u>321</u>
<u>APPENDIX X Photodiode 242 Inspection Results.....</u>	<u>323</u>
<u>APPENDIX Y Photodiode 244 Inspection Results.....</u>	<u>324</u>
<u>APPENDIX Z Photodiode 245 Inspection Results.....</u>	<u>326</u>
<u>APPENDIX AA Photodiode 246 Inspection Results.....</u>	<u>328</u>

1 PREFACE

The context of this thesis is the field of gravitational wave detection which requires input from both scientists and skilled engineers. It is therefore appropriate to outline a basic understanding of the phenomenon of gravitational waves. Design work carried out with the objective of detecting gravitational waves requires at least a basic understanding of the physics underlying the phenomenon.

This thesis begins with a summary of the physics of gravitational waves, their sources, and the means by which their detection is being attempted. This summary is followed by a review of the detection methods and the instrumentation required. Following this, the programme of experimental work necessary to deliver the optical bench for LISA Pathfinder with appropriate levels of quality and reliability for a space mission is set-out. Specifically, the structural modelling, the fracture mechanics analysis, birefringence fracture control inspections, and photodiode engineering are described.

As this work was carried out in support of the LISA Pathfinder project, a number of project specific documents were referenced. It is appreciated that these documents are not generally available; where possible, the salient information in the documents is re-iterated within the thesis to ensure its readability. The project specific references are, however, retained as these may be useful for those reading the thesis who remain involved in the project.

2 REVIEW

2.1 NEWTON'S LAW OF GRAVITATION

Newton's laws of motion, [1], serve very well for many engineering purposes on Earth, although one weakness was that his laws implied the transmission of information about a mass, or gravitational source, at infinite speed. This may be seen by considering equation 1, below;

$$F_G = G \frac{m_1 m_2}{r_{12}^2}, \quad \text{Equation 1}$$

where F_G is the gravitational force mutually attracting the two masses, m_1 and m_2 . The distance between the two masses is represented by r_{12} , while G is the gravitational constant, $6.672 \times 10^{-11} \text{ m}^3 \text{ kg}^{-1} \text{ s}^{-2}$, [2]. Equation 1, Newton's equation of gravitational action does not include any speed of propagation of the signal from mass m_1 to mass m_2 . Even if the two masses were widely spaced, the action at a distance would be understood to be instantaneous by this formulation. The propagation of such a signal faster than light does not comply with the requirements of Einstein's Theory of Special Relativity, where the effect must lie within the forward light cone of the cause, [3].

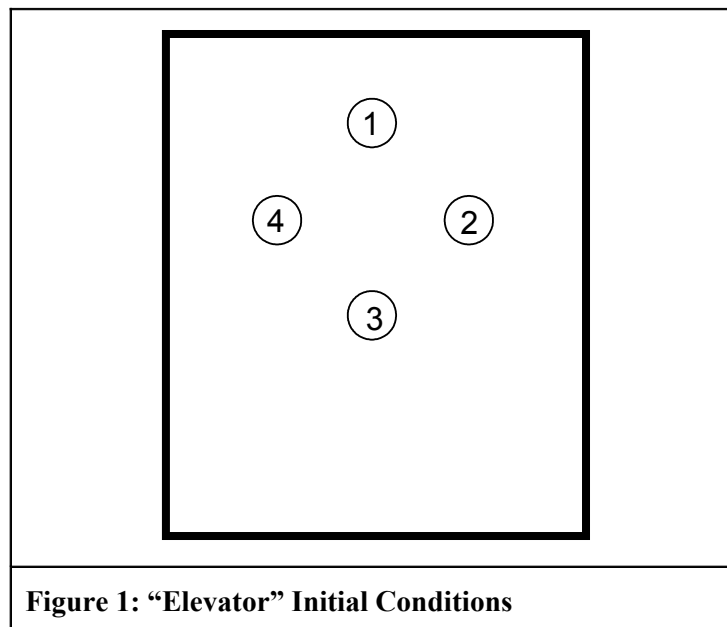
In a local region, F_G , as given by equation 1, may be termed the uniform gravitational force. Local, in this sense means a region which is sufficiently small that the gravitational field is effectively uniform, [4].

With reference to a freely falling container, in a gravitational force field, this uniform gravitational force would not be felt directly. As the uniform gravitational force may be

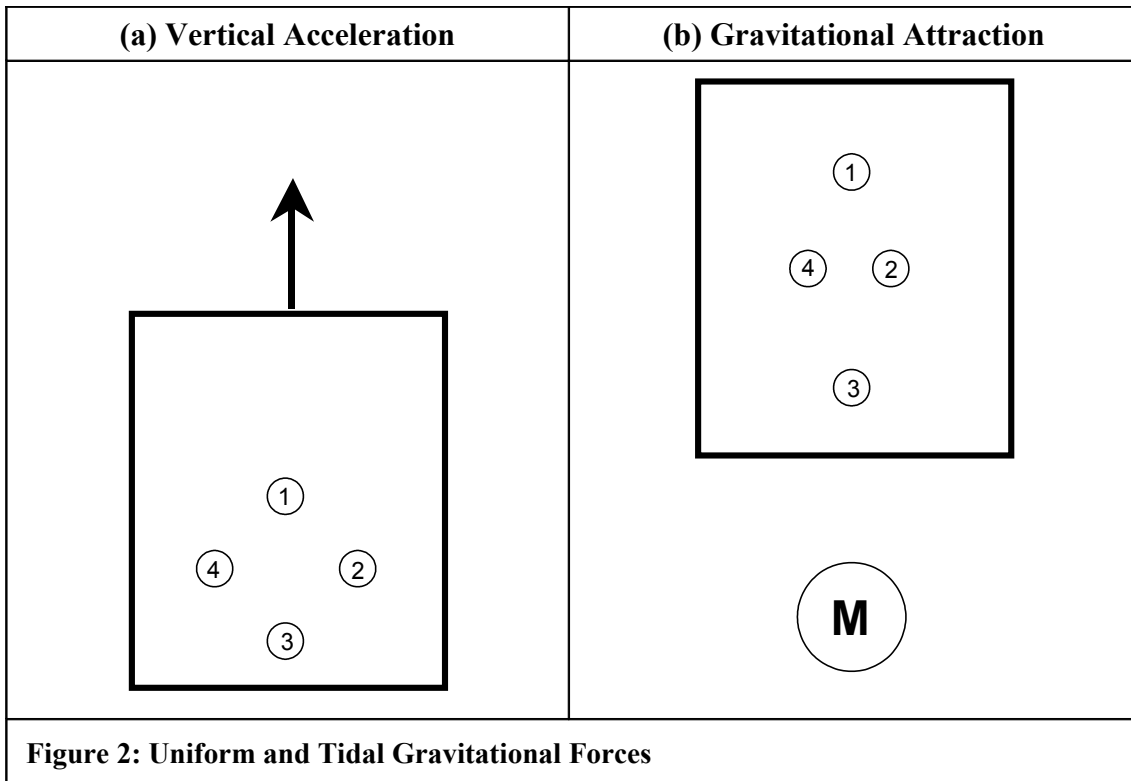
removed by being in free-fall, the uniform gravitational force is simply an effect of a particular choice of co-ordinate system rather than being fundamental.

2.2 TIDAL GRAVITATIONAL FORCE

Consider the four test masses, numbered 1 to 4, relative to the reference frame defined by the elevator in figure 1, below.



Consider two scenarios, in figure 2, below, one in which the reference frame, or elevator, is accelerated upwards, and one in which the elevator is fixed while the test masses are acted upon by the gravitational effects of a massive spherical object, [5], [6]. The massive spherical object is denoted by the encircled “M” in figure 2.



In figure 2, scenario (a), all four masses fall, together, vertically with respect to the reference frame, or elevator. In figure 2, scenario (b), mass 3 falls vertically, further than masses 2 and 4, which in turn fall further than mass 1 owing to the spatial variation in gravitational attraction force, as determined by the denominator of equation 1. In scenario (b), masses 2 and 4 move towards each other.

Figure 2, Scenario (a) shows the action of uniform gravitational attraction, while scenario (b) shows the action of both uniform and tidal gravitational forces. The uniform action of a gravitational force may be “transformed” away by allowing the reference frame to be under free-fall conditions. If scenario (b) were modified by allowing such free fall, mass 1 and 3 would appear to move apart vertically, while masses 2 and 4 would move together laterally.

It is this tidal aspect of gravitation which is predicted to travel in the form of a wave, at the speed of light. Gravitational waves, unlike mechanical, acoustic, and electromagnetic waves do

not represent the propagation of a disturbance of an independent field variable with respect to space and time, they represent a moving disturbance of spacetime itself. During the passage of a gravitational wave, the separation between two test masses might change, but the test masses themselves would experience no inertial acceleration.

2.3 GRAVITATIONAL WAVE PROPERTIES

Gravitational waves are transverse waves. Particles initially in a plane normal to the propagation vector of the wave remain in-plane as the wave passes, although they do move in the plane. Test masses placed around the plane would change their mutual separation during the passage of the wave. However, without further information, the measurement of the amplitude of motion of one test mass would not enable the strength of the wave to be deduced. This is because, if the motion of the test mass were measured with respect to a nearby test point in the plane, its motion would be very small indeed, while if the motion were measured with respect to a distant point on the plane, its motion would be larger. For this reason, the strength of a gravitational wave is expressed as strain, and given the symbol, h , [5].

$$h = 2 \frac{\delta l}{l} \qquad \text{Equation 2}$$

The factor of two in equation 2 is inherent in the detail of the derivation, which is included in Appendix A, while l represents the quiescent length between test points, and δl the change in length during the passage of the gravitational wave.

Gravitational waves are known as transverse traceless waves. Transverse, because the disturbance in spacetime occurs in directions which are everywhere at right angles to the wave

propagation vector; traceless, because the trace of the strain is zero. That the waves are traceless leads to the property that the area within a group of test masses acted upon by a gravitational wave remains unchanged during the disturbance.

There is an analogy with mechanical shear waves, which represent propagating shear strains, which are also transverse, trace free, and area preserving – indeed, in a 3D sense, mechanical shear waves may also be called equivoluminal waves.

The motion of a ring of test particles associated with the passage of gravitational waves is shown in figure 3, below;

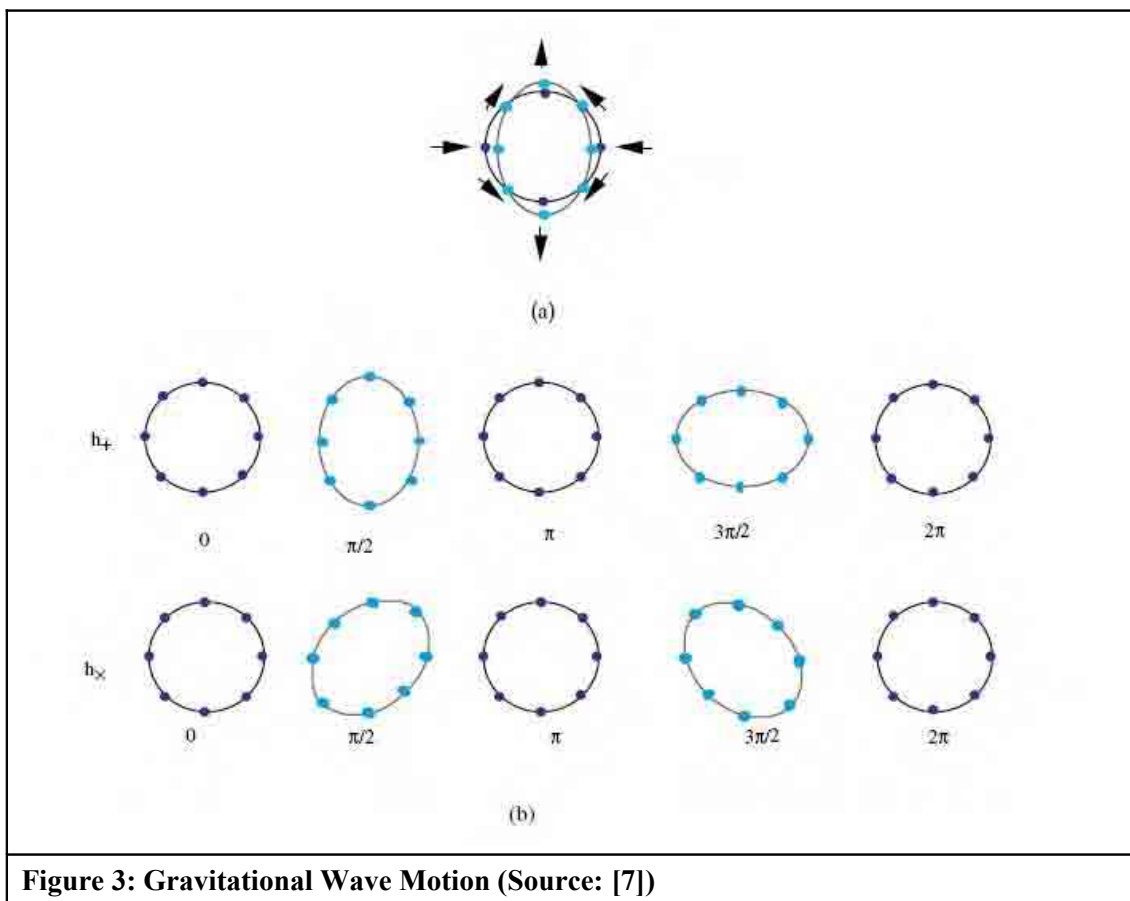


Figure 3: Gravitational Wave Motion (Source: [7])

Figure 3 shows the two polarisation directions of gravitational waves, assuming the gravitational wave is propagating normal to the page. Each point represents a free test mass.

For the + polarisation, (a), the diagonal test masses do not move, while for the × polarisation, the ordinate test masses remain stationary.

Gravitational radiation is predicted to travel at the speed of light. If spacetime is considered as if it were an elastic medium, Newton's law of gravitation implies infinite stiffness. The extreme, finite, stiffness of spacetime is suggested by the propagation speed of gravitational waves. The relationship between the curvature of spacetime and the stress energy causing the deformation may be written as in equation 3, [8], where \mathbf{T} is the stress energy tensor and \mathbf{G} is the Einstein curvature tensor. This “stiffness” can be seen by considering the order of magnitude of the coupling constant, $c^4/8\pi G$, which has the value of approximately $10^{42} \text{ m kg}^{-1} \text{ s}^2$, where c represents the speed of light in vacuum.

$$\mathbf{T} = \frac{c^4}{8\pi G} \mathbf{G} \quad \text{Equation 3}$$

Via analogy with elastic, acoustic, and electromagnetic waves, [9], [10], [11], the emission of gravitational waves may be expressed as a retarded potential. In the case of gravitational waves, it is usual to consider an approximation of this retarded potential, in the form of a multipole expansion. The multipole expansion is valid whenever the distance between the source and the point of interest is large compared with the size of the source.

The quadrupole moment tensor, [12], may be defined as in equation 4, below;

$$I_{\mu\nu} = \int \rho(\mathbf{r}) \left(x_\mu x_\nu - \frac{\delta_{\mu\nu} r^2}{3} \right) dV \quad \text{Equation 4}$$

where, $\rho(\mathbf{r})$ is the mass density at position \mathbf{r} , x_i are the Cartesian components of the vector \mathbf{r} , between the origin and the point of interest, δ is the so called Kronecker delta, having the property $\delta_{\mu\mu}=1$, and $\delta_{\mu\nu}=0$ for $\mu \neq \nu$. The integral is taken over the volume of interest.

The strain of the resulting gravitational wave may be written as in equation 5, below;

$$h_{\mu\nu} = \frac{2G}{Rc^4} \ddot{I}_{\mu\nu} \quad \text{Equation 5}$$

where μ and ν represent coordinate axes, and the right hand side is to be evaluated at the retarded time, $t-R/c$. Equation 5 is derived from the quadrupole approximation. If $I_{\mu\nu}$ does not vary with respect to time, the corresponding strain, $h_{\mu\nu}$, is zero. In equation 5, G is the gravitational constant, R is the radius between the source and the point of interest, c is the speed of light, and $\ddot{I}_{\mu\nu}$ is the second derivative, with respect to time, of the quadrupole moment tensor.

2.4 GRAVITATIONAL WAVE SOURCES

2.4.1 Earth-Bound Sources

In order to estimate the potential strength of the gravitational waves which could be produced using apparatus on earth, consider the simplest possible source of gravitational waves, a rotating bar. For a rotating bar, of mass M and length L , rotating with angular velocity ω radians per second, the average power radiated in the form of gravitational waves under the assumptions of the quadrupole approximation is given, [13], by equation 6;

$$P = \frac{2GM^2L^4\omega^6}{45c^5} \quad \text{Equation 6}$$

assuming that the deflections and resulting stress caused by the Earth's gravitation may be ignored, the stress in the bar is solely caused by its rotation. This stress, σ , which is a maximum at the centre of the bar's length (i.e., at the pivot) may be found, [14], by summing the

contributions of each infinitesimal elemental mass along the length of the bar – or alternatively considering the bar to be made as a dumbbell, with all the mass concentrated at the half radius points. Assuming the bar section and material remain constant, with mass density, ρ , along the length;

$$\sigma = \frac{\rho L^2 \omega^2}{4} \quad \text{Equation 7}$$

Substituting typical values of material yield stress and density into equation 7, enables values of the average power to be estimated. Thus, equation 8 represents the safe limiting rotational speed of the bar, and hence the power radiated;

$$P = \frac{128 G A^2 \sigma_y^3}{45 \rho c^5} \quad \text{Equation 8}$$

where A represents the cross sectional area of the bar. For example, a high quality steel bar, of yield stress 1200 MPa, with a cross sectional area of 2 m², rotating at a speed where the steel approaches its yield stress radiates approximately 7×10^{-29} W in the form of gravitational waves. As the bar is made from ordinary atomic matter, (as opposed to nuclear matter, for example) and all parts of the bar travel slowly when compared with light, the bar does not possess enough stress energy to produce any significant curvature of spacetime, which explains the small radiated gravitational wave power.

It is clear that even extreme Earth-bound sources cannot produce gravitational radiation with anything like the power required to be detectable, as described in section 2.5. The gravitational wave power and strain which can be achieved by Earth-bound sources is remarkably small, and in order to find stronger sources, it is necessary to consider astrophysical sources.

2.4.2 Astrophysical Sources

Astrophysical sources may radiate significant energy in the form of gravitational waves. However, even if the power density, F , were large, the associated strain, h , of the gravitational wave might still be very small, as given by equation 9, below, [5].

$$h \approx \sqrt{\frac{4 G F}{\pi c^3 f^2}} \quad \text{Equation 9}$$

Where f represents the frequency, in cycles per second. As the energy of a gravitational wave is non-negative, it must be proportional to the strain raised to an even power; in fact, it is proportional to the strain squared. Owing to geometrical spreading, in order to comply with energy conservation, the amplitude of a gravitational wave decreases proportional to the reciprocal of the radial distance from the source, [5]. Potential sources of gravitational waves include;

- **Neutron stars.** These spin very rapidly, and if there were a surface irregularity, for example, surface wave motion, the body would change its projected shape once per revolution. This variation in quadrupole moment would lead to the radiation of gravitational energy according to equation 5.
- **Binary star systems.** As these stars orbit about their common centre of gravity, their projected shape changes, in particular, the quadrupole moment in the direction of projection changes. For an equal mass binary system, with an orbit in the x-y plane, the components of the quadrupole moment tensor are given by equation 10, below;

$$\begin{aligned}
I_{XX} &= 2 M r_0^2 (\cos^2(2 \pi f t) - 1/3) \\
I_{YY} &= 2 M r_0^2 (\sin^2(2 \pi f t) - 1/3) \\
I_{ZZ} &= -1/3 M r_0^2 \\
I_{XY} = I_{YX} &= 2 M r_0^2 \cos(2 \pi f t) \sin(2 \pi f t) \\
I_{XZ} = I_{ZX} = I_{YZ} = I_{ZY} &= 0
\end{aligned}
\tag{Equation 10}$$

where the orbital radius is r_0 . As may be seen the z components either are equal to zero, or do not vary with respect to time, therefore these components do not contribute to gravitational radiation, and therefore, these quadrupole moments may be used with equation 5 to determine the strain;

$$\begin{aligned}
h_{XX} = -h_{YY} &= \frac{-32 \pi^2 G}{R c^4} M r_0^2 f^2 \cos(4 \pi f t) \\
h_{XY} = h_{YX} &= \frac{-32 \pi^2 G}{R c^4} M r_0^2 f^2 \sin(4 \pi f t)
\end{aligned}
\tag{Equation 11}$$

For an equal pair, this shape change occurs twice per orbit, i.e., the frequency of the radiated gravitational radiation is twice the frequency of rotation. As the pair of stars begin to merge, the strength of the gravitational wave radiation increases, while the orbital period reduces. This type of source, producing a signal known as a chirp, should pass through the sensitive frequency band of detectors. The strain of the gravitational radiation from a binary system as given by equation 11 may be simplified and expressed in non-dimensional terms of the Schwarzschild radii of each star, r_{s1} , r_{s2} , the orbital radius r_0 , and the distance to the observer, R , [12], as given in equation 12, below.

$$h \approx \frac{r_{s1} r_{s2}}{r_0 R}
\tag{Equation 12}$$

- **Binary Pulsars.** The first binary pulsar was discovered using the Arecibo radio telescope in 1974 by Hulse and Taylor, [15], [16]. The orbital rate of the binary system was determined using the Doppler effect. Over a period of time, it was noticed that the orbital rate of the binary was reducing at a rate too slow to be accounted for by frictional effects. As the mass of the binary system was determined within an accuracy of 0.1 %, [5], the energy loss via the radiation of gravitational waves was estimated, [17], [18], agreeing with the observed reduction in the orbital period within the accuracy of the method. In 1993, Hulse and Taylor were awarded the Nobel Prize for Physics.
- **Black holes.** Black Holes of mass $\sim 10 M_{\odot}$ are expected to be found in binary systems, the great mass of these systems results in the radiation of more gravitational wave energy, making these strong candidates for an early detection.
- **Supermassive Black Holes;** The inspiral of two super-massive black holes (SMBHs; 10^6 to $10^9 M_{\odot}$) is expected to be a strong source of gravitational radiation at low frequencies, in the LISA detection range, [19]. The signal to noise ratios are expected to be sufficiently high to enable the comparison of numerical relativity simulations with the observed merger waveforms.

2.5 GRAVITATIONAL WAVE DETECTORS

The expected magnitude of the strain of $h \leq 10^{-21}$, [20], places great demands on any instrument attempting to detect gravitational waves. For example, such an instrument with $l=1$ km in size needs to be able to measure $\delta l \sim 10^{-18}$ m. To put this requirement into context, the size of a proton (hydrogen nucleus) is 10^{-15} m.

The change in length which must be detected is extremely small and, therefore, challenging, hence, it is necessary both to understand the various contributions to measurement noise, [20], and to understand what practical steps may be taken to reduce such noise contributions. Typical noise contributions arise from;

- **Seismic noise** – the motion of the ground is detected by all Earth-bound gravitational wave detectors, and cannot be separated from the useful signal. Seismic noise presents a fundamental limit which can only be partially removed. However, it is possible to provide isolation from seismic noise which is effective at higher frequencies, thus, in practice, seismic noise presents a low-frequency limit for ground based detector operation.
- **Thermal noise** – for temperatures above absolute zero, the random motion of the atoms which form the mirrors or test masses causes the surface of these items, (which is usually from where the measurement of position is taken) to move. This noise is concentrated at the mechanical natural frequencies of the suspension system.
- **Mechanical Noise** – where any environmental changes such as temperature or humidity result in a change of length of the detector, and any sudden release of residual stress via mechanisms such as micro-cracking or material phase-changes result in a change in length.
- **Shot noise** – this is the inherent fluctuation in the light beam used within the gravitational wave detector; a result of the finite number of photons in the measurement beam. As interferometers are used to infer length changes by measuring changes in the properties of the interfered beams, these fluctuations in the beam intensity are a direct source of noise. Increasing the power of the beam within the interferometer may reduce the sensitivity of the detector to shot noise.

- **Radiation pressure noise** – while shot noise is the direct measurement noise owing to the fluctuation in the number of photons in the interferometer's beam, radiation pressure noise is spurious motion of the test masses which is caused by the fluctuating number of photons being reflected from the test mass. Each photon carries momentum of $\hbar\omega/c$, where \hbar is the reduced Planck constant. The radiation pressure noise results in fluctuating mechanical reaction forces at the mirrors or test masses, resulting in spurious motion, which is therefore detected just as if it were meaningful signal.
- **Laser noise** – variations in the output of the laser source can cause fluctuations in the output signal of the interferometer. The laser output needs to be sufficiently stable in terms of its frequency, amplitude, and beam geometry.
- **Gravity gradient noise** – this is noise caused by the motion of matter in the vicinity of the test mass. Even if the test mass were suspended using a perfect isolation system, the isolation might be rendered ineffective by the fluctuating gravitational attraction between the test mass and the moving matter. Space-borne detectors do possess the advantage of being able to escape the gravity gradient noise caused by the normal, ongoing, seismic activity of the earth.

2.5.1 Ground Based Detectors

2.5.1.1 Resonant Bar Detectors

The development of gravitational wave detectors, using a massive aluminium bar as the sensing element, was begun by Joseph Weber, [21]. The instrumentation surrounding the bar was designed to detect the motion of the bar at the fundamental longitudinal resonance frequency of the bar.

In order to reduce thermal noise, it was possible to cool bar detectors, and detectors have been operated below 100 mK, [7]. The resonant bars were designed with very low mechanical losses, which meant that their resonant response in the fundamental mode was limited to a small range of frequency each side of the resonant peak, and thus, the resonant bars were narrow band detectors.

2.5.1.2 Interferometric Detectors

The test mass motion resulting from the passage of a gravitational wave, as shown in figure 4, below, is ideally suited to measurement using an interferometer, which can directly measure the changes in the path length in two orthogonal directions, as shown, below.

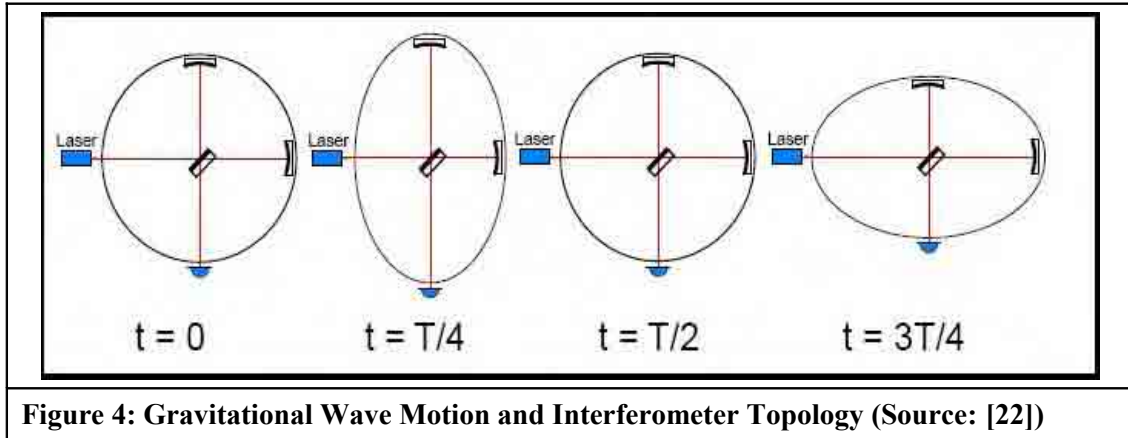


Figure 4: Gravitational Wave Motion and Interferometer Topology (Source: [22])

In the configuration of a detector of gravitational waves, the beamsplitter and mirrors would be suspended, thus isolating them from sources of noise, and allowing them to move freely as inertial test masses. If a gravitational wave of strain, h , passes a Michelson interferometer, [23], [12], [24], of nominal length L in a direction normal to the two orthogonal arms, each arm changes length by;

$$\delta L = \frac{hL}{2} \tag{Equation 13}$$

With one arm becoming longer, while the other becomes shorter. The time delay between the arrival of these waves at the beamsplitter is;

$$\begin{aligned} \tau &= 2 \frac{L + \delta L}{c} - 2 \frac{L - \delta L}{c} \\ &= \frac{2}{c} (L + \delta L - L + \delta L) \\ &= 4 \frac{\delta L}{c} \\ \tau &= \frac{2hL}{c} \\ \tau &\propto h \end{aligned} \tag{Equation 14}$$

If the electric field of the wave in each arm is E_1 and E_2 , and assuming that E_1 and E_2 are of the same amplitude, the re-combined wave is;

$$E(t) = E_1(t) + E_2(t) = E_1(t) + E_1(t + \tau) \quad \text{Equation 15}$$

The resulting time averaged intensity is;

$$\begin{aligned} I &= \langle EE^* \rangle = \langle (E_1 + E_2)(E_1 + E_2)^* \rangle \\ &= \langle E_1 E_1^* \rangle + \langle E_1 E_2^* \rangle + \langle E_1^* E_2 \rangle + \langle E_2 E_2^* \rangle \\ &= I_1 + I_2 + 2 \Re \{ \langle E_1^* E_2 \rangle \} \end{aligned} \quad \text{Equation 16}$$

where \Re represents the operation of taking the real part. Assuming harmonic waves, the time average of the product $E_1^* E_2$ can be evaluated;

$$\begin{aligned} E_1(t) &= E_0 \exp(-i \omega t) \\ \langle E_1^* E_2 \rangle &= \lim_{T_m \rightarrow \infty} \frac{1}{T_m} \int_{-\frac{T_m}{2}}^{\frac{T_m}{2}} |E_0|^2 \exp(i \omega t) \exp(-i \omega (t + \tau)) dt \\ &= |E_0|^2 \exp(-i \omega \tau) \\ &= I_1 \exp(-i \omega \tau) \end{aligned} \quad \text{Equation 17}$$

Substituting back gives;

$$\begin{aligned} I &= I_1 + I_2 + 2 \Re \{ \langle E_1^* E_2 \rangle \} \\ &= I_1 + I_2 + 2 \Re \{ I_1 \exp(-i \omega \tau) \} \\ I &= I_1 + I_2 + 2 I_1 \cos(\omega \tau) \\ I &= 2 I_1 \left(1 + \cos\left(\frac{4 \pi h L}{\lambda}\right) \right) \end{aligned} \quad \text{Equation 18}$$

This results in a change in the degree of constructive or destructive interference registered by the photodiode. Practically, the mirror positions are moved to keep the photodiode at a dark

fringe, and control signals to move the mirrors back to a null position are used as the output signal of the interferometer. Operation with such a null signal is desirable because this reduces the sensitivity of the detector to laser power fluctuations; this approach is also used in the context of Pound-Drever-Hall laser frequency stabilisation.

Upon reading equation 18, it might be thought that increasing the length of the interferometer arms always increases the sensitivity of the detector without limitation. However, the time that it takes the light field to build up in the arms is also proportional to the arm length – this can be viewed in the same way as a time constant for a first order system, such as an RC circuit. This means that longer interferometer arm lengths result in an interferometer with a lower measurement bandwidth, i.e., longer arms limit the upper measurement frequency.

Although figure 4 depicts a Michelson interferometer in its most basic form, the interferometric gravitational wave detectors which have been or are being built use extra optical components to form schemes such as power recycling, dual recycling, synchronous recycling, and detuned resonant recycling in order to make more use of the laser power available. These schemes increase the sensitivity of the detector by allowing optical power to build up in the arms.

2.5.2 Space-Borne Detectors

2.5.2.1 LISA

LISA is a space-borne interferometric gravitational wave detector, envisaged as a NASA/ESA collaborative project. The mission is currently in the mission formulation phase, [25], as such, no flight hardware has been produced.

Whereas typical ground based detectors have arm lengths of the order of thousands of metres, the arm lengths for LISA are 5 million kilometres, [26]. This long arm length means that LISA is sensitive in a lower range of frequencies when compared with ground based interferometric detectors. This arm length tunes the interferometer to be most sensitive in the frequency range where sources of gravitational radiation, particularly the inspirals of massive objects, may be detected.

The LISA mission comprises three identical spacecraft, flying in the formation of an equilateral triangle, each craft 5 million kilometres away from the others. Each craft acts as a shield, protecting freely-flying test masses within from disturbance by variable solar wind pressures; this is known as a drag-free satellite. The undisturbed test masses fly along geodesics in spacetime, and the interferometric system measures the relative locations of the test masses.

The centre of the formation orbits in the plane of the ecliptic, 1 AU from the Sun, lagging the earth by 20° . The plane of the triangular formation is inclined at 60° with respect to the ecliptic. These orbits were chosen in order to minimise the change in arm length due to the differing orbits, although there will be a considerable signal from this source, which must be dealt with. As the orbital motion relative to the source is also a low frequency, the Doppler shift of signals emitted by sources of sufficient strength may be used to obtain an estimate of the direction to the source. A schematic of the orbit is shown in figure 5, below.

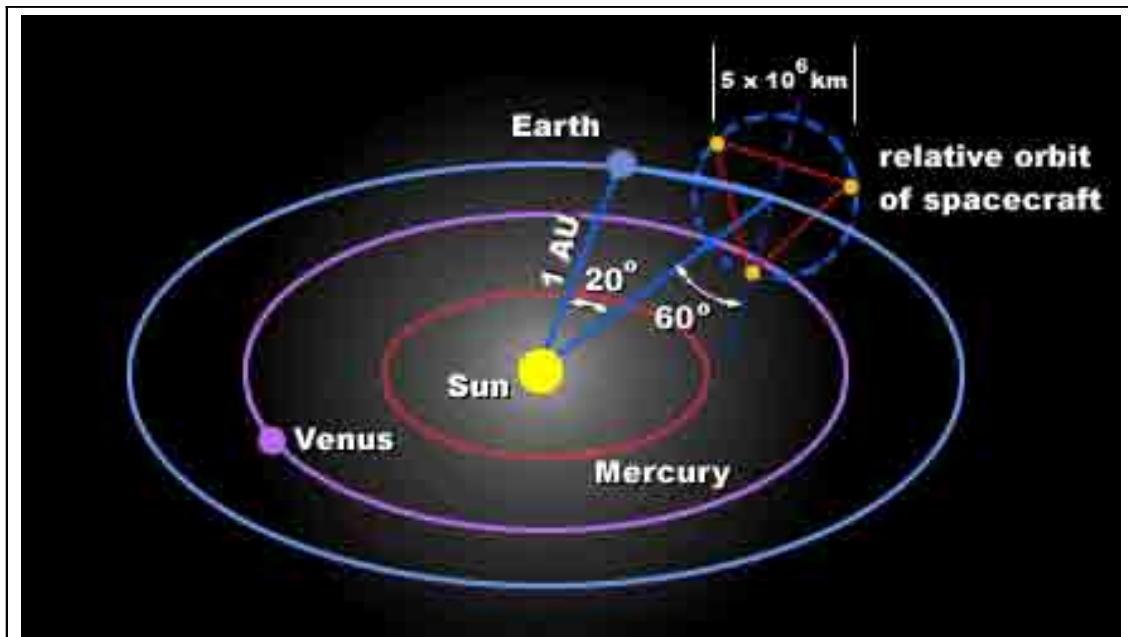


Figure 5: LISA Orbit Schematic (Source: ESA)

Each craft emits 1 Watt infra-red laser beams directed via telescopes at the other two (far) craft. Owing to the distance between the craft, it is not possible to directly reflect an incoming beam because there would not be sufficient power left in the returning beam for adequate detection and measurement on the near craft.

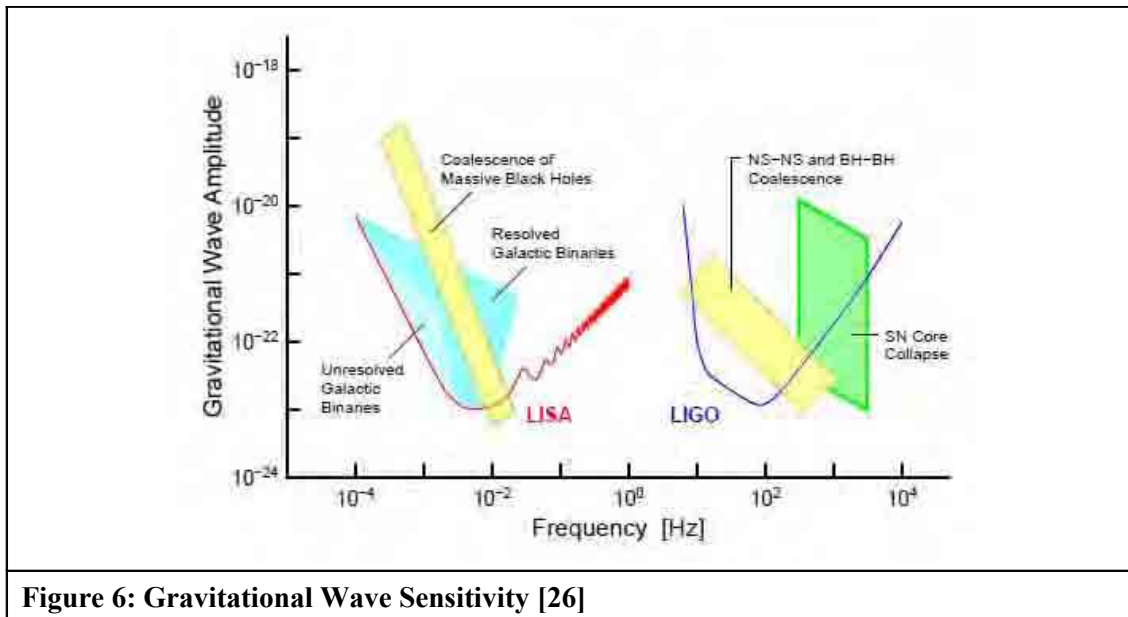
Instead of simply reflecting the beam, the laser on the far craft is phase locked to the incoming signal, thus enabling the power of the reflected beam to be augmented. The returning beam, focused by the telescope, is then mixed with the laser in the near craft, providing information on the phase difference between the beams, and hence length changes between the two craft.

It may be noted that extra information about the behaviour of the system, such as a measure of laser frequency noise may be obtained by other combinations of adjacent arm length measurements. The arm length difference measurement allows LISA to reach a strain sensitivity of $h \sim 10^{-23}$ when averaged over the course of a year (during the year, the angular

configuration of the constellation of craft varies, and so varies the signal, with respect to the source).

The reference points between which the length measurements are made are called “proof”, or “test” masses. They are 4cm polished cubes, made from a platinum-gold alloy, housed in vacuum enclosures. As previously mentioned, the test masses fly freely within these enclosures. Besides the function of supporting the required equipment to carry out the necessary scientific and housekeeping functions of a spacecraft, the spacecraft act as shields, protecting the test masses from the effects of solar radiation pressure. It is necessary to position the craft such that it is centred on the freely flying test mass, in order to reduce local noise sources – for example any spatial changes in the local self-gravitational field of the craft. This is achieved by a so-called “drag-free” control system, where the position of the test mass is measured, relative to the spacecraft, using a non-contact scheme, and the spacecraft is positioned accordingly, using low force thrusters. Potential technologies for test mass position sensing include both capacitive and interferometric sensing. One potential drawback of capacitive sensing is the potential disturbance resulting from electrostatic coupling between the test mass and other charged bodies.

Figure 6, below shows the expected strains of gravitational waves from a range of sources. Also shown on the figure are the design sensitivities of a ground based detector, Advanced LIGO, and a space based detector, LISA, showing how each detector matches the expected gravitational wave strain and frequency range.



2.5.2.2 The Need for LISA Pathfinder

The requirement for LISA to be able to fly a number of freely flying test masses, under effective drag-free control is an aspect of the mission which cannot be tested on Earth, [27], [28], [29]. The concept of LISA Pathfinder is to condense one arm of LISA from 5 million km in length down to a few tens of centimetres, and so demonstrate the required technology for drag-free control and laser interferometry within one satellite, [30].

LISA Pathfinder concurrently provides an experiment in precision metrology, and in General Relativity, and an effective LISA test of;

- The ability to place a test mass in pure free fall within given limits,
- The test mass caging and release mechanisms,
- The ability to provide a satellite with an acceptable self gravitational field,
- The test mass charge control system,

- The low noise test mass position sensing ,
- The satellite drag free control system,
- Stable optical instrumentation, particularly interferometry.

The LISA Pathfinder test-masses will be flown freely with a gap of several millimetres between the test masses and the vacuum enclosure, with no mechanical contact. Using the optical bench interferometer, LISA Pathfinder will track the motion of the test masses.

Using the interferometer readouts, and the fine control available from FEEP thrusters, the spacecraft and test masses will formation fly in a drag free configuration down to an acceptable level of residual test mass acceleration.

3 LISA PATHFINDER

Primarily, LISA Pathfinder is a technology demonstration mission which is being flown to enable technology necessary for the LISA project, which cannot be tested in the gravitational environment on Earth, to be tested in space.

In the heart of the LISA Pathfinder satellite is the LISA Test Package (LTP) [29]. The measurement of the linear and angular position of two test masses flown in a drag-free configuration forms the bulk of the science output of LTP. Each test mass is located in a vacuum enclosure, which also contains a capacitive position sensing transducer, a charge management system, and a test mass capture and release caging mechanism.

The UK's contribution to LTP is summarised below;

- Imperial College London – Charge Management System
- University of Birmingham – Phasemeter, photodiodes, and optical bench interferometer engineering support
- University of Glasgow – Optical bench Interferometer

These instruments and systems are described below, however, emphasis is placed more heavily upon those items which form the subject of this thesis.

3.1 CHARGE MANAGEMENT SYSTEM

Any spurious charge built up on the test masses could disturb them from free flight conditions. It is therefore necessary to manage test mass charge, and provide a means to reduce test mass charge to acceptable levels during the mission, [31].

Any excess charge is removed by shining ultra-violet light of wavelength 254 nm onto the test mass or enclosure surface as necessary to release photoelectrons via the photoelectric effect.

The charge management system for LISA Pathfinder consists of three pieces of equipment;

- The UV light unit (ULU)
- The Fibre Optic Harness (FOH)
- The Inertial Sensor UV Kit (ISUK)

The ULU contains the lamps, the optics to couple the light into the FOH and the necessary drive electronics. Owing to the perceived fragility of the lamp units, there is a high degree of redundancy, with three lamps being provided for each inertial sensor.

The FOH is formed from a bundle of fibre optic cables enclosed within a polyether-ether-ketone (PEEK) sleeve.

As the inertial sensor is mounted within a vacuum enclosure, it is necessary to provide a vacuum compatible feedthrough to allow the UV light to impinge upon the inertial sensor. The fibre passes through a custom made non-magnetic titanium penetration. Owing to the different coefficients of thermal expansion of the fibre and the titanium, and the long, slender shape of the feedthrough, in order to avoid thermal stressing, the fibre is only attached to the titanium at one end.

3.2 OPTICAL BENCH INTERFEROMETER

The precision measurement of the linear and angular position of the two test masses is achieved by means of an interferometric system. The system of interferometers is physically based upon a baseplate made from Zerodur®, a glass ceramic with a very low co-efficient of thermal expansion, typically, $0 \pm 0.02 \times 10^{-6} / \text{K}$ for the class zero material used. The interferometers measure the location and motion of two test masses which are located in vacuum enclosures at each end of the optical bench. The optical bench interferometer and test masses are shown, without the vacuum enclosures, in figure 7, below.

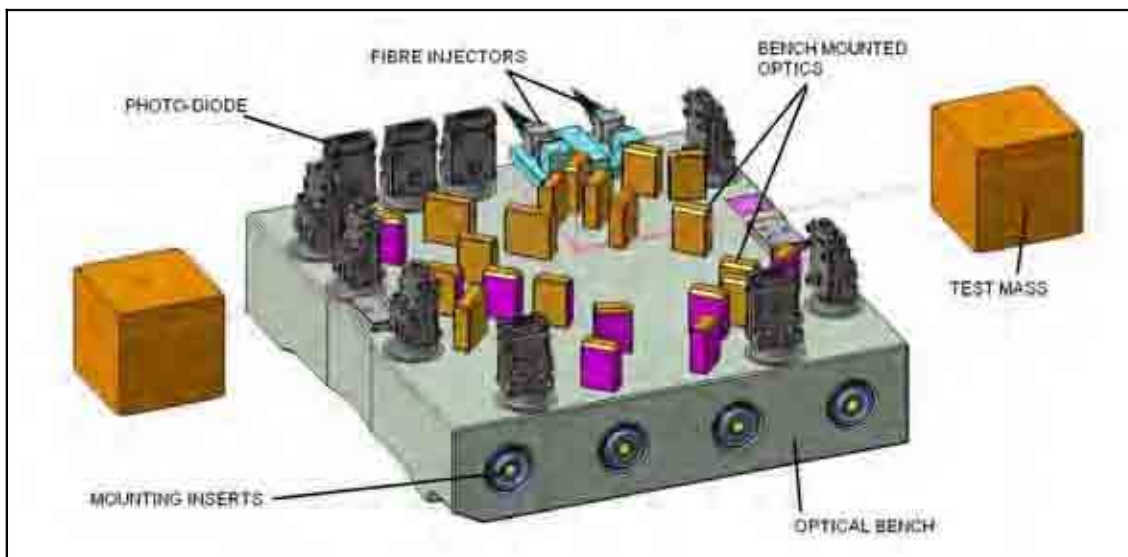


Figure 7: Optical Metrology System (OMS) Schematic, (Source: [32])

Within each of the two vacuum enclosures, there is one test mass. At launch, the test mass is initially caged to provide the test mass with a known starting position, and to react the launch loads. The position of the test mass within the vacuum enclosure is monitored using capacitive sensors. Once released from the caging mechanism, the test masses fly freely – equivalently,

they are in free fall. Each test mass in free fall, under the influence of gravity alone follows a geodesic path in spacetime, [30]. The spacecraft is then positioned about the test mass position. Another way to view this system, is to consider the spacecraft as a shield, protecting the test mass from external disturbances, such as solar radiation pressure.

In order that the self gravitation of the spacecraft does not strongly bias the motion of the test masses, the mass distribution of each component on the spacecraft is modelled, and extra compensating masses were positioned around the test masses and the craft to minimise the gravity gradient experienced by the test masses. These protective steps are undertaken to ensure that gravity is the only significant force acting upon the test mass. Owing to the fundamental weakness of gravity in comparison with the other forces, this represents a difficult undertaking. The flight test of LTP is considered to be satisfactory if the free fall of one test mass is demonstrated to within an acceleration noise limit as defined in equation 19, and documented in [33];

$$S_a^{1/2}(f) \leq 3 * 10^{-14} \left[1 + \left(\frac{f}{3\text{mHz}} \right)^2 \right] \text{ms}^{-2}/\sqrt{\text{Hz}}$$

Equation 19

For the measurement bandwidth of

$$1\text{mHz} \leq f \leq 30\text{mHz}$$

Light from the laser source travels across the spacecraft through two single mode, polarisation preserving, optical fibres which are bonded permanently to the fibre injectors mounted on the optical bench. The coupling at the free fibre ends forms the interface to the optical bench interferometer, defining the boundary, in terms of the light path, between the optical bench interferometer and the remainder of the spacecraft. The fibres terminate in connectors of type Diamond AVIM PM8°, as specified in the OMS Requirements Specification, [32]. At the interferometer end, the fibres are bonded directly to the fibre injectors. Owing to the difficulty

of effecting a repair to this bond, if a fibre were to fail, this would have extremely serious consequences for the entire optical bench interferometer.

The optical bench supports four interferometers, and is an important structural member within the LISA Test Package Core Assembly, (LCA). One measures the distance between the two test masses, (x_2-x_1) , one measures the distance between a point on the bench and test mass one (x_1) , one provides the reference phase measurement for the (x_2-x_1) and (x_1) measurements, and the remaining interferometer is used to measure laser frequency fluctuations, [32], [34]. Via the use of figure 8 and table 1, below, the beam paths for each of these interferometers may be traced.

<i>Photodiode</i>	<i>Photodiode Type - Function / Description</i>
PDA1	Single Element Photodiode - Laser Power, Beam 1
PDA2	Single Element Photodiode - Laser Power, Beam 1
PDFA	Quadrant Photodiode - Frequency Noise (Nominal)
PDFB	Quadrant Photodiode - Frequency Noise (Redundant)
PDRA	Quadrant Photodiode - Reference Length (Nominal)
PDRB	Quadrant Photodiode - Reference Length (Redundant)
PD1A	Quadrant Photodiode - Position of Test Mass 1 (Nominal)
PD1B	Quadrant Photodiode - Position of Test Mass 1 (Redundant)
PD12A	Quadrant Photodiode - Position of Test Mass 2 - Test mass 1 (Nominal)
PD12B	Quadrant Photodiode - Position of Test Mass 2 - Test mass 1 (Redundant)
Table 1: Photodiode Allocation	

The alignment of the test masses may also be determined via differential wavefront sensing, using the phase difference between the signals from different quadrants of the same photodiode.

While operating in science mode, the optical metrology system must measure the test mass displacements and rotations, i.e., using the (x_2-x_1) and (x_1) interferometers, with a measurement noise as defined in equation 20, and documented in [32];

$$S_{\delta_x}^{1/2}(f) \leq 6.3 * 10^{-12} \sqrt{\left(1 + \left(\frac{f}{3\text{mHz}}\right)^{-4}\right)} \text{m}/\sqrt{\text{Hz}}$$

$$S_{\delta(\phi)}^{1/2}(f) \leq 20 * 10^{-9} \sqrt{\left(1 + \left(\frac{f}{3\text{mHz}}\right)^{-4}\right)} \text{rad}/\sqrt{\text{Hz}} \quad \text{Equation 20}$$

For the measurement bandwidth of

$$1\text{mHz} \leq f \leq 30\text{mHz}$$

The acousto-optical modulators provide a frequency difference between the measurement and reference beams of light which are introduced onto the bench via the fibre injectors. This frequency difference can range between 500 and 2000 Hz, and is termed the heterodyne frequency. The interfering laser beams in the interferometer produce a fluctuating power on the photodiode that is sinusoidal in nature.

Assuming the two laser beams have equal power P, frequencies ω_1 and ω_2 and phases ϕ_1 and ϕ_2 and are combined with optical contrast C, the instantaneous incident power on a single quadrant of the photodiode is given by equation 21, below.

$$P_{\text{INST}} = 2P \left(1 + C \cos(\omega_1 t - \omega_2 t + \phi_1 - \phi_2) \right) \quad \text{Equation 21}$$

Since $(\omega_1 - \omega_2)$ is defined as the heterodyne frequency designated ω_h and $(\phi_1 - \phi_2)$ is the required phase caused by proof mass movement designated ϕ_L the expression may be simplified as in equation 22, below.

$$P_{\text{INST}} = 2P \left(1 + C \cos(\omega_h t + \phi_L) \right) \quad \text{Equation 22}$$

Thus, the signal of interest, ϕ_L , is obtained at the heterodyne frequency, ω_h , rather than at a frequency of zero, (DC). Measurements taken at DC, and at very low frequencies suffer from noise which is known as “one over f” noise. Taking the measurement at ω_h , reduces the effect of this source of noise.

Physically the optical bench interferometer consists of a baseplate to which various optical and mechanical components are attached. The baseplate is a slab of low thermal expansion Zerodur[®] of dimensions 200 mm x 212 mm x 45 mm. Material is machined from the underside of the slab to reduce its weight without compromising its structural performance. Four mounting holes are machined into each of two opposing sides of the baseplate to allow mounting of it within the LTP. The top surface of the baseplate is polished flat, within very precise limits; the required flatness is of the order of $\lambda/10$, where, in the context of glass surface specification, $\lambda \approx 600$ nm, [35]. Lambda, in this context is a specialist term used in the specification of the flatness of optical substrates, and does not refer to the wavelength of the laser light used for test mass motion measurement during the mission. This high degree of flatness serves both to maintain the optical alignment, and allows the use of hydroxide catalysis bonding to attach the critical components to the baseplate

The optical layout of the optical bench interferometer is shown in schematic form, in figure 8, below.

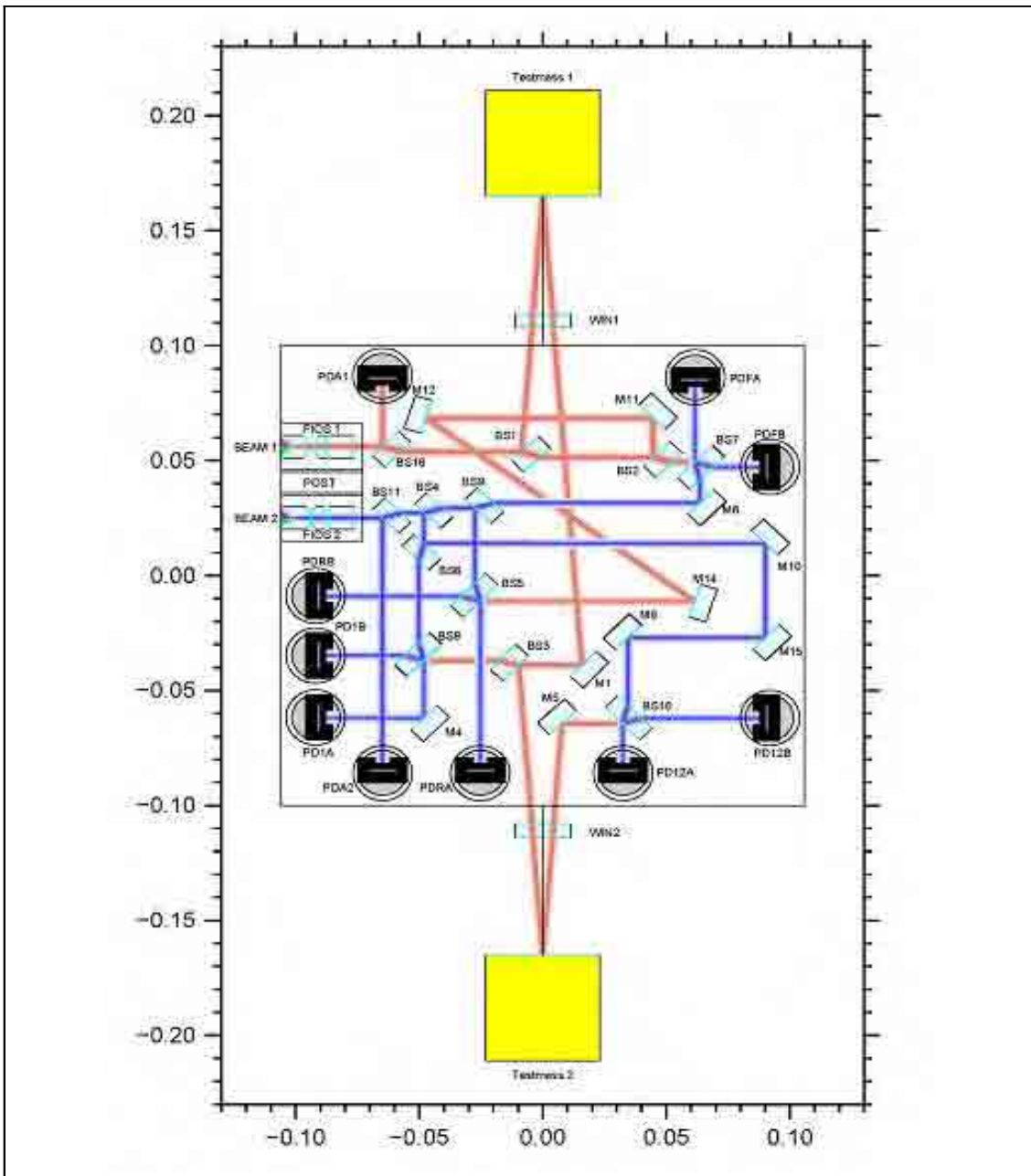


Figure 8: Optical Bench Interferometer Optical Layout, Source[36])

The windows and test masses within the inertial sensor housings while important in defining the beam path are not part of the optical bench interferometer, as defined by the LISA Pathfinder project, but are included here to show the complete optical paths.

The optical bench interferometer takes in light through two single-mode, polarisation preserving optical fibres. This light is then collimated in two custom built fibre injector optical assemblies (FIOS) to produce two free space optical beams each of diameter approximately 1.4 mm. These 2 FIOS are then bonded to the baseplate using hydroxide catalysis bonding. This process ensures that the alignment of the optical beams is very stable with respect to the optical bench interferometer, with the beams being required to hit the test masses within a 50 μm target circle during the life of the mission.

The two optical beams then each pass through a beamsplitter which directs some light onto single element photodiodes that measure the intensity of each optical beam. The remaining light passes through the beamsplitters and into the main body of the interferometer. Here the light is directed by the various mirrors and beamsplitters to form the four interferometers mentioned above. The alignment and positional stability of the mirrors, beamsplitters and photodiodes is critical to ensure that:

- the optical beams reflect from the correct positions on the test masses
- the measurement of the positions of the test masses is not compromised by mechanical noise on the optical bench interferometer
- there is optimal overlap of the interfering beams at the output of the interferometer

To give the required high strength and stability all the mirrors and beamsplitters are bonded to the baseplate using hydroxide catalysis bonding, [35]. This technique forms a strong bond, of effectively zero thickness, between the component and the baseplate.

3.3 PHOTODIODES

The output from each interferometer consists of two complementary optical beams which are directed onto separate quadrant photodiodes; e.g. the output from the reference interferometer is detected on quadrant photodiodes PDRA and PDRB. This provides a level of redundancy as all the optical information is present at both quadrant photodiodes. The photodiode mounts are titanium pieces that are bonded to the baseplate using an epoxy. The photodiodes themselves then are fixed using a kinematic, or Kelvin, clamp to these mounts, [37]. For optimal performance the quadrant photodiodes must be well centred to the optical beams. The required positional accuracy of the photodiodes is described in more detail in section 6.8.1. The adjustment is achieved in the photodiode mounts which can be finely adjusted to optimise their alignment.

3.4 PHASEMETER

The optical bench interferometer is a heterodyne interferometer, which means that it works by measuring the phase of the beat signals obtained when two light beams are interfered with each other. Therefore the required distance, beam angle and laser noise information is encoded in the phase of the photodiode photo-currents signals. The function of the Phasemeter, [32], is therefore to derive the phase of each of the 16 nominal and 16 redundant input channels. This derivation of phase is achieved using a Discrete Fourier Transform (DFT) technique. Therefore each photocurrent signal is initially amplified and anti-alias filtered, and then converted to the digital domain by 16 bit analogue to digital converter (ADC).

The anti-alias filters are required to limit the bandwidth of the measured signal to ensure compatibility with the sampling rate specification of the phasemeter; it is necessary to ensure that the process of sampling does not corrupt the useful portion of the signal. Practically, the anti-alias filters are low-pass filters which ensure that no significant part of the analogue signal exists above some fraction of the sampling frequency. The Nyquist and Shannon sampling theorem, [38] states that the sampling frequency should be at least twice the maximum frequency content of the signal. Typically, one does not know the frequency content of a signal prior to measuring it, but one does know the sampling frequency, so, a low pass filter is an appropriate way to limit the bandwidth of the signal.

To maintain the highest sample rate and ensure simultaneous channel sampling (to reject laser phase noise), each channel is connected to its own independent ADC. The DFT function is then provided by a dedicated digital signal processor (DSP) implemented on a Field Programmable Gate Array (FPGA). The four signals from a single quadrant photodiode are processed on a FPGA. Since the photocurrent is at a fixed and known frequency, only a single DFT bin need be calculated by the DFT algorithm. The DSP function is therefore termed a Single Bin DFT (SBDFT). It should be noted however that the zero frequency, or DC, bin is also computed to provide alignment and diagnostic information. For each signal channel, the outputs from the SBDFT process are the complex vectors $(x+jy)$ and the real DC vector. These data are transmitted to the LTP Data and Diagnostics System (DDS) for further processing and packaging prior to being transmitted back to Earth via the craft's telemetry system.

4 PROJECT ENGINEERING CONTROL

Owing to the complexity of the precision instrumentation and the rigours of the space environment, [39], UBI's contribution to the LISA Pathfinder project required significant input beyond the purely technical.

4.1 MY RESPONSIBILITIES

As this thesis describes my work, it is appropriate to make clear which aspects of the project work carried out at Birmingham were my responsibility. I have been responsible for;

- Preparing structural calculations and finite element models to qualify the phasemeter, optical bench interferometer, and photodiodes against launch and flight design loads,
- Preparing the photodiode requirements specification, which allowed the procurement of photodiodes which were compatible with the scientific requirements of the optical bench interferometer, the specific requirements of a precision gravitational experiment, and the mission engineering requirements,
- Designing a photodiode mounting system which enables photodiodes removal and replacement with the minimum of disruption to the surrounding optical bench structure,
- Overseeing the production of the mechanical parts for LISA Pathfinder, liaising with both internal machine shop staff and outside contractors where appropriate,

- Preparing the qualification test procedures for the LISA Pathfinder hardware, ensuring compliance with higher level satellite requirements,
- Instigating non-conformance reporting procedures, and chairing the resulting international review boards,
- Presenting the design, assembly, integration, test and schedule status at formal design reviews and project progress meetings,
- Designing, building, and commissioning an optical test facility which was used to provide detailed response scanning of the photodiodes. The facility was used to grade the detectors, allowing the selection of the detectors with the least deviations from ideal responsivity for flight use,
- Preparing fracture mechanics calculations and photo-elastic inspections to ensure the integrity of the brittle, ceramic, optical bench. I presented a technical report combining the elements of calculation and inspection to allow the flight qualification of the optical bench with an acceptably low probability of failure during the extreme mechanical environment of launch.

As a result of these activities, the new knowledge that represents my own intellectual input to the project includes:

- a) Conceptual and experimental design of the fracture control system for the optical bench interferometer,
- b) Analysis and interpretation of the optical bench interferometer fracture inspection scanning data,

- c) Conceptual and experimental design of the photodiode mounting system and demonstration that it meets the mission environmental requirements and the stability requirements for use on the optical bench interferometer
- d) Conceptual and experimental design of the photodiode responsivity scanning facility
- e) Analysis and interpretation of the photodiode responsivity data

4.2 DOCUMENT MANAGEMENT

4.2.1 Document Numbering System

In order to allow documentation to be identified and referenced, and project wide numbering system was established, and made mandatory for project participants, [40].

The format of the numbering system was defined as per this example;

S2-UBI-DRW-3004

S2 – The project identifier, Smart 2, i.e., LISA Pathfinder

UBI – The institution identifier, in this case, the University of Birmingham

DRW – The document type identifier, in this case, a **drawing**

3 – Project element identifier, in this case, LISA test package level

004 – The sequential document number, in this case, the fourth document of its type

The available project identifiers are defined below;

	<i>Project Element Identifier</i>
1	Management
2	Spacecraft
3	LISA Technology Package
4	Launcher
5	Ground segment mission analysis
6	Disturbance Rejection System

The available document type identifiers are defined below;

Architectural Design Document	ADD	Management Requirements	MR
Budget Report	BR	Non Conformance Report	NCR
Schedule, Network Chart	CH	Others	OTH
Contract	CON	Plan	PL
Certificate	CE	Project Managers Meetings Reports	PMM
Contract Change Notice	CCN	Procedure	PR
Change Proposal	CP	Progress Report	PRR
Change Request	CR	Presentations / Handout	PRS
Configuration Status List	CS	Purchase Specification	PS
Detailed Design Document	DDD	Product Tree	PT
Development and Verification Plan	DVP	Parts List, or Documents List	PTL
Document Requirements List	DRL	Requirement Control Document	RCD
Drawing / Diagram	DRW	Request for Deviation	RFD
Data Package	DP	Request for Quotation	RFQ
Design Specification	DS	Request for Waiver	RFW
Engineering Change Proposal	ECP	Report	RP
Experiment Interface Document	EID	Requirement Specification	RS
H/W Architectural Design Document	HAD	Statement of Compliance	SC
Interface Control Document	ICD	Statement of Work	SOW
Information Item	INF	S/W Requirements Document	SRD
Interface Requirements Document	IRD	Technical Note	TN
Invitation To Tender	ITI	Test Procedure	TP
List	LI	Test Report	TR
Manual	MA	Test Specification	TS
Minutes of Meeting	MN	Verification Control Document	VCD
		Work Breakdown Structure	WBS
		Part Approval Document	PD

PS – was a UBI document identifier, which was not recognized by the ESA documentation system, but, was useful internally.

4.2.2 Documentation Creation and Management

In order to comply with the document numbering convention described in section 4.2.1, a document register was created. Alongside the register, a consistent directory structure was created, and all project staff were encouraged to save documents to this directory rather than into personal data storage space. The register provided a means of identifying the next available document number for each document type, and via the use of hyperlinks, finding and opening the latest version of a document was simplified.

One weakness of the spreadsheet solution was that it relied upon all members of the team always updating the register after making changes. If this system were being recreated, this aspect of the documentation control would be implemented in a more automatic manner.

The document control system worked well during the LISA Pathfinder project, and the centralised document storage facilitated concurrent contributions by members of the team.

4.3 REVIEW PREPARATION

Owing to the multi-institutional nature of the LISA Pathfinder project, the design and analysis work carried out at Birmingham was subject to formal external reviews.

4.3.1 Preliminary Design Review

The preliminary design review, (PDR), was held on 10th November 2005. In order to allow the review to take place, the documents were prepared by the team and submitted to the industrial architect and the agency approximately a month earlier. The preliminary design review enabled a review and feedback of the flight design to take place before the end of the detail design stage, thus allowing the design to be updated using the latest feedback and specification changes.

The submitted documents included;

- Plans
 - EMC control plan
 - Magnetic control plan
 - Cleanliness and contamination control plan
 - Integration and verification planning
- Specifications
 - Proto-Flight Model Phasemeter requirements specifications
 - Photodiode requirements specifications
 - Bread board model phasemeter requirements specifications
- Interface control documents

- Mechanical Interface definition
- Thermal Interface definition
- Electrical Interface definition
- PA documentation
 - Product Assurance & Safety Plan
 - Critical Item List
 - Declared Material List
 - Declared Process List
 - Declared Component List
 - Failure modes and effects analysis
 - Verification control document
- Detailed design documentation
 - Thermal design & Analysis Report
 - Design Description
 - Thermal Mathematical. Model (ESATAN, ESARAD)
 - Structure Design & Analysis Report
 - Power Supply design & analysis report

- Data Handling Design & Analysis Report
- Gravitational Control Analysis Report
- Gravitational Mathematical Model
- EMC & Electrostatic Control status report
- Mechanical Environmental & limit loads analysis report
- LISA Test Package, (LTP), Subsystem Design Synthesis Report
- Subsystem/Unit Budget Report
- Geometric / configuration model (CAD)

After the documents were submitted and reviewed, the Review Item Discrepancies, (RIDs) were published on the ESA Project Reporting Integrated System for Management and Administration (PRISMA) web-page, [41]. After responding to these RIDs a telephone conference was held to discuss them, and any RIDs which could be dealt with and dismissed were disposed of. The remaining, outstanding, RIDs were considered in more detail during the PDR co-location meeting.

Following the creation and discussion of the RIDs, the design and technical planning were revised, and the associated documentation was updated accordingly.

4.3.2 Critical Design Review

The critical design review, (CDR) was held on 23rd & 24th November 2006, and followed a similar agenda to the PDR.

Among documents created for the CDR, the verification matrix collected together all of the technical, qualification, testing, and procedural requirements for the proto-flight model phasemeter and the flight and flight spare photodiodes. The list comprising over 1300 requirements was sub-divided into requirements verified via test, analysis, inspection, review, or combinations thereof. The verification matrix allowed the team to identify how each requirement might be met, and if any of the requirements were impossible to fulfil. The requirements which were identified as impossible, or impractical became the subject of requests for waiver which were submitted to the industrial architect and the agency.

Using the verification matrix, the requirements verified by test were identified. This sub-list was used in order to ensure that all the relevant requirements were correctly transposed into the test procedure documents.

The critical design review enabled the design to be checked, reviewed, and feedback incorporated before any irrevocable steps were taken in the build process, i.e., the last chance to make changes before metal was cut and components were soldered into place.

4.3.3 Oversight Committee

As the UK contribution to the LISA Pathfinder project was funded via STFC, this meant that significant sums of public money were being spent. Owing to the use of public money, the

oversight committee was formed to provide independent scrutiny over the project teams. The committee comprises senior space scientists, the National Project Manager, and representatives of the Science and Technology Funding Council.

Meetings were held where the UK project teams, namely Imperial College London, The Universities of Glasgow, and Birmingham submitted details of their technical progress and financial status to the committee. As of 7th May 2009, 12 oversight committee meetings had been held for the LISA Pathfinder project.

4.4 PROJECT REPORTING AND PROGRESS MEETINGS

During the earlier stages of the project, progress was reported to the project on a monthly basis via a formal document. The documents included sections describing;

- Progress summary,
- Documentation Status,
- Outstanding Action Item Status,
- Work Package status,
 - Project Management
 - Travel
 - Prototype development
 - Proto-flight model design

- Proto-flight model build
- Environmental Test
- AIT
- Spacecraft AIV and Test Support
- Spacecraft in-orbit support.
- Schedule Status,
- Risk Assessment Status,
- Procurement Status,
- Change Status,
- Meetings Plan,
- Project Staff.

Presentations of project activities were presented at regular progress meetings which were held with the industrial architect and the agency.

As the project neared the build phase, this level of formal reporting was agreed to be both too infrequent, and too time consuming. It was mutually agreed to provide weekly “Flash Reports” in the form of a brief email to update the project of progress and problems.

4.5 PRODUCT ASSURANCE

4.5.1 Product Assurance Planning

Ideally, it is usual practice to have independent technical oversight of the project. Usually a member of staff who bears no direct responsibility for the delivery of the instrument carries out this product assurance, (PA) role.

Owing to the small size of the group, it was not possible to provide the level of independence which is normally sought, and an experienced, ESA qualified member of staff acts as a point of contact for PA activities.

Guided by project requirements, [42], a PA plan was devised which defined how the following activities would be managed, controlled, or carried out;

- PA Management
- Quality Assurance
- Dependability Assurance
- Safety
- EEE Components
- Materials, Processes and Mechanical Parts
- Configuration Control
- Software Product Assurance

- Off the Shelf Equipment
- Ground Support Equipment

As UGL were considered by the project to have insufficient space PA experience, UBI offered PA support for the optical bench and photodiodes.

4.5.2 Non Conformance Reporting

During the procurement and build phases of flight equipment, it was necessary to inform the project when any problems which would affect the quality of the flight parts were found. The reporting of non-conformances, the resulting investigations, action tracking, and close out details were managed by a centralised ESA database, accessible via a web browser, [41]. An example of the non-conformance handling is included in the context of brittle fracture of an optical fibre in appendix C.

5 OPTICAL BENCH STRUCTURAL INTEGRITY

In order to reduce the risk of fracture of the optical bench, considerable effort was expended in calculation and finite element modelling work, aimed at estimating the severity of the stress borne by the bench, particularly during launch and separation from the launch vehicle. Unlike more common structural materials, the Zerodur® of the optical bench was particularly brittle, and was susceptible to failure via the propagation of initially small cracks or defects.

Many engineering materials fail via yielding, followed by plastic collapse. In assessing such ductile materials, there are well defined failure criteria, the most common being the Von-Mises criterion, [43]. This criterion, also sometimes called the distortion-energy theory allows the tri-axial stress state which might exist within a solid to be related to the yield stress of the material as determined during a uni-axial tensile test. The Von-Mises criterion requires knowledge of the three principal stresses, and is shown in equation 23, below.

$$2 \sigma_y^2 = (\sigma_1 - \sigma_2)^2 + (\sigma_2 - \sigma_3)^2 + (\sigma_3 - \sigma_1)^2 \quad \text{Equation 23}$$

Where σ_y is the uni-axial yield stress, σ_1 , σ_2 , and σ_3 , are the principal stresses (in descending order of magnitude). Further information on principal stress is presented in the section describing the stress birefringence inspection of the optical bench, section 5.3.4.2.

This plastic failure mode is more benign than brittle fracture, as the material continues to support load after it has yielded and suffered plastic deformation. If a small volume of material within a structure is loaded beyond its yield point, the load is simply re-distributed across the working section, and it is only when the entire working section approaches the yield stress that failure is imminent.

In contrast to this ductile behaviour, Zerodur® is a brittle material, which means that it fails via the propagation of a crack across the section with little or no plastic deformation. As the crack propagates through a volume of material, the material behind the crack front becomes unloaded – this actually re-distributes the load to the remaining material ahead of the crack, thus accelerating crack propagation.

Because the Zerodur® failure criterion was dependent upon the initial status of each individual piece of Zerodur®, the environmental treatment undergone by that particular sample, and the loading history and loading duration, it was not possible to simply set a failure stress for parts made from this material, [44].

5.1 MECHANICAL MODELLING

During the design phase of the project, the response of parts to mechanical loadings were assessed via methods of increasing complexity and detail. At the initial stages, and for simple components with simple loadings, hand calculations were completed first. If required, owing to either complexity, or because of a low margin result, the component's response might be assessed via computer based modelling techniques such as finite element analysis. Appropriate post-processing of finite element models highlights the critical areas of a component design.

Besides the fracture control issue, it was also necessary to demonstrate compliance with a number of project mechanical requirements, for example, in order to reduce the dynamic interaction between the spacecraft structure and the equipment mounted upon it, each component must have a natural frequency above 140 Hz. This natural frequency requirement ensures sufficient separation between the frequency content of the loads imparted from the launch vehicle to the payload and the response natural frequencies of that payload, [45].

In order to reduce the complexity of any hand calculations and finite element modelling, the detail of the optical components mounted upon the surface of the optical bench was not explicitly modelled. However, their mass was added to that of the baseplate via a modified density.

Owing to the thin layer of epoxy between the titanium insert and the cylindrical housings bored into the sides baseplate, it was a complex task preparing a model which had sufficiently small elements to allow the stresses in the epoxy layer to be correctly calculated, with sufficiently gradual transitions to larger elements in the Zerodur[®], and with a sufficiently small number of total elements to allow solution of the model within tolerable timescales with the available computing resources, [46], [47].

5.1.1 Introduction and Configuration

The optical bench consists of a baseplate formed from Zerodur[®] glass ceramic material. Into the two opposing sides of the baseplate, a total of eight titanium inserts were placed. These inserts contained internal threads which allowed the baseplate to be secured to the side plates. A rendered image of the CAD model of the optical bench, with generic photodiode mounts, is shown in figure 9, below.

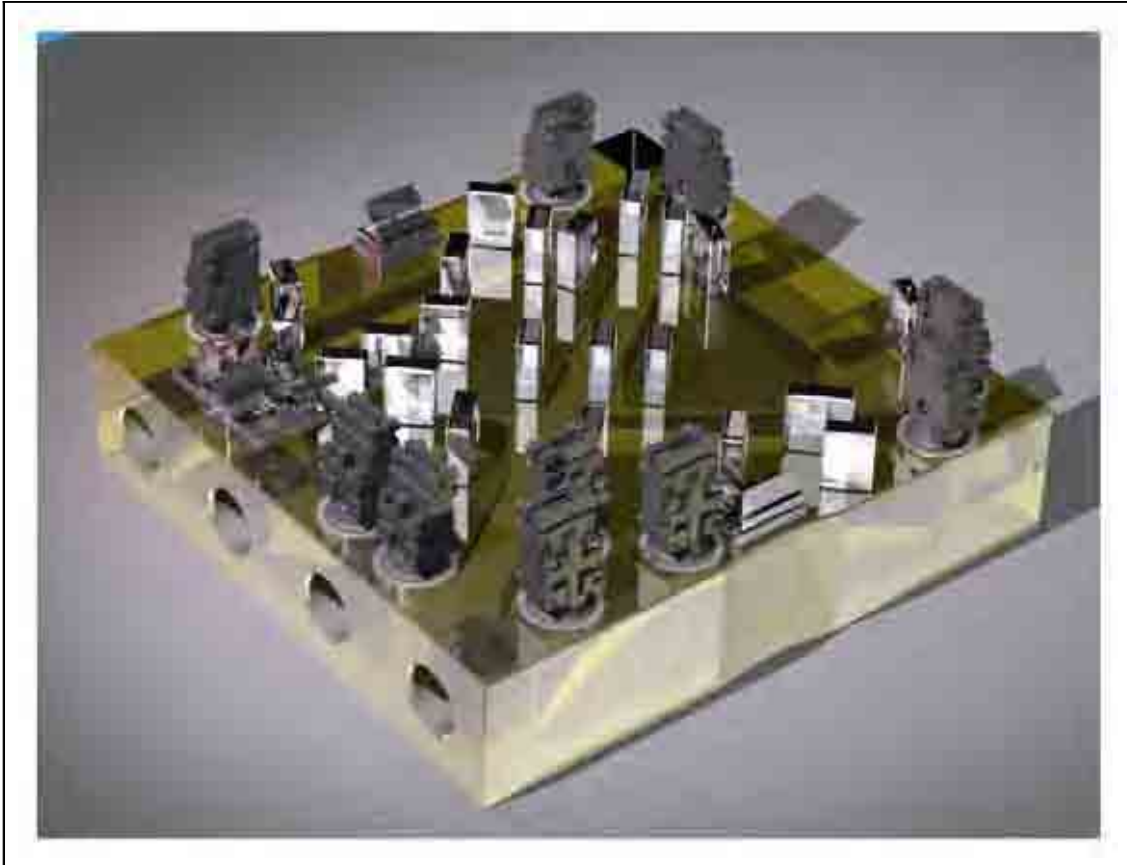


Figure 9: Optical Bench CAD Rendering (Source: [48])

The upper surface of the baseplate was polished flat within a tolerance of $\lambda/10$, (in this context, $\lambda \sim 600$ nm) over any 30 mm. Onto this surface, a number of optical components were bonded using the hydroxyl catalysis technique. Photodiodes were also bonded to the upper surface of the optical bench, using epoxy, as described in, [49], and as shown in figure 10, below, where the grey epoxy extruded during the bonding process may be seen around the periphery of a titanium photodiode base.



Figure 10: Photodiode Bond Detail

Owing to the restrictions of available time and computing resources, it was not possible to produce a model which combined realistic modelling of the inserts with realistic modelling of the lightweighting features. A sub-model of one insert was prepared thus enabling the estimation of the mechanical stiffness of the insert, and obtaining some insight into the stress distribution in the insert hole.

It was envisaged that the areas of concern for stress would be inside the insert hole, the points of attachment of optical devices on the upper surface of the baseplate, and in the fillet radii of the

lightweighting features. As the photodiodes were of light construction, circa 100 grammes each, and partially mechanically isolated from the Zerodur[®] by a relatively compliant layer of epoxy, it was initially envisaged that the dynamic mechanical loading of the photodiodes did not represent a concern. In order to estimate these mechanical loads, consider the response of a photodiode to a vertical quasi-static acceleration of 30 g, assuming the epoxy bond was formed by a thin cylindrical section of diameter 20 mm.

$$\begin{aligned}
 \sigma &= \frac{\text{Force}}{\text{Area}} \\
 &= \frac{\text{Mass} * \text{Acceleration}}{\text{Area}} \\
 &= \frac{4 * 0.1 * 30 * 9.81}{\pi * (20 * 10^{-3})^2} \\
 \sigma &= 94 \text{ kPa}
 \end{aligned}
 \tag{Equation 24}$$

This average stress level was over one hundred times lower than even the most conservative estimates for the failure stress of Zerodur[®], 10 MPa, [44]. The material properties for Zerodur[®] are listed in table 2, below, [44];

<i>Property</i>	<i>Value</i>
Young's Modulus @ 20 °C	90.3 GPa
Poisson's Ratio	0.243
Density	2530 kg/m ³
Plane strain fracture toughness	0.9 MPa √m
Table 2: Zerodur[®] Mechanical Properties	

As may be seen in figure 9, the optical bench interferometer is not a simple instrument, however, in order to simulate the body forces on the Zerodur® baseplate, the presence of the optical components mounted on the upper surface of the optical bench was modelled by an increased material density (2900 kg/m^3), and thus, the as modelled, mass of the optical bench baseplate was 4.2 kg

5.1.2 Scoping Calculations

In order to obtain preliminary estimates of the response of the optical bench, simplified scoping calculations were carried out, [50], using the engineering model optical bench geometry as input data. The important results of these calculations are also shown in equations 25 and 26, below.

The optical bench was represented in these calculations as an idealised beam. In order to bound the potential boundary conditions as encountered when integrated into the LCA, the calculations were carried out for the case of simply supported and fully fixed support conditions, [51], [14].

Owing to uncertainty in the load sharing between the optical bench and the adjacent structure, well defined loads were not available, and would not become available as the load in the inserts was not measured during the LCA shock and vibration development testing carried out by ASD. A conservative loading was therefore used for initial design analysis in order to provide a bounding case. The calculations were based upon a body load equivalent to a quasi-static acceleration of 256 g. An acceleration level of 64 g was the stipulated design load as defined by the OMS Requirements specification, [32]. This 64 g load was then multiplied by a further factor of four to account for uncertainties in the inertial sensor mass, and in the suspension philosophy for the LCA, Thus, the 256 g load was agreed as a basis for design between ESA, ASD, and UBI.

The optical bench is supported using inserts which interface with corresponding inserts in the sideslab assemblies. A section through the optical bench, showing the insert, and the interface plane is shown in figure 11, below. Figure 11 also shows the radius cut into the Zerodur at the blind end of the insert hole. The insert is bonded to the optical bench using a thin layer of epoxy.

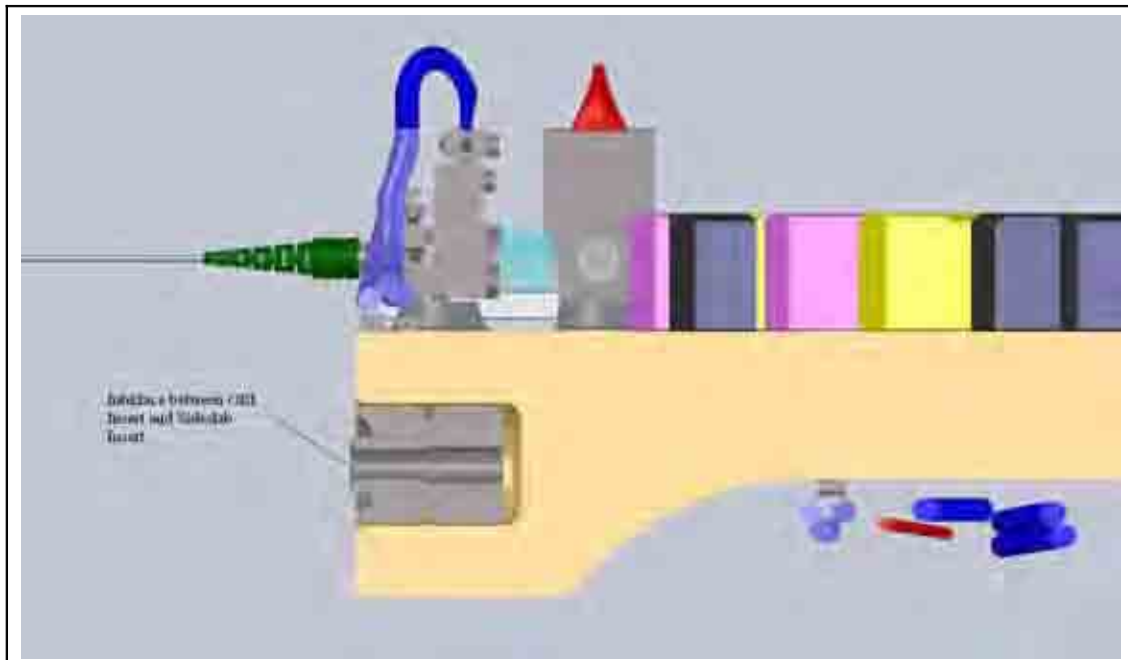


Figure 11: Section Through Optical Bench Showing Insert and Interface

For simply supported boundary conditions, as shown in figure 12, below, the maximum deflection and stress, occurring at mid span, may be calculated [52];

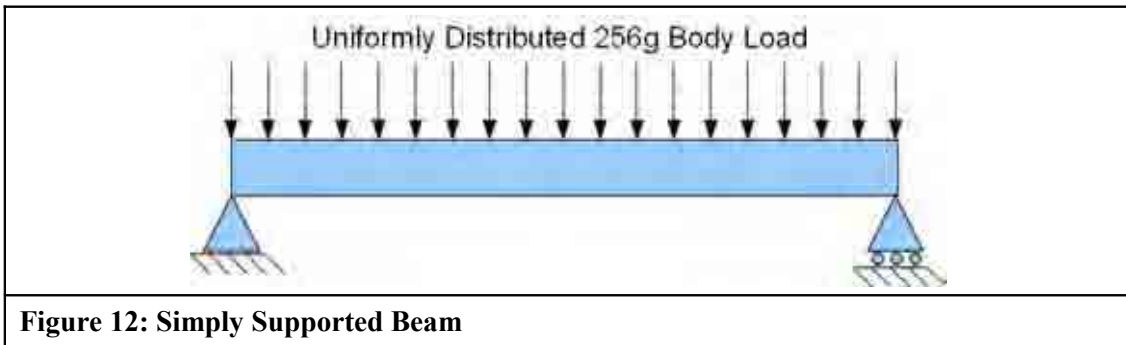


Figure 12: Simply Supported Beam

$$\begin{aligned}
 y_{MAX} &= \frac{5 w_a l^4}{384 EI} \\
 &= 9.5 \mu m \\
 \sigma_{MAX} &= \frac{w_a b l^2}{16 I} \\
 &= 18.4 \text{ MPa}
 \end{aligned}
 \tag{Equation 25}$$

For built in boundary conditions, as shown in figure 13, below, the maximum deflection and stress may be calculated;

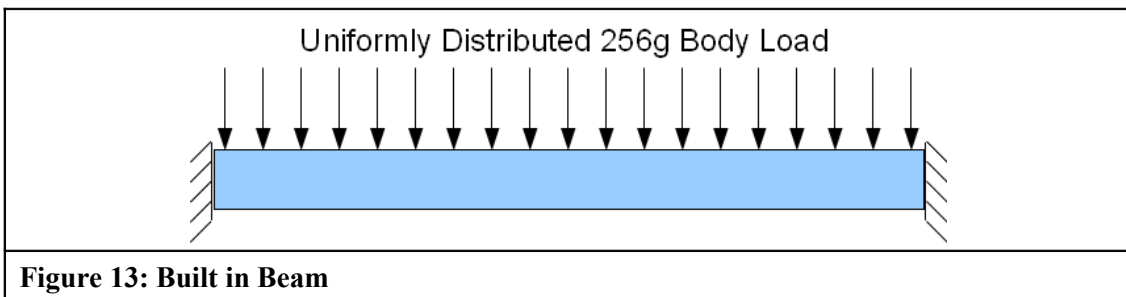


Figure 13: Built in Beam

$$\begin{aligned}
 y_{MAX} &= \frac{w_a l^4}{384 EI} \\
 &= 1.9 \mu m \\
 \sigma_{MAX} &= \frac{w_a b l^2}{24 I} \\
 &= 12.2 \text{ MPa}
 \end{aligned}
 \tag{Equation 26}$$

where w_a is the uniformly distributed load, l , the length spanning between the supports, E , the Young's modulus of the Zerodur[®], and I , the second moment of area of the section. Under a 256 g body load, the deflections estimated by this method were between 1.9 and 9.5 μm , while the estimated stress was between 12.2 and 18.4 MPa.

The proto-flight model optical bench had been lightweighted, and in reality contained locating features, such as insert holes. The stress local to these features was expected to be higher than that found using the 256 g estimate, although the bulk stress and maximum deflections were perhaps lower, owing to the reduced body load of a lightweighted bench.

The complex geometry of the lightweighted proto-flight model optical bench precludes any meaningful attempt to carry out more extensive scoping hand calculations.

5.2 FINITE ELEMENT ANALYSIS

5.2.1 Initial Model

In defining a finite element model, it was envisaged that the areas of concern would be inside the insert holes, the points of attachment of optical devices on the upper surface of the baseplate, and in the fillet radii of the light-weighting features. In order to gain an initial overview of the stress distribution, a finite element model was created with a simplified representation of the inserts and the boundary conditions enforced by the inserts. This model and its results are described below.

Two extreme support conditions for the optical bench: simply supported, and fully fixed were modelled. The optical bench baseplate CAD model was converted to MSC NASTRAN, [53], format, and was modelled as a linear isotropic solid, using tetrahedral elements, [46], [47].

The initial finite element model used a fictitious, comparatively rigid, insert with no epoxy layer, combined with the rigid inserts being constrained simply, while a vertical acceleration body load was applied

The resulting (exaggerated) deflections for accelerations applied in the positive and negative Z directions are shown in figures 14 and 15, below.

Although the assumption of a simply supported boundary condition led to an underestimation of the stress in the area of the insert as there was no constraint moment applied at the insert, it was conservative when considering the stress in the bulk Zerodur[®] as the effective hinge provided by the simple supports allowed a larger bulk deflection.

While the mesh was not yet fully refined, the results allowed the design work to proceed while further analysis was carried out.

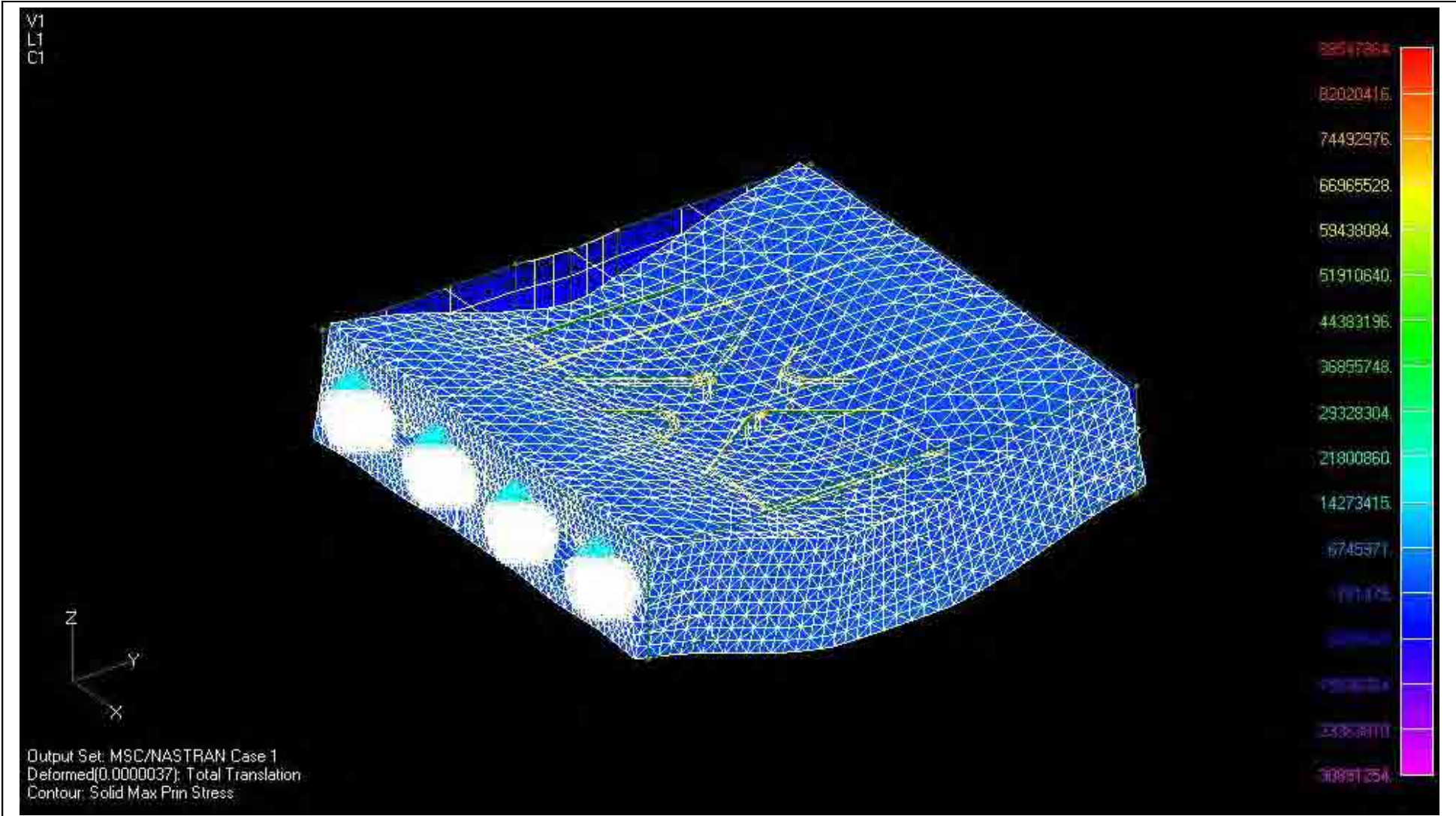


Figure 14: Optical Bench Principal Stress; +256g Z Direction

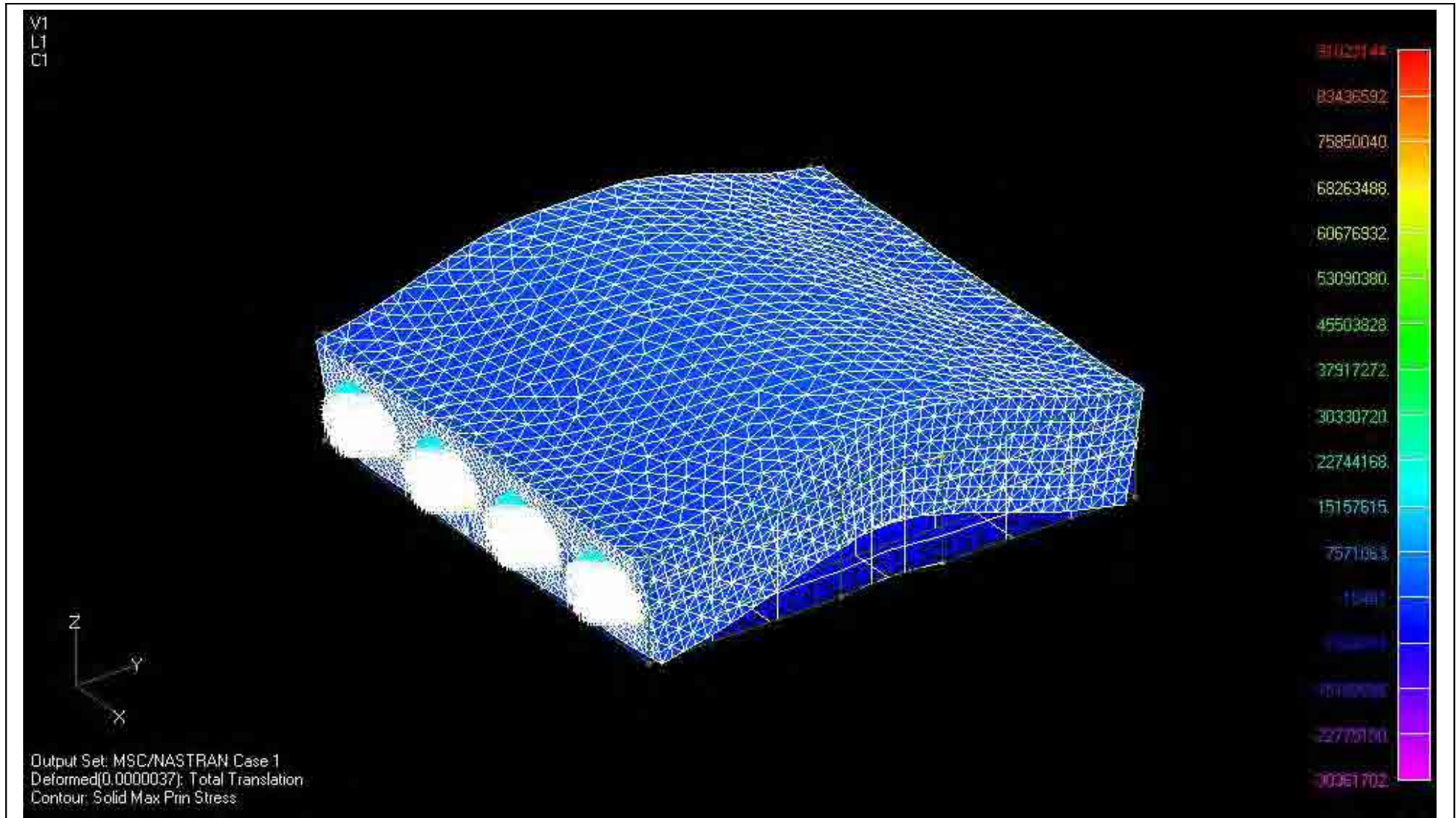


Figure 15: Optical Bench Principal Stress; -256g Z Direction

The maximum principal stress in the bulk of the simply supported lightweighted Zerodur® baseplate was found to be approximately 14 MPa, which compares with 18.4 MPa as previously estimated for the entire optical bench, [50].

The local stress level variations found in the model for the light-weighted optical bench may be partially explained by the reduction in the active volume of stress bearing material and the geometrical stress concentration factor in the area local to the cruciform where the stiffeners cross or meet, indeed, in areas removed from the cruciform, the stress levels reduced to approximately 6 MPa, suggesting the stress concentration was the dominant effect.

For the baseplate with simply supported boundary conditions, the deflection had previously been estimated, [50], as approximately 9.5 μm , while the finite element model reported a deflection of 17 μm .

Assuming the 17 μm deflection was produced by constant curvature, which is a reasonable assumption for a simply supported beam, this would be equivalent to a distortion of 1.7 μm from plane across the width of a photodiode. A representation of the optical bench surface curvature and the deflection of the photodiode bond is shown in figure 16, below. The photodiode finite element model was revised to consider the load on the joint resulting from this distortion. The maximum shear stress in the epoxy was 11 MPa, which compared favourably with the epoxy shear strength of approximately 22 MPa, i.e., the joint was not considered susceptible to failure via the mechanism of peel under deflection of the optical bench baseplate itself. Although peel failure is predominantly a bending failure, the shear strength of the epoxy is always lower than its tensile strength, and therefore, shear strength forms a conservative failure criterion.

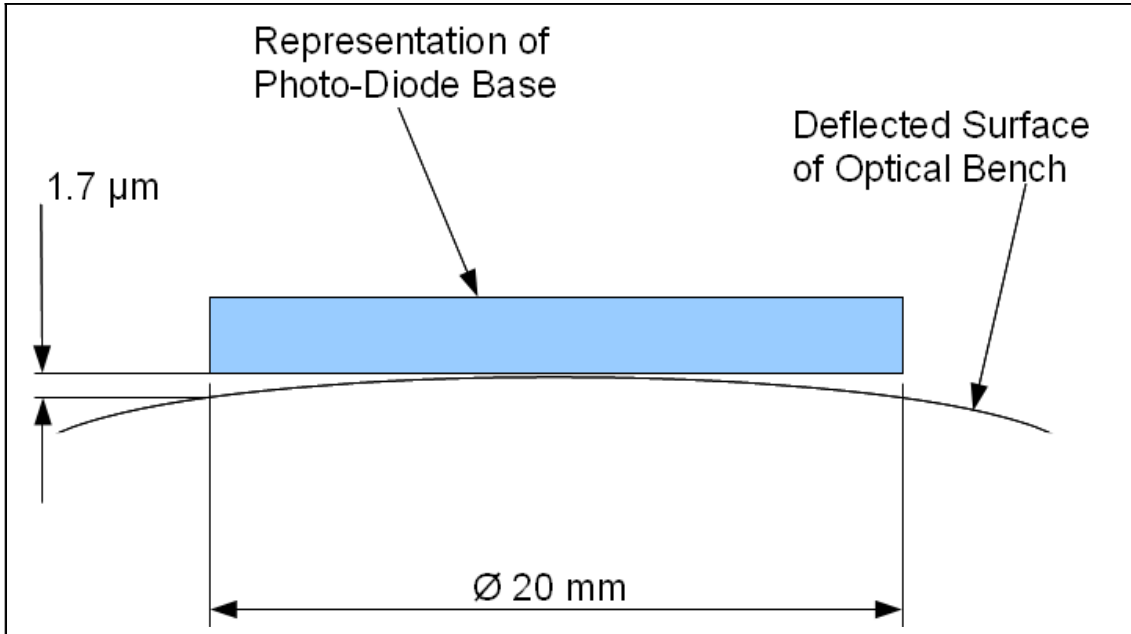


Figure 16: Representation of Optical Bench Deflection and Photodiode Bond Peel

In the bulk of the built-in Zerodur® baseplate, the maximum localised principal stress was approximately 8.3 MPa, which compares with 12.2 MPa as previously estimated for the entire optical bench, [50].

For the built-in lightweighted baseplate, the deflection has previously been estimated, [50], as approximately 1.9 μm. The deflection of the lightweighted optical bench under similar loading conditions is reported by the finite element model as 3.6 μm. These data are summarised in table 3, below;

<i>Calculation Method and Boundary Condition</i>	<i>Deflection (μm)</i>	<i>Stress (MPa)</i>
Hand calculation – Simply Supported	9.5	18.4
Finite Element Analysis – Simply Supported	17	14
Hand calculation – Built-in	1.9	12.2
Finite Element Analysis – Built-in	3.6	8.3

Table 3: Initial Analysis Results

The data in table 3, broadly indicate that the hand calculations provided an over estimate of the stress levels, but, they provided under estimates of the deflection.

As the optical bench interferometer would not be not active during these loading events, the deflections were not of primary importance, and were all of such a low level that neither mechanical interference of parts, or of problems with epoxy peel failures were envisaged. The stress levels, on the other hand, were considered sufficiently onerous to warrant further work.

5.2.2 Insert Analysis

Inserts are used to connect the optical bench to the sideslabs, as shown in figure 11 and then via struts, to the spacecraft structure, as shown in figure 17, below.

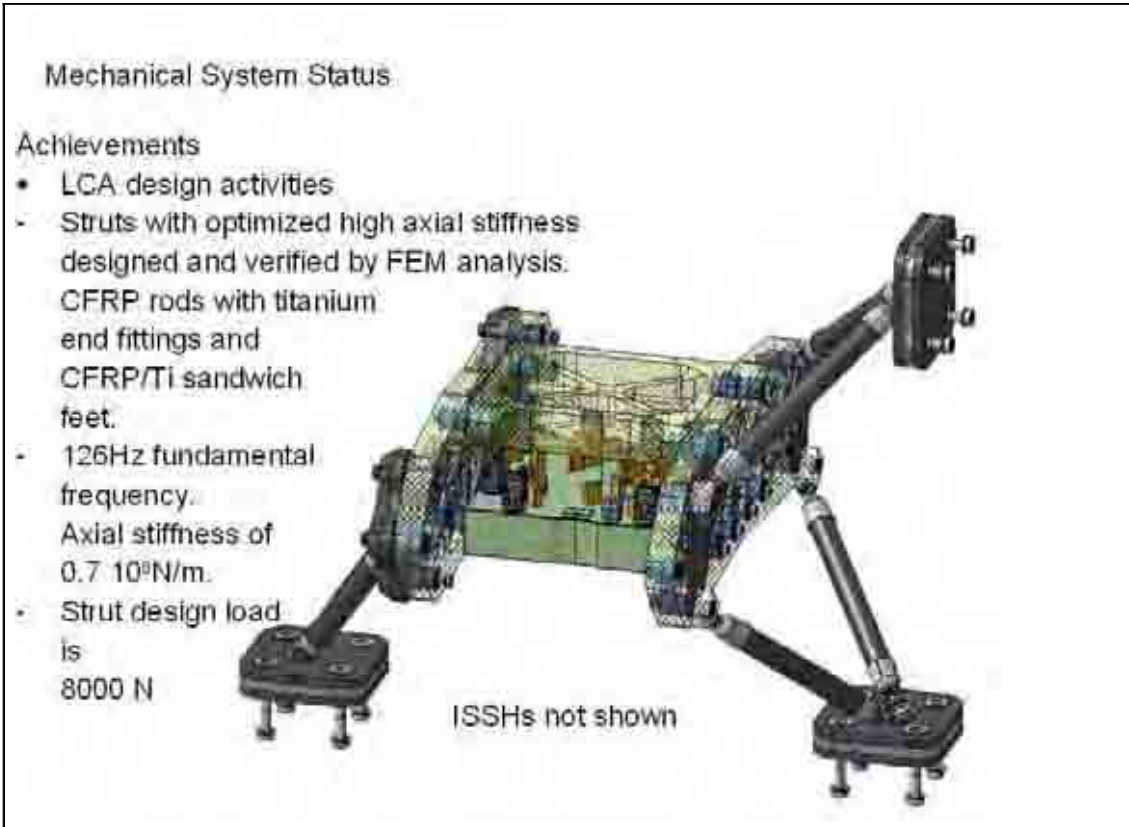


Figure 17: LCA, showing optical bench, sideslabs and support struts [54]

In order to improve the accuracy of the modelling, particularly in the area of the inserts, a sub-model was created. The layer of epoxy between insert and baseplate was modelled explicitly. This led to a large number of elements in the solid model, which led to slow and cumbersome model building, and extended computer run times when solving and post-processing, [55].

The stress in the area around the inserts was considered important, and was potentially the most onerously loaded part of the optical bench. Beyond simpler axi-symmetric models of the insert, this model allowed the application and analysis of off axis, or lateral loads. The solid mesh is shown in figure 18, below.

The larger diameter cylinder represented the Zerodur® of the optical bench itself, with the titanium insert hidden. The smaller cylinder in the upper part of figure 18 represented the

titanium insert in the Zerodur[®] sideslab – this was used to apply loads to the model at a realistic location, and via a loadpath with realistic stiffness.

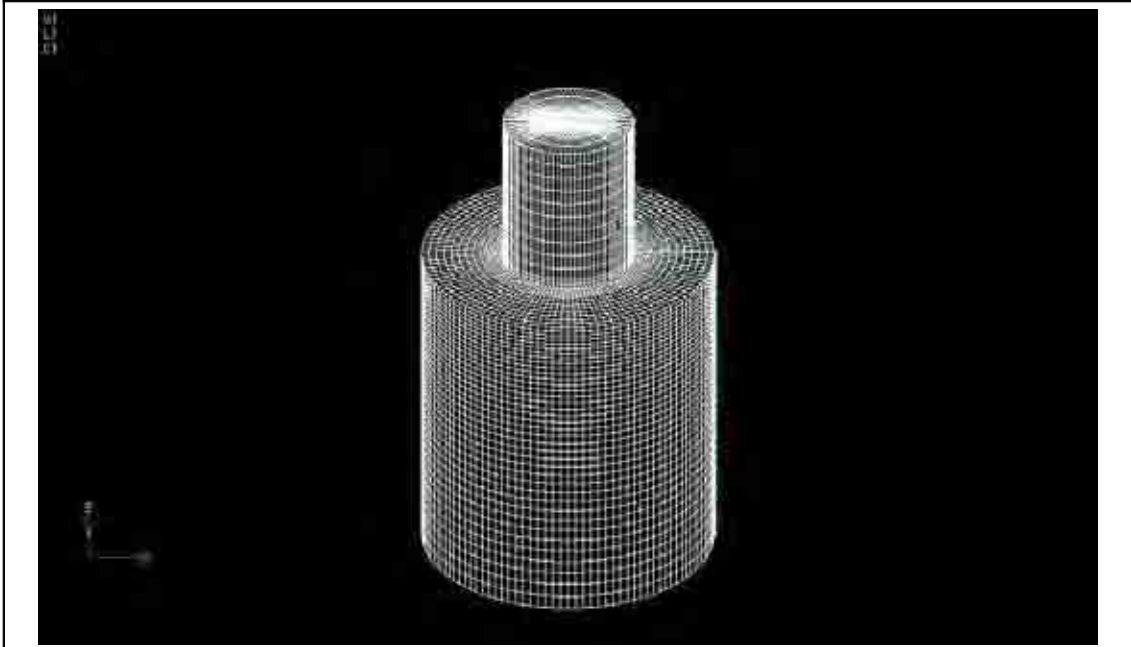


Figure 18: Insert Detailed Solid Model Mesh

Figures 19 and 20, below, shows the maximum principal stress in the Zerodur[®] under the application of 1320 N (1320N corresponds to 256g body load shared between inserts) in the Z, axial, direction, with a blend radius of 0.5 mm in the tip of the insert hole . For a section view of this hole and the radius, see figure 11. The load was applied to the extended titanium insert. The contours show the maximum principal stress in the area by the epoxy was 4.8 MPa, while the maximum principal stress in the area of the radius was 3.6 MPa.

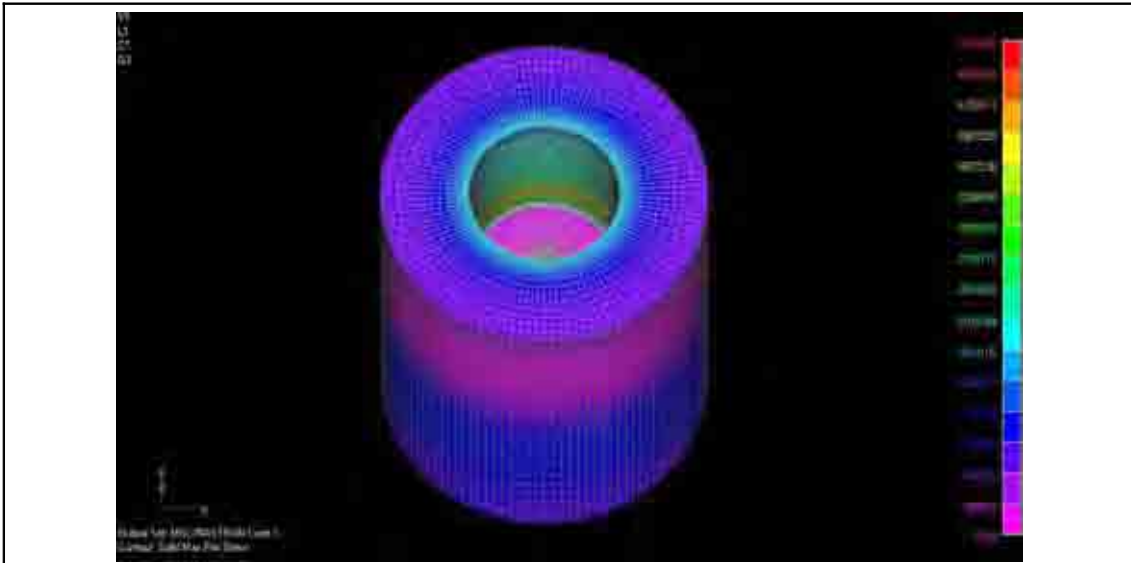


Figure 19: Zerodur® Insert Bore – 0.5 mm Radius – 1320 N Axial Load

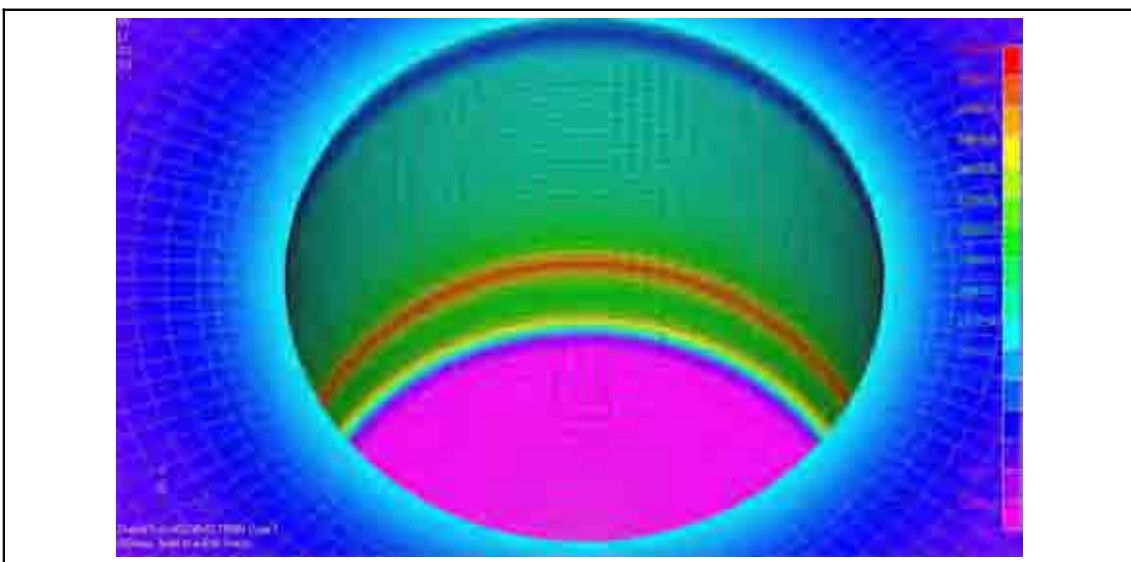
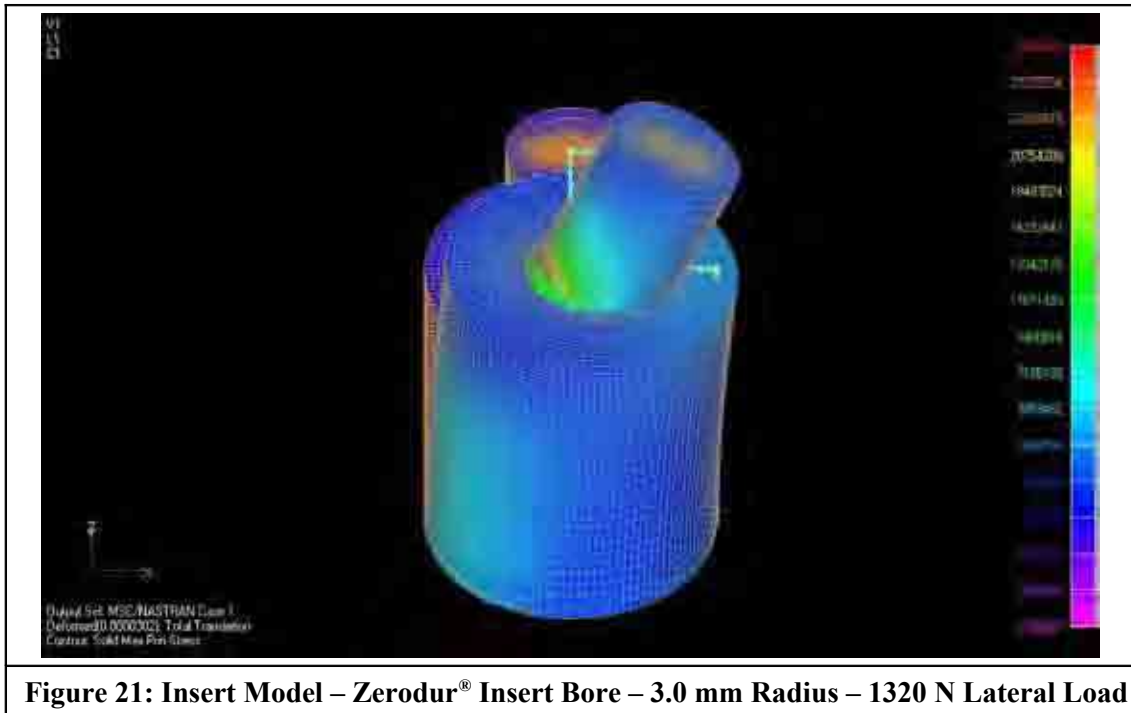


Figure 20: Zerodur® Insert Bore - 0.5 mm Radius - 1320 N Axial Load - Detail

Figures 21 and 22, below, show the maximum principal stress in the Zerodur® under the application of 1320 N in the X, lateral, direction, with a blend radius of 3.0 mm in the tip of the insert hole. The load was applied to the extended titanium insert. The stress contours indicate a

much larger stress, approximately 14 MPa, located near the outer edge of the epoxy was borne by the Zerodur[®].



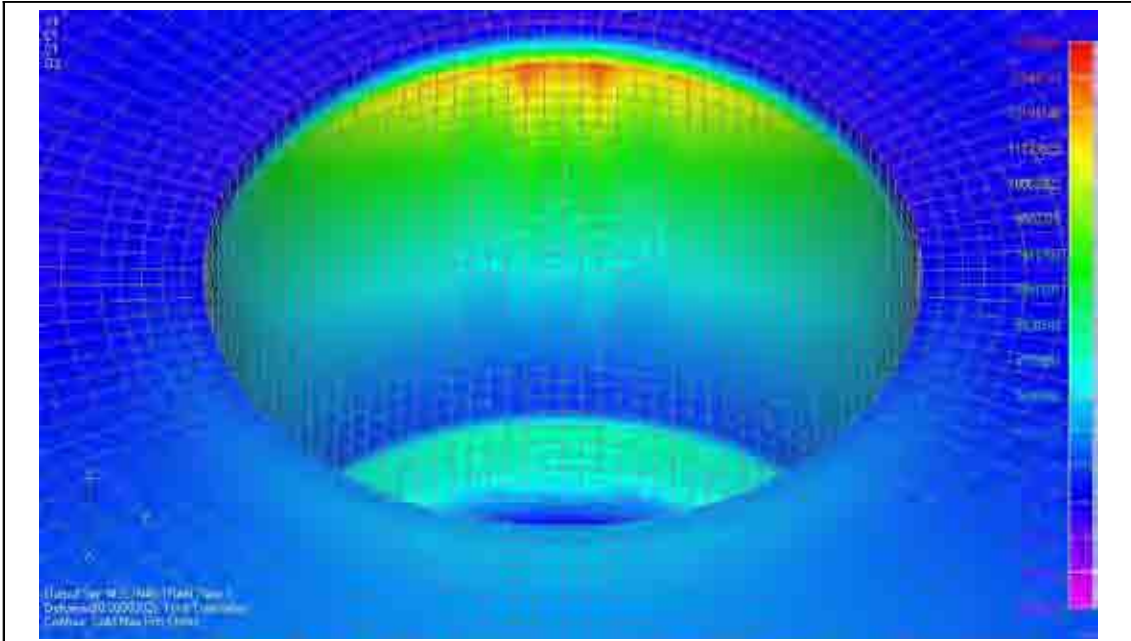


Figure 22: Insert Model – Zerodur® Insert Bore – 3.0 mm Radius – 1320 N Lateral Load – Insert Suppressed

Figure 23, below, shows the maximum principal stress in the Zerodur® under the application of a 30 °C change in temperature, with a blend radius of 0.5 mm in the tip of the insert hole. Owing to the differences in the coefficients of thermal expansion of the component materials, the application of a change in temperature to the structure results in the materials being stressed. Under this thermal load case, the estimated maximum principal stress in the Zerodur® was 13.5 MPa. This result had a direct relevance to the temperature limits which may be applied during the build processes of the bench, particularly, the curing cycles for the hydroxyl catalysis bonds between the fused silica optical components and the Zerodur® of the bench itself.

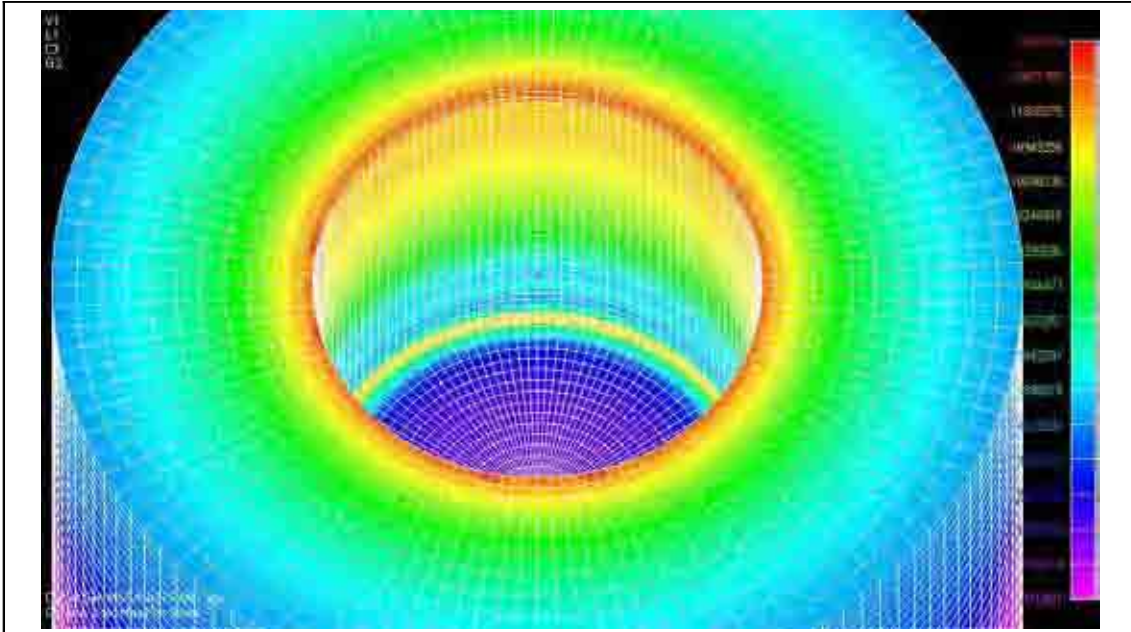


Figure 23: 0.5 mm Radius, 30 °C Thermal Load

The detailed insert model was also used to investigate the effect of changing the radius at the tip of the insert hole. The results are shown in table 4, below.

<i>Geometry</i>	<i>Stress Under Axial (Z) Loading (MPa)</i>	<i>Stress Under Lateral (X) Loading (MPa)</i>
0.5 mm Radius	4.81	13
1.0 mm Radius	4.81	14.3
1.5 mm Radius	4.82	14.4
2.0 mm Radius	4.83	14.5
2.5 mm Radius	5.1	14.4
3.0 mm Radius	4.9	14.3

Table 4: Stress Levels in Detailed Insert Model

The results shown in table 4 were somewhat surprising. It had been previously thought that a small radius would lead to a larger stress concentration, and hence, to a larger stress. However, the load was applied to the Zerodur[®] via the epoxy, and reducing the radius led to a larger separation between the point of load application and the stress concentration formed by the radius.

Among the purposes of the model was to obtain equivalent spring properties for the insert/epoxy combination. These spring properties were required in order to further understand how forces and moments would be applied to the optical bench.

By applying a load to each node within the insert, and separately to the section of insert outside the Zerodur[®], it was possible to apply a pure translational force in each of the three orthogonal directions in turn. Using the resulting average nodal displacement, the deflection of the insert was estimated. With knowledge of the total applied force and the average nodal displacement, the linear spring constants were estimated. A similar method was used to obtain the moment stiffness, by applying the nodal load in the opposite direction for nodes outside the Zerodur[®] – thus, the total applied force on the insert was zero, but, the moment was given by summing the product of force and axial location for each node. The spring constants so obtained are listed in table 5, below.

<i>Direction</i>	<i>Stiffness</i>
X (Radial)	2.0×10^{10} N/m
Y (Radial)	2.0×10^{10} N/m
Z (Axial)	1.3×10^{10} N/m
X Rotation	7.6×10^5 Nm/Rad
Y Rotation	7.8×10^5 Nm/rad
Z Rotation	1.3×10^6 Nm/Rad
Table 5: Insert Stiffness	

Owing to the thin layer of epoxy between the Zerodur[®] and the insert, these stiffness values were very high. Misalignments between adjacent inserts, even at the level of 10 μm have the potential to cause very large forces in the Zerodur[®]. The consequence of these stiffness values was that the optical bench must be initially assembled with the mating Zerodur[®] sideslabs with the epoxy un-cured, i.e., the alignment accuracy required precludes the use of an assembly fixture. Therefore, it was necessary to send the optical bench to ASD for insert integration with the sideslabs.

5.2.3 Revised Shape Baseplate Analysis

In order to provide extra mass reduction, and to simplify construction, a revised lightweighting scheme was proposed by ASD. This revision necessitated further analysis in order to ensure the adequacy of the re-design.

It was envisaged that the areas of concern would be inside the insert hole, and the points of attachment of optical devices on the upper surface of the baseplate. In order to gain an initial

overview of the stress distribution, a finite element model was created with a simplified representation of the inserts and the boundary conditions enforced by the inserts. This model and its results are described in section 5.2.4.3, below.

As before, two extreme support conditions, simply supported, and fully fixed were modelled.

In light of the difficulty in creating and running a fully detailed model, a sub-model was prepared, enabling the characteristic of the insert to be found. Using the equivalent spring constants, as given in table 5, for the inserts, the optical bench baseplate was modelled with representative boundary conditions. Finally, in order to obtain the stress distribution in the insert hole, the forces and moments obtained from a detailed analysis of the LCA, performed by ASD, were reapplied to the detailed insert model.

5.2.4 Baseplate Modelling

5.2.4.1 Simply Supported Model

The optical bench baseplate CAD model was converted to MSC NASTRAN format, and was modelled as a linear isotropic solid, using tetrahedral elements, [46], [47].

The initial finite element model used a fictitious, comparatively rigid insert with no epoxy layer, combined with the rigid inserts simply constrained, while a vertical acceleration body load was applied

The resulting deflections for accelerations applied in the negative Z directions are shown in figures 24 and 25, while the response to positive acceleration are shown in figures 26 and 27, below. Although this led to an underestimation of the stress in the area of the insert, it was conservative when considering the bulk Zerodur®.

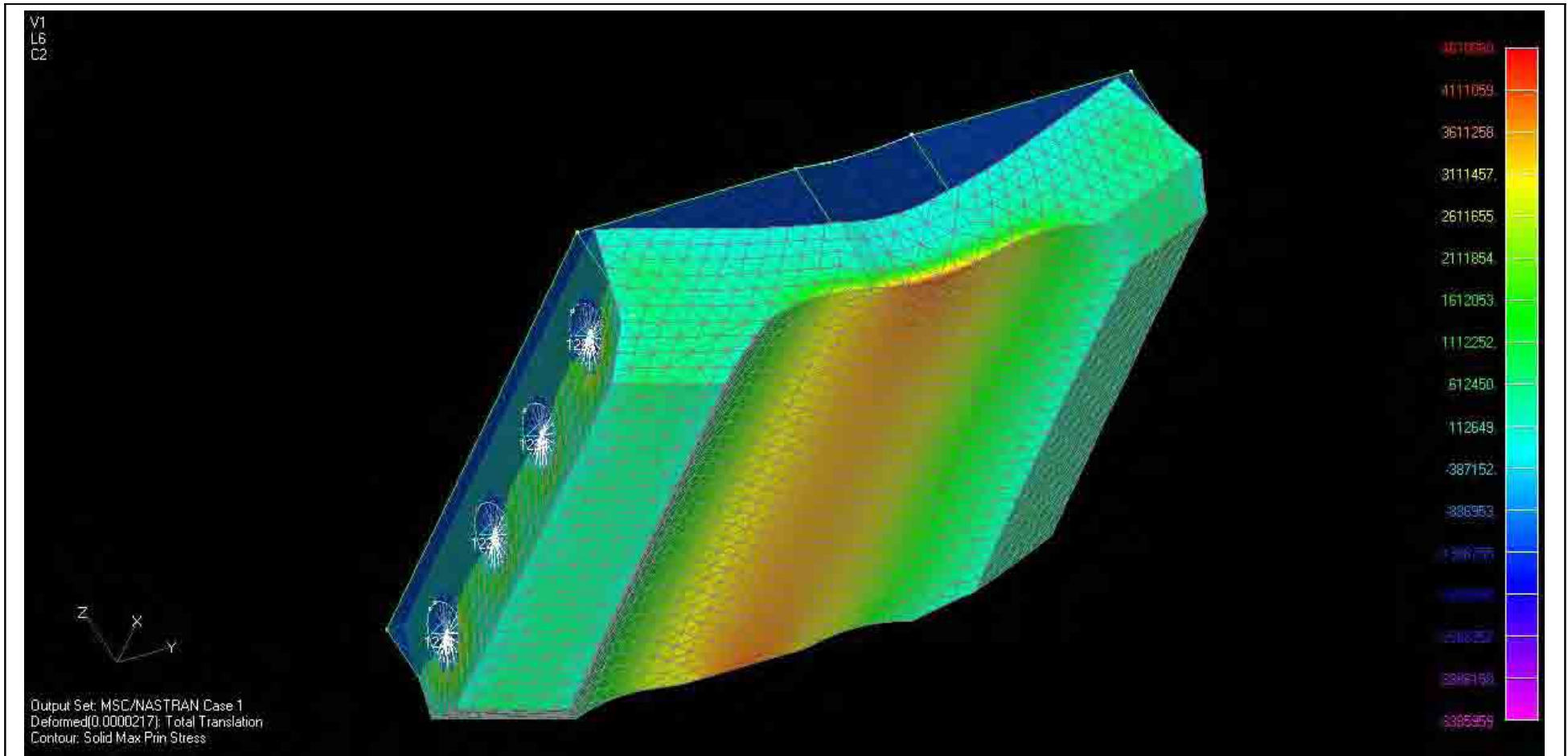
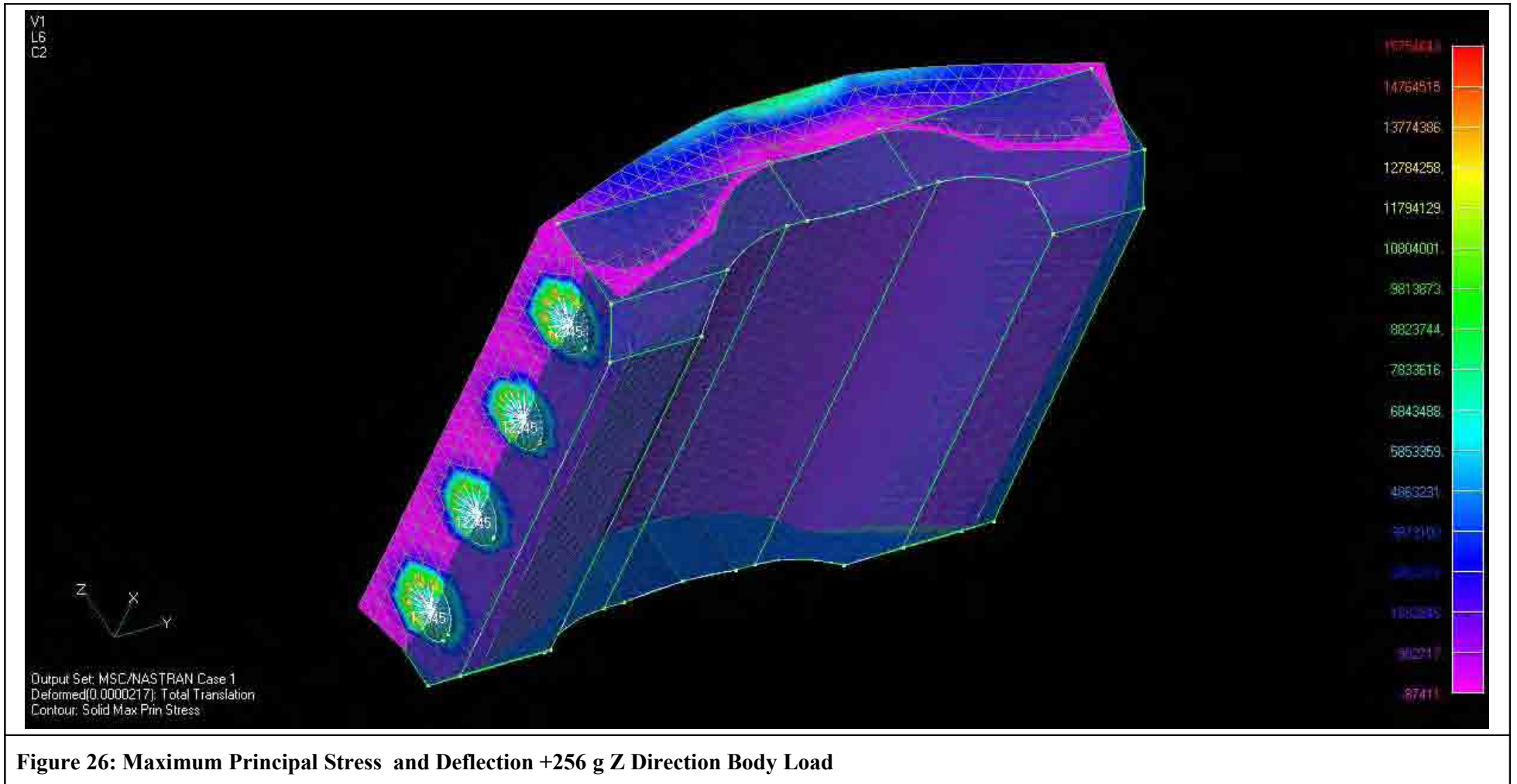


Figure 24: Maximum Principal Stress and Deflection –256 g Z Direction Body Load



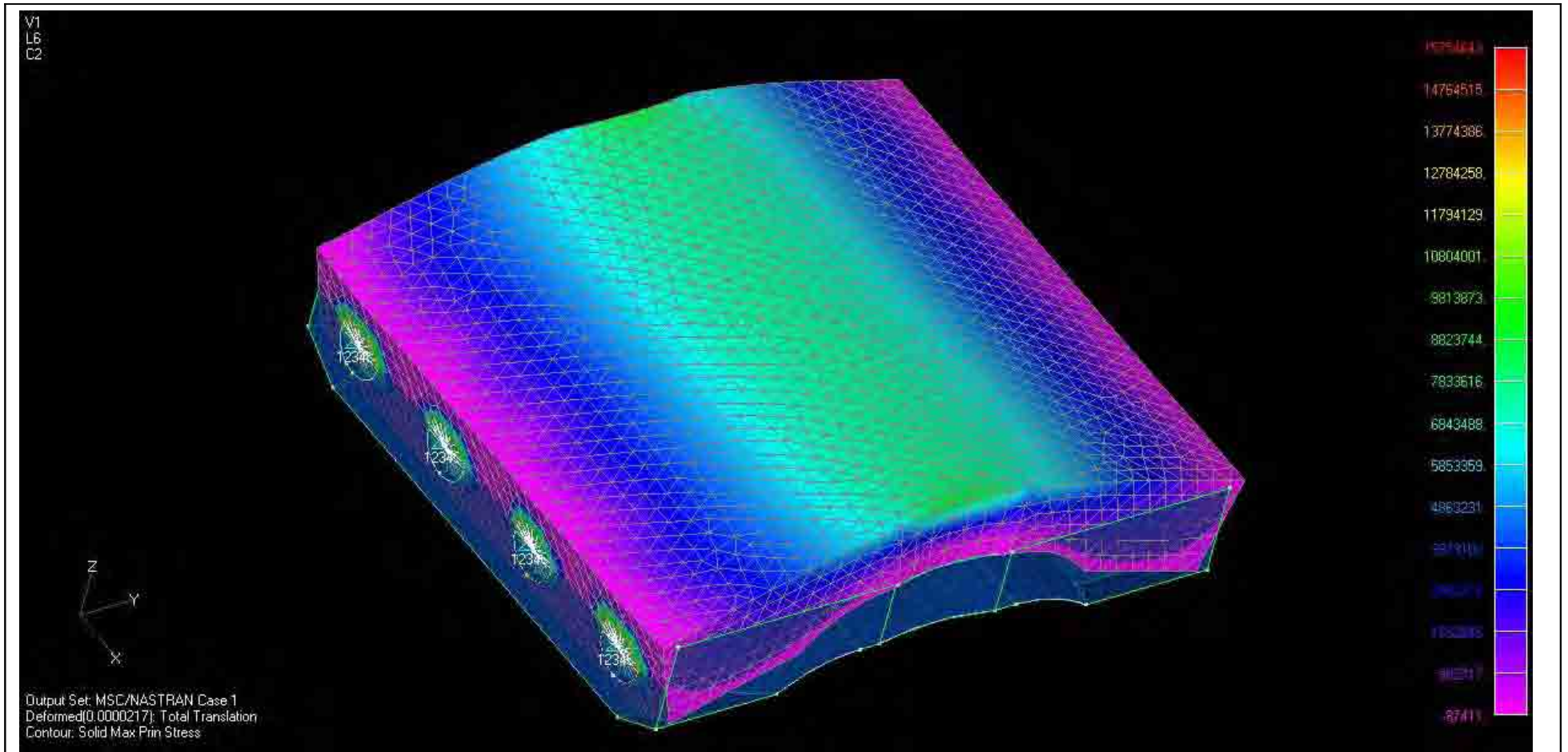


Figure 27: Maximum Principal Stress and Deflection +256 g Z Direction Body Load

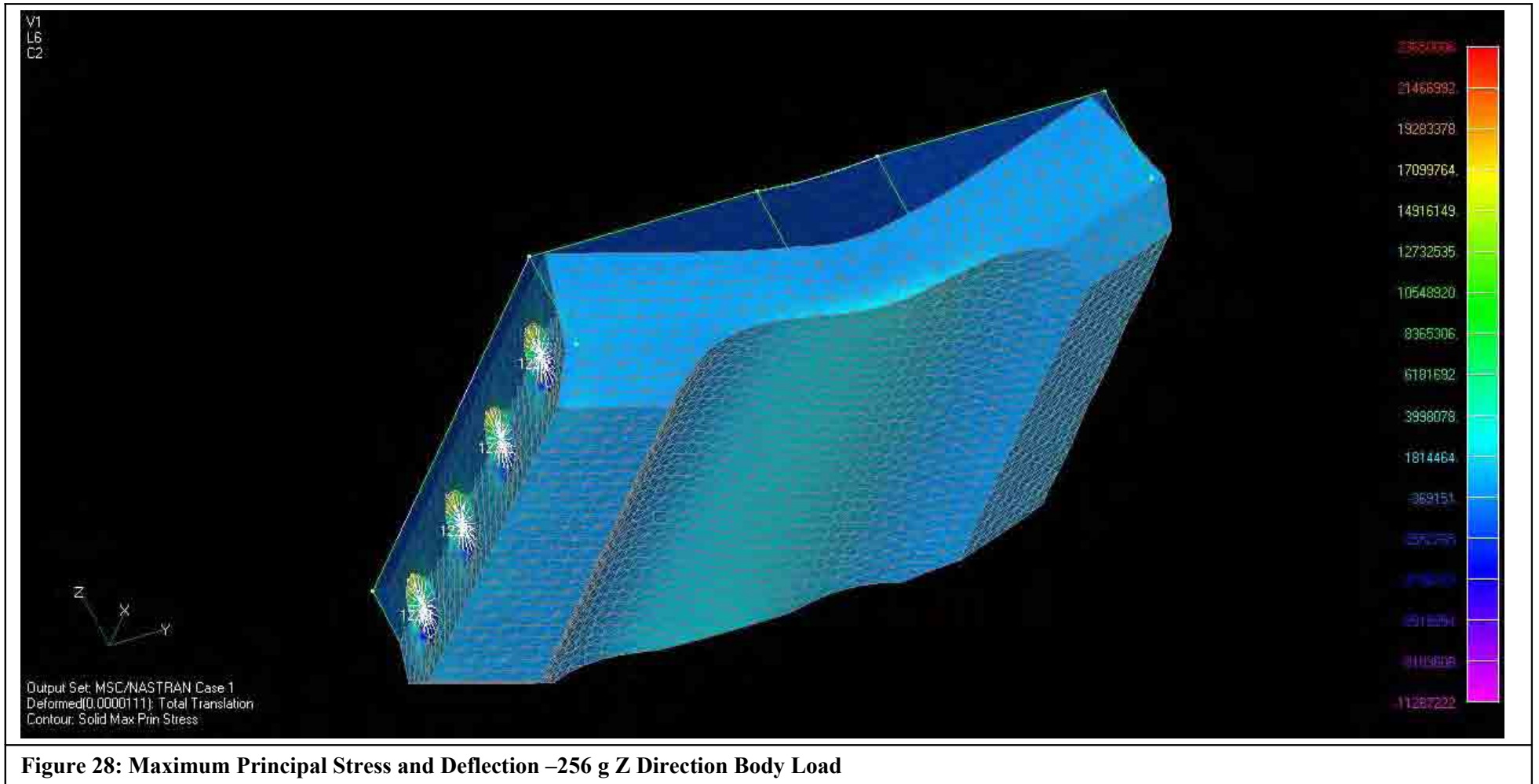
The maximum principal stress in the bulk of the simply supported lightweighted Zerodur® baseplate was approximately 9.1 MPa. Owing to the absence of abrupt changes in section, there were no significant stress concentrating features within the bulk of the Zerodur®. The deflection of the revised-shape simply supported lightweighted optical bench under similar loading conditions was reported by the finite element model as 21 µm.

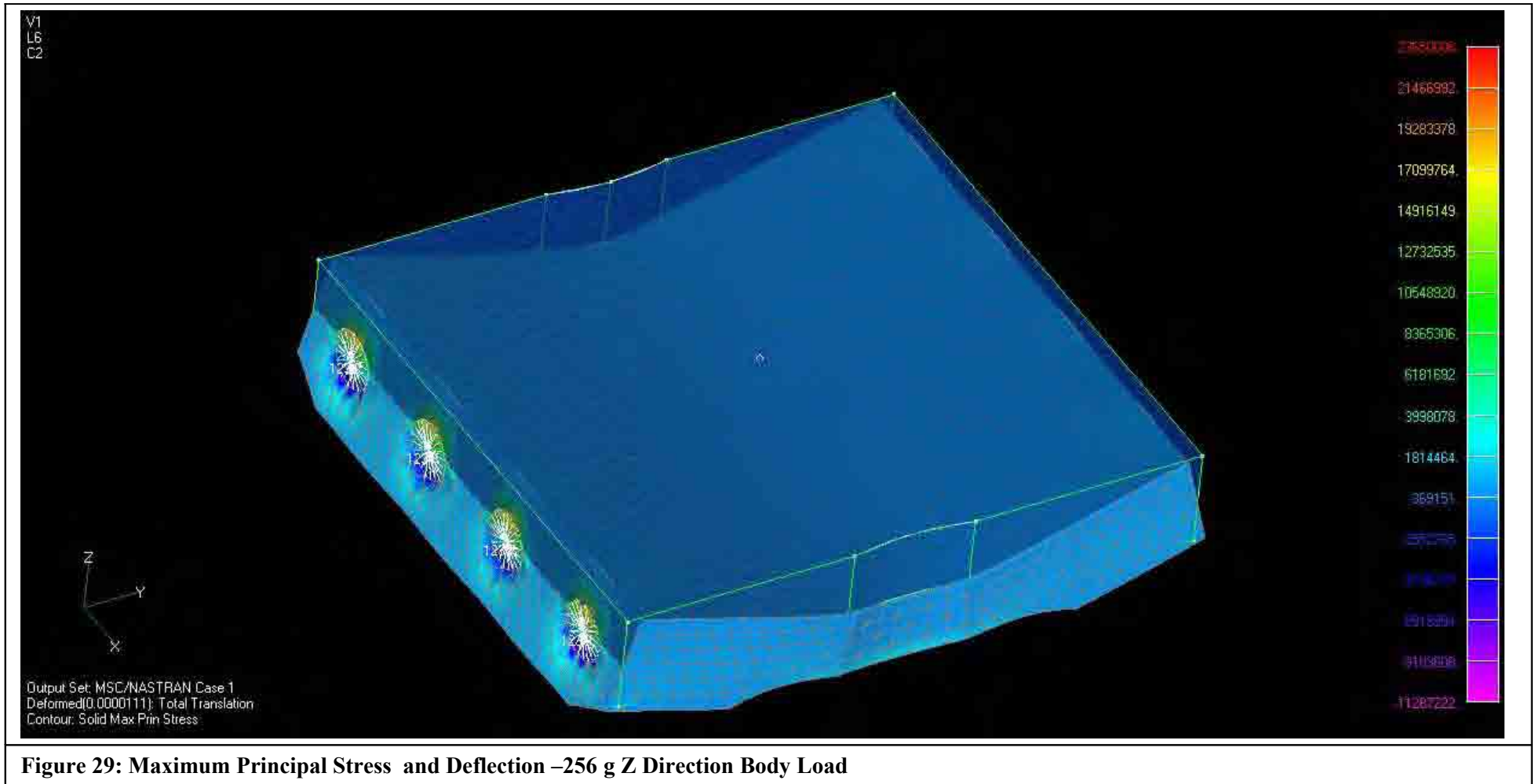
5.2.4.2 Built-in Model

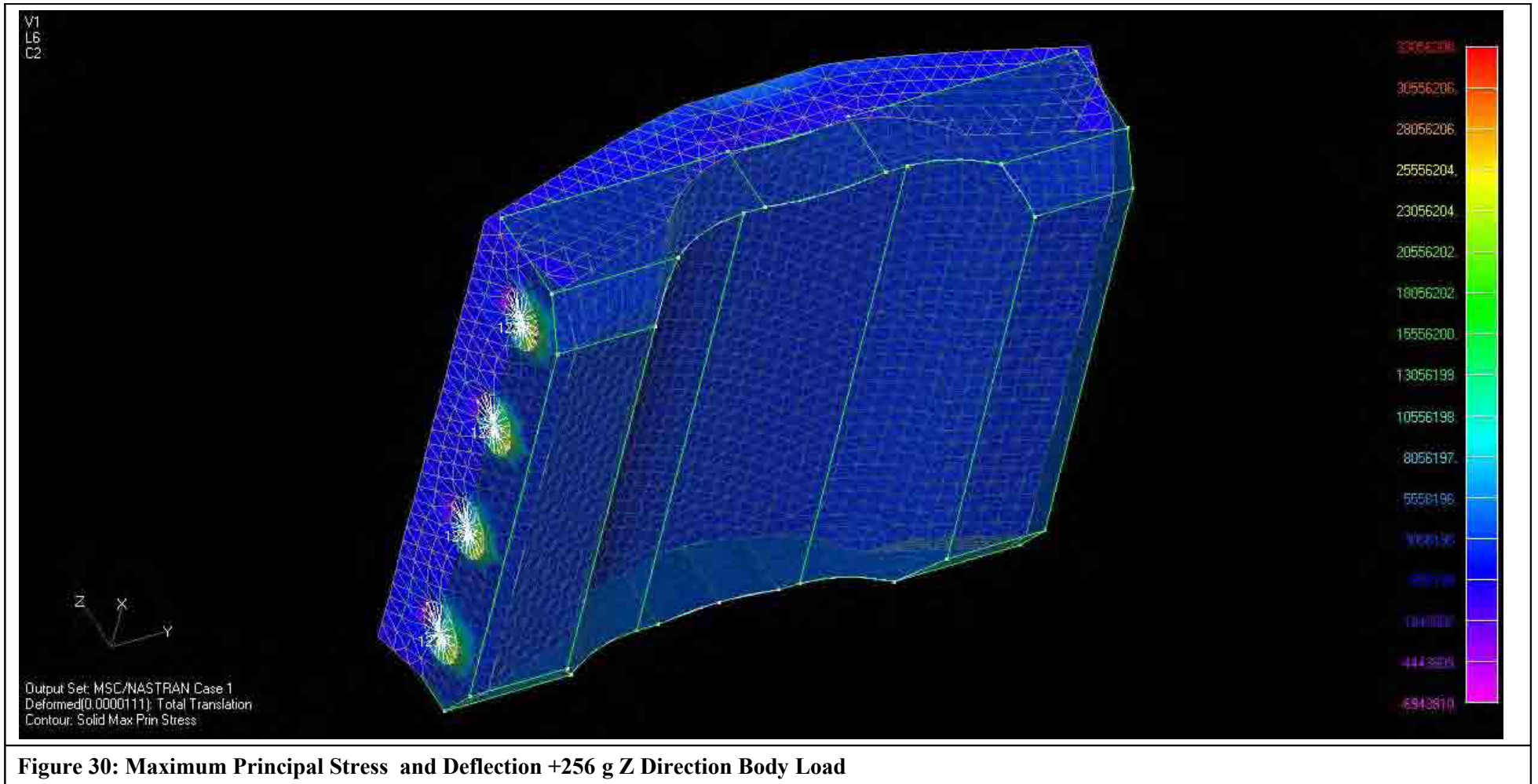
The optical bench baseplate CAD model was converted to MSC NASTRAN format, and was modelled as a linear isotropic solid, using tetrahedral elements.

The initial finite element model used a fictitious, comparatively rigid insert with no epoxy layer, combined with the rigid inserts constrained fully on their outer circular face, while a vertical acceleration body load was applied

The resulting deflections for accelerations applied in the negative Z directions are shown in figures 28, 29, while the response to positive acceleration is shown in figures 30, and 31, below.







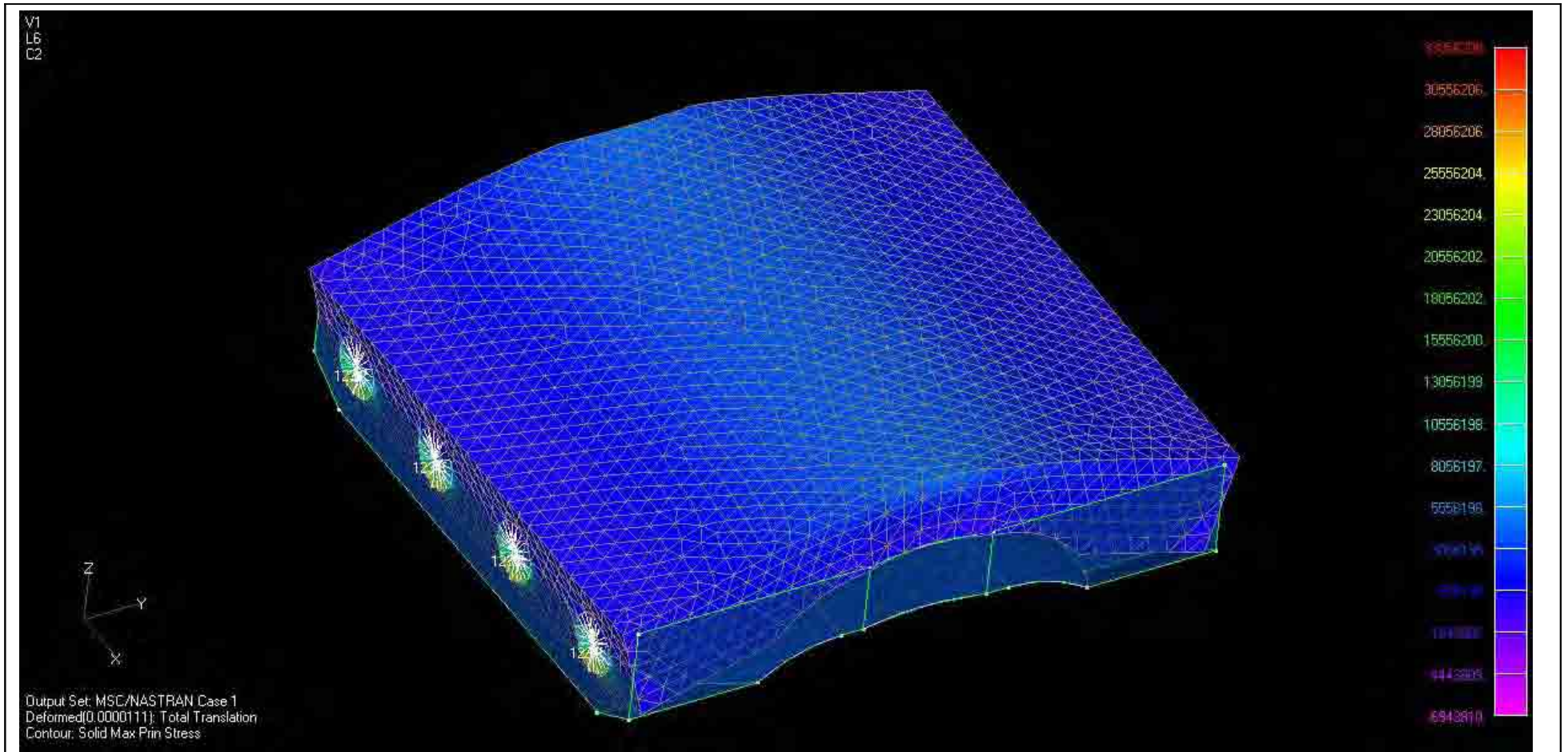


Figure 31: Maximum Principal Stress and Deflection +256 g Z Direction Body Load

The maximum principal stress in the bulk of the fixed clamped support light-weighted Zerodur® baseplate was approximately 5.5 MPa. Owing to the absence of abrupt changes in section, there were no significant stress concentrating features within the bulk of the Zerodur®. The deflection of the revised-shape light-weighted optical bench under similar loading conditions was reported by the finite element model as 11 µm. The stress and deflections for both simply supported and built in models are summarised in table 6, below.

<i>Boundary Condition</i>	<i>Simply Supported ±256 g</i>	<i>Built In ±256 g</i>
<i>Deflection (µm)</i>	21	11
<i>Maximum Principal Stress (MPa)</i>	9.1	5.5
Table 6: Stress and Deflection Summary		

These deflections cannot readily be compared with those reported in table 3, as the detail of the fictitious insert boundary condition was updated when the revised shape baseplate modelling was carried out. The fictitious insert used during the initial modelling had the undesirable effect of also providing a fictitious stiffness in-between elements on the edge of the insert hole. The insert modelling for the revised shape analysis was at least in part responsible for the increased deflections reported in table 6.

However, as described in section 5.2.1, above, the deflections were not of primary importance, while stress levels remained sufficiently high to warrant concern.

5.2.4.3 Insert Interaction and Local Zerodur® Modelling

Owing to a revision of the insert design by ASD, it was necessary to revisit the insert modelling. Also, as the effect of load transfer between inserts could not be assessed via the model described in section 5.2.4, the revised insert model was built into a more complete optical bench model where all eight inserts and their epoxy bonds were explicitly modelled.

Beyond the axi-symmetric model of the insert, this solid model allowed the application and analysis of of axis, or lateral loads. The solid mesh of $\frac{1}{4}$ of the insert is shown in figure 32, below, showing the modified cut-out for epoxy injection at mid depth.

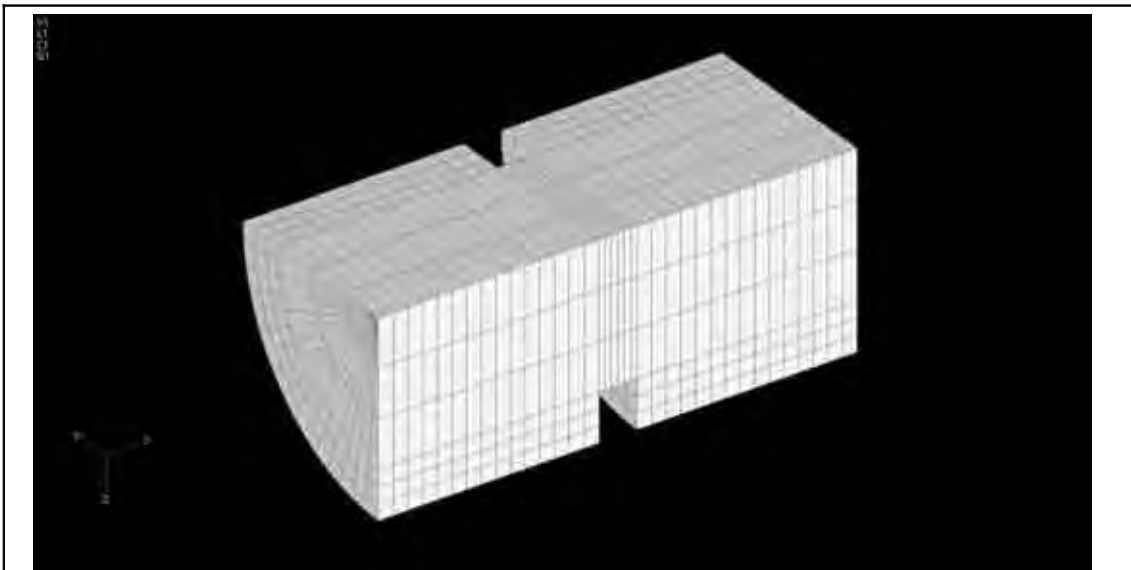


Figure 32: Insert Detailed Solid Model Mesh

The model was constructed entirely of 20 node hex elements, [46], [47], [53], using material properties as defined in table 2.

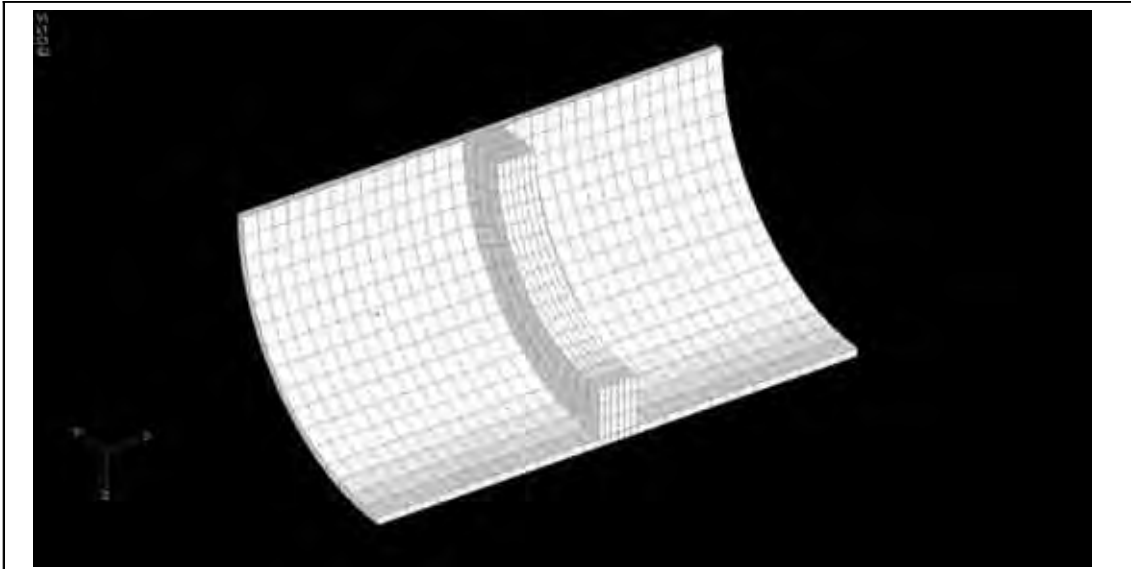


Figure 33: Epoxy Detailed Solid Model Mesh

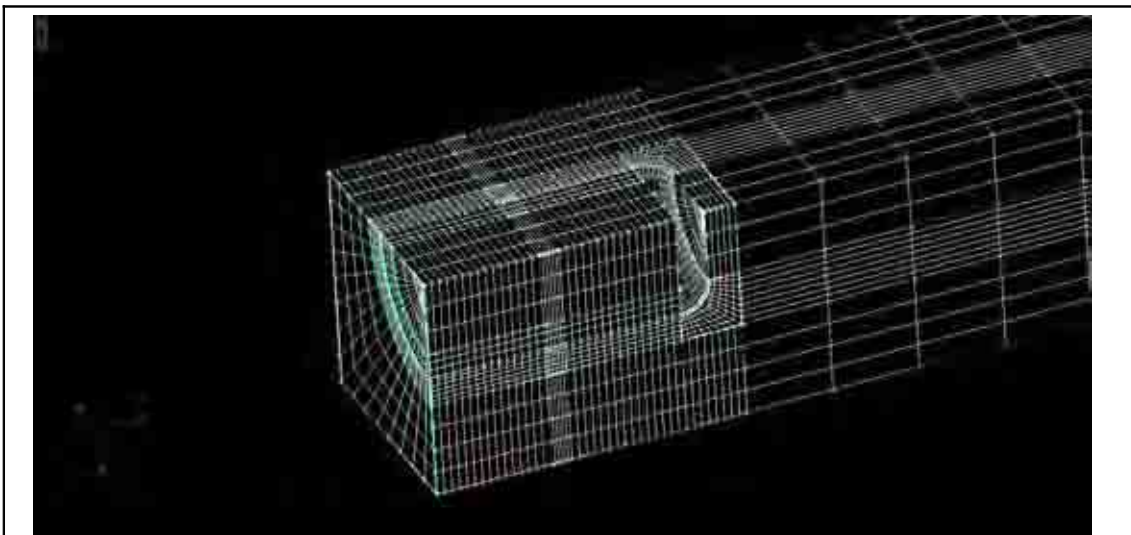


Figure 34: Assembled Insert, Epoxy and Zerodur® Detailed Solid $\frac{1}{4}$ Model Mesh

Using the revised insert model described above, a more complex model of the optical bench, epoxy inter-layer, and revised inserts was built. This model was built by repeated mirroring of the quarter insert model described above, maintaining element and material properties.

The revised loading derived by ASD required a complete optical bench model with seven of the eight inserts held fixed, while loads were applied to the eighth insert. As the optical bench was doubly symmetric, it was only necessary to apply load to a corner and a middle insert.

The loading is given in table 7, below;

<i>Direction</i>	<i>Load / Moment</i>
F_x	± 500 N
F_y	± 5500 N
F_z	± 800 N
M_x	± 3.1 Nm
M_y	± 0.8 Nm
M_z	± 4.8 Nm
Table 7: Optical Bench Interferometer Insert Loading	

As there were 6 loads, each with two possible directions, there were 64 possible combinations of loading for each insert. As there were two distinct loading locations, namely at a corner insert, or at a middle insert, this meant that 128 combinations of load were considered.

For fracture control purposes, only the maximum principal stress was of interest, [56], [57], [58], therefore, the results of each run were combined, and the maximum principal stress at each location was evaluated. These “enveloped” results are presented below.

Although the LPF optical bench was lightweighted, this feature was not included in the optical bench insert model, because incorporating the lightweighting geometry would add significant size, complication and solution time to the model. As the majority of load was transferred

directly to the adjacent insert, and insignificant load was transferred via the lightweighted areas of geometry for these loadcases, the omission of the lightweighting geometry did not significantly affect the results. The optical bench mesh is shown in figure 35, below

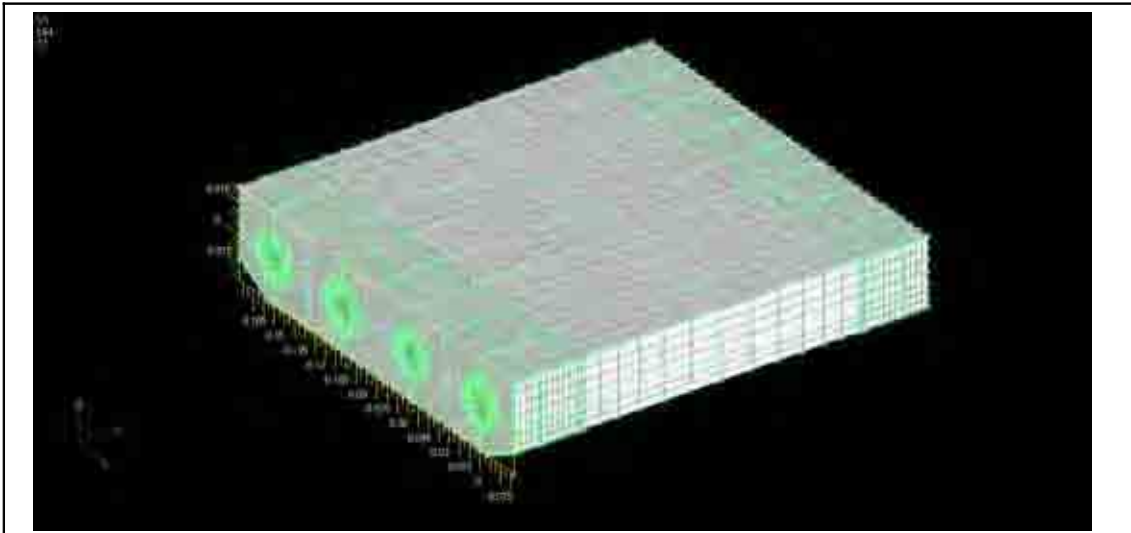


Figure 35: Optical Bench Model Mesh

The detail of the optical bench model is shown in figure 36, below, where the method of mirroring the quarter insert model to build the complete model may be seen,

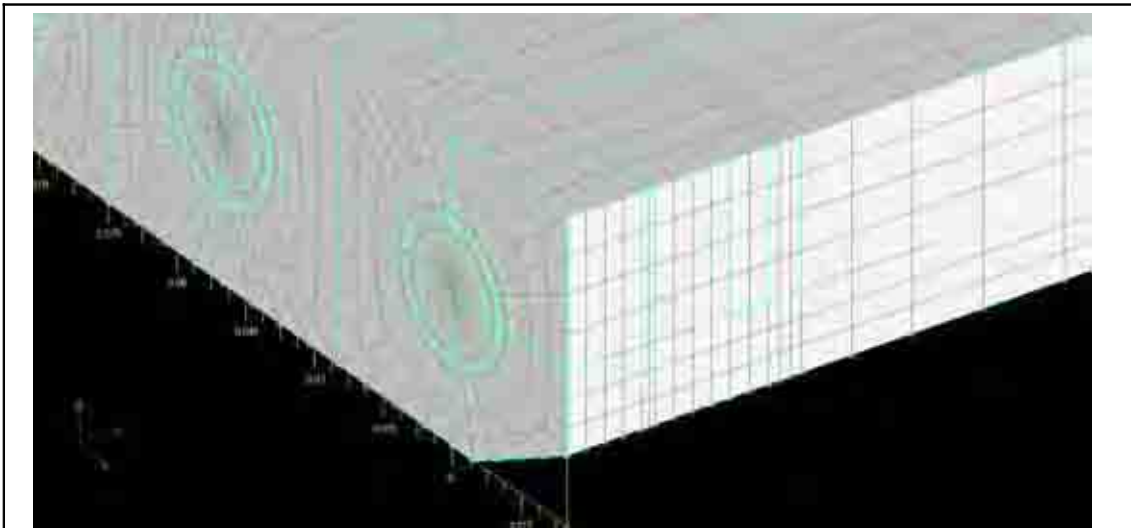


Figure 36: Optical Bench Model Mesh Detail

The (exaggerated) deformation and maximum principal stress for a sample corner insert loadcase, $(+F_x, -F_y, +F_z, -M_x, -M_y, -M_z)$ is shown in figure 37, below. The maximum stress was in the area where the inner edge of the epoxy ends, and the Zerodur® fillet at the base of the insert hole began.

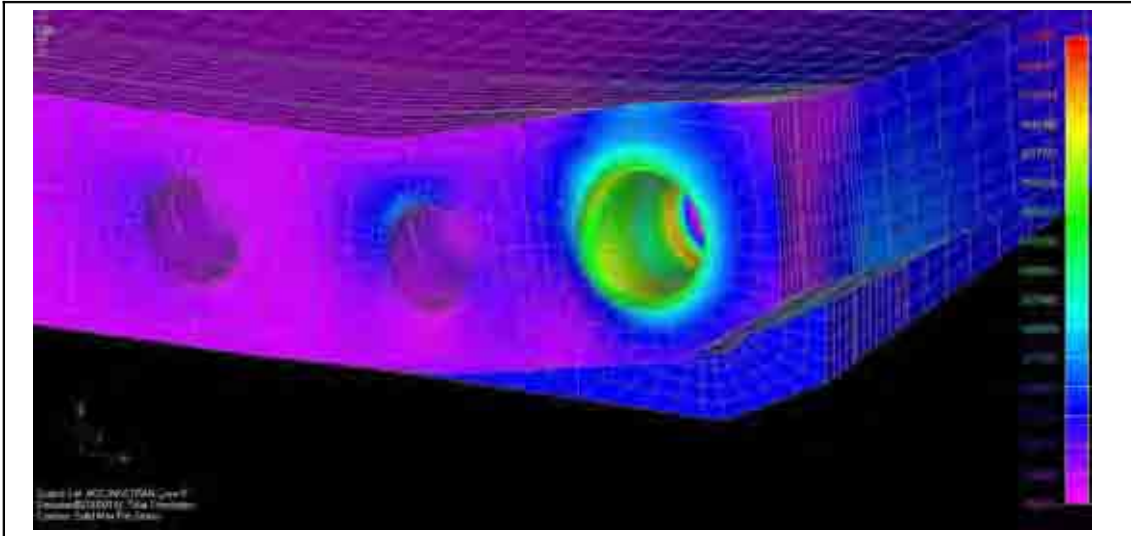


Figure 37: Example Model Run Results $(+F_x -F_y +F_z -M_x -M_y -M_z)$

The maximum envelope of 64 model runs where all of the six corner insert loads were considered with all possible sign combinations is shown in figure 38, below. Although this image does not represent any particular physical loadcase, it does show in a general sense how the load applied at one insert was transferred via the stiffest load-path to ground, i.e., via the adjacent insert. This justified the decision not to model the lightweighting geometry in the main body of the optical bench, as so little load was transferred beyond the adjacent insert. It also shows that the most highly stressed area, as noted above, was near the base of the insert hole, between the edge of the epoxy bond and the radius at the blind end of the hole.

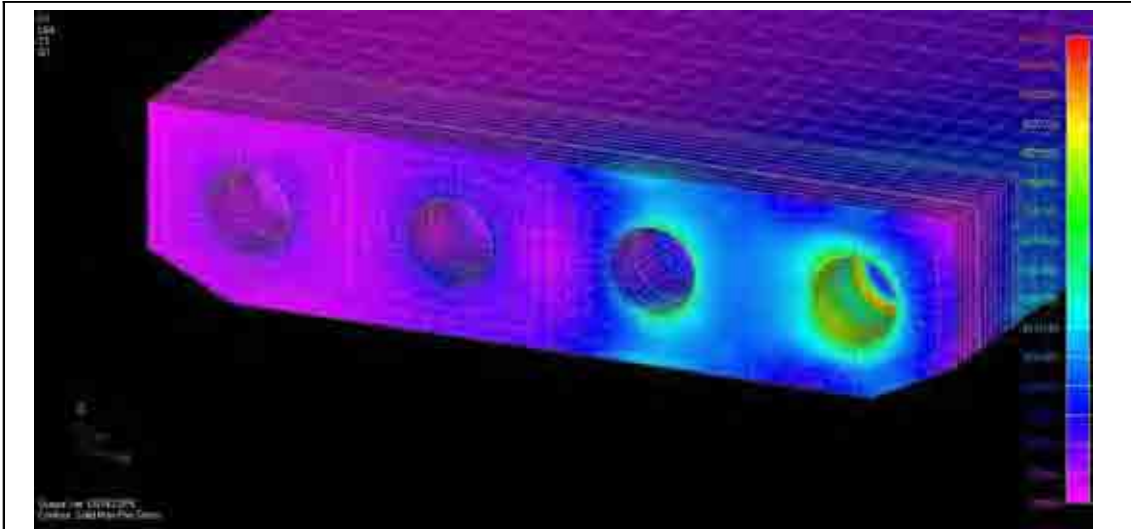


Figure 38: Enveloped Stress Results for Corner Insert

The maximum envelope of 64 model runs where all of the six middle insert loads were considered with all possible sign combinations is shown in figure 39, below. Again, this image shows that the most highly stressed area, as noted above, was towards the base of the insert hole. As the load may be transferred to either the adjacent insert to the left, or right, the maximum stress levels in this case were a little lower than the case where a corner insert with only one adjacent insert was loaded.

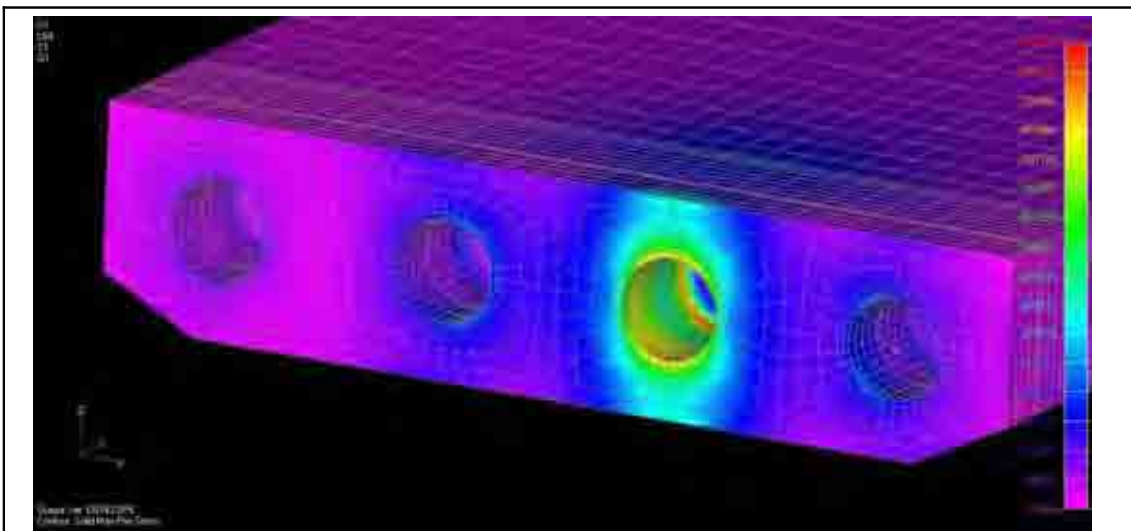


Figure 39: Enveloped Principal Stress Results for Middle Insert

The maximum values of the enveloped maximum stress data obtained from these model runs are shown in table 8, below.

<i>Loading</i>	<i>Maximum Principal Stress (MPa)</i>
Loaded Outer Insert	11.5
Loaded Middle Insert	10.6
Table 8: Enveloped Stress Data	

The case of a misaligned insert was also considered. The nodes comprising the insert and the epoxy, except for those nodes on the interface between the epoxy and Zerodur[®] were moved, and the model was run again. The corner insert was moved in the negative x direction, towards the adjacent insert. The loadcase considered was +FX, -FY, +FZ, -MX, -MY, -MZ. The results of these model runs are shown in shown in table 9, below.

<i>Misalignment (mm)</i>	<i>Maximum Principal Stress (MPa)</i>
0	11.24
0.1	11.48
0.2	13.18
0.3	16.70
Table 9: Misaligned Insert Stress Data	

The data in table 9 were used to define the positional tolerances of both the insert holes themselves, and the placement of the titanium inserts within the holes as ± 0.1 mm. The holes were cut by Schott Guinchar, while the bonding of the inserts was undertaken by ASD.

5.3 OPTICAL BENCH FRACTURE CONTROL

This section describes the work carried out in mitigation of the risk of brittle fracture of the Zerodur[®] glass ceramic material from which the optical bench was constructed.

5.3.1 Linear Elastic Fracture Mechanics

Owing to the brittle nature of the fracture critical items identified, linear elastic fracture mechanics was the appropriate assessment method, [44],[56]. The margin against intrinsic material failure was large, as might be seen by considering a very small crack size, for example a typical intermolecular spacing, 1 nm.

$$\begin{aligned}
 \sigma_{Intrinsic} &= \frac{K_{IC}}{Y \sqrt{a \pi}} \\
 &= \frac{0.9 * 10^6}{1.122 * \sqrt{\pi * 1 * 10^{-9}}} \\
 \sigma_{Intrinsic} &= 14.3 \text{ GPa}
 \end{aligned}
 \tag{Equation 27}$$

The estimate of the intrinsic failure stress of the Zerodur[®] material, 14.3 GPa, is large when compared with the yield stress for a typical engineering material like steel, which, depending upon composition and treatment may vary between 220 and 1980 MPa, [59].

The value of fracture toughness, K_{IC} used in equation 27 is that quoted by the manufacturer, and is the result of their experimental testing of their product. Although the value of the fracture toughness will vary between batches of material, manufacturers quoted values for structural properties are usually conservative.

This section of the thesis shows that these values were very large when compared with the stress levels required to cause pre-existing cracks or defects in the Zerodur[®] to grow and propagate to failure,

In order to explore the material properties of the Zerodur[®], a small number of Vickers indentations were carried out. Usually, Vickers indentations are made in ductile measurements and the contact force used, and the size of the pyramidal indentation used to estimate the material's hardness, from which the yield stress may be inferred. However, in brittle materials, a Vickers indentation may be used in order to initiate surface, and sub-surface cracking. That Zerodur[®] was a brittle material for which linear elastic fracture mechanics were an appropriate analysis technique may be seen by considering the indentation patterns, and the radial / median crack pattern left after an indentation, as per figure 40, below, [56].

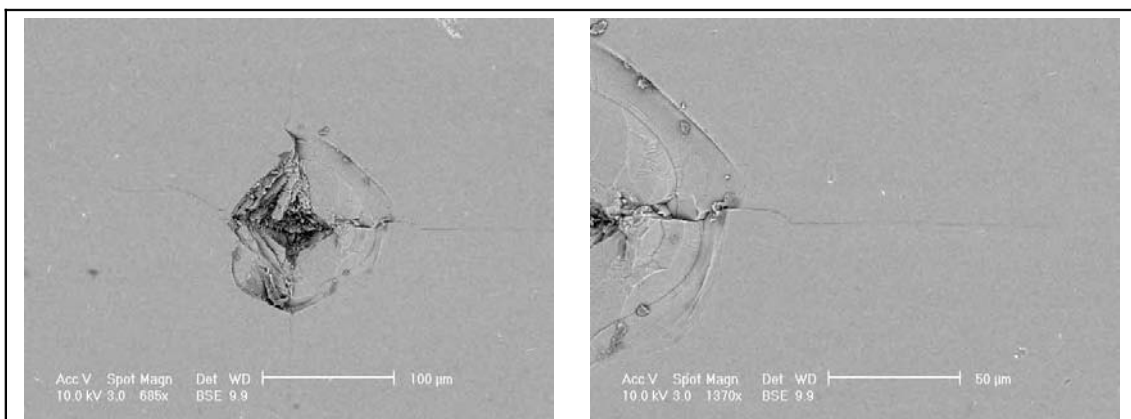


Figure 40: Vickers Indentation of Zerodur[®] (RH Image Zoomed)

As the complicating issue of plasticity was not important in this application, the use of linear elastic fracture mechanics was directly related to the Griffith crack growth theory, [60]. This theory states that in order for a crack to grow, the decrease of strain energy in the solid must be balanced by the increase in the surface energy at the crack faces. This criterion enables a critical crack size to be calculated once the applied load and material properties are known.

Practically, the calculations were carried out using the concept of stress intensity, [56], [57], [58], [61], rather than directly in terms of energy. The required material properties, particularly the fracture toughness, were well known for Zerodur[®], [44], and are listed in table 2. The fundamental relation governing crack behaviour in brittle solids, as described by stress intensity is shown in equation 28, below.

$$K = \sigma Y \sqrt{(\pi a)} \quad \text{Equation 28}$$

Where K is the stress intensity. K_{IC} , the plane strain fracture toughness may be considered as the limiting case of stress intensity at the point of sudden failure.

The behaviour of the crack may be determined by comparing the value of stress intensity against known material parameters. While the stress intensity remains below the so-called Threshold Stress Intensity, no crack growth may occur. If the stress intensity exceeds a level known as the fracture toughness, then catastrophic failure via rapid growth of the crack becomes likely. While the stress intensity is between the threshold stress intensity and the fracture toughness, crack growth occurs slowly. This slow crack growth occurs both as a function of the duration of exposure to a constant stress, and also as a function of the number and range of stress cycles undergone during dynamic loading.

By re-arranging equation 28, and replacing the stress intensity by the limiting value, i.e., the plane strain fracture toughness, the critical crack size can be estimated.

$$a_{critical} = \pi \left(\frac{K_{IC}}{\sigma Y} \right)^2 \quad \text{Equation 29}$$

The optical components which were not explicitly modelled using the finite element method were considered in the fracture mechanics analysis. The stress in the area of the joint between the optical component and the baseplate was estimated using both the finite element results and classical analysis.

5.3.2 Fracture Control Methodology

Owing to project cost and time-scale constraints, it was unlikely that a true “Experimental Fracture” programme would have been feasible, because a systematic test of the failure stresses for a sufficient sample of replica optical benches to determine the safe stress levels for the design represented a task larger than timescales or finances allowed. The properties of glass, [62], are such that catastrophic failure may occur via the rapid growth of so-called micro-cracks. Statistical trials, some results from which are shown in figures 41 and 42, demonstrated that of the order of thousands of destructive tests of representative samples would be needed to generate sufficient statistical confidence. The costly and time consuming repetition of such a level of testing would become necessary if any design change or variation in the processing method were made. This type of approach would be extremely costly and prohibitive in time, and would also be of limited philosophical value.

This was because the real requirement was to verify the mechanical integrity of the one item that would fly rather than to verify the design itself. For example, it was possible that the design was adequate, but the flight component itself contained a critical flaw – the result would have been failure. Of course, if the design itself were not adequate, the result again would have been failure, but, the adequacy of the design could be assessed via finite element analysis and structural tests of a representative model. The success of such a structural model test would

validate the acceptability of the design, but it would not offer any verification of the adequacy of the actual flight component. i.e., a successful test of a structural model would not mitigate all risk.

In order to simulate a hypothetical loading event, a computer based statistical trial was prepared, [63], [64], [65], [66]. The following assumptions were made for each trial;

- Crack size (a) - uniformly distributed between 0 and 0.4 mm (0.4 mm being the largest crack which would not be detected during final inspection by the Zerodur[®] manufacturer, Schott.)
- Orientation (θ) - uniformly distributed between 0 and 180 ° with respect to the direction of the principal tensile stress
- Fracture toughness (K_{IC}) - Normally distributed with a mean of 0.9 MPa \sqrt{m} and a standard deviation of 0.02 MPa \sqrt{m}
- Stress intensity factor (Y) - calculated from the crack length

For each trial, the statistical input data were used to calculate the failure stress using equation 30, below.

$$\sigma_{FAIL} = \frac{K_{IC}}{Y |\cos(\theta)| \sqrt{a\pi}} \quad \text{Equation 30}$$

Where, K_{IC} is the plane strain fracture toughness, σ , the principal stress, Y , the stress intensity factor, and a , the crack length. The stress intensity factor is a geometry specific factor which accounts for the relative size of the crack and the total stressed area of the section containing the crack.

The results of 5000 trials are shown in figure 41, below. The left hand graph shows the histogram of the failure stress frequency. The right hand graph shows the cumulative failures against the failure stress. The bin width is 0.5 MPa. Although the manufacturer suggests a safe stress of 10MPa, the figures demonstrate that the numbers of failures begins to rise most sharply at approximately 20MPa – there is, however a long tail to this distribution.

The variation between bins on the histogram indicated that insufficient trials were considered to give statistical confidence. Owing to the summing mechanism, the variation in the data may be seen to be smoothed when plotted in the form of the cumulative failure graph.

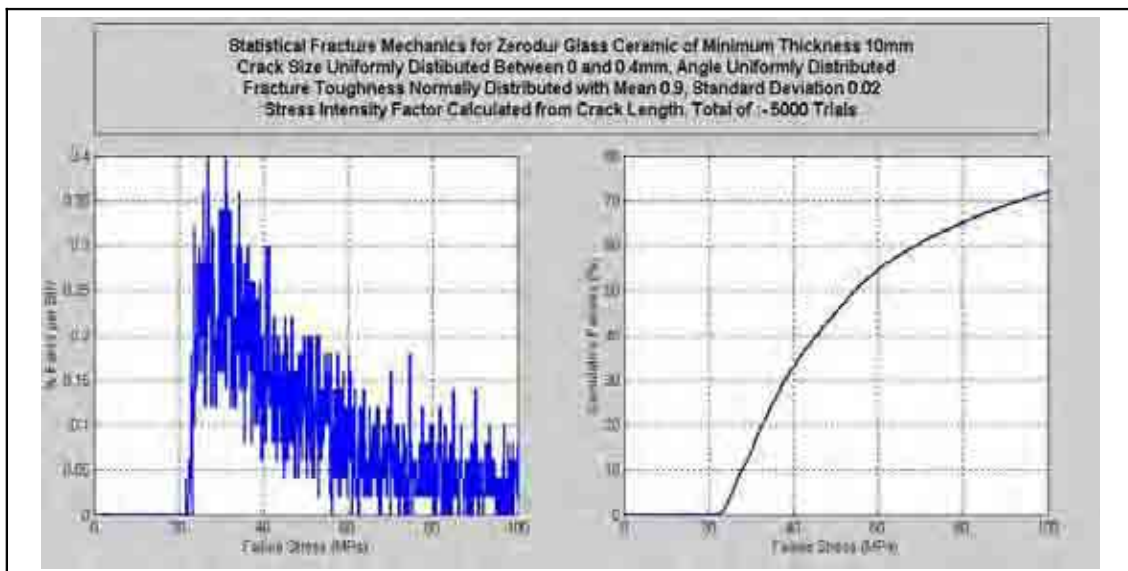
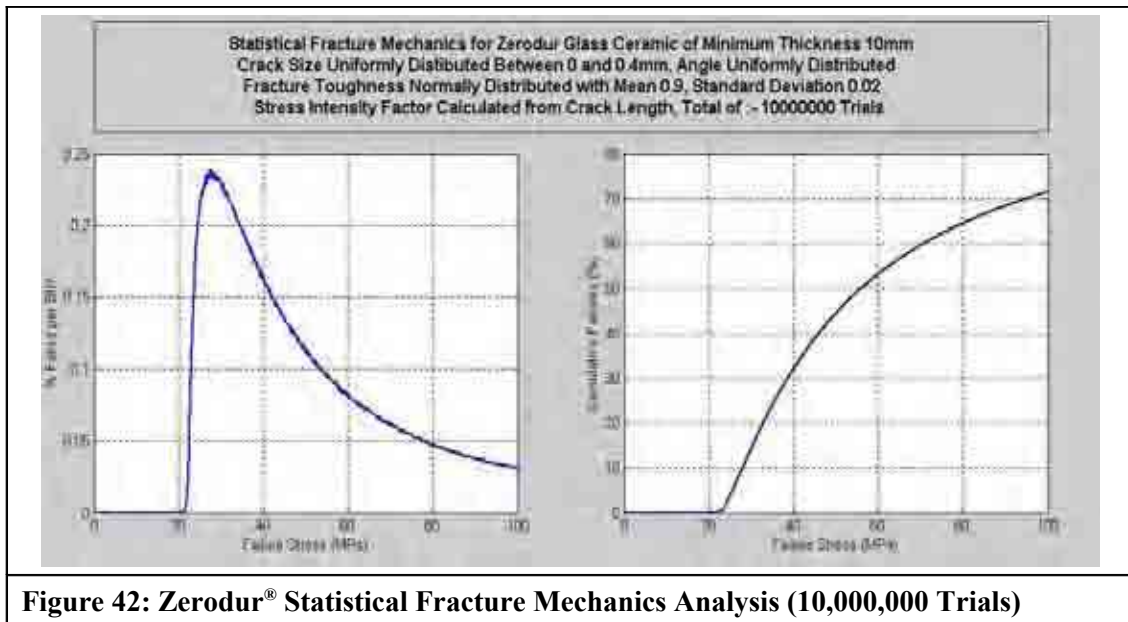


Figure 41: Zerodur® Statistical Fracture Mechanics Analysis (5,000 Trials)

Figure 42, below, shows the result of 10,000,000 trials, where the variation between histogram bins was much reduced. However, as even the breaking of 5000 samples for each configuration of geometry and surface finish would not have been feasible and would not have sufficiently demonstrated the adequacy of the flight component, an experimental approach was not pursued.



A very detailed inspection of the actual flight optical bench at several stages, in conjunction with detailed finite element stress modelling was considered more effective. In order to do this efficiently, at the required moments in the programme, the test facility was commissioned before the availability of the flight baseplates using test samples, thus demonstrating its accuracy and sensitivity prior to use. Some of these test samples were tested to flight levels to demonstrate consistency of the optical measurement with the fracture mechanics, using few samples. This was agreed with the industrial architect, (ASD), the launch agency, (ESA) and the project oversight committee as a much more effective philosophy, i.e., examine via detailed photo-elastic inspection the samples that might fly and separately calibrate the photo-elastic inspection on samples that would not fly.

5.3.3 Fracture Mechanics Analysis

This section describes the fracture mechanics analysis carried out on the proto-flight model model of the optical bench interferometer. This analysis enabled the definition of “allowable” stress levels for the optical bench. In order to assess the acceptability of each physical optical bench, the results of this analysis were considered along with the flaw inspection and the residual stress inspection results for that bench. This analysis does not allow all optical benches of a particular design to be deemed acceptable, each single bench must be considered individually.

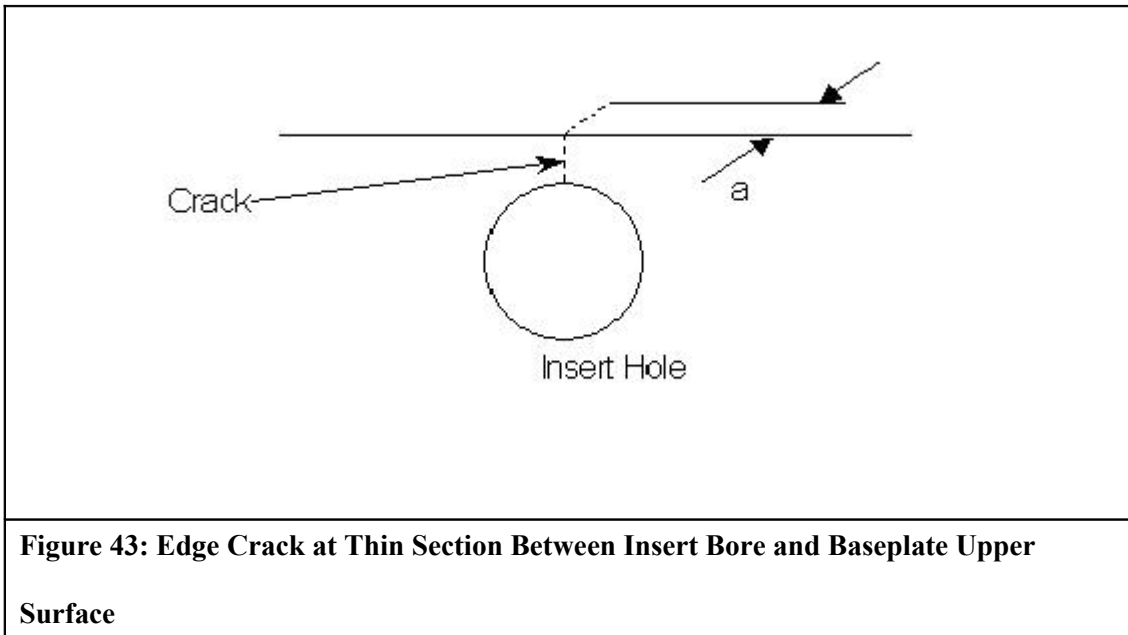
As the geometry of the crack relative to the stress distribution in the material can affect how the crack grows, [56], [67], a number of possible crack geometries, appropriate to the optical bench physical layout, were considered. The crack geometries considered are given in table 10, below;

1.	Edge crack at thin section between insert bore and baseplate upper surface
2.	Edge crack at interface between mirror or beamsplitter and baseplate
3.	Corner crack in highest stress area of underside ribs
4.	Surface crack “penny crack” in light-weighting fillet area
5.	Surface crack in interior of insert bore
6.	Edge crack between insert bores
7.	Edge crack across centre of underside light-weighting ribs

Table 10: Crack Geometries

Although cracks are two dimensional features, they may be characterised for fracture mechanics assessment in terms of their most critical dimension – the direction in which further crack growth will most likely cause failure.

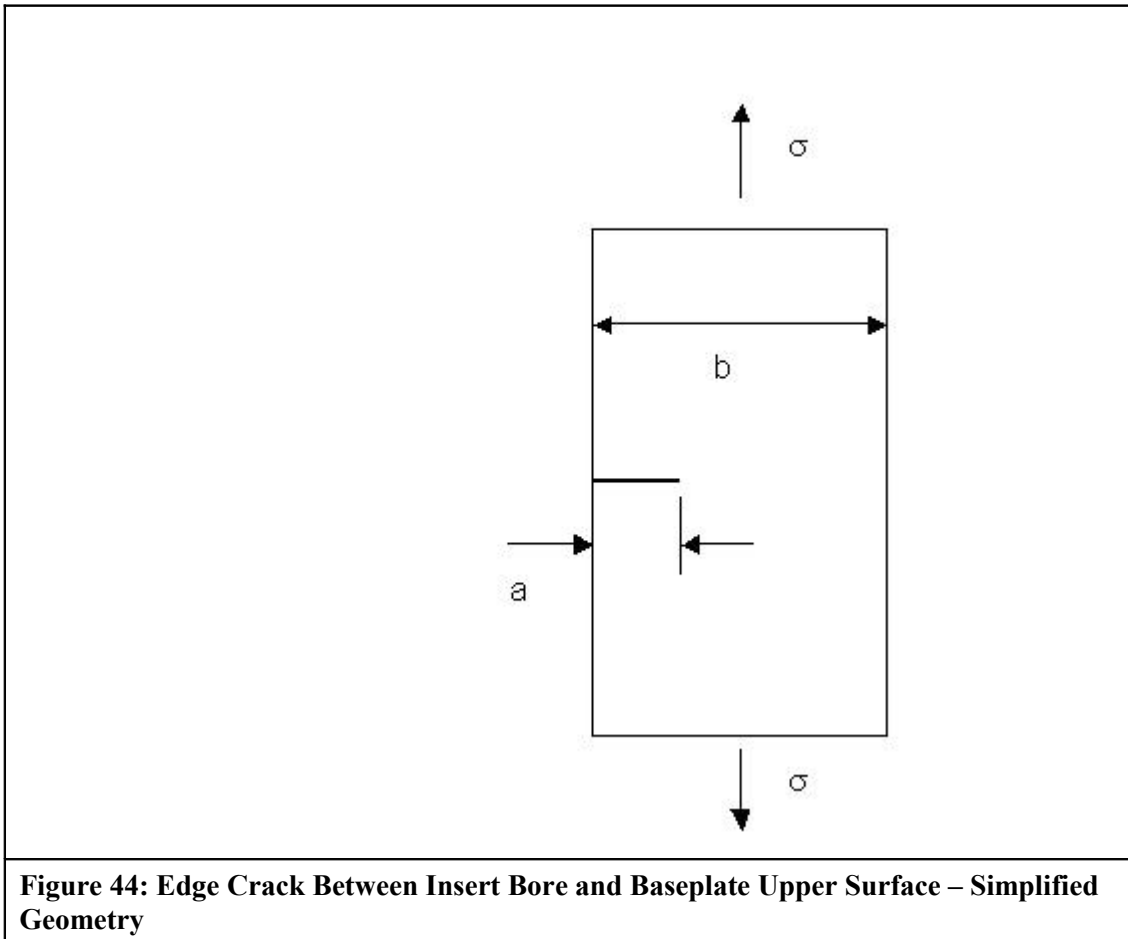
5.3.3.1 Edge crack at thin section between insert bore and baseplate upper surface



This geometry was complicated by the presence of the insert hole, which in itself was a stress concentrating feature. As the geometry of the optical bench was not simple, an accurate stress concentration factor solution was difficult to find. It was therefore appropriate to make conservative assumptions in order to derive a simplified geometry for which stress concentration factor solutions were available.

For crack propagation calculations, the optical bench was considered as a flat plate with its lower surface tangent to the upper edge of the insert hole, i.e., the stiffening effect of any

material below was ignored. The stress, local to the postulated crack, estimated from finite element modelling, which included all the relevant geometry, was applied to the “plate”, as given in figure 44, below.



The expression for the stress intensity factor, [68], is shown in equation 31, below;

$$K_I = \sigma Y \sqrt{\pi a}$$

Where

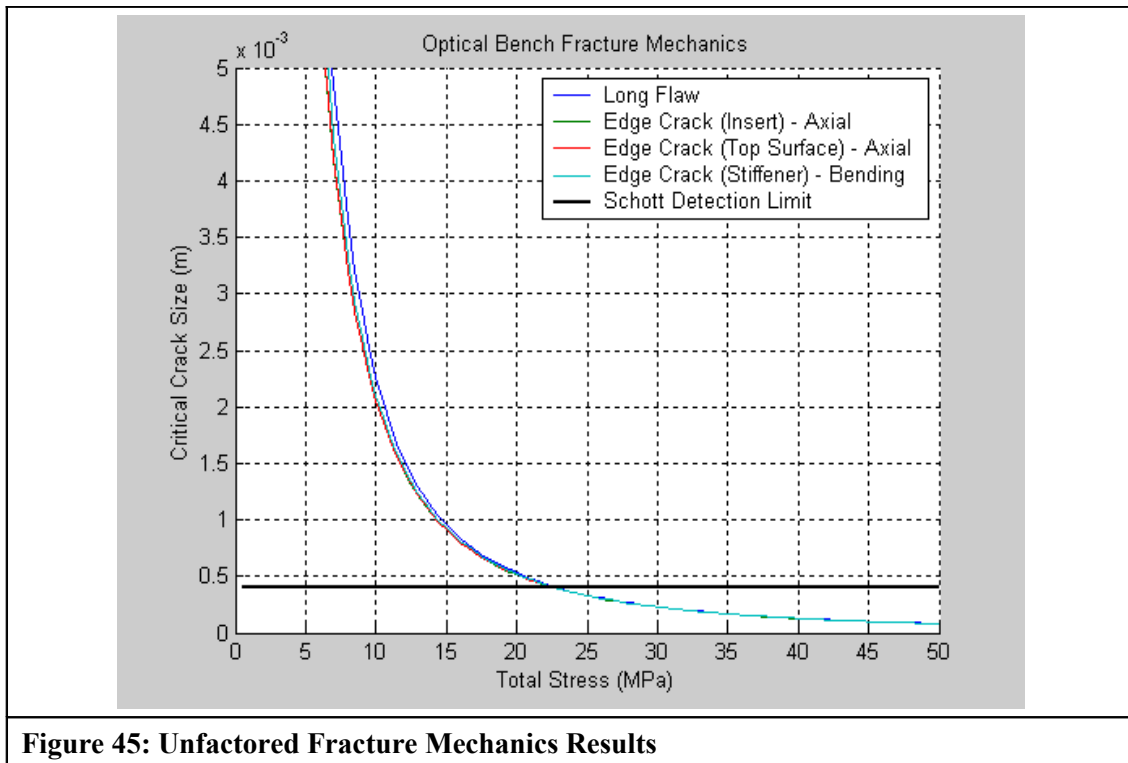
$$Y = 1.122 - 0.231 \left(\frac{a}{b}\right) + 10.55 \left(\frac{a}{b}\right)^2 - 21.71 \left(\frac{a}{b}\right)^3 + 30.382 \left(\frac{a}{b}\right)^4$$

Equation 31

Where b is the width of the plate, 212 mm. A MATLAB program was written, [64], [69], estimating the allowable stress for various values of the crack length, a .

5.3.3.2 Derivation of Factors of Safety

While a factor of safety of four was applied to the quasi-static acceleration load, this safety factor included some allowance for uncertainty in the loading and analysis, and finally, some margin against failure. Figure 45, below, represents the critical crack size, as given by equation 29. Each curve represents a different crack geometry, as listed in table 10, i.e., a different expression for Y , the stress intensity factor was used. It may be seen that in all cases, the curves almost overlay each other. This was because the critical crack size was so small, there was little chance for the crack to grow and interact with the geometry before failure.



Where the horizontal line represents the smallest defect, 0.4 mm, which may be detected by the material's manufacturer, Schott, during their routine inspection.

The reliability of launch vehicles is subject to significant variation between types, [70], [71], with realised success rates between 0 and 100 %. Some example data are shown in table 11, below.

<i>Vehicle</i>	<i>Successes</i>	<i>Tries</i>	<i>Realized Rate</i>	<i>Last Failure</i>
Soyuz FG	18	18	1	None
CZ-4 (A/B/C)	17	17	1	None
CZ-2D	10	10	1	None
Soyuz FG / Fregat	9	9	1	None
Minotaur 1	8	8	1	None
CZ-2F	7	7	1	None

<i>Vehicle</i>	<i>Successes</i>	<i>Tries</i>	<i>Realized Rate</i>	<i>Last Failure</i>
Proton-K/17S40	6	6	1	None
Delta IV - M	6	6	1	None
Soyuz U / Fregat	4	4	1	None
Proton-M/DM-2	3	3	1	None
Shtil'	2	2	1	None
Ariane 5ES	1	1	1	None
Soyuz 2-1B/Fregat	1	1	1	None
Soyuz 2-1B	1	1	1	None
Delta 2	141	143	0.99	17 th Jan 1997
Tsyklon 2	104	105	0.99	25 th April 1973
STS	124	126	0.98	1 st February 2003
Soyuz U	723	743	0.97	15 th October 2002
CZ-2 (C) (/SD/SM)	31	32	0.97	5 th November 1974
Kosmos 3M	421	444	0.95	20 th November 2000
Proton-K/DM-2M	40	42	0.95	25 th November 2002
Ariane 5-ECA	18	19	0.95	11 th December 2002

Table 11: Launch Vehicle Success Statistics (Source [70], including failures to attain correct orbit)

The launch vehicle for LISA Pathfinder is the ESA VEGA launcher, which has not been flown, therefore there were no historic launch data from which to work.

In order to consider the risks associated with the structural integrity of the optical bench, the probability of the launch of LISA Pathfinder, represented by $P(A)$, being a success was assumed to be 95 %. The probability of survival of the optical bench, $P(B)$, should not reduce the overall probability of success significantly. As the two events are independent;

$$\begin{aligned}
 P(A \text{ and } B) &= P(A \cap B) \\
 &= P(A) * P(B)
 \end{aligned}$$

Therefore,

$$\begin{aligned}
 P(A) - P(A \text{ and } B) &= P(A) - (P(A) * P(B)) \\
 &= P(A)(1 - P(B))
 \end{aligned}$$

Equation 32

In order to ensure this, the term $(1-P(B))$ needed to be small, i.e., the probability of optical bench failure needed to be small. The LTP consists of over 120 configuration items, [72], i.e., items developed, tracked, and maintained under configuration control. Owing to the design of the spacecraft, many of these configuration items had the same type of criticality as the optical bench wherein a failure of the component would result in the failure of the mission, and there would be reductions in the overall probability of mission success from contributions from $P(C)$, $P(D)$, $P(n)$. Assuming a tolerable reduction in the probability of overall mission success from 95 % for the launcher alone to 94 % for the complete mission, and accounting for the number of critical items led to a tolerable failure probability budget allocation for the optical bench being in the region of 0.1 %.

In order to compare this failure probability budget for the optical bench, another mission with centrally important glass components representing potential single point mission failures was the NASA James Webb Space Telescope, (JWST). The NASA JWST design requirements identified an acceptable probability of failure for glassy structural materials of 0.1%. This requirement was laid out in INSU-1658 of JWST-IRD-000781. The logic behind this requirement has much in common with the design context of LISA Pathfinder.

It is at least possible the combination and analysis work carried out may not capture or include each and every failure mechanism for the Zerodur[®] material / optical bench structure. Therefore, some rational means of estimating a factor of safety was required.

The failure mechanisms in glass components follow the Weibull distribution- the probability distribution caused by the weakest link in the chain. Zerodur[®], made by the Schott Glass Company is a well characterised material, and the Weibull factor, γ , has been determined experimentally, [44].

$$F(\sigma) = 1 - e^{-\left(\frac{\sigma}{\sigma_0}\right)^\gamma} \quad \text{Equation 33}$$

Re-arranging equation 33 gives;

$$\left(\frac{\sigma}{\sigma_0}\right) = (-\ln(1-F))^{1/\gamma} \quad \text{Equation 34}$$

Where $F(\sigma)$ is the probability of failure at stress σ , and σ_0 represents the unfactored stress value.

The Weibull factor, γ , is dependent on the quality of the Zerodur® and on the programme of surface treatment undertaken. D64 Zerodur® with an acid etch is specified with a Weibull factor of $\gamma=6.0$, [44]. Substituting this factor into the Weibull distribution gives a required margin of $(\sigma/\sigma_0)=0.32$, or, inverting, a stress factor of safety of 3.125, [56].

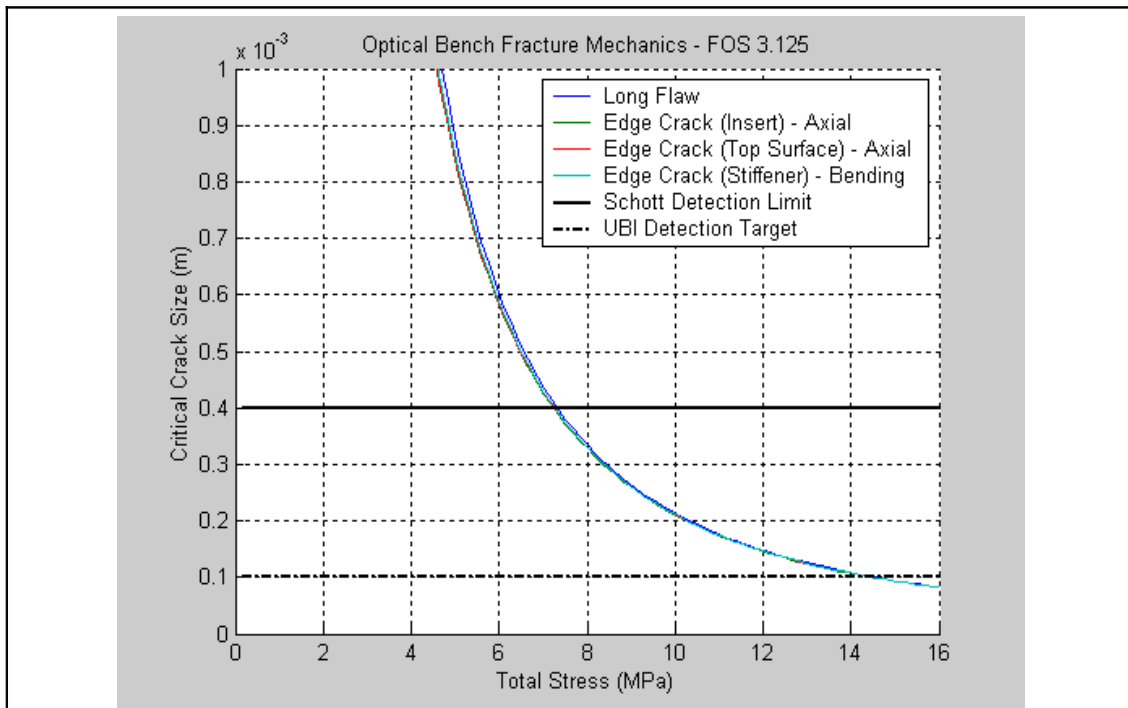


Figure 46: Factored Fracture Mechanics Results

The effect of incorporating the factor of safety was to render the critical crack size corresponding with the 0.4 mm Schott detection limit inadequate. If the Schott inspection alone

were relied upon, it would be necessary to limit the optical bench to stress levels below 8 MPa. However, via the combination of detailed stress analysis, fracture mechanics analysis and inspection at the 100 μm level, described in this thesis, stress levels up to 14 MPa became tolerable.

5.3.4 Optical Bench Inspection

The fracture control inspections were carried out by UBI in addition to any inspections carried out by Schott, who manufactured the optical bench, and carried out the machining.

Prior to any machining activity, the inspection polished blank afforded an opportunity for detailed inspection. The blanks were inspected, using a polariscope, [73], [74], in order to detect stress birefringence interference fringes. The disturbance in the stress field, being larger than the defect, [61], enabled the detection of small defects, to a resolution, of a few tens of microns.

Defects which were to be machined away in their entirety during the manufacture of the features of the optical bench baseplate and which would not result in a failure of the component, would have been considered acceptable.

A component containing defects which would not be machined away would have been removed from the flight manufacturing path, and most likely rejected completely. Such a component would be able to continue in manufacture only after the successful completion of a detailed fracture mechanics analysis demonstrating that the risk of the defect becoming critical were acceptably low. The standard project method for the reporting and management of non-conformances was followed for these items.

After machining, the optical benches might have contained machining induced micro-cracks. These were at least blunted, and perhaps removed entirely by a process of acid etching, carried out by Schott. The efficacy of this process may be determined by observing the stress birefringence in the Zerodur[®], [75]. In order to facilitate the inspection the lower plane surfaces of the optical bench were inspection polished rather than being acid etched.

5.3.4.1 Inspection Method

The inspection was based on the principle of stress birefringence, [76], [77], [78]. This property of stressed materials to affect the polarisation of light passing through them gave rise to an experimental stress analysis method called the photoelastic method, [14], [76], [79]. Prior to the ready availability of computer based numerical solutions to stress analysis problems, photoelastic methods were commonly used to assess stress concentrations and the stress distributions in plane geometric configurations which could not be solved using classical techniques. Among modern uses of the photoelastic method are the validation of finite element mathematical models, and in operational testing of structures in-situ, using a reflective variant of the process applied to the structure's surface.

In this application, the birefringence method was used to identify disturbances in the background stress pattern caused by the presence of a defect or crack. Rather than carrying out analysis on the fringe pattern for any quantitative assessment of the stress field, the presence or absence of fringes was all that was sought by the inspection method used.

A crossed polariser inspection apparatus is shown in outline form in figure 47, below.

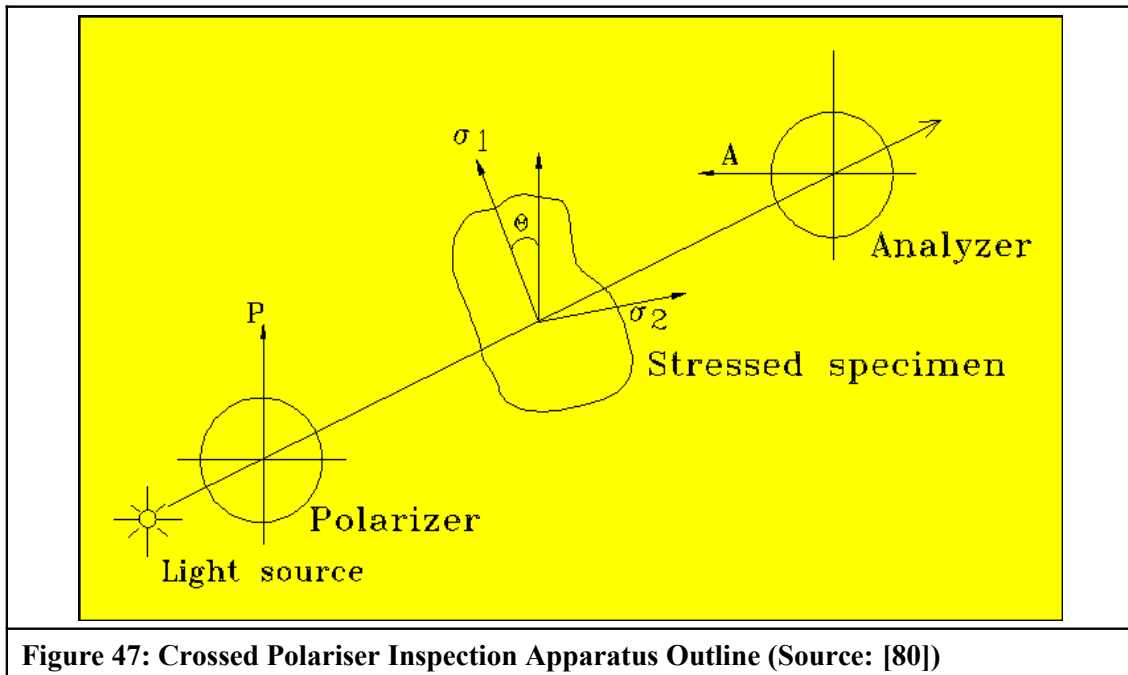


Figure 47: Crossed Polariser Inspection Apparatus Outline (Source: [80])

The Zerodur[®] optical bench baseplate took the place of the Stressed Specimen, and while the optical bench was not externally stressed, the local disturbance around any defects caused a local stress, which was seen during the inspection. The light leaving the analyser was focussed by a Nikon 55-200mm zoom lens and recorded by a LaVision Imager QE digital camera (1376x1040 pixel) for further analysis.

In order to correctly interpret the patterns in the images detected by the digital camera, it was necessary to consider the effect on the light of the polariser, the stressed specimen and the analyser. In order to approximate the inspection of the optical bench, the theory for a two-dimensional stress system is considered below. As the optical bench has significant thickness and variations of stress with respect to depth, the image seen in the actual inspection would be formed by the through thickness integration of the birefringence effect.

5.3.4.2 Birefringence Measurement

Consider an infinitesimal area of an elastic lamina, initially square under a general system of two-dimensional stress, as in figure 48, below. When loaded with a constant load, the state of stress in a vanishingly small volume in a linear elastic solid remains constant, but, this stress state may be described in a number of different ways. These descriptions of the stress state may be related by means of a stress transformation.

Typically, the stress transformation is used to convert between direct and shear stresses which align with the analysis co-ordinate system, and the directions within the stressed material known as principal stress directions.

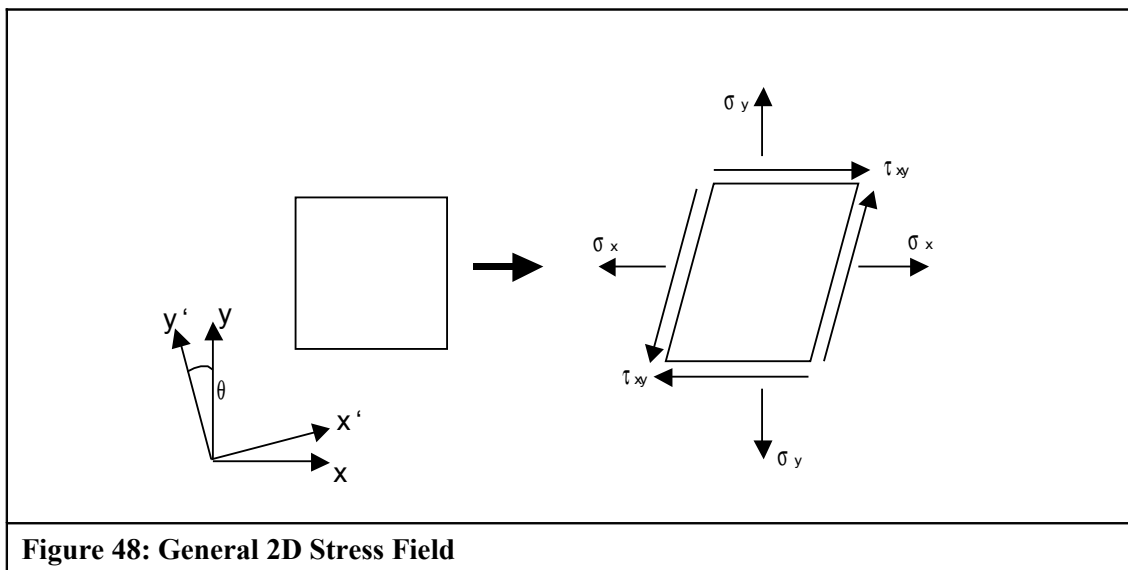


Figure 48: General 2D Stress Field

The stress transformations equations can be written as in equations 35, [81], below;

$$\begin{aligned}\sigma_1 &= \frac{\sigma_x + \sigma_y}{2} + \frac{\sigma_x - \sigma_y}{2} \cos(2\theta) + \tau_{xy} \sin(2\theta) \\ \sigma_2 &= \frac{\sigma_x + \sigma_y}{2} - \frac{\sigma_x - \sigma_y}{2} \cos(2\theta) - \tau_{xy} \sin(2\theta) \\ \tau_{MAX} &= \frac{\sigma_y - \sigma_x}{2} \sin(2\theta) + \tau_{xy} \cos(2\theta)\end{aligned}\quad \text{Equations 35}$$

Where σ_1 and σ_2 are principal stresses, σ_x , and σ_y , the direct stresses in the x and y directions respectively, τ_{xy} and τ_{MAX} , the shear stresses aligned with the X and Y axes, and the maximum shear stress (at 45° to the directions of the mutually orthogonal principal stresses) in the plane, [14].

While it is possible to carry out the stress transformation under a rotation purely using equations 35, it is sometimes easier, and clearer to visualise using a Mohr's circle construction, as shown in figure 49. It must be borne in mind, that both the equations and the Mohr's circle construction represent different orientations, or axes, from which the same physical stress distribution or field may be viewed. A complication of the Mohr's circle representation is that angles are scaled by a factor of two.

Within the Mohr's circle representation, the abscissa represents the principal stress direction, while the ordinate represents the maximum shear direction. Owing to the scaling of angles, these axes are orthogonal on the Mohr's circle, while in the elastic solid, these directions are actually only 45° apart.

To construct Mohr's circle, the centre of the circle is located along the abscissa by taking the average of the orthogonal direct stresses (as per the first terms of the first two equations in equations 35). Points are plotted corresponding to (σ_x, τ_{xy}) , and (σ_y, τ_{yx}) , and the circle is drawn, passing through these diametrically opposite points.

To use the Mohr's circle, the stress description at an angle θ from the abscissa in the elastic solid may be found by reading off the co-ordinates on the circumference of Mohr's circle which are 2θ away from the points corresponding to (σ_x, τ_{xy}) , and (σ_y, τ_{yx}) .

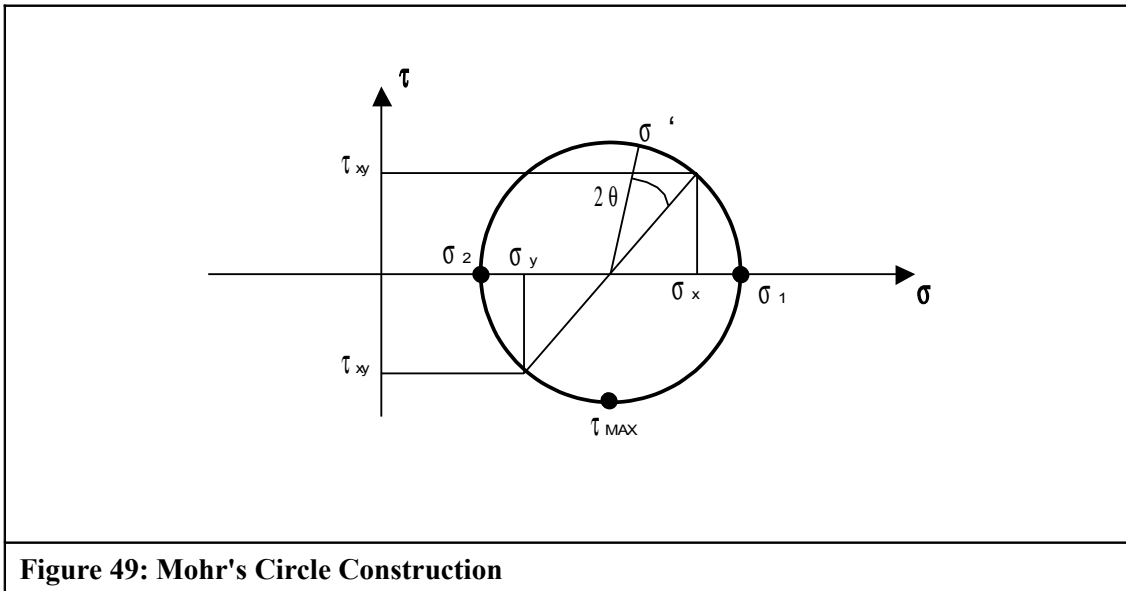


Figure 49: Mohr's Circle Construction

There are two orthogonal directions in the elastic lamina where the shear stress is zero (180 degrees apart on the Mohr's Circle). These orthogonal directions are principal directions, and the corresponding direct stresses are called principal stresses. For isotropic materials, the planes of principal stress are also planes of principal strain. The plane of maximum shear stress is at 45° to the plane of principal stress (90° on Mohr's Circle)

Having considered the possible two-dimensional states of stress, it is next required to understand how light propagating through such a lamina would be affected, [73]. The following two rules effectively described how the indices of refraction are altered as an initially isotropic medium becomes anisotropic under the effect of strain.

i) At any point in a stressed transparent solid the axes of polarisation of light passing through the solid are parallel to the directions of the principal stresses in the plane of the wave-front at that point.

ii) The difference in the velocities of the two opposite polarised rays at the point is proportional to the difference of these two principal stresses, and is independent of stresses perpendicular to the plane of the wave front.

The stress optical co-efficient, C , can be defined in terms of the retardation, Δz , and the thickness of material, d , between the orthogonal polarisations of light as per i);

$$C = \frac{\Delta z}{(\sigma_1 - \sigma_2) d} \quad \text{Equation 36}$$

Consider a stressed transparent lamina between two crossed (orthogonal) polarisers.

The wave input to the sample can be written;

$$u = a \sin\left(\frac{2\pi}{\lambda}(V_0 t - z)\right) \quad \text{Equation 37}$$

Where λ is the wavelength of the light, a , the amplitude, and V_0 , the speed of light in the unstressed material. Within the stressed lamina, the two orthogonally polarised waves which align with the axes of principal stress at an angle of α with respect to the polariser.

$$\begin{aligned} u_1 &= a \cos(\alpha) \sin\left(\frac{2\pi}{\lambda}(V_0 t - z)\right) \\ u_2 &= a \sin(\alpha) \sin\left(\frac{2\pi}{\lambda}(V_0 t - z)\right) \end{aligned} \quad \text{Equations 38}$$

As the wave leaves the stressed lamina, the relative retardation can be included

$$\begin{aligned}
 u_1 &= a \cos(\alpha) \sin\left(\frac{2\pi}{\lambda}(V_0 t - z - C(\sigma_1 - \sigma_2)d)\right) \\
 u_2 &= a \sin(\alpha) \sin\left(\frac{2\pi}{\lambda}(V_0 t - z)\right)
 \end{aligned}$$

Equations 39

The wave is further modified by the analyser, or second polariser.

$$\begin{aligned}
 u_{OUT} &= u_1 \sin(\alpha) - u_2 \cos(\alpha) \\
 &= a \sin(\alpha) \cos(\alpha) \sin\left(\frac{2\pi}{\lambda}(V_0 t - z - C(\sigma_1 - \sigma_2)d)\right) \\
 &\quad - a \cos(\alpha) \sin(\alpha) \sin\left(\frac{2\pi}{\lambda}(V_0 t - z)\right) \\
 &= a \sin(2\alpha) \sin\left(\frac{\pi C(\sigma_1 - \sigma_2)d}{\lambda}\right) \\
 &\quad \cos\left(\frac{2\pi}{\lambda}(V_0 t - z - C(\sigma_1 - \sigma_2)d)\right)
 \end{aligned}$$

Equation 40

This is a wave of amplitude;

$$|u_{OUT}| = a \sin(2\alpha) \sin\left(\frac{\pi C(\sigma_1 - \sigma_2)d}{\lambda}\right)$$

Equation 41

The first term of equation 41, $\sin(2\alpha)$ expresses the condition that the output wave would have zero amplitude when the principal stress is in the same direction as either the polariser or analyser. These isoclinic fringes are of no use to the fracture mechanics inspection, and they obscure the information of interest, namely the isochromatic fringes which indicate changing stress magnitude. The isoclinic fringes can be removed, by a method described below.

The second term of equation 41, which expresses the conditions required for the formation of isochromatic fringes may be more easily seen if the second term of equation 41 is re-written in terms of the retardation.

$$\sin\left(\frac{\pi C (\sigma_1 - \sigma_2) d}{\lambda}\right) = \sin\left(\frac{\pi \Delta z}{\lambda}\right) \quad \text{Equation 42}$$

Whenever $\Delta z = n\lambda$, where $n=1,2,3,\dots$, the amplitude (and hence intensity) of the transmitted light is zero. With monochromatic light, the output light is extinguished whenever the principal stress difference is zero, or the retardation is an integer number of wavelengths whatever the direction of the principal stress. With white light, a cyclic range of colours is observed in the output light, corresponding to the remaining light after that wavelength which “fits” has been removed.

To remove the troublesome isoclinic fringes, consider the situation if the polariser and analyser were both rotated quickly about the z-axis, maintaining their 90° phase difference. The isochromatic fringes would remain unchanged, while the isoclinic fringes would move alternating between light and dark. If the rotation were sufficiently fast, the isoclinic fringes would disappear into a blur. Instead of rotating the polarisers, it is easier to introduce circular polarisation of the light by means of crossed quarter wave plates, one placed between the sample and each polariser.

The outline of the apparatus as shown in figure 47 was not used for the optical bench inspection as it did not reject the isoclinic fringes. The apparatus was modified by the addition of a pair of quarter wave plates, as depicted in figure 53.

5.3.4.3 Birefringence Measurement – Theoretical Example

In order to illustrate the application of the analysis given above, the stress in the area around a cracked plate was evaluated, and the corresponding photo-elastic fringe pattern estimated, and compared with a similar pattern found in the published literature.

The geometry used for the example was a large, thin plate in tension on two opposite edges, with the other two edges free. Normal to the principal tensile stress, far away from the edges was a small crack. The crack was located at $X=0$, and extends from $Y=-0.5$ to $Y=0.5$. The solution used is given in [82], and the stress contour plots are given in figure 50, below;

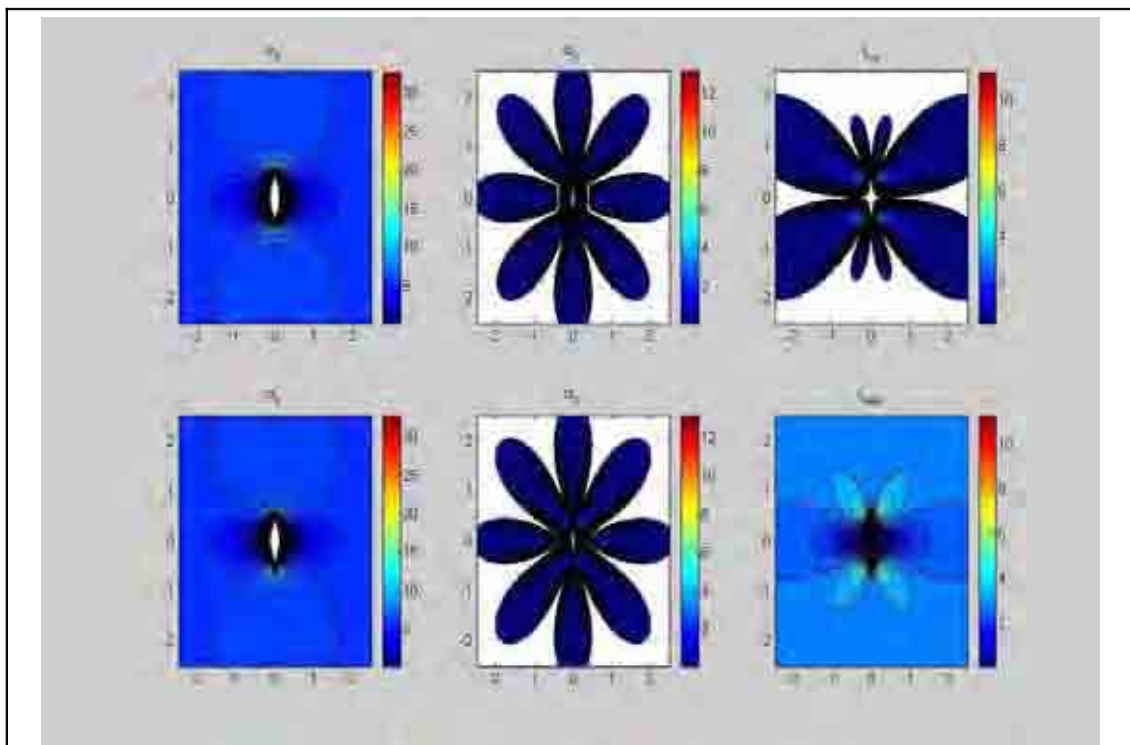
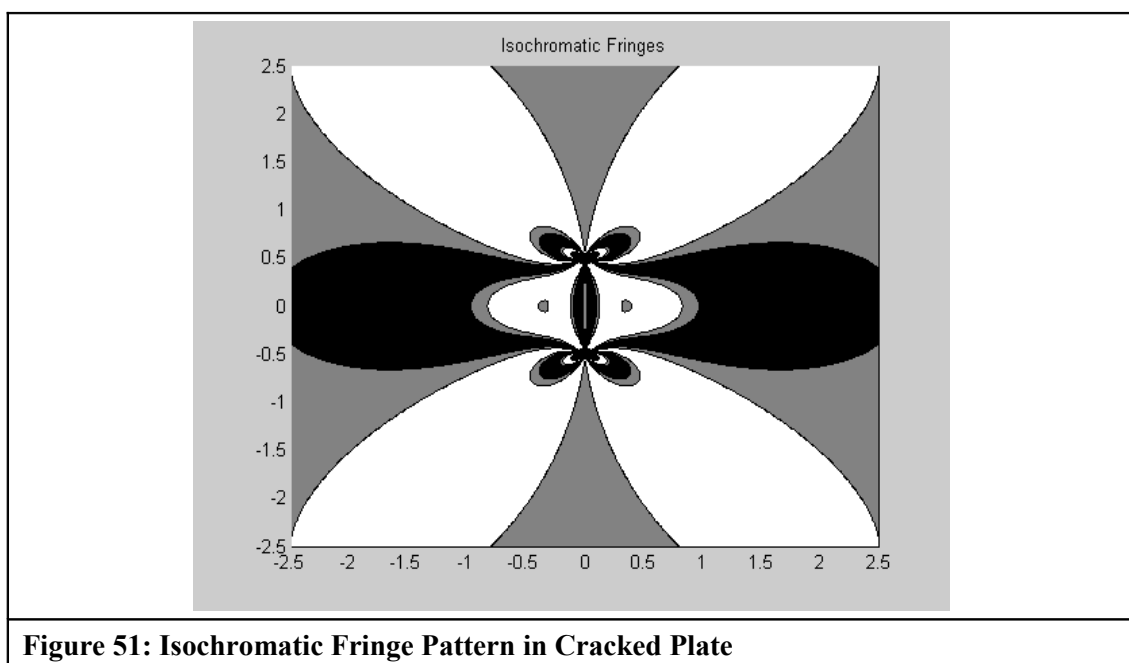


Figure 50: Stress Analysis of a Cracked Plate

Where, σ_x is the principal stress in the x direction, σ_y , the principal stress in the direction, τ_{xy} , the shear stress aligned with the x and y axes, σ_1 , the maximum principal stress, σ_2 , the minimum principal stress, and τ_{MAX} , the maximum shear stress.

The stress results were post-processed using equation 42 in order to estimate the fringe patterns which would be observed in the vicinity of the crack if an experimental set up like that shown in figure 53 were used. The results of this post-processing, with isoclinic fringes removed, are shown in figure 51, below.



This may be compared with a pattern obtained from a physical specimen, as shown in figure 52, below.



Figure 52: Isochromatic Fringe Pattern in Cracked Plate, (Source: [80])

5.3.4.4 Inspection Apparatus

As stated, the apparatus as shown in figure 47 was not that actually used. A pair of quarter wave plates were also used in order to remove the isoclinic fringes. The inspection configuration as used is shown in figure 53, below.

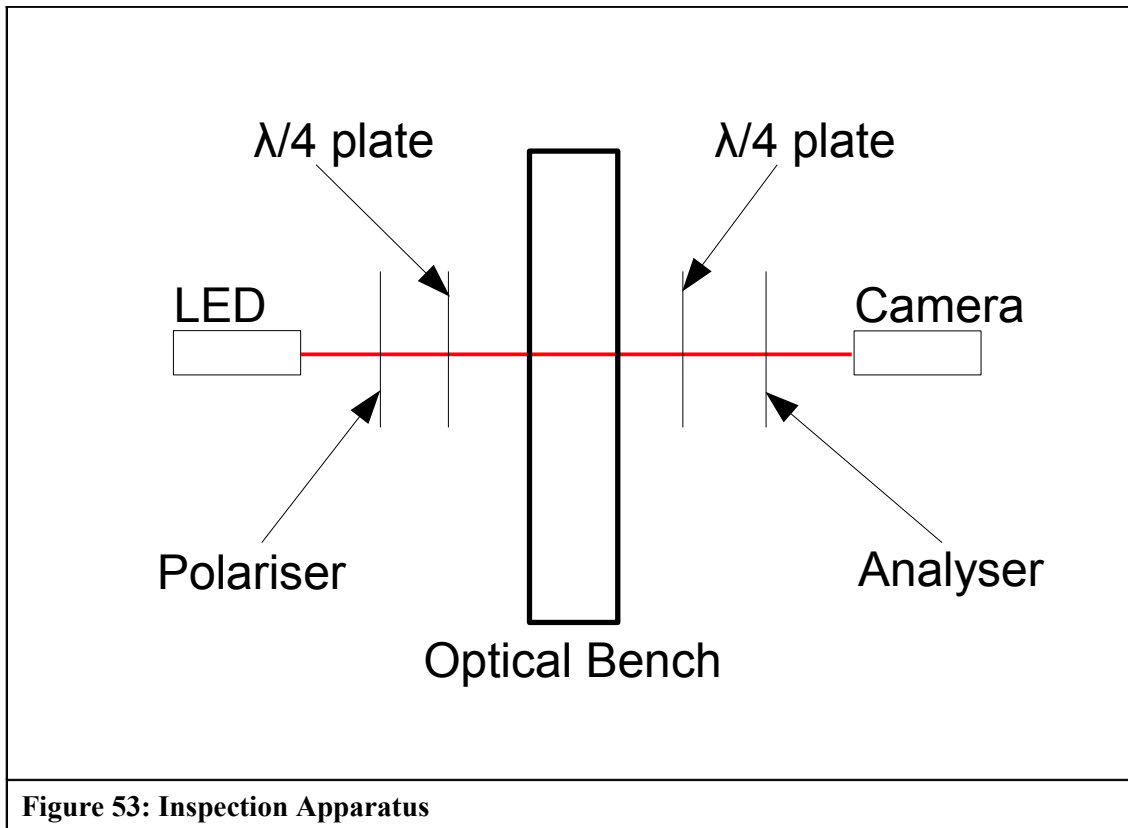


Figure 53: Inspection Apparatus

The light source was a 1W high intensity red (625 nm) light emitting diode. The light, after being passed through the polarisers, quarter wave plates and the optical bench was detected by the LaVision digital camera described above, and the image stored on hard disk. The inspection rig is shown, in figure 54, below.

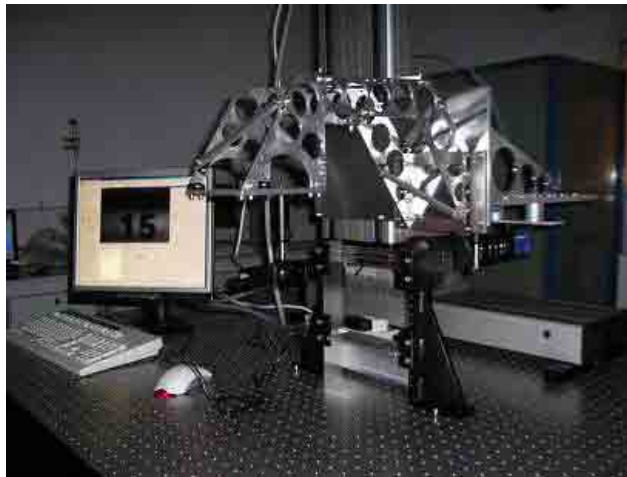


Figure 54: Inspection Rig

The polarisers and quarter wave plates were set up to give a dark field when there was no test object in position, which meant that any light detected above the normal background was the result of birefringence in the test specimen. The image was corrected automatically for both the camera's dark response, and for background light before being saved. The images were focussed and magnified using a Nikon zoom lens system, and captured using a digital camera. The camera was positioned by a pair of stepper motor driven linear stages. The entire system was computer controlled via a macro program within the LaVision data acquisition software, allowing a scan of the test object to be undertaken with minimal supervision.

5.3.4.5 Optical Bench First Inspection

Owing to the large magnification used, the volume of material which could be inspected in one camera image was limited both in lateral extent and in depth. That the images were limited laterally to the extent of 5.5 mm in the abscissa, and 4 mm in the ordinate may be seen in the axes of figure 55, below.

Figure 55 shows surface damage on the optical bench (serial No. 3) lower surface. In order to scan the area of the optical bench, some 212 mm by 200 mm, 2255 images were recorded. Again, owing to the large magnification, the corresponding depth of field was small, of the order of 2 mm. In order to scan an optical bench of thickness total thickness 50 mm, it was necessary to reposition the test object with respect to the camera for each of the required scan slices, each slice being 2 mm deep.

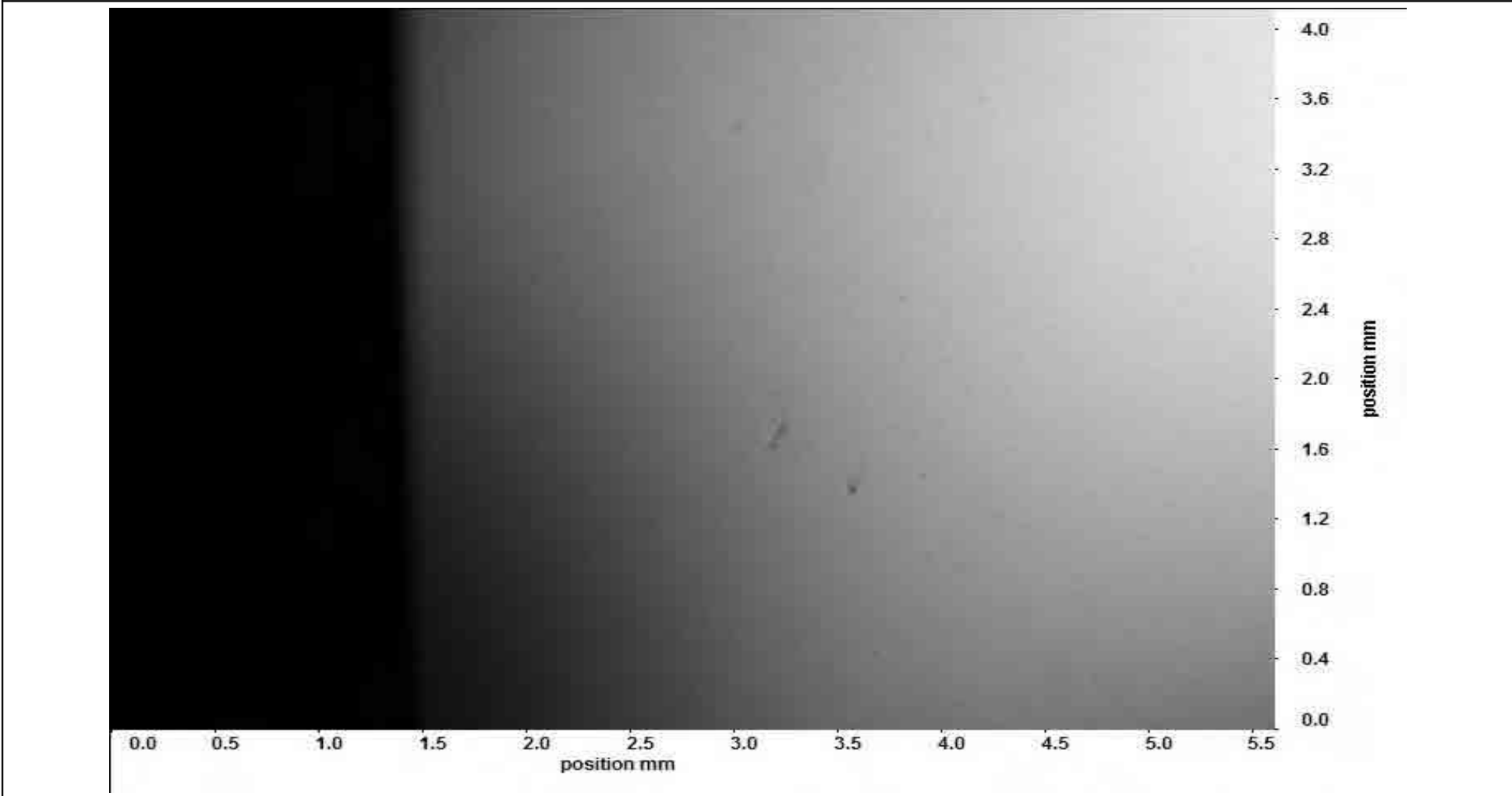
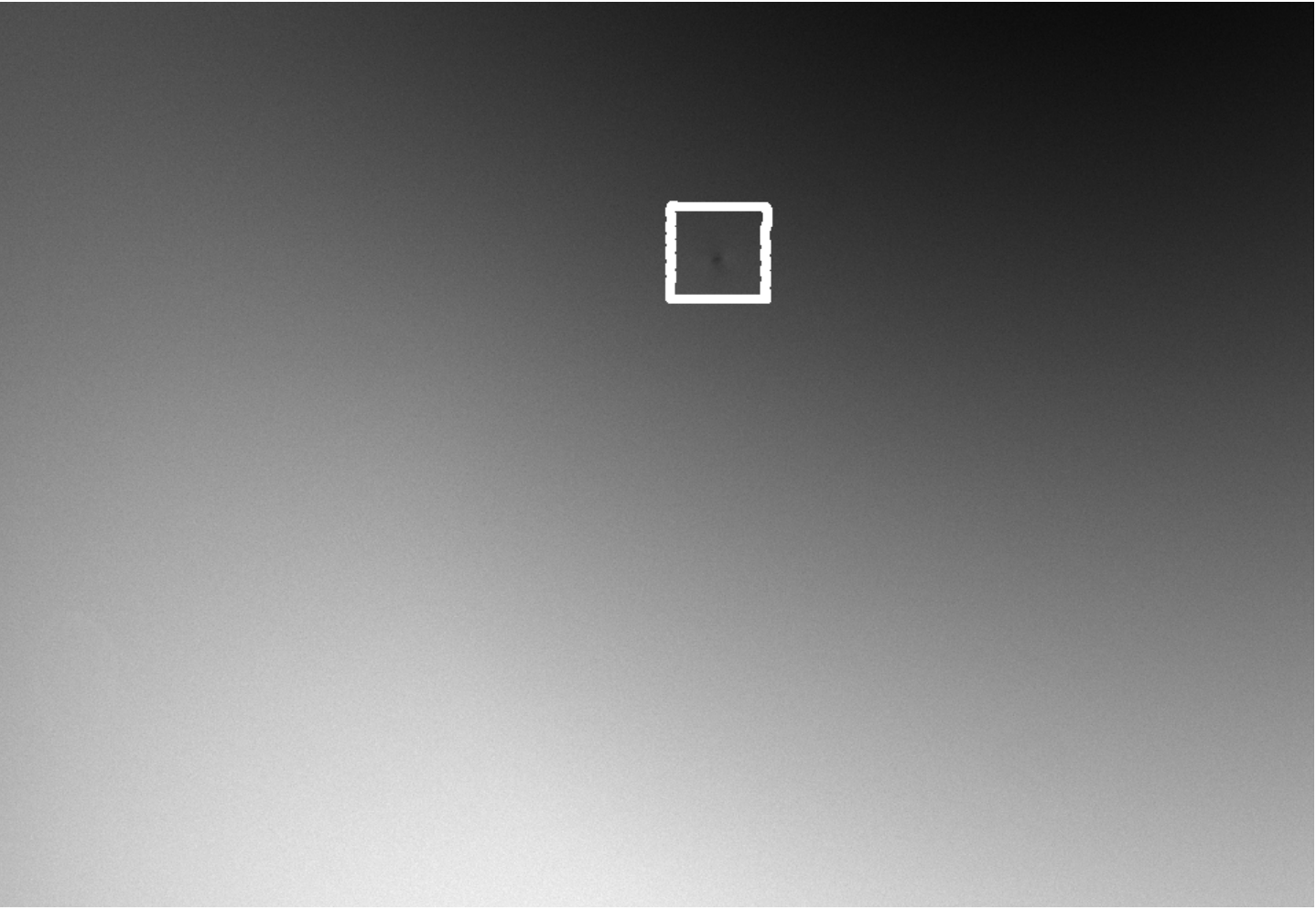


Figure 55: Damage on Lower Surface of Optical Bench (Serial No 3)

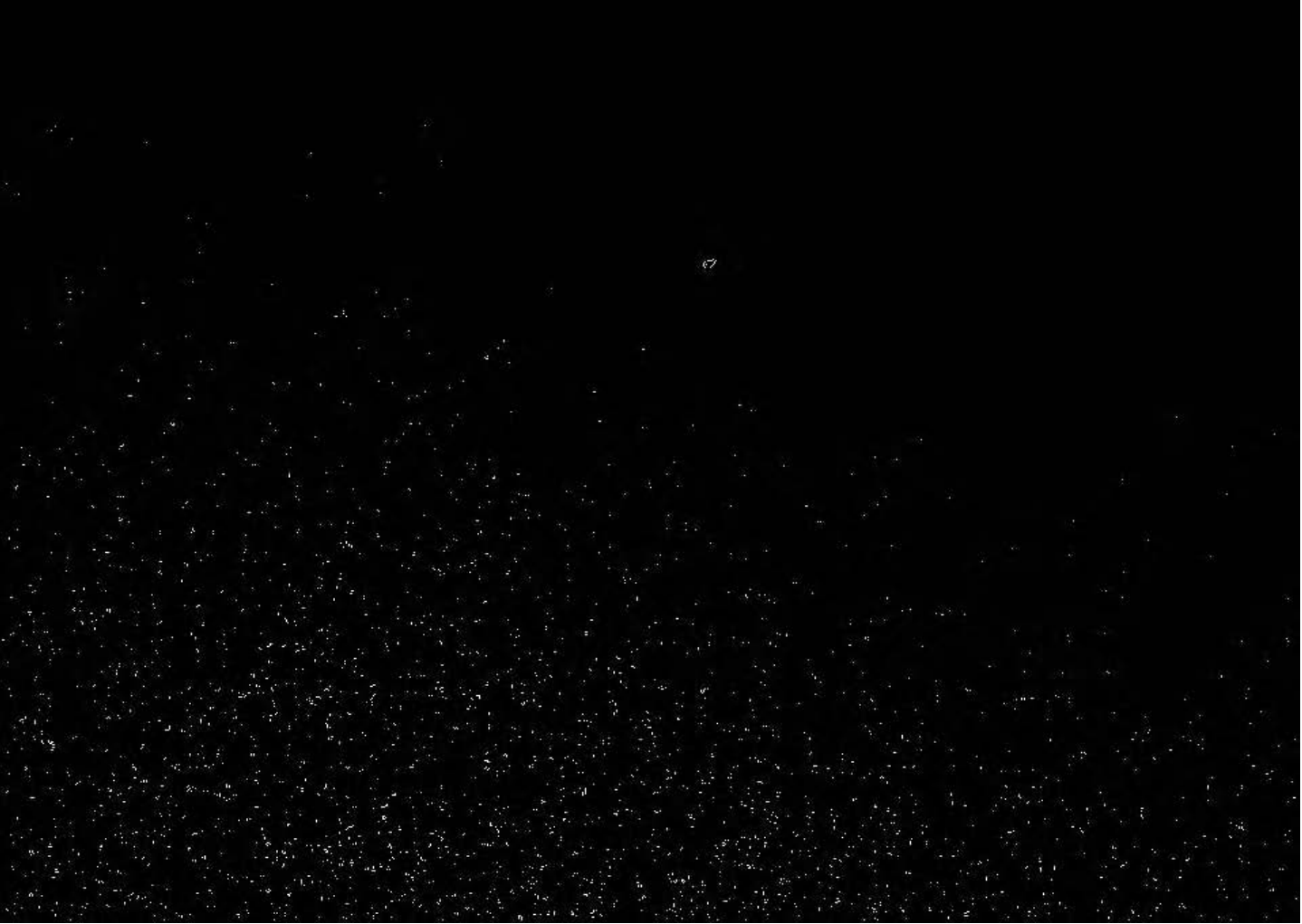
Owing to the large number of images which were necessary to complete the scan of an optical bench, it was necessary to perform some degree of data reduction. To give an idea of the scale of the data set, each scan comprised 2255 images, and 27 2 mm slices were required per bench, i.e., approximately 61,000 images per bench; there were 5 benches scanned.

In order to manage the assessment of such a large number of images, an automatic first pass assessment was designed. The algorithm consisted of the following steps;

<i>Processing Step</i>	<i>Example Image</i>
0. Image as recorded (Defect highlighted in white square)	
1. Gaussian filter blur	

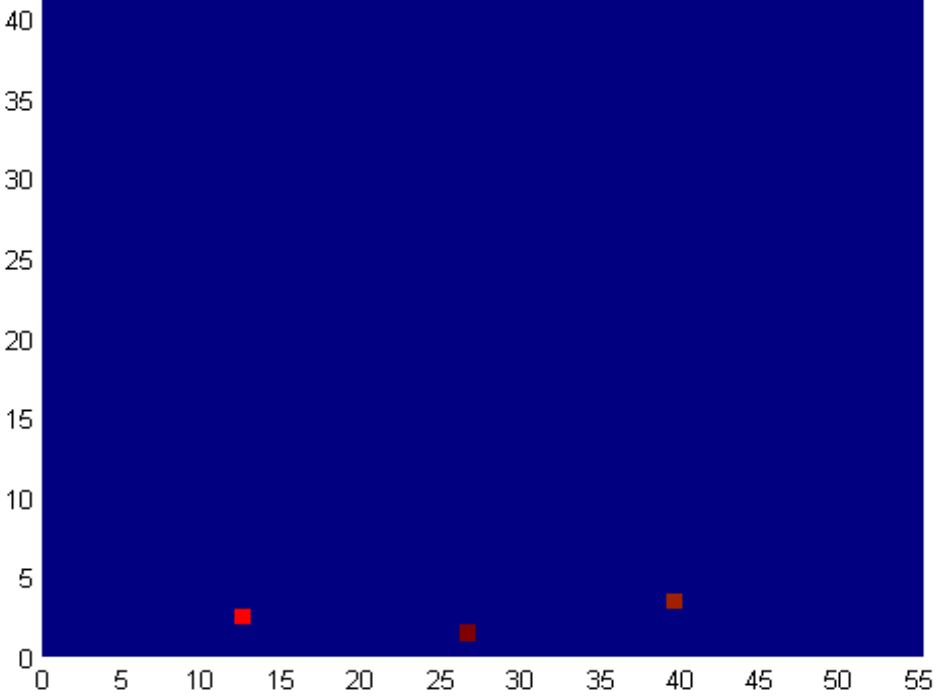
<i>Processing Step</i>	<i>Example Image</i>
a. (3x3)	a. (3x3) 

<i>Processing Step</i>	<i>Example Image</i>
b. (5x5)	b. (5x5) 

<i>Processing Step</i>	<i>Example Image</i>
<p>2. Edge detection followed by contrast enhancement → monochrome</p>	<p>a. (3x3) Gaussian filtered</p>  The image is a dark, almost black, square with a dense distribution of small, bright white and light gray specks. These specks are scattered across the entire area, representing the detected edges and noise after processing. The overall appearance is that of a high-contrast, noisy binary or near-binary image.

<i>Processing Step</i>	<i>Example Image</i>
	<p data-bbox="598 231 907 271">b. (5x5) Gaussian filtered</p> 

<i>Processing Step</i>	<i>Example Image</i>
<p>3. Counting of black and white pixels</p>	<p>a. (3x3) Gaussian filtered</p> <p>3022 non zero pixels</p> <p>b. (5x5) Gaussian filtered</p> <p>53 non zero pixels</p>
<p>4. Collation and presentation of results</p>	<p>For each image obtained during each scan of the optical bench, the pixel counts as described in the processing steps above were assembled into a matrix, representative of the location. An example is shown below.</p>

<i>Processing Step</i>	<i>Example Image</i>
	 <p data-bbox="598 1093 1948 1189">The non-blue squares represent image files which resulted in a larger pixel count, and, therefore, the images which correspond to these coloured squares were manually inspected.</p>
Table 12: Image Processing	

The Gaussian blur was used in order to remove from the image any very small glitches or artefacts which would interfere with the operation of the edge detection process. In order to ensure that the Gaussian blur was not removing important information, two sizes of blur were used, namely 3x3 and 5x5, thus, for each image recorded during a scan, the two blurred images were used in further analysis.

Edge detection was trialled using a number of different algorithms, but, the Sobel method, [83], was used. Among other properties, the Sobel method is symmetric rather than having any bias for edges in the x direction or y direction.

After pixel counting, the image data were collated, and any image which showed an anomalous pixel count, in either 3x3 or 5x5 versions of the image was reviewed visually. The pixel counts found using the 3x3 blur and the 5x5 blur differed significantly, however, the extra pixels found on images which were only 3x3 blurred, when individually inspected did not correspond to any defects of significant size. Most images returned a zero pixel count, therefore, the problem of setting an appropriate threshold pixel count did not arise.

The visual review of these images showed no defects or problems which prevented the optical benches being allowed forward into the manufacturing process. While this largely automated process had removed the possibility of the existence of any gross defects from the optical benches, the benches were also subjected to machining and integration processes after this inspection, therefore, it was not possible to allow the benches to progress directly to delivery for flight without further inspection. As a result of this further mechanical work and machining of the optical bench, another detailed inspection of the highly stressed areas of the bench was carried out, and this is described in section 5.3.4.7, below.

5.3.4.6 Optical Bench Inspection Records

The optical bench candidates which were inspected, deemed acceptable, and released to the project are summarised in table 13, below;

<i>Optical Bench</i>	<i>Controlling Document</i>	<i>Release Date</i>
Serial No. 000	S2-UGB-RP-3006 - LTP OBI BASEPLATE - Production Traveller Report - Serial No. 000	20 th August 2007
Serial No. 001	S2-UGB-RP-3003 - LTP OBI BASEPLATE - Production Traveller Report - Serial No. 001	26 th July 2007
Serial No. 002	S2-UGB-RP-3004 - LTP OBI BASEPLATE - Production Traveller Report - Serial No. 002	31 st July 2007
Serial No. 003	S2-UGB-RP-3005 - LTP OBI BASEPLATE - Production Traveller Report - Serial No. 003	2 nd August 2007
Table 13: Optical Bench Post Inspection I Release		

5.3.4.7 Optical Bench Re-Inspection

The pre-machining inspection scans which were analysed using the method described in table 12, did not show any serious defects, and all inspected benches were cleared to continue to the next stage of manufacture.

The most onerous defects were seen during the re-inspection of the optical benches, where particular attention was paid to the highly stressed area close to the inserts. In order to allow the inspection of the largest possible volume of material around the inserts, a revised fixture was used, as shown in figure 56, below. The fixture allowed the optical bench under inspection to be rotated about the axis of any pair of opposite inserts.

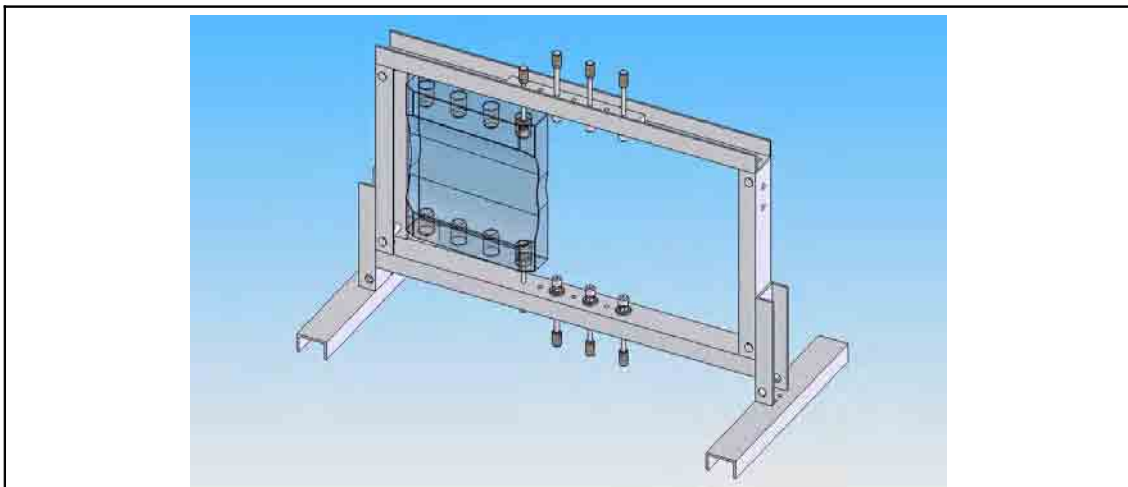


Figure 56: Optical Bench Rotation Fixture

Via the use of this fixture, instead of scanning the bench at discrete depth increments, the volume of material around the insert under inspection was rotated slowly, which means that defects passed through the field of view slowly, and the position and orientation of the bench could be adjusted to bring the defect into focus, thus allowing the determination of the position of the defect relative to the insert.

This detailed inspection found a number of features and defects, some of which are shown in figures 57 to 60, and summarised in table 14, below.

The benches were inspected after the inserts were bonded in place by ASD. During the inspections an anomaly was observed in glass adjacent to the midpoint along the insert. This anomaly may be seen in figure 57, below.

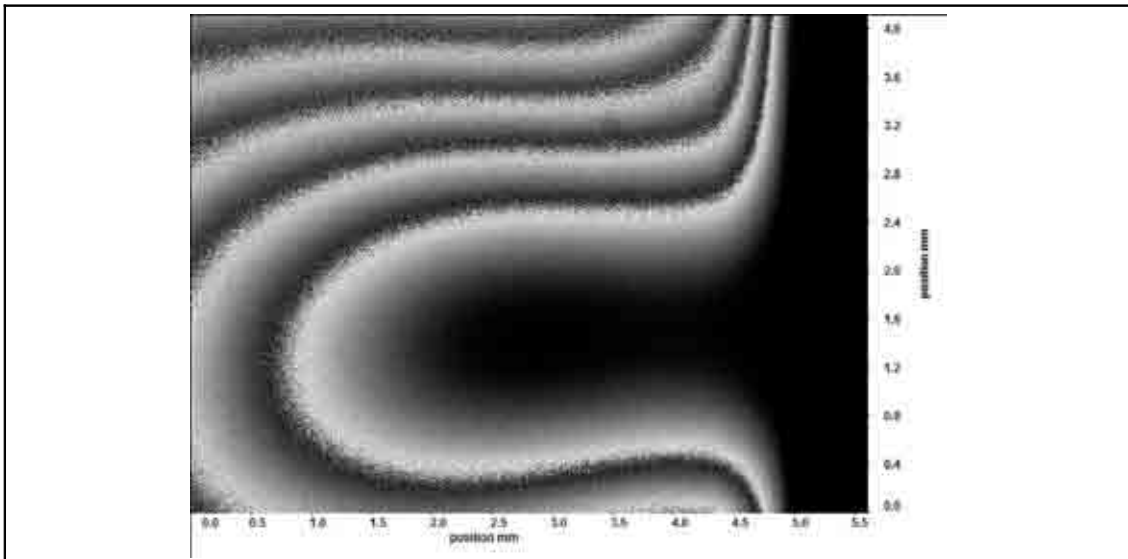


Figure 57: Insert Anomaly

As the anomaly was consistent throughout all samples, and was found in all inserts inspected, it was not deemed a fault or defect. The stress pattern aligned with the area where epoxy was extruded out of the mid length groove in the insert, and the stress represents how the shrinkage of the epoxy was affected by the flow patterns during injection (see figure 32). As there were no defects found in this volume of material, the residual stress left by the epoxy intrusion could not cause failure. Had any defects been found in the area affected by the residual stress, quantitative analysis of the magnitude of the residual stress and its interaction with the applied stress during insert loading would have become necessary to allow the optical bench to pass the inspection – in practice, a non-conformance report would have been raised, and this extra analysis would have been agreed with the project.

Surface scratch damage was found, as shown in figure 58, below. As the defect was larger than 100µm in size, a non-conformance report was raised, and the defect was investigated, in some detail, by a non-conformance review board. The scratch was measured to determine its depth using a surface measurement machine at UGL. Owing to the combination of the depth of the defect, and its location relative to the stress field, it was decided that this defect was, in fact, tolerable.

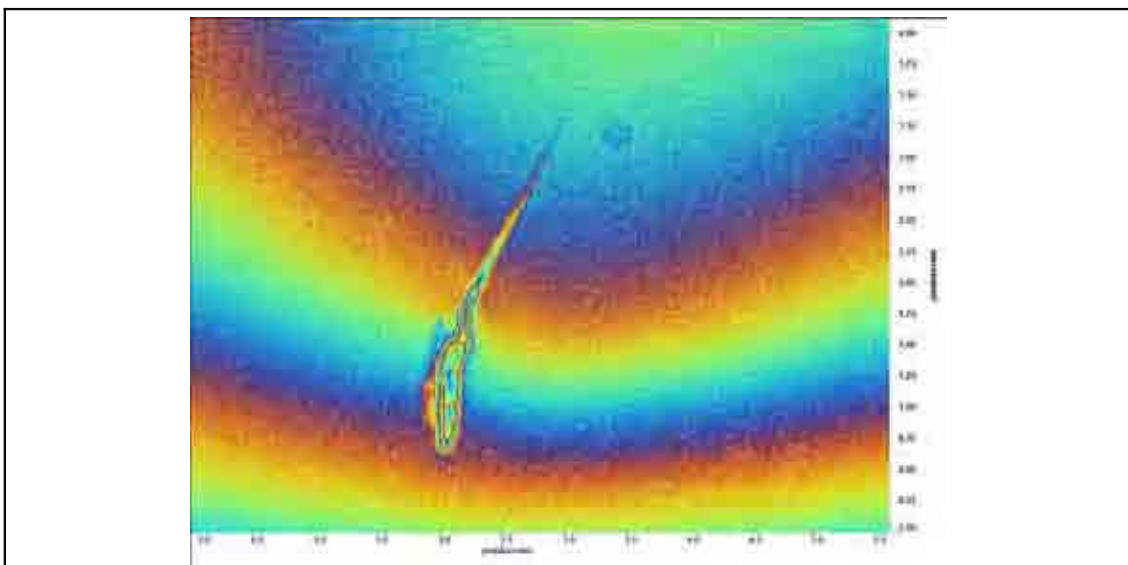


Figure 58: Scratch in Optical Bench Surface Adjacent to Insert 3 (False colour used to enhance image)

Figure 59, below, shows an embedded 60 µm defect. The stress pattern around the defect can clearly be seen. As the defect was below 100 µm in size, it was not considered critical. As individual defects were not logged during the first inspection, it cannot be said whether a defect seen during the re-inspection is the same as one seen during the first inspection. The first inspection was not as detailed as the second inspection, and the goal was simply to make sure there were no gross defects at that stage.

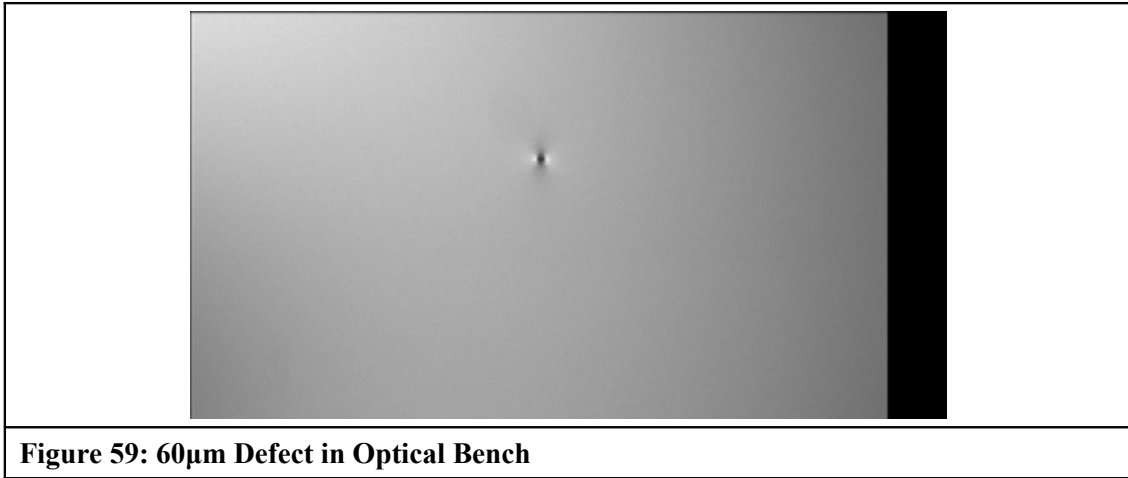
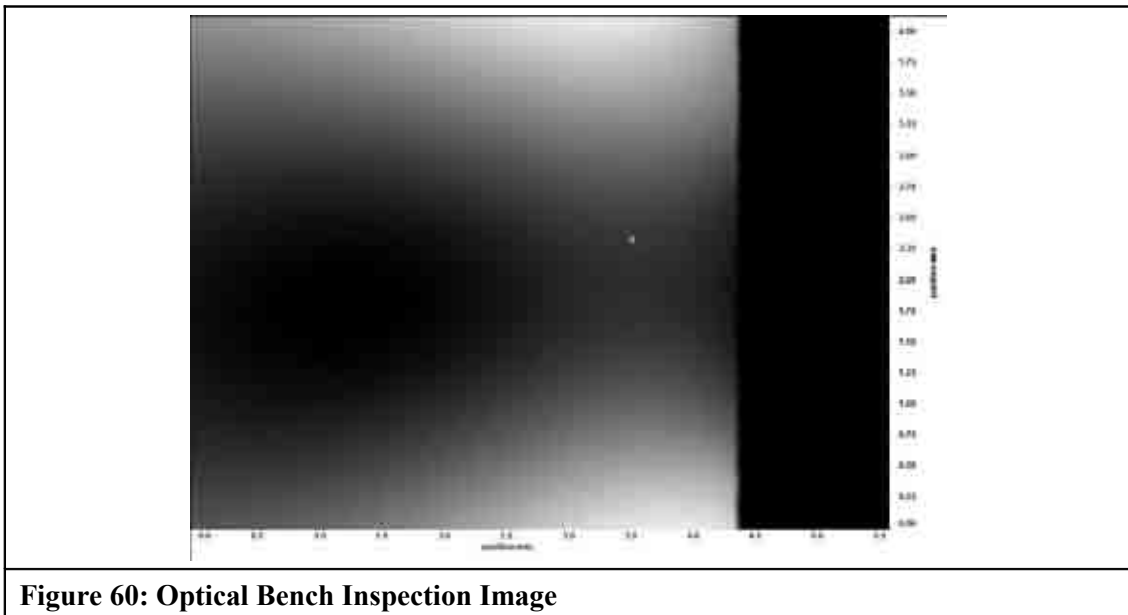


Figure 60, below, shows a defect which was adjacent to the insert. As the insert was the most highly loaded part of the bench, this was the most sensitive area of the bench. The defect was only 40 µm when compared with the limit of 100 µm, therefore, the defect was deemed tolerable



While there were more defects and a number of anomalies seen, none was found larger than 100 μm in size AND in a critical area of the optical bench. Therefore, the optical bench passed the inspection. The defects found in optical bench interferometer serial number 03 are listed in table 14, below.

<i>Defect No.</i>	<i>Defect Size (μm)</i>	<i>Defect Location</i>	<i>Comments</i>
1.	40	3 mm away from insert edge	Although the defect was close to the highly stressed inserts, it was too small to cause concern
2.	45	In bulk material	The defect was away from the highly stressed area of the bench, and was also too small to cause concern
3.	60	In bulk material	The defect was away from the highly stressed area of the bench, and was also too small to cause concern
4.	65	3.5 mm away from insert edge	Although the defect was close to the highly stressed inserts, it was too small to cause concern
5.	65	0.75 mm away from insert edge and radius	Although the defect was close to the highly stressed inserts, it was too small to cause concern
6.	130	In bulk material	A larger defect than would be tolerated in a high stress area, but, this defect was safely located in a low stress area
7.		Lower surface of optical bench	Surface scratch – although the scratch was long, it was not wide. This was verified via a surface profile measurement taken by staff at UGL.

Table 14: Optical Bench Interferometer Number 03 – Defect Summary

The benches were inspected, once via a scanning technique, and once again, after machining via a detailed inspection of the volume of material in the area of the inserts. As a result of these

inspections, optical bench interferometer serial number 02 and 03 were allowed to progress into flight and flight spare manufacture.

5.3.4.8 Inspection Verification

While it was possible to be confident of the ability of the inspection rig to resolve detail which was 0.1 mm in size, it was not known whether cracks which were smaller would be adequately detected. For this reason, a validation scheme was devised, [84], whereby samples of Zerodur[®] were inspected, and then tested in tension to ensure that the samples reached the predicted ultimate load. The samples were 50x50x5mm, and the tension test fixture apparatus is shown in figure 61, below. A number of the samples were processed to introduce damage; in some cases by scratching the surface in order to mimic a surface breaking crack, in others by the initiation of a small crack in the body of the material using a 3D laser engraving process typically used to prepare awards, trophies and corporate gifts. This testing work also provided an opportunity to gain experience in the use of the epoxy selected for the purpose of bonding the photodiodes, [85],[86].

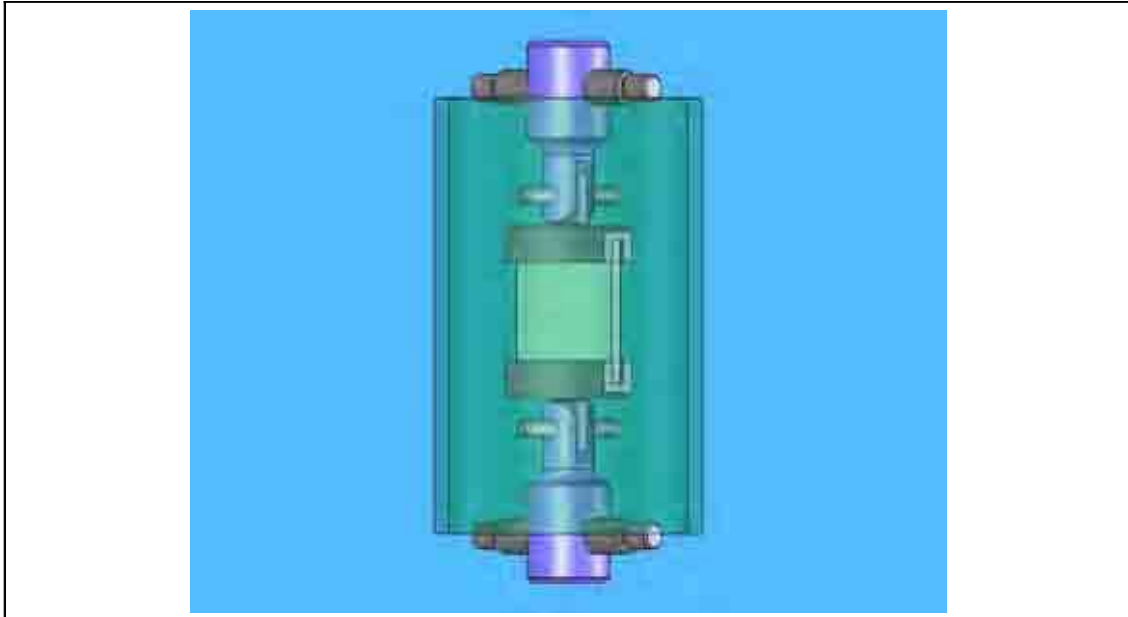


Figure 61: Tensile Testing Fixture

Initial inspection and tensile tests of five samples were undertaken. The samples were named as;

- LC01 – A sample with a 0.1mm defect burnt in by laser – expected failure load 10.94 kN [estimated without using the factor of safety at nominal stress of 43.75 MPa]
- LC02 – A sample with a 0.1mm defect burnt in by laser – expected failure load 10.94 kN [estimated without using the factor of safety at nominal stress of 43.75 MPa]
- Scratched Sample – A sample with a 5x0.1mm scratch in the surface – expected failure load 10.94 kN [estimated without using the factor of safety at nominal stress of 43.75 MPa]
- Sample 1 – A nominally pristine sample – expected failure load >10.94 kN [estimated without using the factor of safety at nominal stress of 43.75 MPa]
- Sample 4, 5, 6, and 7 – Nominally pristine samples – expected failure load >10.94 kN [estimated without using the factor of safety at nominal stress of 43.75 MPa]

The samples were tested, and the results are shown in table 15, below.

<i>Sample</i>	<i>Failure Load (N)</i>	<i>Comments</i>
LC01	6750	Epoxy Failure – joint slipped
LC02	8200	Epoxy Failure – joint slipped
Sample 1	8630	Zerodur® Failure – near bondline
Sample 4	8160	Zerodur® Failure – near bondline
Scratched Sample	8690	Zerodur® Failure – near bondline
Table 15: Initial Zerodur® Fracture Test Results		

These results were not as expected. The tests were limited by the failure of the epoxy joint, rather than the failure of the Zerodur® itself. The failures which occurred within the Zerodur® all initiated close to the interface between the Zerodur® and the test fixture rather than within the body of the material, or, more significantly where there were known defects, i.e., that local stresses near the epoxy joint between the metal fixture and the Zerodur® were the dominant cause of failure rather than any weakness in the bulk of the Zerodur® itself.



Figure 62: Failed Sample, Showing Cracking Along Interface

One possibility which might explain this behaviour was that the test fixture was insufficiently stiff, and during the application load was deforming, and applying a non-uniform tensile load to the Zerodur[®].

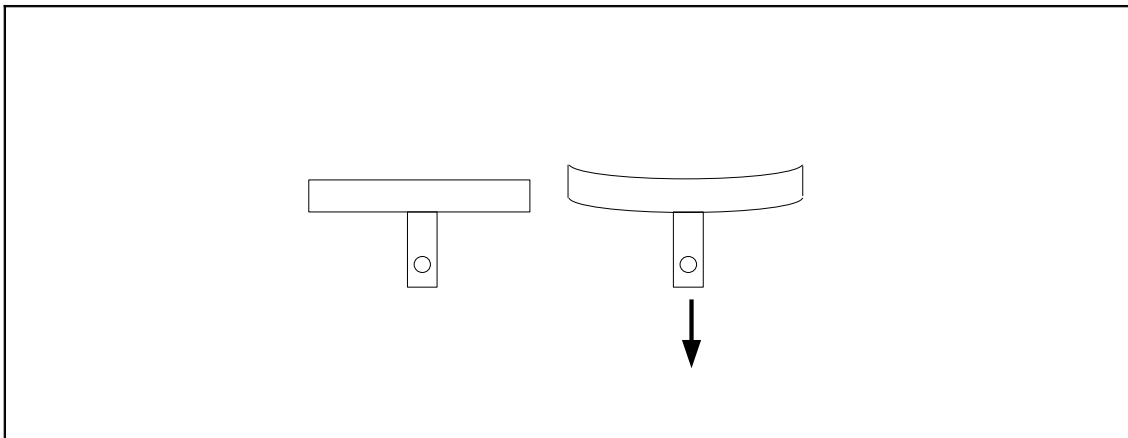


Figure 63: Potential Fixture Inadequacy – Exaggerated Deflection in Bending

In order to assess the interplay between the deflections of the fixture, epoxy, and the Zerodur[®], the assembly was modelled as a beam with an elastic foundation, [87]. This is shown, in

schematic form in figure 64, below. The fixture was modelled as the beam, the epoxy was modelled as the elastic support, and the Zerodur® was assumed completely rigid.

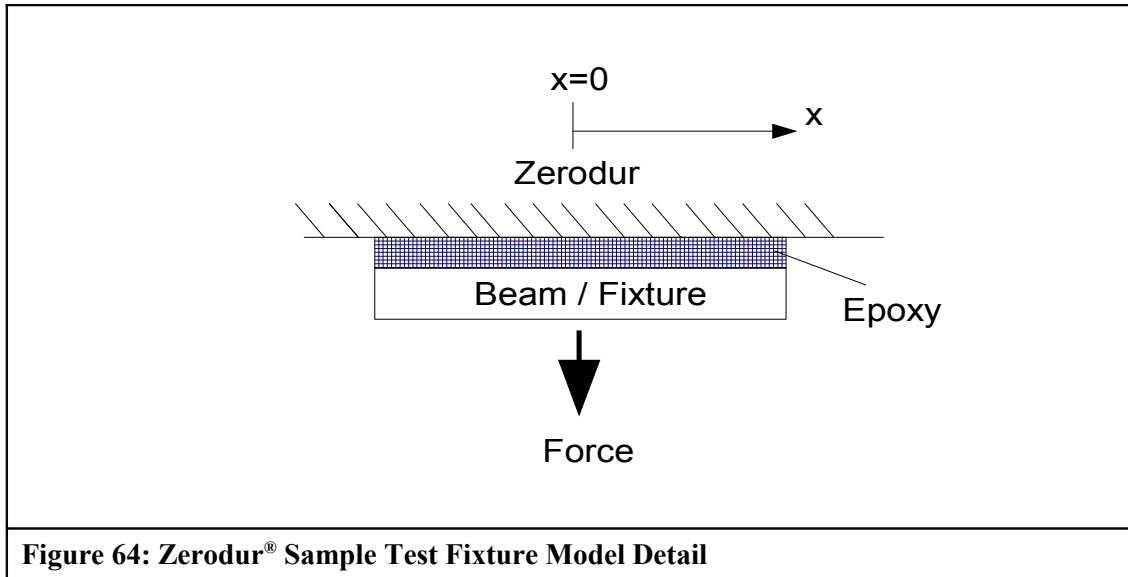


Figure 64: Zerodur® Sample Test Fixture Model Detail

The shear stiffness of the epoxy/Zerodur® joint was used to evaluate the tensile stiffness of the epoxy joint per unit length of the joint. The Zerodur® was conservatively considered as a rigid material – any deflection of the Zerodur® would tend to reduce the deflection across the epoxy, and would thus reduce the load applied to the Zerodur®.

The elastic support required a modification to the usual Euler-Bernoulli beam theory, via the inclusion of a term describing the elastic restoring force per unit length of the beam, kw , as shown in equations 43, below.

$$EI \frac{d^4 w}{dx^4} + kw = 0$$

$$\frac{d^4 w}{dx^4} + 4\beta^4 w = 0$$

$$\beta^4 = \frac{k}{4EI}$$

Equations 43

Where E represents the Young's modulus of elasticity of the beam material, I, the second moment of area, k, the Winkler constant, representing the stiffness per unit length of the epoxy bond, and x is the dimension along the length of the beam. The deflection of the beam, w, can be written as shown in equations 44, below.

$$\begin{aligned}
 w(x) &= Ae^{\beta x} e^{i\beta x} + Be^{\beta x} e^{-i\beta x} + Ce^{-\beta x} e^{i\beta x} + De^{-\beta x} e^{-i\beta x} \\
 w(x) &= Ae^{(1+i)\beta x} + Be^{(1-i)\beta x} + Ce^{(-1+i)\beta x} + De^{(-1-i)\beta x}
 \end{aligned}$$

Equations 44

The standard derivation of the Euler-Bernoulli formulae which govern the bending of beams, the modification to incorporate an elastic foundation (a so-called Winkler foundation), and a demonstration that equations 44 form valid solutions to the governing differential equation may be found in appendix D.

The beam was symmetric about the point of application of the load, which can be taken as the origin. The appropriate boundary conditions were:

- i) Zero slope at the origin (mid length of the beam)
- ii) Zero shear force at the beam tip
- iii) Zero bending moment at the beam tip
- iv) Shear force at origin equals half of the applied force

The boundary conditions may be written as equations 45, below;

$$\begin{aligned} \frac{dw}{dx} &= A+B+C+D &= 0 \\ \frac{d^3w}{dx^3} &= \begin{pmatrix} (2i-2)A+(-2-2i)B \\ +(2+2i)C+(2-2i)D \end{pmatrix} &= F/2 \\ \frac{d^2w}{dx^2} &= \begin{pmatrix} 2iAe^{(\beta L/2)}e^{(i\beta L/2)} \\ -2iBe^{(-\beta L/2)}e^{(-i\beta L/2)} \\ -2iCe^{(-\beta L/2)}e^{(i\beta L/2)} \\ +2iDe^{(-\beta L/2)}e^{(-i\beta L/2)} \end{pmatrix} &= 0 \\ \frac{d^3w}{dx^3} &= \begin{pmatrix} (2i-2)Ae^{(\beta L/2)}e^{(i\beta L/2)} \\ +(-2-2i)Be^{(-\beta L/2)}e^{(-i\beta L/2)} \\ +(2+2i)Ce^{(-\beta L/2)}e^{(i\beta L/2)} \\ +(2-2i)De^{(-\beta L/2)}e^{(-i\beta L/2)} \end{pmatrix} &= 0 \end{aligned} \quad \text{Equations 45}$$

The four simultaneous equations in four unknowns may be solved to give the coefficients, A, B, C, and D. The deflection of the fixture may then be calculated by substituting the values of A, B, C, and D back into equations 44, and, as β is known, the force as a function of length along the beam may be calculated, from which, the variation in force applied to the Zerodur[®] may be estimated.

Figure 65, below shows the results evaluated in terms of normalised stress for varying beam thickness. The original fixture had an equivalent beam thickness of approximately 10 mm, and it may be seen that the maximum stress applied to the Zerodur[®] in this case was some 1.8 times the nominal stress.

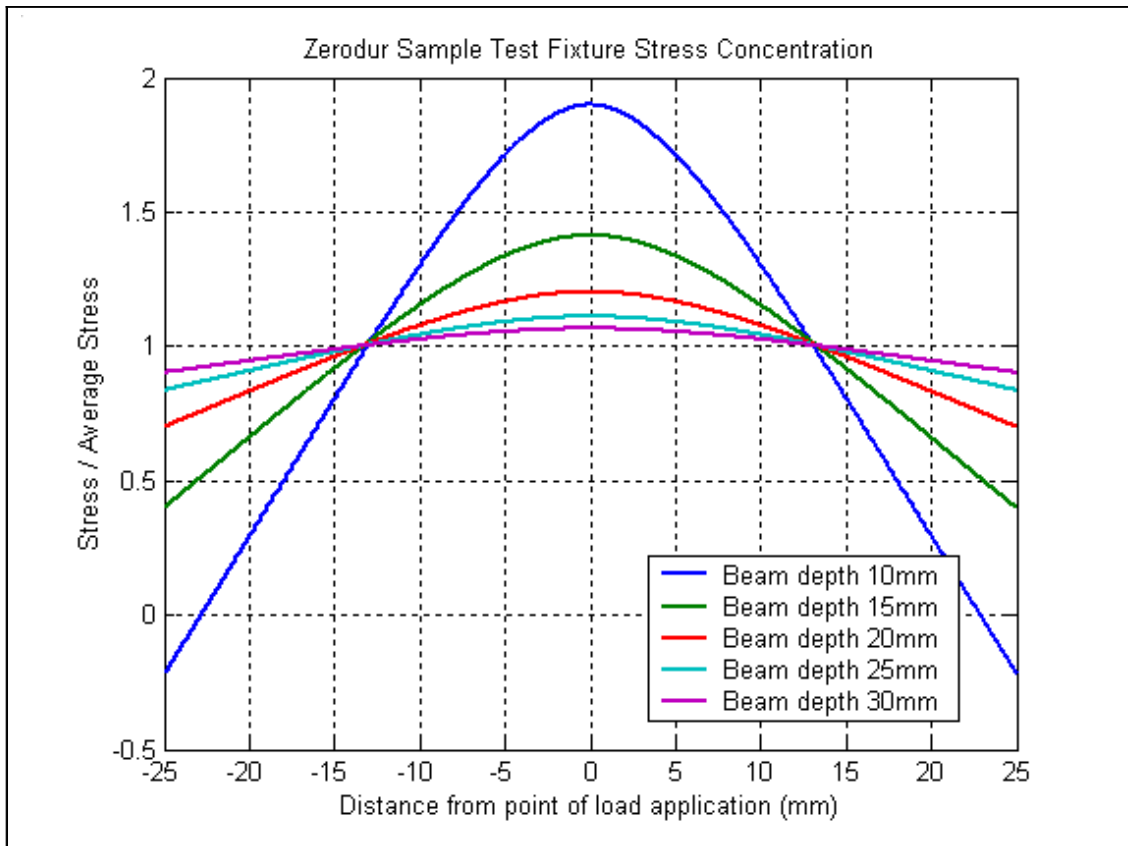


Figure 65: Stress Concentration Results

These data indicated that the original test fixture was, indeed, inadequate, and was responsible for a significant variation in the load applied to the Zerodur® along the length of the epoxy joint, in fact, there was a factor of 1.8 between the highest stress, near the centre of the bond, and the nominal stress. Also, near the ends of the sample, the applied stress was significantly lower than the nominal stress, becoming negative at the extremes. Thus, the test results as written in table 15 were not valid.

Using these data, a further set of test fixtures were made, with an effective beam thickness in excess of 40 mm, as shown in figure 66, below.

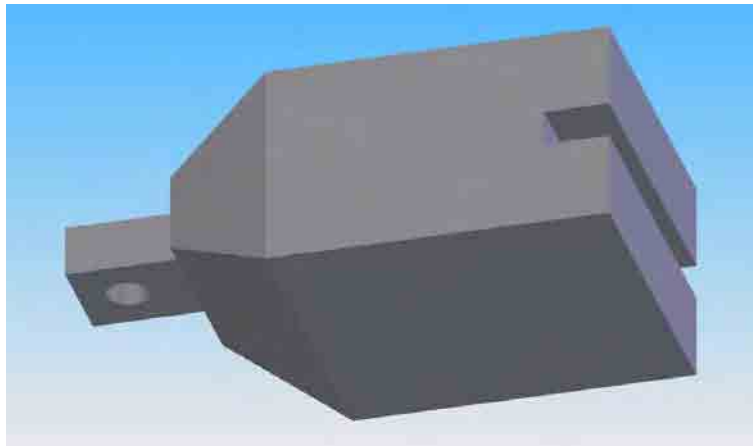


Figure 66: Re-designed Tensile Testing Fixture

The tests were repeated, and the results are in table 16, below.

<i>Sample</i>	<i>Failure Load (N)</i>	<i>Nominal Stress (MPa)</i>	<i>Factored Stress (MPa)</i>	<i>Comments</i>
Sample 5	> 9800	39.2	12.54	Load Limit of Test Machine
Sample 6	> 9800	39.2	12.54	Load Limit of Test Machine
Sample 7	> 9800	39.2	12.54	Load Limit of Test Machine
LC01	> 9800	39.2	12.54	Load Limit of Test Machine
LC02	7500	30	9.6	

Table 16: Zerodur® Fracture Test Results

From table 16, it can be seen that the samples all withstood a nominal stress significantly above that seen during the previous tests, as reported in table 15. Owing to the deficiency in the test fixture which was identified and rectified, the results of table 15 should be disregarded.

Samples 5, 6, and 7 were undamaged samples, while LC01 and LC02 were samples which were modified via the inclusion of a laser ablated 0.1mm sized defect.

The samples LC01, shown in figure 67, and LC02 contained a 0.1 mm defect, which was clearly seen during the sample inspections.

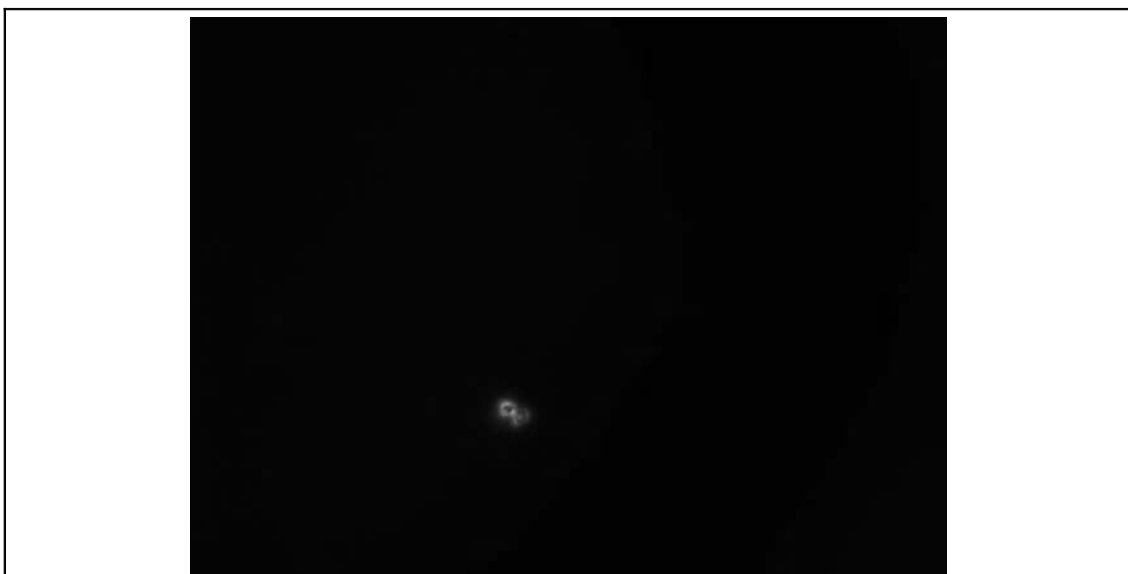


Figure 67: Inspection Data – 0.1 mm Defect in Sample LC01

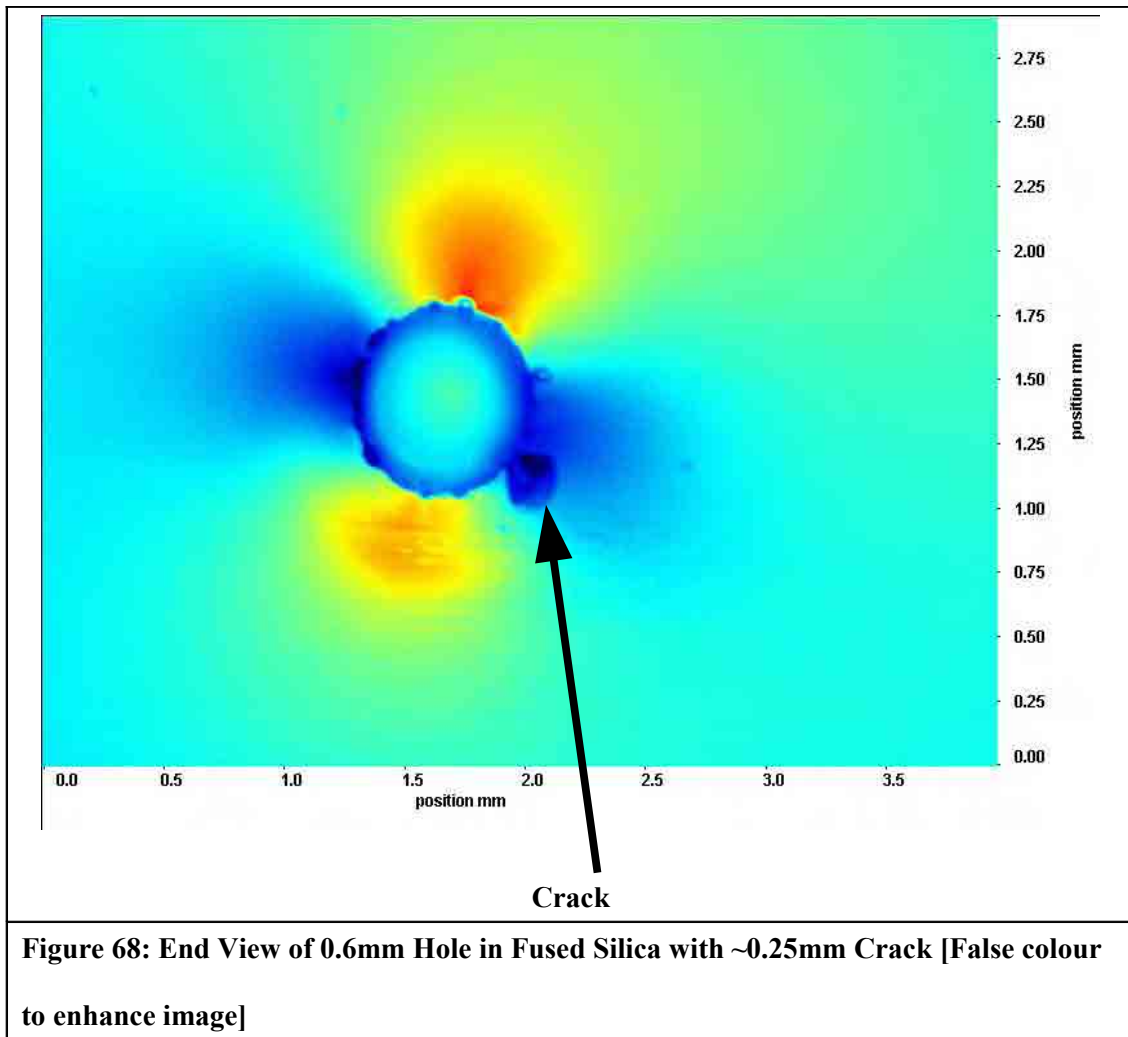
The results in table 16 show that the pristine samples of Zerodur® can withstand stress levels over 12 MPa, which was expected. That one sample with a 0.1 mm defect, LC02, failed at a factored stress of 9.6 MPa, a lower load than was expected. The fracture surface did pass through the damaged section of the sample. Possible reasons for this failure include the possibility that the LC02 sample suffered extra damage in being recovered from the old fixtures, or that they became damaged during the first round of testing when the epoxy joint slipped.

It was accepted that the data in table 16 do not represent a complete or adequate verification of the optical bench inspection, but, it was not feasible to conduct a complete experimental fracture program.

5.3.4.9 Fibre Injector Sample Inspection

In order to support development work of the fibre injector, and to gain an appreciation of the appearance of a known damaged specimen in the inspection facility, a fused silica cylinder 10 mm diameter blank, with a 0.6 mm diameter through hole was inspected. The hole had been produced by a mechanical drilling process, and it was not known whether this process was adequate for flight use.

Figure 68, below shows an end view of the hole, and a crack, approximately 0.25 mm in size, arrowed. Some smaller cracks were also visible around the periphery of the hole. The areas in yellow and red were the more highly stressed while the blue and black areas were comparatively unstressed.



The cracking identified by this inspection allowed the drilling process which had produced the hole to be discounted for flight use; the less mechanically aggressive technique of grinding was used instead. No ground sample was made available for inspection.

5.3.4.10 Conclusion

In order to ensure that the actual flight components were sufficiently free of defects, a scheme of inspection was devised. The inspection measurement used the principle of stress

birefringence, with the object of viewing the disturbance in the stress field around a defect, which was larger than the defect itself.

A theoretical example of the birefringence method was assembled. This model was used to check that the apparatus would produce a useful isochromatic fringe pattern, and to check that the stress optical co-efficient of Zerodur® would be sufficient for the method to work.

Inspection apparatus was designed, built and commissioned.

The optical benches were inspected via a scanning process prior to machining and insert integration. Optical benches serial number 02 and 03 were then re-inspected, paying particular attention to the highly stresses area around the inserts. Both optical benches were cleared for further progress as flight and flight spare.

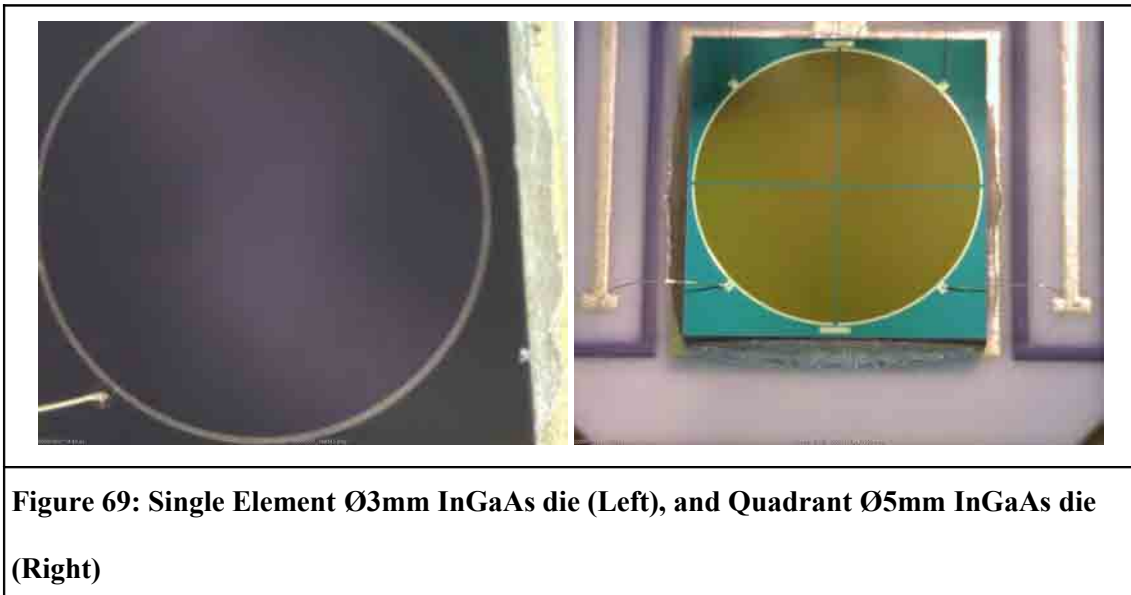
Fixtures were designed, and test samples procured, both pristine and weakened with known defects. The samples were tested, to destruction in some cases, although both the sample size and tensile testing machine capacity were insufficient to allow strong conclusions to be drawn.

A sample fibre injector part was inspected, and a gross defect was found, thus allowing an unsuitable machining process, drilling, to be discounted in favour of a grinding process.

6 PHOTODIODE DESIGN

6.1 PHOTODIODE MOUNT DESIGN

The photodiodes are mounted on the upper surface of the optical bench. Two types of photodiode are fitted, namely single element, (SEPD), and quadrant types, (QPD). Single element and quadrant photodiode InGaAs die may be seen in figure 69, below, while a quadrant photodiode die assembled into a cassette holder may be seen in figure 84, below. The inter quadrant gap for the quadrant photo-diode is 45 μ m.



The single element photodiodes are used to obtain a measurement of light beam power on the bench, thus allowing for any losses in the optical fibres, the connections, and the fibre injectors themselves. This measurement was used to provide a feedback signal to allow the tight control of laser power.

The quadrant photodiodes are used in four interferometers on the optical bench, namely the interferometer which measures the distance between the test masses, (x_2-x_1) , the distance between the optical bench and test mass 1, (x_1) , the frequency interferometer, and the reference phase interferometer for both the (x_2-x_1) and (x_1) interferometers.

It was important that these quadrant photodiodes were installed well aligned with the beam, and also for them to remain in position, as instability in photodiode position relative to the beam may couple into the measurement, and was thus an unwanted source of noise. Achieving this positional stability was an important requirement in enabling the mission to meet its challenging goals, as described in section 2.5.

As a result of the testing which was carried out on the engineering model photodiode and mount, a re-design was proposed for the proto-flight model. The re-design was specifically targeted towards maintaining the features of the engineering model photodiode which performed well, while making improvements, specifically where shortcomings or deficiencies had been identified.

The improvements sought were;

- A reduction in complexity,
- A simplification of the method of positional adjustment,
- The ability to remove and replace the photodiode as a cassette assembly,
- The ability to remove and replace a faulty photodiode after integration of the OBA into the LCA,
- The removal of all magnetic parts,

- The elimination of a connector on each photodiode.
- Development and demonstration of bond design

The re-designed photodiode is shown in exploded view in 70, below.

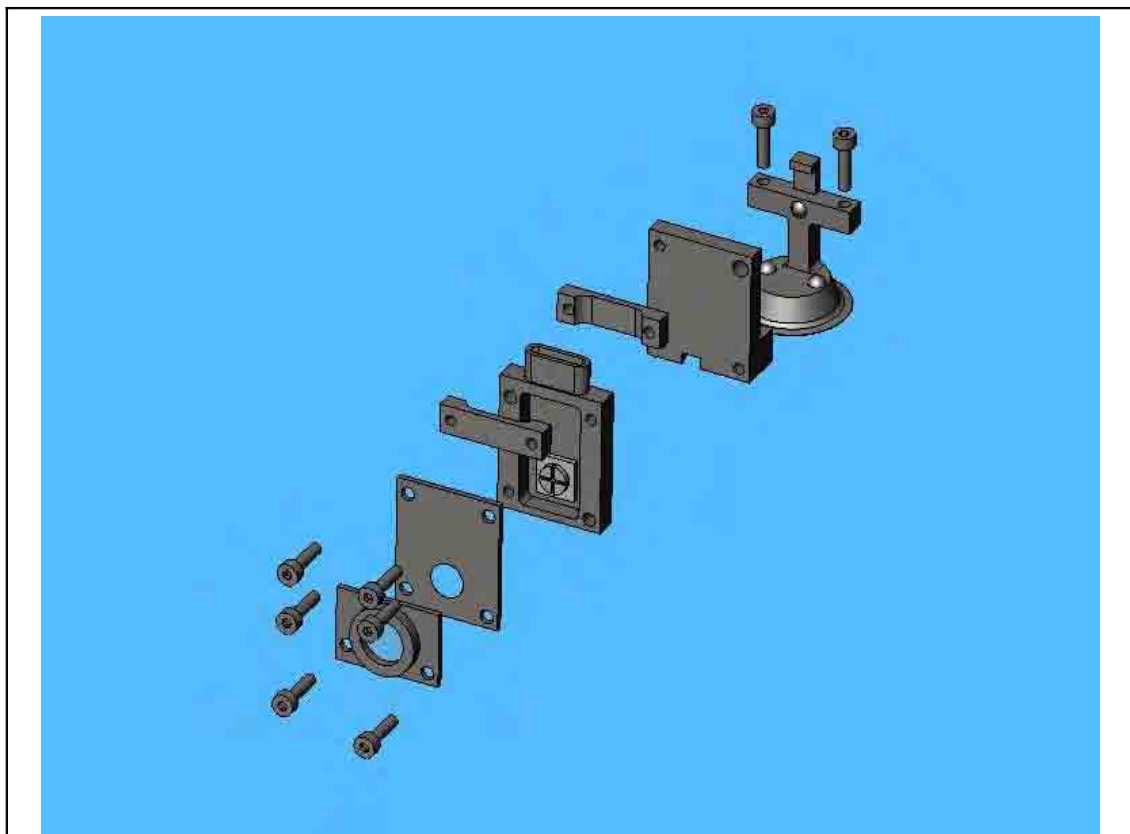


Figure 70: Exploded View of Proto-Flight Model Photodiode Mount Design

6.1.1 Photodiode Bond Design and Verification

Although the bond between photodiode mount and Zerodur® baseplate on the engineering model of optical bench was considered to have adequate performance, it was desired to

introduce a new design of photodiode mount for the flight model. As bond performance is influenced by all materials with interfaces to the bond, it was desirable to investigate the mechanical characteristics of this bond, in order to increase confidence in the design.

The bond between the photodiode and the engineering model optical bench, [88], was between the Zerodur® optical bench baseplate and a titanium photodiode mount. The adhesive specified in the engineering model application was 3M Scotchweld 2216. The important loadings presented in reference [88] are discussed and reviewed below.

This section describes the design analysis carried out in order to assess the adequacy of the bond between the plane circular base of the photodiode mount and the Zerodur® optical bench flat upper surface. The analysis informed material choices between the candidate materials, namely, aluminium alloy, or titanium for the photodiode mount, while epoxies, 3M Scotchweld 2214 and 2216 and Henkel Hysol EA 9361 were considered as potential adhesives, [89], [90], [85]. In order to simplify manufacture and surface preparation for bonding, the underside of the photo-diode was made flat, albeit roughened to provide a good key to the epoxy. A visual representation of the proposed photodiode and mount is shown below in figure 71.



Figure 71: Assembled Proto-Flight Model Photodiode

A mathematical model of the bond mechanics was constructed using the finite element method, [53]. MSC Nastran was chosen as the finite element solver because it offers the axi-symmetric element types, and is widely used, meaning that the model would possibly be useful to other parties. During the development of the model, simple tests were carried out to determine the adequacy of the elements and the boundary conditions to represent the physical configuration under consideration. Upon completion of the model geometry, a number of potential mesh densities were considered, with the chosen mesh density chosen to give stress convergence within 1%. This accuracy was adequate, since it was lower than typical inter-batch material property variation, and similar in magnitude to the linear and geometrical tolerances which were specified for the parts.

Using this model, the sensitivity of the bond to changes in bond thickness, photodiode mount material, and geometry of the photodiode mount base to imposed thermal loading was estimated. It was appreciated that the strength of the bond was not solely dependent upon the strength of the constituent parts, it was also dependent upon how well these constituent adhered together. These adhesive properties were not considered via analysis, and the bond design was verified by development testing, and also via qualification test during the vibration testing of the optical metrology system which was the responsibility of ASD.

Using the results of these analyses, recommended photodiode mount geometry, material, and bond thickness were proposed, accepted, and implemented.

The bond is loaded via shock and vibration during launch, and via the differential thermal expansion of the constituent components.

Previous analyses, [88], demonstrated that thermal loading was the most onerous mode of loading, by a factor of more than 50 over inertia based pull and inertia based peel loadings of the photodiode itself, i.e., ignoring the effect of the deformation of the optical bench.

In order to provide a check of the previous analyses, an approximate calculation was used to assess the thermal stresses compared with those caused by accelerations due to vibration during launch.

Using a typical epoxy stress level of 10 MPa, as obtained using the thermal finite element models, and conservatively, using the total mass of the photodiode and cable (circa 200 grammes), the acceleration which would be necessary to produce a comparable stress was estimated.

$$\begin{aligned}
 \sigma_{THERMAL} &= 10 \text{ MPa} \\
 \text{Diameter}_{BASE} &= 20 \text{ mm} \\
 \\
 \text{Area}_{EPOXY} &= \pi * 20 * 20 / 4 \text{ mm}^2 \\
 &= 100\pi \text{ mm}^2 \\
 \\
 \text{Force}_{EPOXY} &= \sigma_{THERMAL} * \text{Area}_{EPOXY} \\
 &= 1000\pi \text{ N} \\
 \\
 \text{acc}_{EQUIV} &= \text{Force}_{EPOXY} / \text{mass}_{PHOTO-DIODE} \\
 &= \frac{1000\pi}{0.2} \text{ ms}^{-2} \\
 &= 5000\pi \text{ ms}^{-2} \\
 \text{acc}_{EQUIV} &\approx 1500 \text{ g}
 \end{aligned}
 \tag{Equations 46}$$

The accelerations used during qualification testing are shown in tables 21 and 22, and were much lower than the 1500 g estimated in equations 46. Shock loads were not considered during photo-diode bond design.

The temperature limits for OMS equipment are shown in figure 72, below;

Unit	OBA		PMU		LCU		LMU		RLU		Fiber Box	
	[°C]		[°C]		[°C]		[°C]		[°C]		[°C]	
Temperature Limits	Lower Limit	Upper Limit	Lower Limit	Upper Limit	Lower Limit	Upper Limit	Lower Limit	Upper Limit	Lower Limit	Upper Limit	Lower Limit	Upper Limit
Operating	+10	+30	-10	+40	0	+40	+23	+29	+23	+29	-10	+50
Switch-On*	+10	+30	-10	+40	-10	+40	+10	+30	+20	+30	-30	+50
Non-Operating	0	+40	-20	+50	-20	+50	-10	+50	-20	+50	-30	+50
Storage	0	+40	-30	+50	-30	+50	-10	+50	-30	+50	-30	+50

Figure 72: OMS Temperature Limits [32]

As the extremes of ambient temperature for the optical bench were 0 and 40°C, and the bonding of the photodiode mount to the Zerodur® substrate was undertaken at room temperature, typically, 20°C, a nominal temperature range during the LISA pathfinder mission of ±20°C was defined for the bond.

In order to investigate the effect of varying the thickness of the epoxy bond, the constituent materials, and the photodiode mount geometry, a number of finite element models were built, using the epoxy manufacturers' material specifications and data, [90],[89],[85],[44]. As the epoxy was applied such that it was extruded some little way beyond the periphery of the photodiode base, the epoxy was modelled to protrude 2mm beyond the outer edge of the photodiode mount.

The thermal data for the dominant parts of the photodiode, namely the mount itself, are described in table 17, below.

<i>Part</i>	<i>Mass (g)</i>	<i>Material</i>	<i>CTE ($\mu\text{m/mK}$)</i>	<i>Specific Heat Capacity (J/g K)</i>	<i>Heat Capacity (J/K)</i>
Mount post	5.9	Grade 2 Titanium	8.6	0.523	3.09
Cassette & holder	18.8	Grade 2 Titanium	8.6	0.523	9.83
Total Photodiode mount	24.7	Grade 2 Titanium	8.6	0.523	12.92
Table 17: Photodiode Mechanical Parts Thermal Data					

In order to check the model, a number of “sanity checking” hand calculations were carried out. These demonstrated that the model was producing results of adequate quality and accuracy.

The base of the photodiode mount was circular, there was symmetry about an axis normal to the Zerodur® Baseplate surface, centred on the centre of the circular photodiode base. The finite element model used in this analysis took advantage of this axial symmetry, which enabled the modelling of a three dimensional system using a two dimensional representation.

All of the nodes which lay on the axis of symmetry were constrained against rotating about any axis and constrained against moving off axis. This constraint still allowed sliding along the axis of rotational symmetry. In order to prevent this remaining freedom, one node was constrained against movement along the axis of symmetry.

Six noded triangular elements, CTRIA6, were used throughout. At the outer radius of the photodiode mount, and the outer radius of the epoxy, and the corresponding adjacent area of the Zerodur® baseplate, the mesh was made dense. This corresponded to the location where the maximum shear strain in the epoxy was anticipated, and also to a point of mechanical discontinuity. Away from this area, the mesh was less refined.

Figure 73, below, shows the axi-symmetric shear stress distribution created by a 20 °C temperature change, 45° base taper angle, aluminium photodiode mount and 0.2 mm thickness of 2216 epoxy. All results concerning the effect of varying bond thickness were carried out using this geometry and loading.

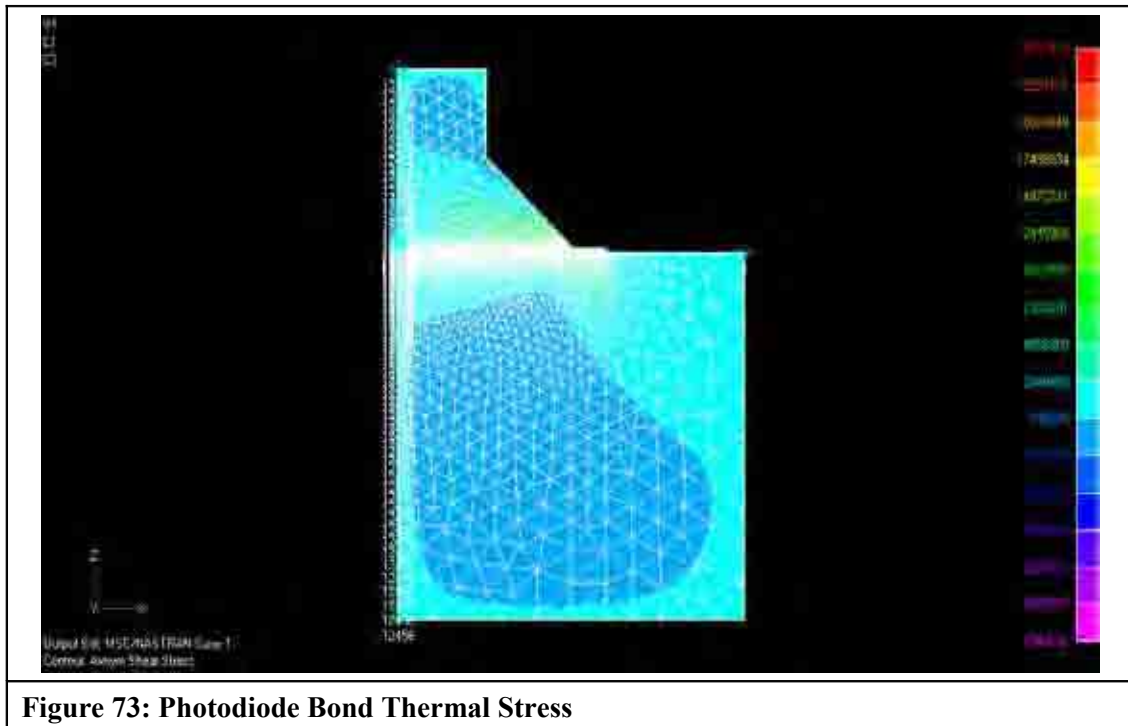


Figure 74 shows the area of stress concentration at the outer edge of the photodiode mount more clearly. Sufficient epoxy was applied to ensure that some epoxy was extruded beyond the periphery of the photodiode base, and this extra epoxy was modelled; it was noteworthy that the extension of the epoxy, beyond the photodiode mount base prevented a second stress concentration between the epoxy and Zerodur®.

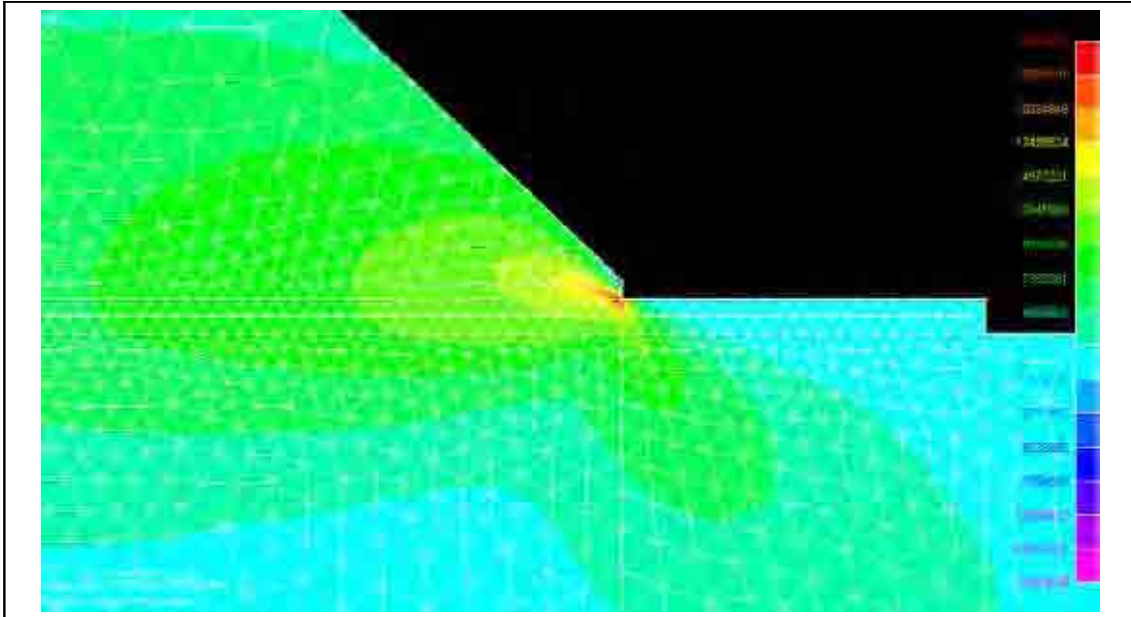


Figure 74: Photodiode Bond Thermal Stress - Detail of Outer Bond Radius

Axi-symmetric shear stress data for the epoxy were extracted from the models, and saved in the form of ASCII text files. These data were then processed using MATLAB.

The stress values reported were averaged, by taking the average of all elements through the thickness of the epoxy at each radial location. While this process did not capture the maximum value of stress reported by the model in the area local to the stress concentration, it represented the stress field adequately elsewhere. As the stress values near the stress concentration were not realistic, and were not critical to the choice of epoxy type and bond line thickness, this averaging was an appropriate method of data reduction. An example showing both raw and averaged stress data is shown in figure 75, below.

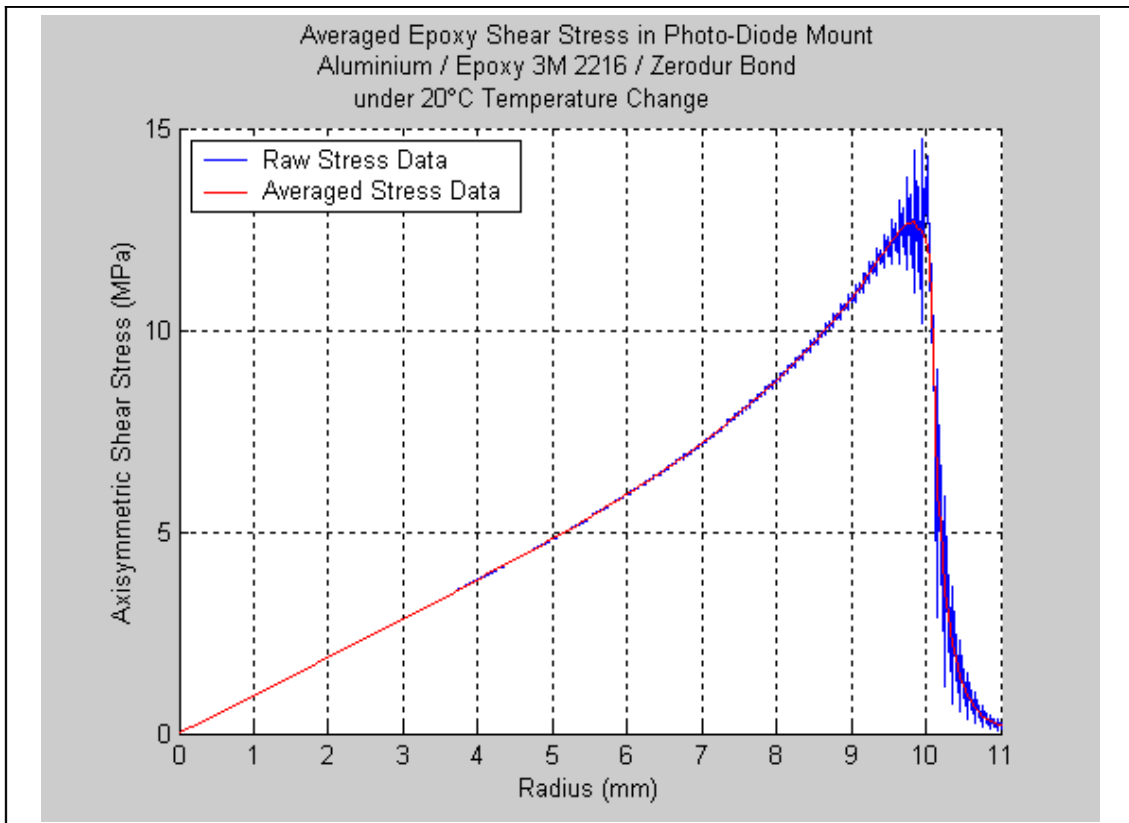


Figure 75: Through Thickness Averaging

The variation of through thickness averaged stress results with respect to varying the thickness of the epoxy bond is shown in figure 76, below for a titanium photodiode mount.

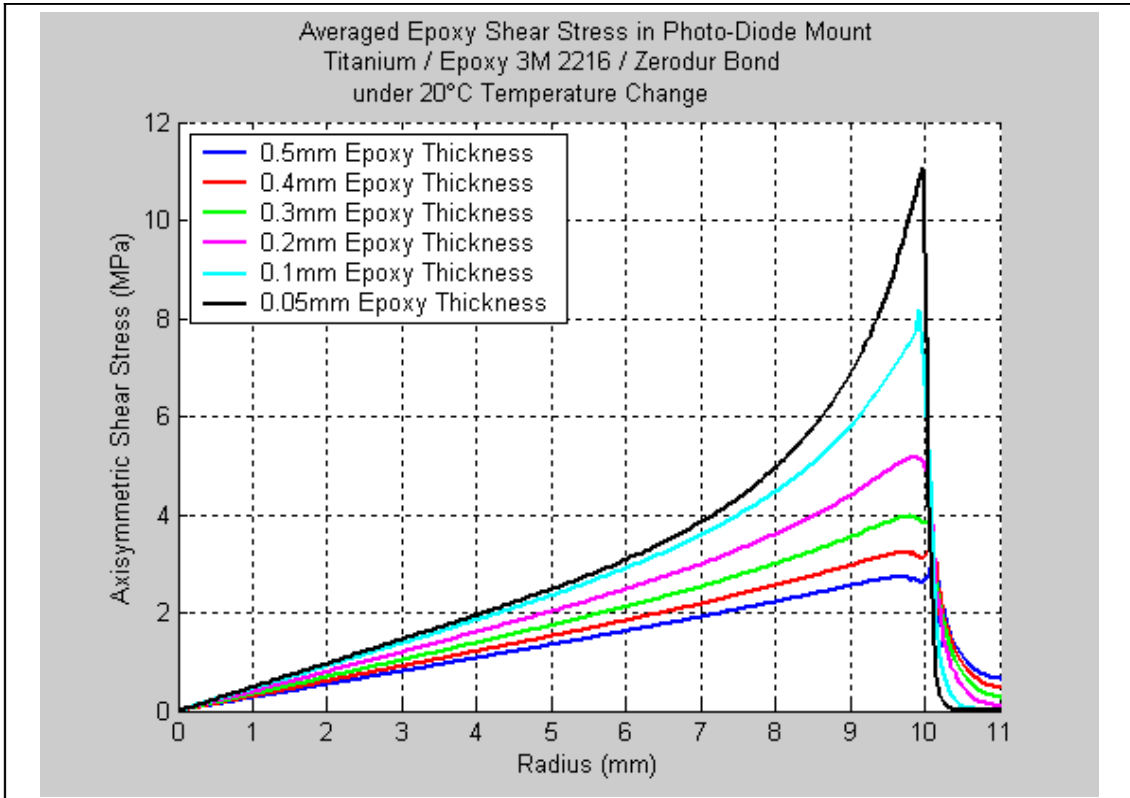


Figure 76: Thermal Stress with respect to varying Bond Thickness

The peak values of averaged stress are summarised in table 18, below.

<i>Bond Thickness</i> <i>(mm)</i>	<i>Aluminium</i> <i>(MPa)</i>	<i>Titanium (MPa)</i>
0.5	7	2.8
0.4	8	3.1
0.3	10	4
0.2	12.5	5.1
0.1	18	8
0.05	25	11

Table 18: Photodiode Bond Stress Summary

The proposed geometry is shown, with the finite element mesh, in figure 77, below. This geometry was modelled for the case of 0.2mm epoxy thickness, 20°C temperature change, for both aluminium and titanium photodiode mounts.

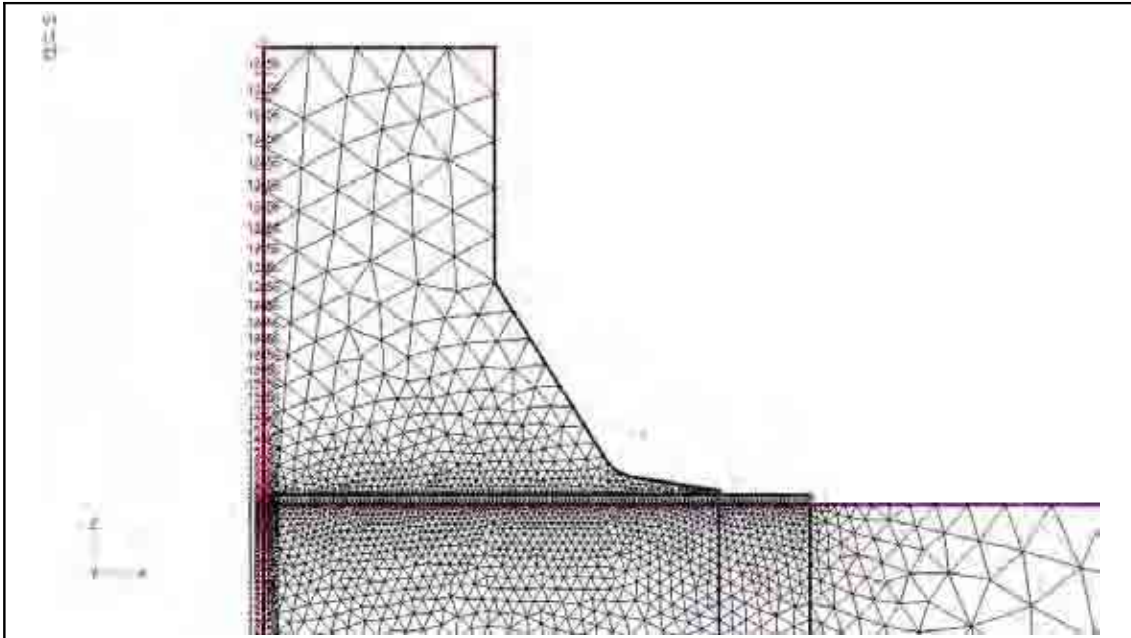


Figure 77: Proposed PD Mount Geometry

The averaged, axi-symmetric shear stress for both aluminium and titanium photodiode mounts is shown in figure 78, below.

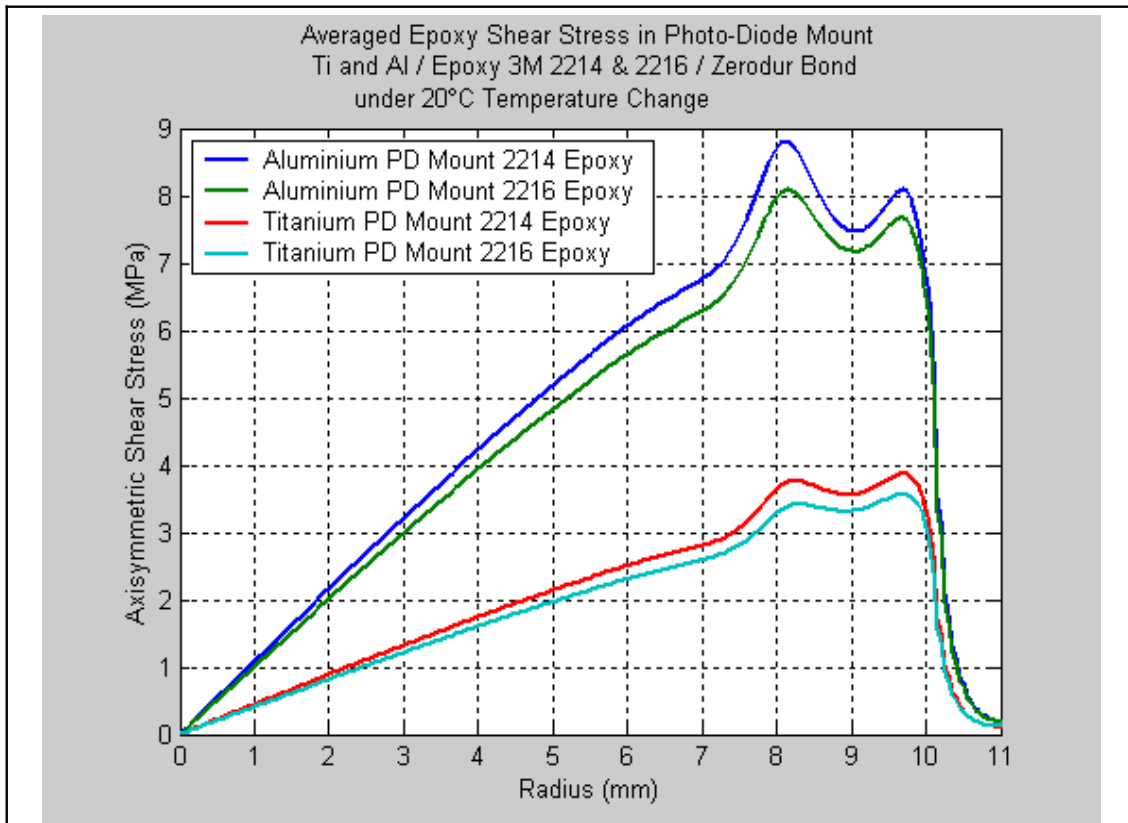


Figure 78: Thermal Stress of Proposed Geometry

The finite element model results showed that shear stress increased from zero to a maximum value in the area of the periphery of the photodiode mount. The abrupt change in shape at the outer radius of the photodiode mount was responsible for a local stress concentration.

Owing to the right angled corner, the stress concentration there was infinite. The values of stress reported by elements in this area were not realistic. Further refinement of the mesh would have produced ever larger estimates of the stress near the corner – a process which could continue ad infinitum.

As may be seen in figure 74, by allowing the epoxy layer to protrude beyond the outer radius of the photodiode mount, the stress concentration between the epoxy and Zerodur® was alleviated successfully.

The shear stress was greater for an aluminium photodiode mount when compared with an equivalent titanium mount, as shown in figure 78. The stress was reduced by a factor of approximately 2.5, while the ratio between the coefficients of expansion was 2.8. The disparity between these ratios was due to the difference in elastic properties between aluminium and titanium and, the mismatch in coefficients of thermal expansion between the metal of the photodiode mount and the epoxy itself.

The maximum shear stress was highest for small bond thickness, and the stress reduced for thicker bond lines. There was a system of diminishing returns owing to the mismatch in coefficients of thermal expansion between the metal of the photodiode mount and the epoxy itself. That there was little to choose between the candidate epoxies may be most clearly seen in figure 78, where the stress difference between the 2214 and 2216 was always below 0.5 MPa.

Owing to the high temperature curing requirements of epoxy 2214, an alternative epoxy, Hysol EA 9361 was considered. Hysol EA 9361 was the epoxy which was being used to bond the inserts into the Zerodur[®] baseplate. Using the published material properties for EA 9361, the finite element model was revised to include EA 9361 material properties, and was re-solved, using the modified geometry, titanium mount, and a 20 °C temperature change.

As the available Hysol data sheet, [85], provided Young's modulus data only at 25 °C, the elastic properties were not worst case because the epoxy was partially softened at this temperature. The model results were therefore not comparable with the earlier modelling of epoxy 2216 and 2214 where more onerous, cold Young's moduli were used in the analysis.

Although not directly comparable, the maximum shear stress in the 0.2 mm thick Hysol EA 9361 layer was estimated as 2 MPa, which compared favourably with a corresponding strength at this temperature of 24.1 MPa.

Owing to the potential non-conservative nature of the input data for EA 9361, it remained desirable to conduct strength testing on bonds which had undergone thermal cycling. This thermal cycling testing is described in section 6.1.2, below.

The chosen bond design was EA 9361 epoxy, with a 0.2 mm bond line thickness, with the bond being made at 20 °C.

6.1.2 Photodiode Bond Testing

In order to build confidence in the photodiode design and in order to reduce the risk of bonding inadequate photodiode mounts onto the optical bench, a testing program was undertaken. The strength of a number of test bonds was tested, while the mechanical stability of a photodiode and mount was also determined.

If subject to an extreme loading of 256 g, the epoxy bond between the Zerodur® and photodiode mount would bear an inertial loading of 250 N. This served as a development test loading for the bonds. The test fixtures for the photodiode bonds are shown in figure 79, below.

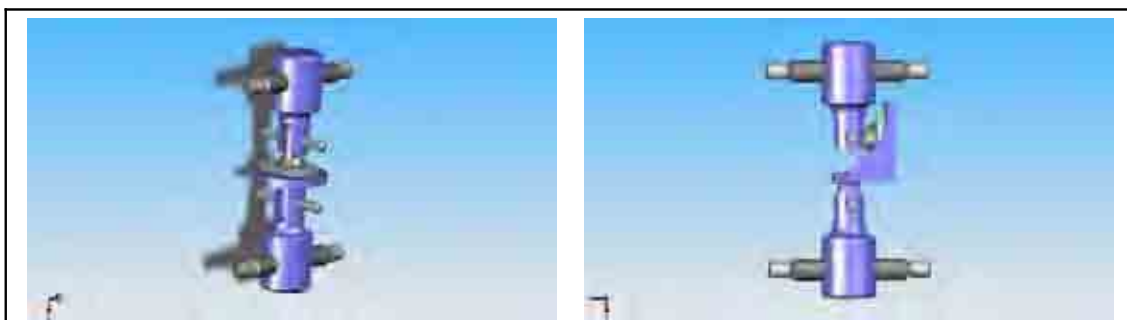


Figure 79: Photodiode Bond Test Fixture Design (Tensile - Left, Shear - Right)

The photodiode bonds, using EA 9361 epoxy, and 0.2 mm bond line thickness, were first tested using an Instron tensile testing machine, then thermally cycled between -10 °C and +40 °C, [91], [32], and then tested in the Instron tensile testing machine again. The results were as given in table 19, below;

	<i>Pre-Thermal Cycling</i>	<i>Post-Thermal Cycling</i>
PDS1	250 N OK	250 N OK
PDS2	250 N OK	250 N OK
PDS3	250 N OK	250 N OK
PDS4	250 N OK	250 N OK
PDS5	250 N OK – proceeded to failure load at 1.01 kN	N/A
PDT1	250 N OK	250 N OK
PDT2	250 N OK	250 N OK
PDT3	250 N OK	250 N OK
PDT4	250 N OK	250 N OK
PDT5	250 N OK – proceeded to failure load at 5.40 kN	N/A
Table 19: Photodiode Bond Test Results		

In order to verify the adequacy of the mechanical design as well as the photodiode to Zerodur® bond, a test bond and electrically non-functioning photodiode assembly was subjected to LISA Pathfinder qualification level mechanical testing.

Prior to the test, the photodiode had been bonded using the as-flight procedure, [92], and the as-bonded position of the photodiode was measured and recorded using a co-ordinate measuring

machine, (CMM). The bonded photo-diode was also subjected to thermal cycling loads, namely 5 cycles between -10°C and +40°C, [91], [32]. The position of the photo-diode was monitored via CMM measurement during the period of a few days after the bond was made and after the clamps were released in order to determine that the photo-diode did not change position or suffer from creep effects.

The mechanical test loads were derived from the spacecraft level requirements, [91], modified to account for the response of the mechanical structure between the launcher interface and the optical bench. These mechanical testing levels were agreed between ASD and UBI, [93], the shock testing loads are summarised in table 20, below.

<i>Shock Test Levels (SRS, Q=10)</i>			
<i>X and Y Direction</i>		<i>Z Direction</i>	
<i>Frequency (Hz)</i>	<i>Acceleration (g)</i>	<i>Frequency (Hz)</i>	<i>Acceleration (g)</i>
70	5	70	5
1000	200	700	50
10000	200	10000	50

Table 20: Shock Test Levels

The random test loads are shown in table 21, below.

<i>Random Test Levels</i>			
<i>X and Y Direction</i>		<i>Z Direction</i>	
<i>Frequency (Hz)</i>	<i>Acceleration (g²/Hz)</i>	<i>Frequency (Hz)</i>	<i>Acceleration (g²/Hz)</i>
20	Ramp up with +6dB per octave	20	Ramp up with +6dB per octave
80	0.13 g ² /Hz	100	0.5 g ² /Hz
400	0.13 g ² /Hz	150	0.5 g ² /Hz
2000	Ramp down with -7 dB per octave	200	Ramp down to 0.08 g ² /Hz
		700	0.08 g ² /Hz
		2000	Ramp down with -7 dB per octave
	(8.9 g RMS) Duration: 120 s		(11.1 g RMS) Duration: 120 s

Table 21: Random Test Levels

The sine test loads are shown in table 22, below;

<i>Sine Test Levels (sweep rate: 2 octaves per minute - all axes)</i>					
<i>X Direction</i>		<i>Y Direction</i>		<i>Z Direction</i>	
<i>Frequency (Hz)</i>	<i>Load</i>	<i>Frequency (Hz)</i>	<i>Load</i>	<i>Frequency (Hz)</i>	<i>Load</i>
5	8 mm 0-pk	5	9.3 mm 0-pk	5	13.6 mm 0-pk
20	13 g	20	15 g	20	22 g
70	13 g	40	15 g	60	22 g
90	13 g	60	20 g	80	27 g
100	13 g	100	20 g	100	27 g

Table 22: Sine Test Levels

The test item in place on the shaker and the test configuration for Z axis vibration are shown in figure 80, below.

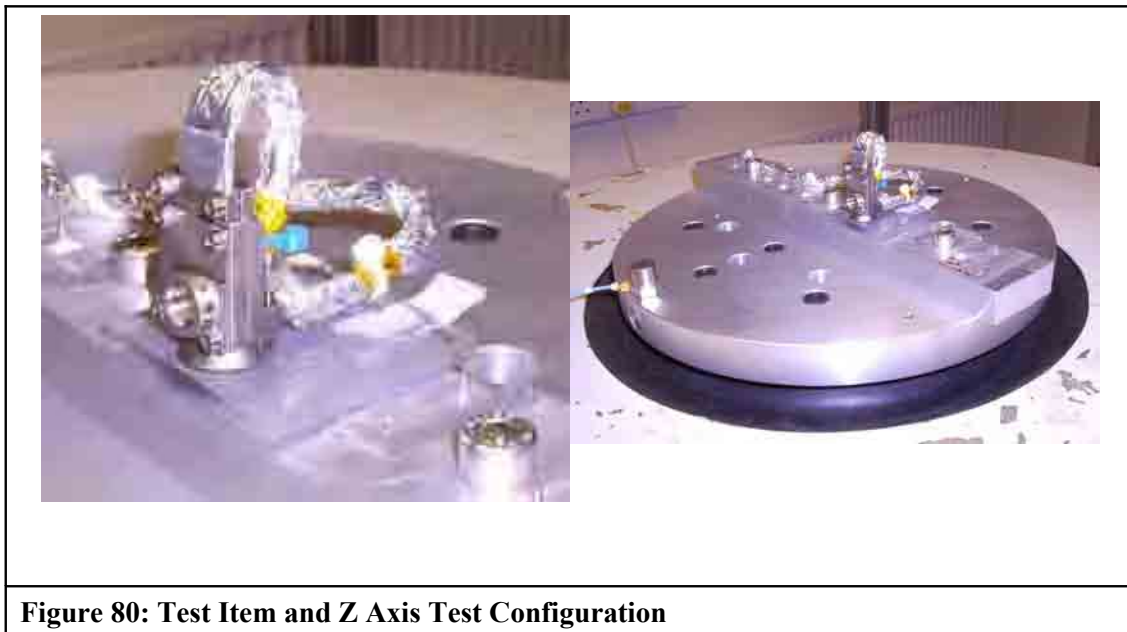


Figure 80: Test Item and Z Axis Test Configuration

The test configuration for X and Y axis vibration are shown in figure 81, below.



Figure 81: X Axis Test Configuration (Left) and Y Axis Configuration (Right)

After the testing, the photodiode and bond were visually inspected. No damage or debris was found. The photodiode was re-measured using the CMM. The CMM program produced point location data with a repeatability of the order of 5 μm . No discernible movement had taken place since the photodiode was first bonded. The bond had withstood thermal cycling, shock and vibration loading, and manual handling, and had not moved discernibly, i.e., beyond the 5 μm repeatability of the CMM. Therefore, the acceptability of both the mechanical design of the photodiode and the design of the epoxy bond had been shown for use in the LISA Pathfinder mission, and analysis and testing had demonstrated sufficient mechanical stability to allow their use in the optical metrology system.

6.2 PHOTODIODE DESIGN SUMMARY

6.2.1 Photodiode Design Description

The schematic layout of the optical bench is shown in figure 82, below.

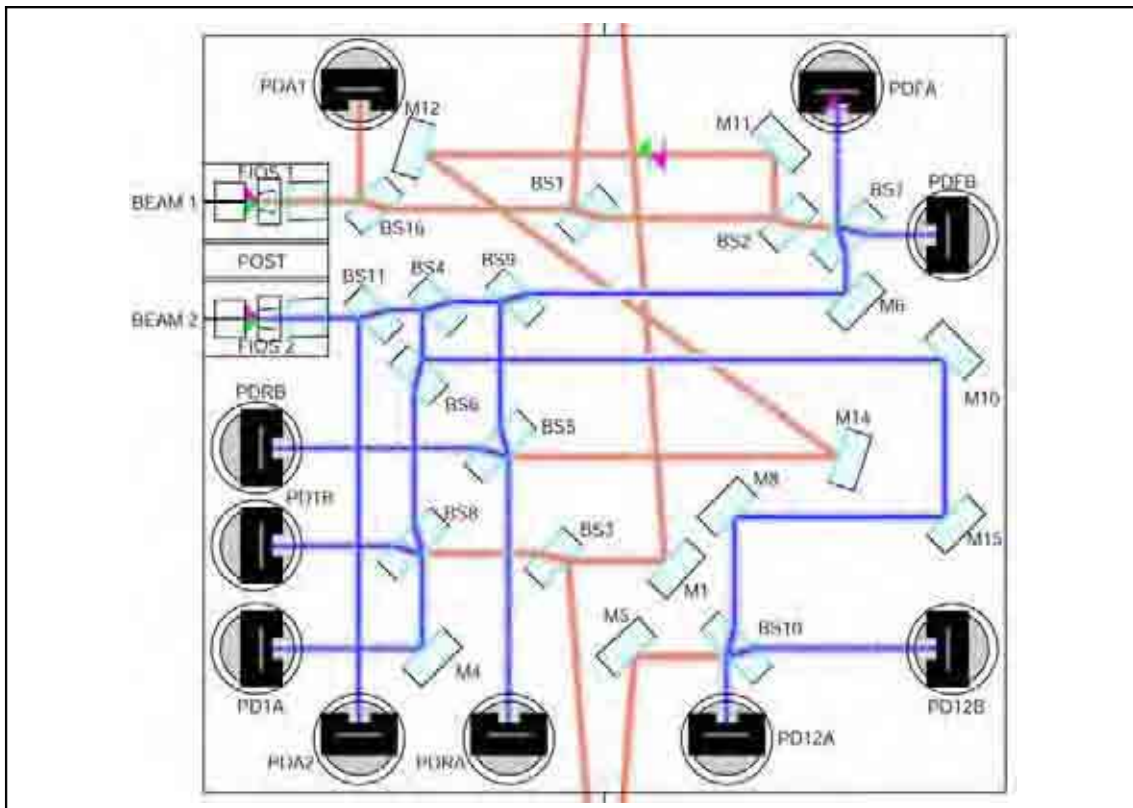


Figure 82: Optical Bench Schematic Layout, Source: [36]

The type and function of the photodiodes are shown in table 23, below.

<i>Photodiode</i>	<i>Photodiode Type - Function / Description</i>
PDA1 *	Single Element Photodiode - Laser Power, Beam 1
PDA2 *	Single Element Photodiode - Laser Power, Beam 1
PDFA	Quadrant Photodiode - Frequency Noise (Nominal)
PDFB	Quadrant Photodiode - Frequency Noise (Redundant)
PDRA	Quadrant Photodiode - Reference Length (Nominal)
PDRB	Quadrant Photodiode - Reference Length (Redundant)
PD1A	Quadrant Photodiode - Position of Test Mass 1 (Nominal)
PD1B	Quadrant Photodiode - Position of Test Mass 1 (Redundant)
PD12A	Quadrant Photodiode - Position of Test Mass 2 - Test mass 1 (Nominal)
PD12B	Quadrant Photodiode - Position of Test Mass 2 - Test mass 1 (Redundant)
Table 23: Photodiode Allocation	

* Photodiodes PDA1 and PDA2 provide laser power feedback to the laser system to allow laser power stabilisation.

The quadrant photodiodes are connected (via the LCA connector bracket) to the phasemeter. As the optical bench will be integrated into the LCA by ASD, it was not appropriate for the cables to be routed and terminated before delivery. The photodiode cables were fitted and routed along the surface of the optical bench, and for a short distance beyond the edge, beyond which, the cable was left free. The cables were temporarily terminated with a test connector, thus allowing the functional testing of the photodiodes in an efficient and repeatable manner.

The two types of InGaAs photodiode, single element and quadrant are shown in the form of bare dice in figure 83, below;

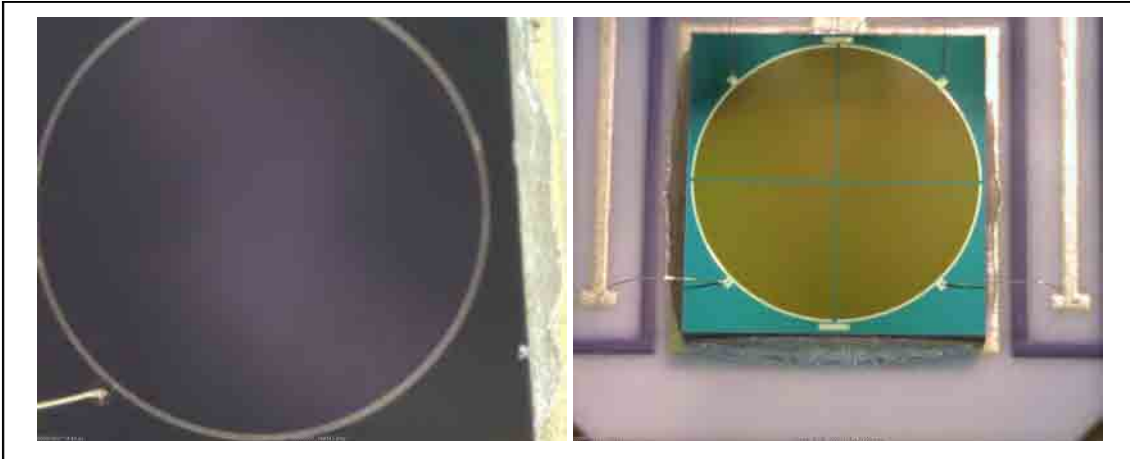


Figure 83: Single Element Ø3mm InGaAs die (Left), and Quadrant Ø5mm InGaAs die (Right)

A quadrant photodiode electrically integrated into the cassette holder is shown in figure 84, below;

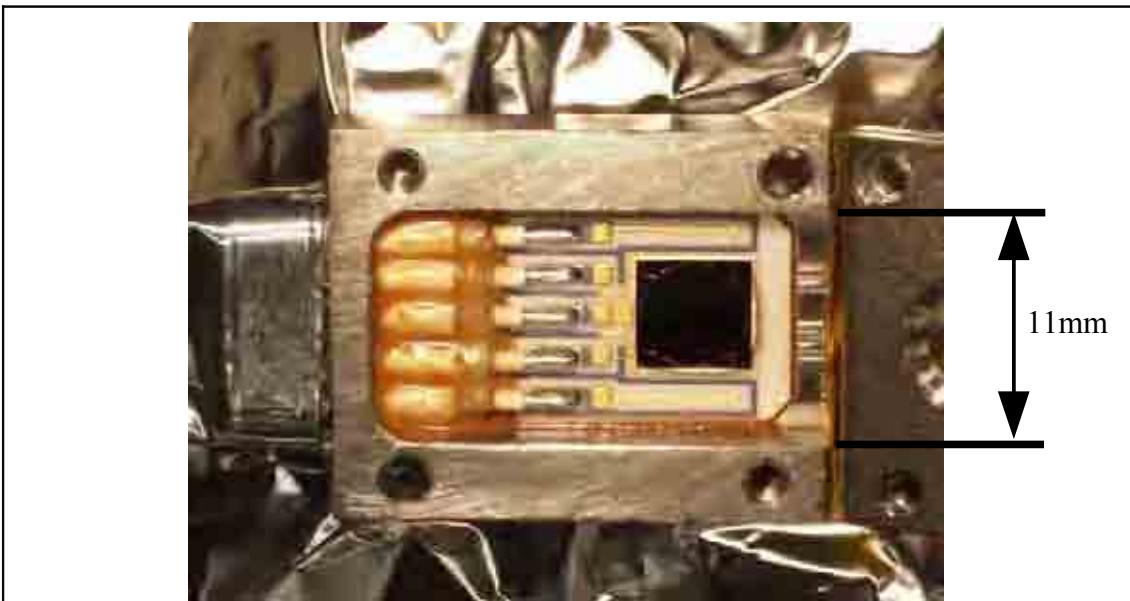


Figure 84: Electrically Assembled Quadrant Photodiode

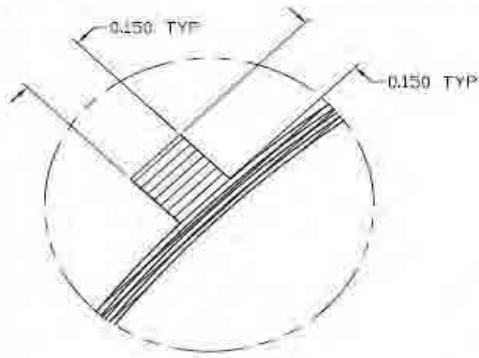
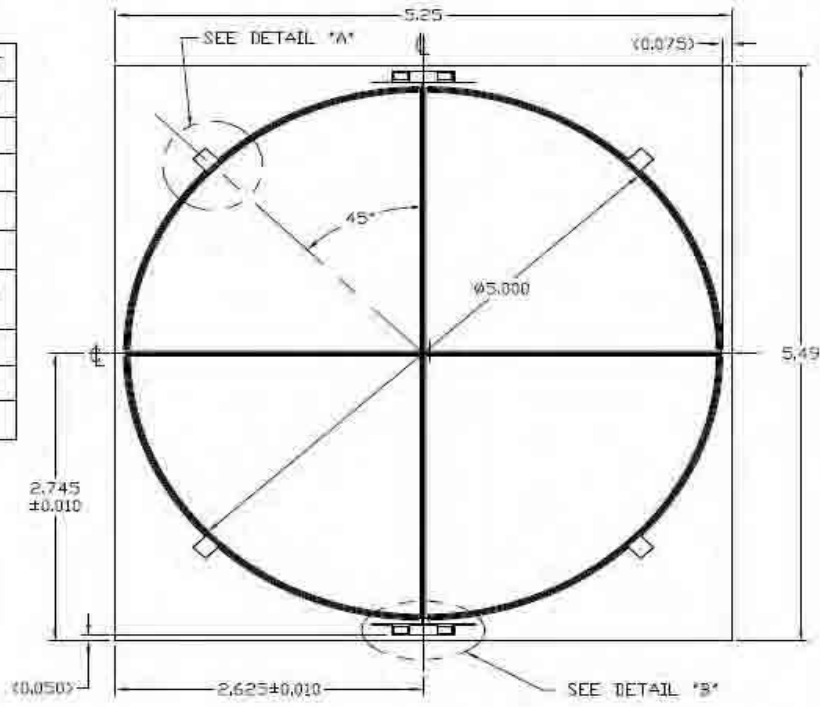
The specification of the quadrant photo-diode die is shown in figure 85 below; (The SEPD die is similar)

THIS DRAWING CONTAINS INFORMATION AND SPECIFICATIONS THAT ARE THE PROPERTY OF OSI SYSTEMS, INC., AND SHALL NOT BE REPRODUCED, COPIED OR USED, IN WHOLE OR IN PART WITHOUT THE WRITTEN CONSENT OF OSI SYSTEMS, INC.

APPLICATION			REVISION		
NEXT ASSY	USED ON	LTR	DESCRIPTION	DATE	APPROVED

ELECTRO-OPTICAL SPECIFICATIONS @ 23°C

EACH ELEMENT	MIN	TYP	MAX	UNIT
RESPONSIVITY @ 1064nm, -5V	0.5			A/W
DARK CURRENT @ $V_R = -5V$		2	75	nA
CAPACITANCE @ $V_R = -5V$, 1MHz			500	pF
FORWARD VOLTAGE @ 10mA		0.7	1.0	V
CROSSTALK @ -5V, 1064nm, 5 KHz			1	%
RISE TIME @ -5V, 1064nm, 50 OHMS LOAD			60	nS
OPERATING TEMPERATURE	-40 TO +100			°C
STORAGE TEMPERATURE	-55 TO +125			°C
ESD	300			V



DETAIL "A"

CHIP THICKNESS 0.550±0.015mm

UNLESS OTHERWISE SPECIFIED, DIMENSIONS ARE IN MILLIMETERS. TOLERANCES ARE: FRACTIONS DECIMALS ANGLES XXX.XX XXX.XX XXX.XX XXX.XX XXX.XX XXX.XX XXX.XX XXX.XX XXX.XX XXX.XX XXX.XX XXX.XX	APPROVED	DATE	OSI FIBERCOMM, INC. AN OSI SYSTEM COMPANY			
	DRAWN: J. CHIACHIO	11-09-05				
	CHECKED:		TITLE: 5.00mm DIA ACTIVE AREA InGaAs QUADRANT DETECTOR OSIF-1289			
	MATERIAL:			SIZE: A	CODE IDENT NO: 50486	DRAWING NO: 42-00032
FINISH:	FORM: FD0031C	QA CODE:	SCALE: NTS			
DO NOT SCALE DRAWING	CAD FILE: 42-00032.B.DWG	SHEET 1 OF 3				

Figure 85: QPD Die Specification

6.2.2 Photodiode Mechanical and Thermal Summary

An exploded view of the photodiode assembly is shown below.

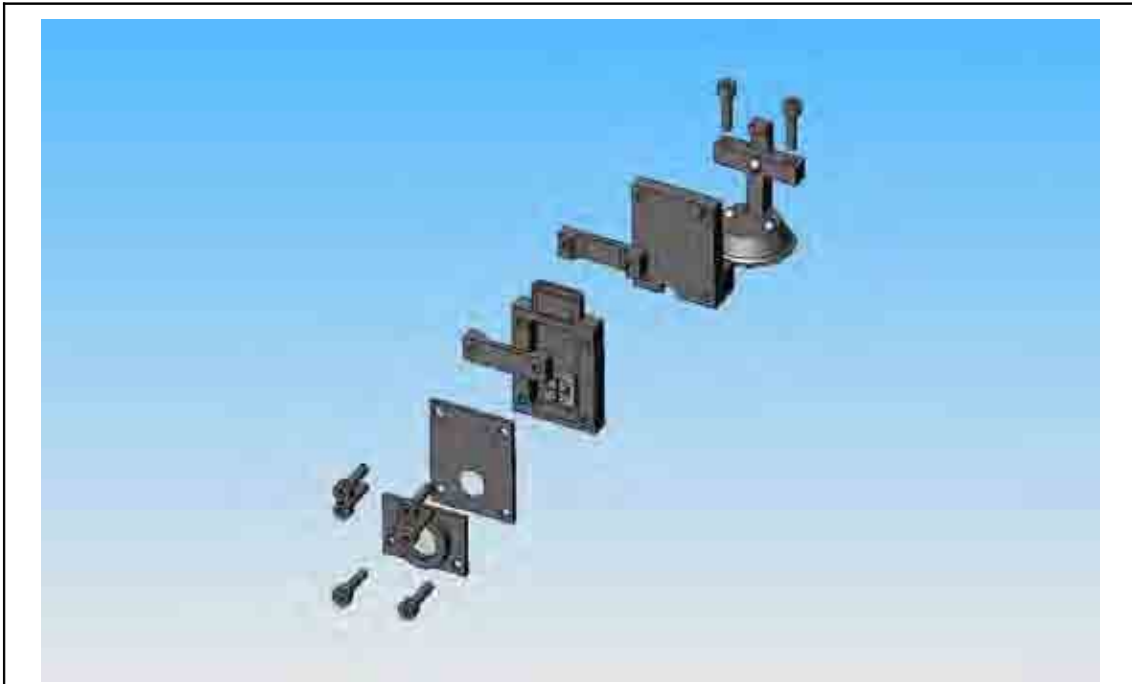

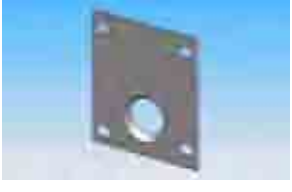






Figure 86: Exploded View of Quadrant

The individual parts of the photodiode are listed in table 24, below;

<i>Part</i>	<i>Drawing Number(s)</i>	<i>CAD View</i>
Window & Holder ¹⁾	S2-UGB-DRW-3055	
Photodiode Cover ²⁾	S2-UGB-DRW-3007 (QPD) S2-UGB-DRW-3027 (SEPD)	
Photodiode Base	S2-UGB-DRW-3006 (QPD) S2-UGB-DRW-3028 (SEPD)	
Cassette Holder	S2-UGB-DRW-3005	
Photodiode Mounting Post	Comprises; S2-UGB-DRW-3004 and 3 off Ø3mm titanium balls	
Cable Clamp	S2-UGB-DRW-3008 (clearance holes) S2-UGB-DRW-3009 (M2 Thread)	
Table 24: Photodiode Allocation		

¹⁾ The optical properties of the photodiode window are defined below;

- **Material:** Suprasil Fused Silica (from UGL stock)
- **Diameter:** 10mm ± 0.1mm

- **Edges:** Fine ground with nominal chamfer
- **Thickness:** 1mm -0.00mm +0.15mm
- **Optical Path Difference:** 1-2λ at 633nm (combined material, flatness and parallelism)
- **Coating:** <0.25%R at 1064nm, over central 8-9mm

²⁾ The width of the cylindrical section of the aperture is <0.05mm.

These parameters were formally documented in the Photodiode and Mounts Requirements Specification, [94]. To avoid magnetic contamination, and to minimise thermal expansion, the photodiode mounting was machined from titanium. In order to reduce the reflection of light, the exterior front surface of the photodiode mount was made dull by lightly sand-blasting the titanium surface. There were no coatings applied to the photodiode mountings.

It was necessary to ensure adequate cassette clamp load, two M2 titanium fasteners were used, with a torque of 0.3 Nm. Using a nut constant of 0.25, the force in each vertical bolt was estimated using equation 47, below;

$$\begin{aligned}
 P &= \frac{T}{KD} \\
 &= \frac{0.3}{0.25 * 2e-3} \\
 P &= 600 \text{ N}
 \end{aligned}
 \tag{Equation 47}$$

The dimensions of the photodiode cassette are shown in figure 87, below;

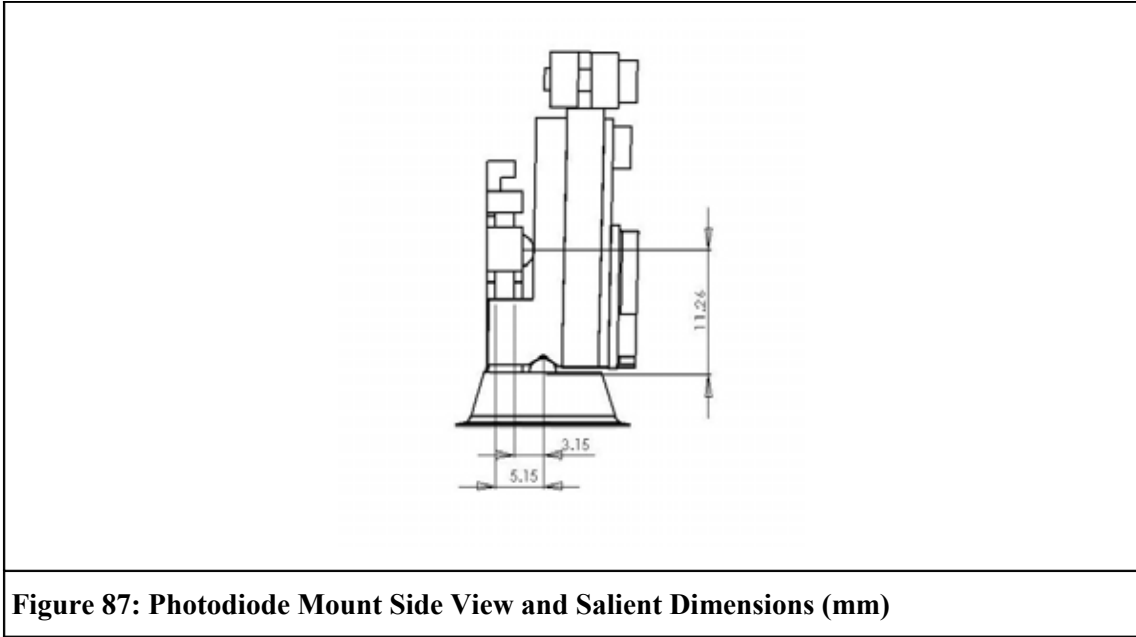


Figure 87: Photodiode Mount Side View and Salient Dimensions (mm)

The masses of the components involved were obtained from the CAD model, and are listed in table 25, below;

Total Mass of photodiode mount	24.7 g
Mass of mount post	5.9 g
Mass of cassette & holder	18.8 g

Table 25: Photodiode Component Mass

To assess the ability of the photodiode to withstand inertial loads, the accelerations which would cause gapping, i.e., the separation of parts which should remain in contact, are estimated in equations 48, below,

$$\begin{aligned}
 Acc_z &= \frac{2P}{mg} \\
 &= \frac{2*600}{9.81*18.9e-3} \\
 Acc_z &= 6470 \text{ g}
 \end{aligned}$$

Equations 48

$$\begin{aligned}
 Acc_x &= \frac{2P*4.15}{11.26 \text{ m g}} \\
 &= \frac{2*600*4.15}{11.26*9.81*18.9e-3} \\
 Acc_x &= 2385 \text{ g}
 \end{aligned}$$

The bending stress on the mount arm was estimated using equations 49 and 50, below;

$$\begin{aligned}
 M &= PL \\
 &= 600*5.6e-3 \\
 M &= 3.36 \text{ Nm}
 \end{aligned}$$

$$\begin{aligned}
 d &= 4 \text{ mm} \\
 b &= 3.8 \text{ mm}
 \end{aligned}$$

Equations 49

$$\begin{aligned}
 I &= bd^3/12 \\
 &= \frac{3.8e-3*(4e-3)^3}{12} \\
 I &= 2.03e-11 \text{ m}^4
 \end{aligned}$$

$$\begin{aligned}
 \sigma &= \frac{My}{I} \\
 &= \frac{3.36*2e-3}{2.03e-11} \\
 \sigma &= 331 \text{ MPa}
 \end{aligned}$$

Equations 50

$$\begin{aligned}
 MOS &= \frac{\sigma_y}{\sigma} - 1 \\
 &= \frac{340}{331} - 1 \\
 MOS &= 0.03
 \end{aligned}$$

Where MOS was the margin of safety, which must always remain positive. These calculations indicate that there was positive margin of safety against the design loads defined in the GDIR, [91].

6.2.2.1 Harness Clamping

The photodiode harness was clamped to the surface of the optical bench using titanium tie-downs, which allow the use of cable ties, as shown in figure 88, below. The tie-down was bonded to the optical bench using the same epoxy as used for photodiode mounting. For scale, the tie-down was 10mm in length (between the green dots in figure 88, below).

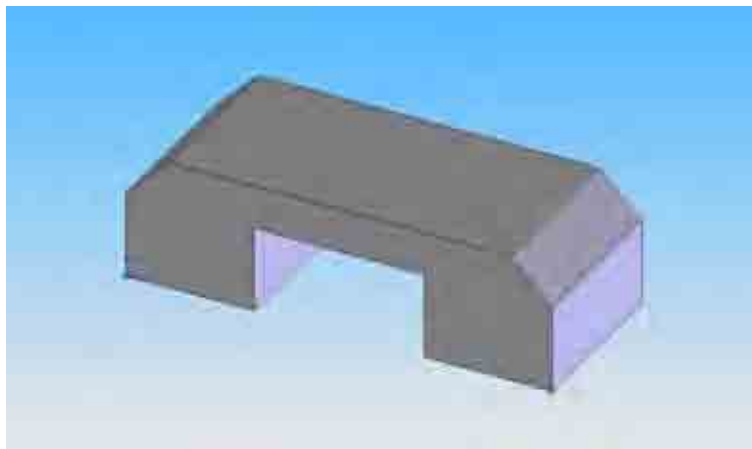


Figure 88: Titanium Harness Tie Down (S2-UGB-DRW-3056)

The location of the clamps on the surface of the optical bench may be seen in the optical bench interferometer assembly drawing, [95], and may also be seen in-situ in figure 89, below.

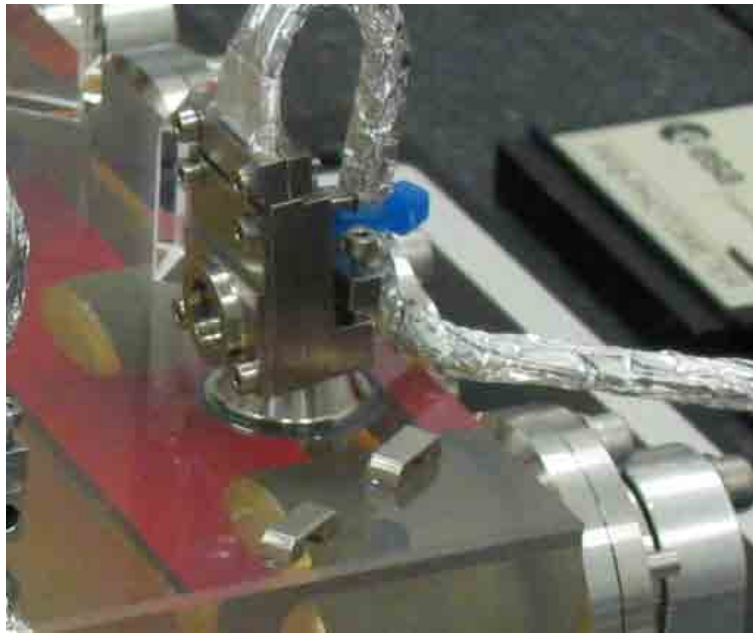


Figure 89: Titanium Harness Tie Down

6.3 PHOTODIODE PROCUREMENT

The InGaAs photodiodes are important components in the measurement chain determining test position and orientation, and therefore their performance was crucial to the success of the mission. As the photodiode was classified by ESA as a non-standard Electronic, Electrical and Electromechanical (EEE) component, compliance with ESA's requirements during the procurement of these parts was required.

6.3.1 EEE Requirements and Qualification

In order to use the photodiodes on the mission, it was necessary to obtain a signed Parts Approval Document, (PAD). These documents were prepared at UBI, and submitted to ESA, [96], [97]. These PAD documents formed the first step in a negotiation between ESA and UBI, the result of which was the submission of a qualification plan, [98].

The main output of the qualification plan was a definition of the test route, as shown for the quadrant photodiodes in figure 90, below.

As the photodiodes were assembled in Norway and California, it was not possible to witness the testing defined by the qualification plan. The photodiode supplier issued traveller documents and a data pack which accompanied the photodiodes when delivered to UBI. The data pack contained test data indicating the photodiode performance at each stage of the qualification procedure.

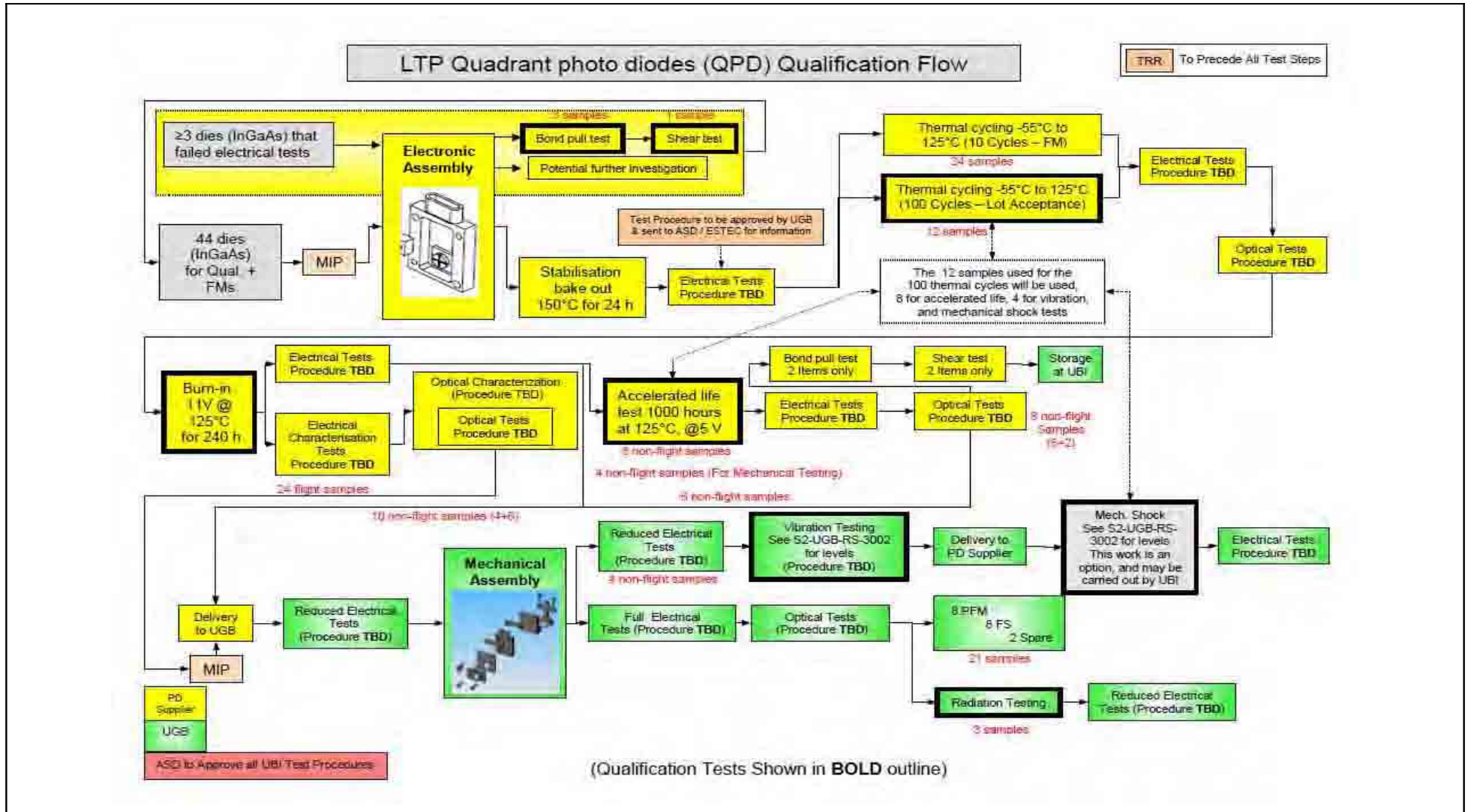


Figure 90: Photodiode Qualification Plan

6.3.2 Photodiode Status

As problems were encountered at a number of stages during photodiode procurement, an example of which is described in section 6.6, the photodiodes described here were not selected for flight use. Instead, a new procurement of photodiodes was instigated, and the existing photodiodes were used in the thermo-optical qualification model optical bench (TOQM).

6.4 PHOTODIODE ASSEMBLY INTEGRATION AND VERIFICATION

As the photodiode, particularly the quadrant photodiode, was part of the measurement chain of the instrument, the adequacy of the photodiode's electro-optical performance was paramount. It was necessary to ensure both that there was good responsivity at 1064 nm, and that the responsivity was uniform across the face of the photodiode.

Uniformity of response was important because any tilt of the test mass affects the position of the illuminated area of the beam on the face of the photodiode. Any change in photodiode response as a function of beam position would therefore be incorrectly interpreted as test mass motion. A specific test was designed, built and implemented to ensure that the photodiodes would meet the stringent requirements for parts in the measurement chain of gravitational wave detectors, as described in section 2.5.

6.4.1 Photodiode Inspection

The photodiode was illuminated with light from a 1064 nm diode laser. While a beam diameter of 150 μm or lower was required to comply with the requirement given in S2-UGB-RS-3002,

[94], with the available step size from the scanning rig of 100 μm , and a desire to ensure all of the photodiode surface was adequately illuminated, a 175 μm diameter beam was used. The laser used to provide the test beam, a BWTEK BWR-1064-20 20mW diode laser, was a class IIIb device, and so was enclosed in an interlocked lightproof enclosure, as shown in figure 91, below.



Figure 91: Laser Enclosure (25mm tapped hole pitch in bench for scale)

Also shown in figure 91 was the lens tube and the device under test. The device under test was mounted on a travelling baseplate which was scanned in front of the non-moving beam. The support arm passed through the wall of the lightproof enclosure to the linear translation stages. In order to prevent any escape of light, the penetration was protected by large black anodised baffle plates both on the inside and outside of the enclosure.

The lens system was used to adjust the beam spot size at the photodiode active surface. The raw beam from the laser were measured using a Dataray WinCamD beam profiling camera, as shown in figure 92, below. Using a non-linear least squares fit, the beam waist and the Rayleigh range were estimated.



Figure 92: Laser Beam Profiling Camera

Using the beam parameters and a mode matching program, JamMt version 0.22, a system of standard lenses was designed which would provide an adequately small spot size at the desired location. As can be seen in figure 93, below, the beam diameter varied as a function of the position along the beam, and in practice, moving the lens tube towards or away from the photodiode provided a way to fine tune the system in-situ. In figure 93, the laser was on the left hand side of the image, and the photodiode active surface was placed near the waist of the output beam, represented towards the right hand side of figure 93.

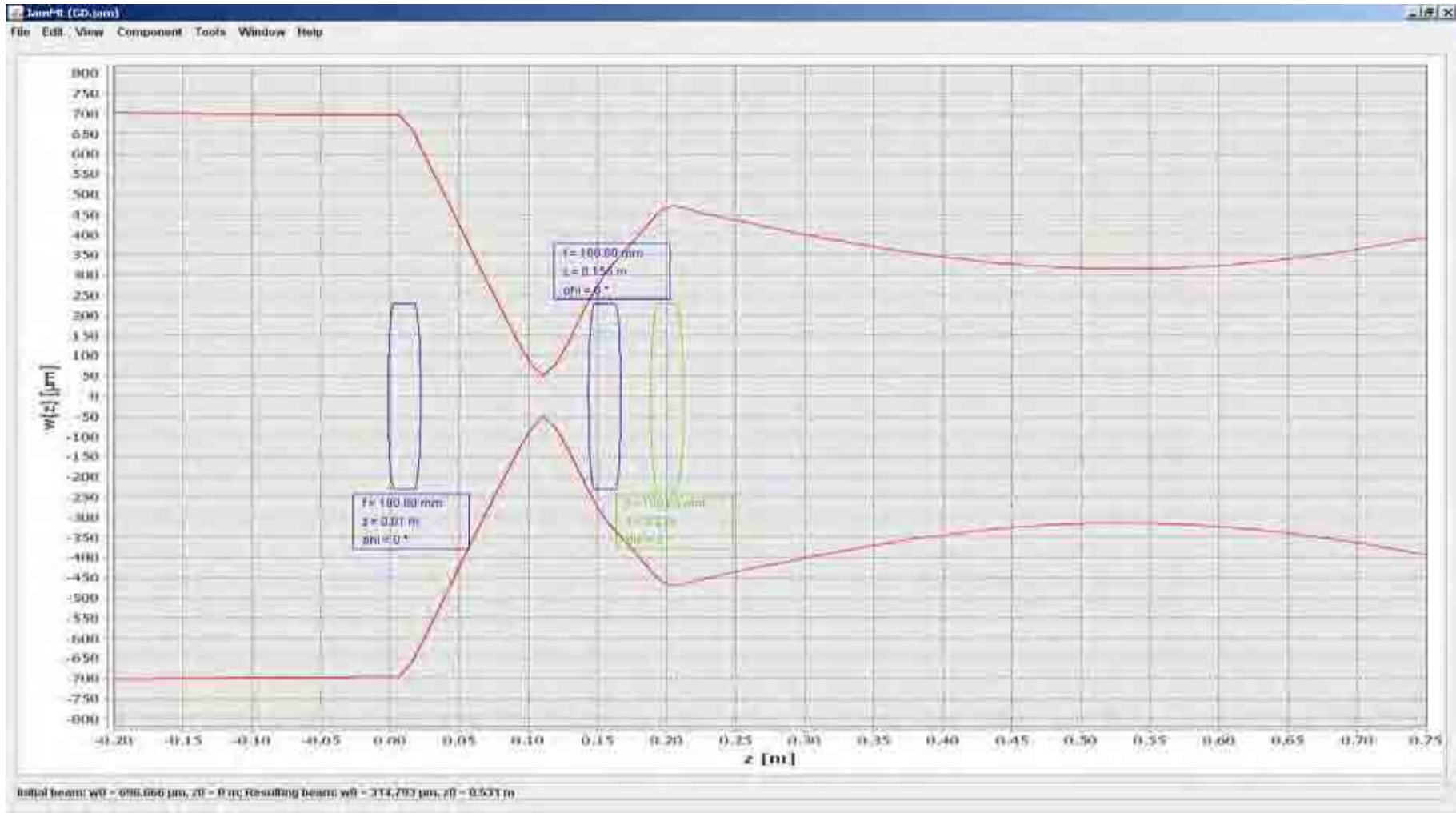


Figure 93: Lens System Simulation – all lenses convex with focal length of 100 mm

The beam used for the scanning is shown in figure 94, below;

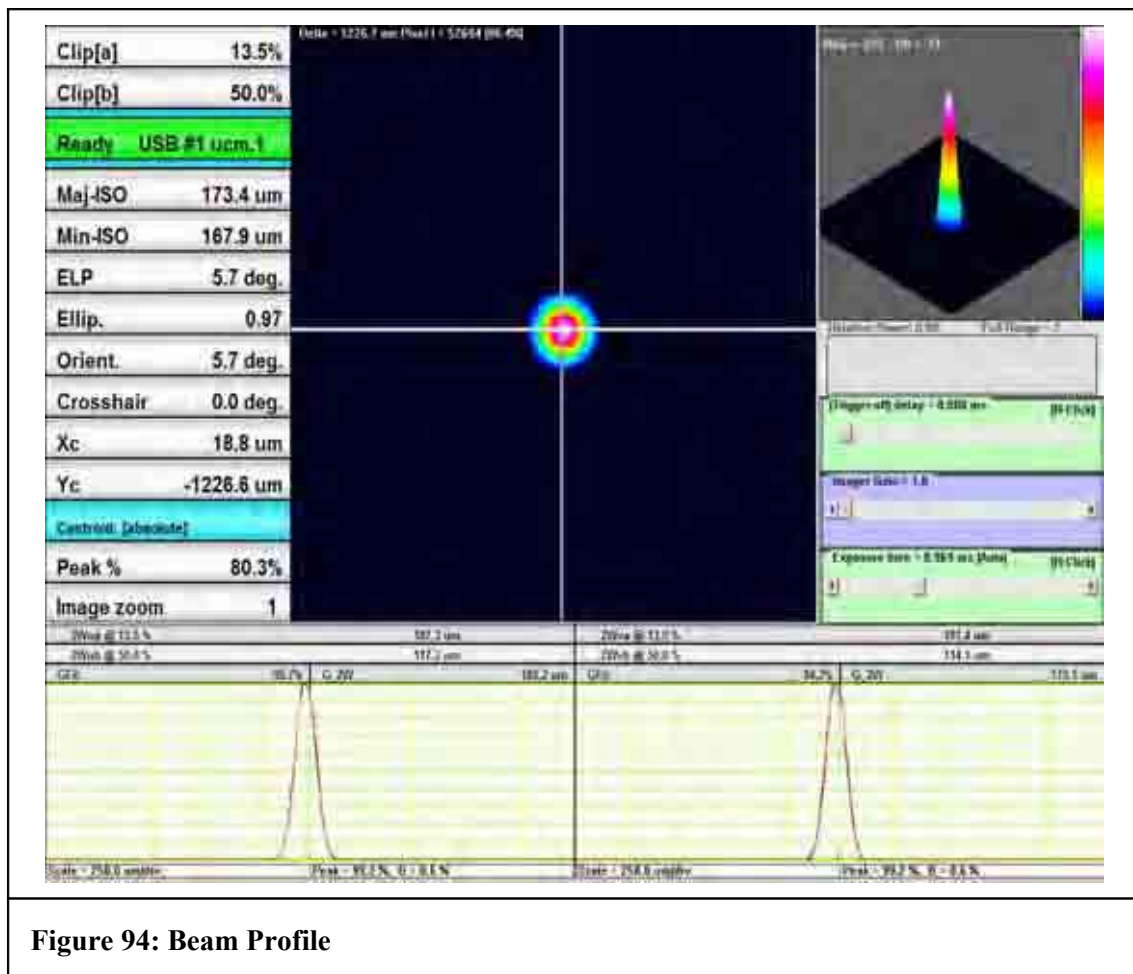


Figure 94: Beam Profile

The photodiode was placed in a fixture on a moving platform. The platform was programmed to move in a raster pattern, and the controller was programmed to send a trigger pulse to a data acquisition unit each time the photodiode was re-positioned. The beam was attenuated using absorptive neutral density filters of total optical density 1.85. The photocurrent was amplified using transimpedance amplifiers with a transimpedance of 3.3k Ω , schematics for which are shown in figure 95, below. A bias voltage of zero volts was used for all tests.

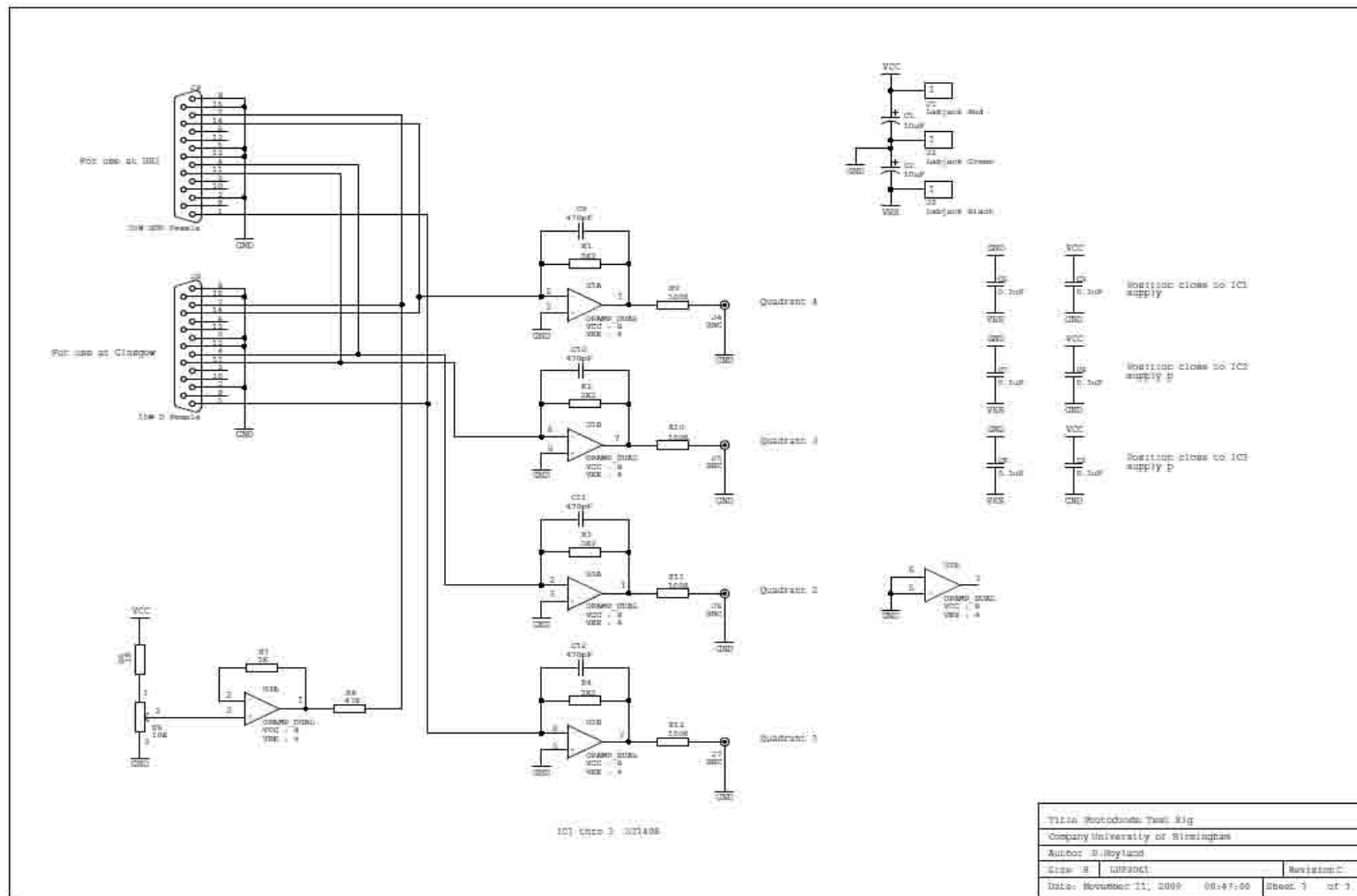


Figure 95: Transimpedance Schematic

At each scan location, using a wavebook WBK 512 12 bit data acquisition system, using the 0-1volt range, nominally DC data were sampled at 1 kHz for 100 ms, thus obtaining 100 data points. These 100 data points were scaled, averaged, and saved to disk. The data set from a complete scan of a photodiode were re-ordered to form a matrix representing the physical layout of the photodiode.

The apparatus for the scanning rig can be seen in figure 96, below.

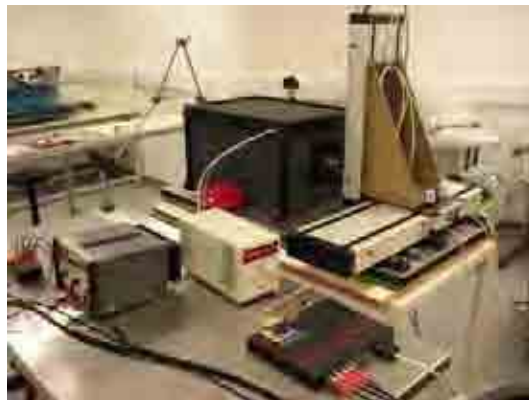


Figure 96: Scanning Apparatus

In order to generate a reference level for each quadrant, each channel of data was scanned and the values compared with a threshold to obtain a region of data points within the active area of the quadrant. The mean value of the response within the active area of the quadrant was used as the reference value, i.e., 100%..

An example scanning test result, for quadrant photodiode 205 is shown in figures 97 to 101, below.

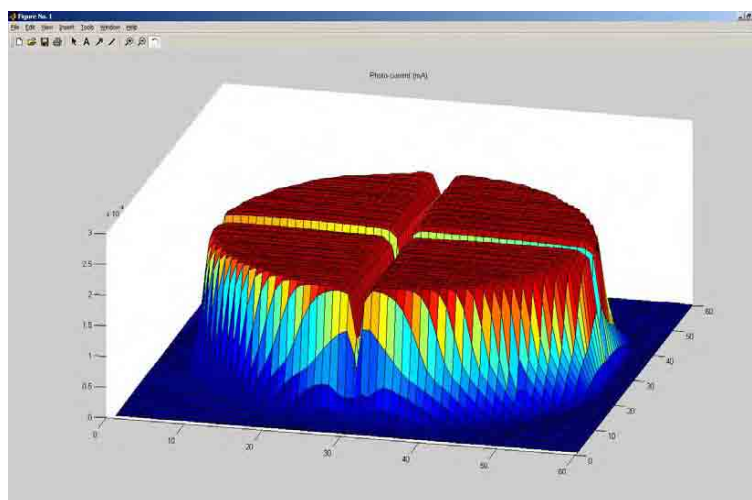


Figure 97: Photodiode 205 Response (QPD is Ø5mm)

The maximum photocurrent was 0.2094 mA, the contour plots of the individual quadrants, shown below, show the 3 %, 97 %, and 103 % response contours. The reference data for each quadrant is shown in table 26, below.

<i>Quadrant</i>	<i>Reference Photo-current (mA)</i>	<i>Relative Reference levels (%)</i>
<i>1</i>	0.2047	0.00
<i>2</i>	0.2042	-0.26
<i>3</i>	0.2044	-0.15
<i>4</i>	0.2047	0.00

Table 26: Photodiode 205 Reference Data

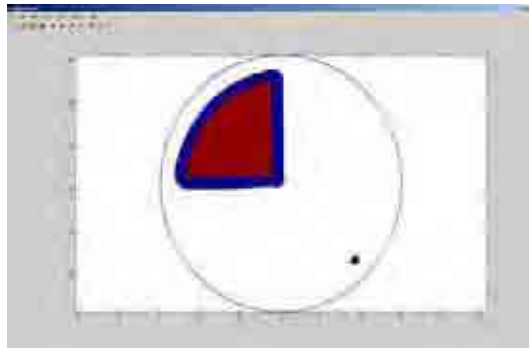


Figure 98: Photodiode 205 Q1 Contour

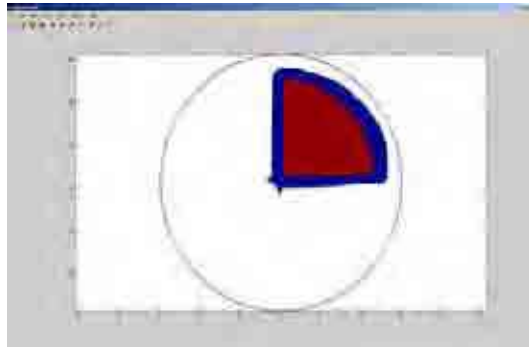


Figure 99: Photodiode 205 Q2 Contour

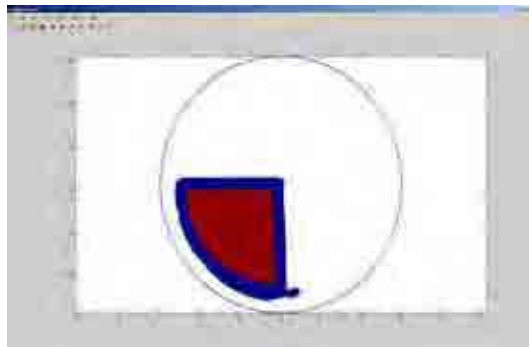


Figure 100: Photodiode 205 Q3 Contour

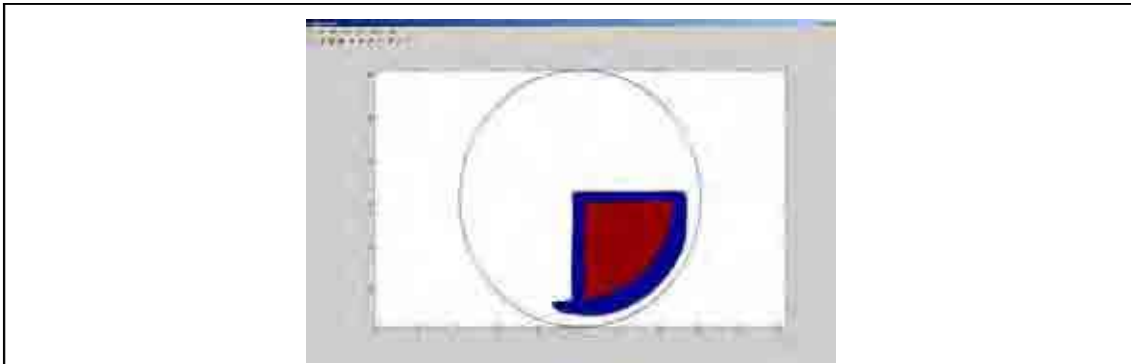


Figure 101: Photodiode 205 Q4 Contour

The remainder of the scanning results are included in appendices E to AA.

As the cross talk and non-uniformity requirements both stipulated $<3\%$, contours of the photodiode's response at 3% , 97% , and 103% of the detector's reference response are presented in figures 98 to 101. The inner, red area of the contour plots represents areas of the photodiode which had a response over 97% of the threshold, the blue areas represent response over 3% of the threshold, but, below 97% . While the calculation of the 103% contour was included in the post processing, no part of the response was above this level, and therefore, this contour was not actually seen on the plots.

The thin blue circle drawn around the photodiode response represents the knife edge aperture – on the plots, this circle was placed with its centre coincident with the centroid of the response distribution, however, owing to tolerance stack up on the real photodiodes, the real knife edge aperture may be displaced from the centre of the photodiode by up to $200\ \mu\text{m}$. Even in cases where the full $200\ \mu\text{m}$ displacement occurs, the knife edge would not obscure any of the active area of the photodiode. Across the flight batch of photodiodes, the responsivity varied between 0.695 and $0.792\ \text{A/W}$, while within each photodiode, the local variation may be seen in appendices E to AA.

6.4.2 Selection of Photodiodes

The selection of photodiodes based upon the following logic which was agreed between UBI and UGL.

Any non-uniformity of the response of the quadrant photodiodes was considered to be most problematic when one or more of the optical beams was moving across the surface of the photodiode. Only those beams which reflect from a test mass have any appreciable movement.

Two of the interferometers on each bench involve a beam reflected from one or more moving test masses. These are the (x_1) and (x_2-x_1) interferometers and have a total of 4 quadrant photodiodes per bench.

The reference and frequency noise interferometers comprise only optical beams that are reflected from components fixed to the optical bench interferometer so there should be virtually no relative movement between beams and photodiodes. These interferometers therefore impose less tight requirements on photodiode uniformity. The reference and frequency noise interferometers account for another 4 quadrant photodiodes per bench.

The final 2 photodiodes are single element devices, used for the power monitoring. Again these beams are fixed to the bench so there is virtually no beam movement relative to the photodiode. Also these final two photodiodes are not directly involved in phase measurements. There was therefore a clear hierarchy of requirements for photodiode uniformity:

- (x_1) and (x_2-x_1) interferometers required the most uniform (4 photodiodes per bench)
- Reference and Frequency Noise were the next most critical (4 photodiodes per bench)
- Optical Power monitors were the least critical (2 photodiodes per bench)

The photodiodes for X1 and X12 interferometers formed “Group A”

The photodiodes for Reference and frequency noise formed “Group B”

The photodiodes for optical power monitoring formed “Group C”

Table 27, below, lists the photodiodes tested, and gathers together the comments and observations made.

<i>Photodiode S/N</i>	<i>Comments</i>
202	Some non-uniformity on quadrant 2, maximum photo-current, 0.2098 mA, GROUP B
203	Slight cross talk near centre of photodiode, maximum photo-current, 0.2066 mA, GROUP A
205	Slight cross talk near centre and edge of photodiode, maximum photo-current, 0.2094 mA, GROUP A
206	Some non-uniformity along quadrant divider, maximum photo-current, 0.2084 mA, GROUP B
208	Slight cross talk near edge of photodiode, maximum photo-current, 0.2116 mA, GROUP A
209	Some non-uniformity along quadrant divider of Q1, maximum photo-current, 0.2129 mA, GROUP B
211	Slight cross talk near centre and edge of photodiode, maximum photo-current, 0.2033 mA, GROUP A
213	Some non-uniformity along quadrant divider of Q1 and cross talk near centre and edge of photodiode , maximum photo-current, 0.2102 mA, GROUP B
217	Slight non-uniformity and cross talk, maximum photo-current, 0.2120 mA, GROUP A
218	Slight non-uniformity and cross talk, maximum photo-current, 0.2130 mA GROUP A
219	Some non-uniformity along quadrant dividers and cross talk near centre and edge of photodiode ,maximum photo-current, 0.1958 mA, GROUP B

<i>Photodiode S/N</i>	<i>Comments</i>
221	Slight cross talk near centre of photodiode, maximum photo-current, 0.2075 mA, GROUP A
222	Some non-uniformity along quadrant dividers and cross talk near centre and edge of photodiode, maximum photo-current, 0.2121 mA, GROUP B
232	Slight cross talk near centre and edge of photodiode, maximum photo-current, 0.2116 mA, GROUP A
233	Photodiode not re-scanned
236	Poor uniformity Q2 and Q3, but Q4 OK, maximum photo-current, 0.2066 mA, GROUP C
238	Slight cross talk near centre and edge of photodiode, maximum photo-current, 0.2064 mA, GROUP A
239	Slight cross talk near centre and edge of photodiode, and poor uniformity near edge of Q4, maximum photo-current, 0.2067 mA, GROUP B
241	Slight cross talk near centre and edge of photodiode, and poor uniformity Q3, but Q4 OK, maximum photo-current, 0.2117 mA, GROUP C
242	Photodiode not re-scanned
244	Poor uniformity in Q1 Quadrant divider, but Q4 OK, maximum photo-current, 0.1941 mA, GROUP C
245	Poor uniformity in all quadrants, maximum photo-current, 0.1916 mA, GROUP C
246	Good uniformity, maximum photo-current, 0.1951 mA, GROUP A
Table 27: Photodiode Scan Data Summary	

The grouping of photodiodes is shown in table 28, below;

<i>Group</i>	<i>Location</i>	<i>Photodiodes</i>
<i>A</i>	(x_1) or (x_2-x_1) Interferometer	203, 205, 208, 211, 221, 232, 238, 246, 217
<i>B</i>	Reference or Frequency noise Interferometer	202, 206, 209, 213, 218, 219, 222, 239
<i>C</i>	Optical Power Monitoring	236, 241, 244, 245
Table 28: Photodiode Grouping		

6.4.3 Photodiode Inspection and Test Summary

An inspection facility was designed, built, commissioned and used in order to check and grade the photodiodes. The inspection facility enabled the responsivity and the uniformity of the photodiode's response to be measured and recorded.

Using the inspection facility, the photodiodes were tested, and graded in order to determine their optimum installation position on the optical bench.

6.5 THE POSSIBLE USE OF QPDS AS SEPDS

6.5.1 The Use of QPD as SEPD

Owing to the low yield of SEPDS, (7 from a batch of 17 were found to have failed when electrically tested after the stabilisation bake) it was necessary to consider technical options to allow the assembly and testing of the optical bench without causing excessive delay to an already delayed project. Among the suggestions raised was the possibility of using QPDs in the

place of SEPDs; this section describes possible implementations, and considers possible consequences for the connected hardware.

As may be seen from table 24, the only mechanical parts which were specific to the QPD or SEPD were the photodiode base and the photodiode cover. All other mechanical parts were interchangeable.

6.5.1.1 QPD & SEPD Electrical Connections and Cable

The electrical schematic for the common cathode QPD is shown in figure 102,below.

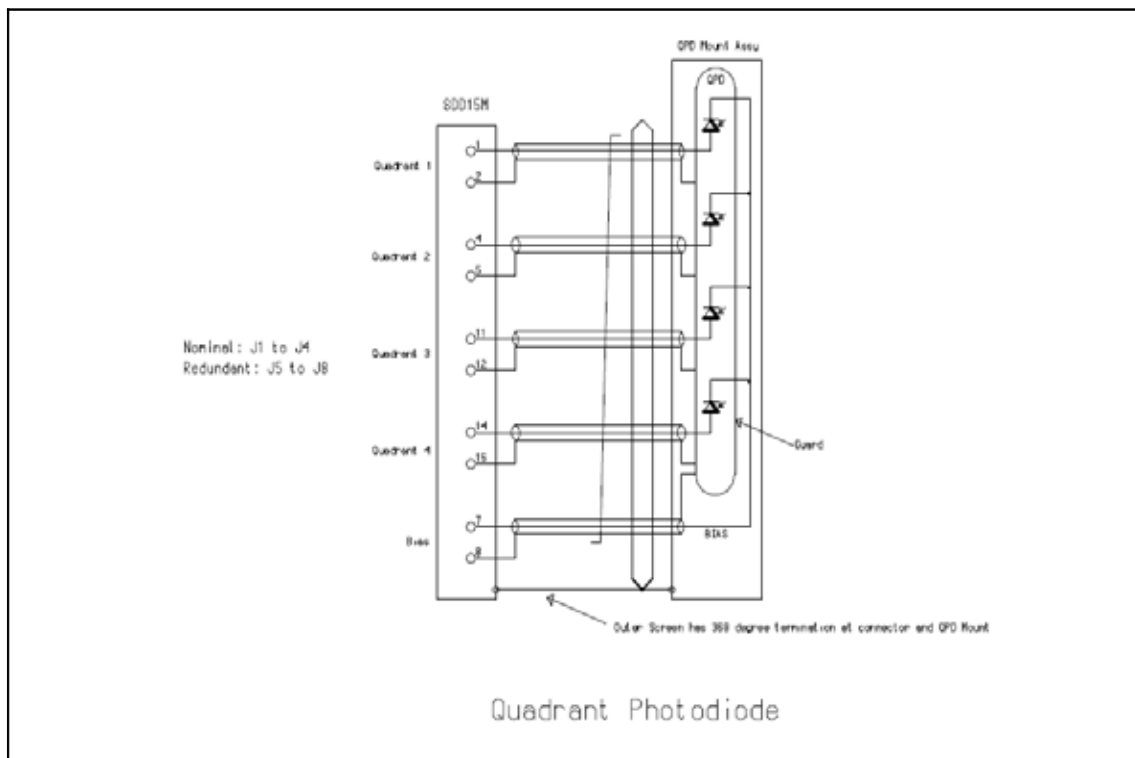


Figure 102: Quadrant Photodiode Electrical Schematic

The electrical schematic for the SEPD is shown in figure 103,below.

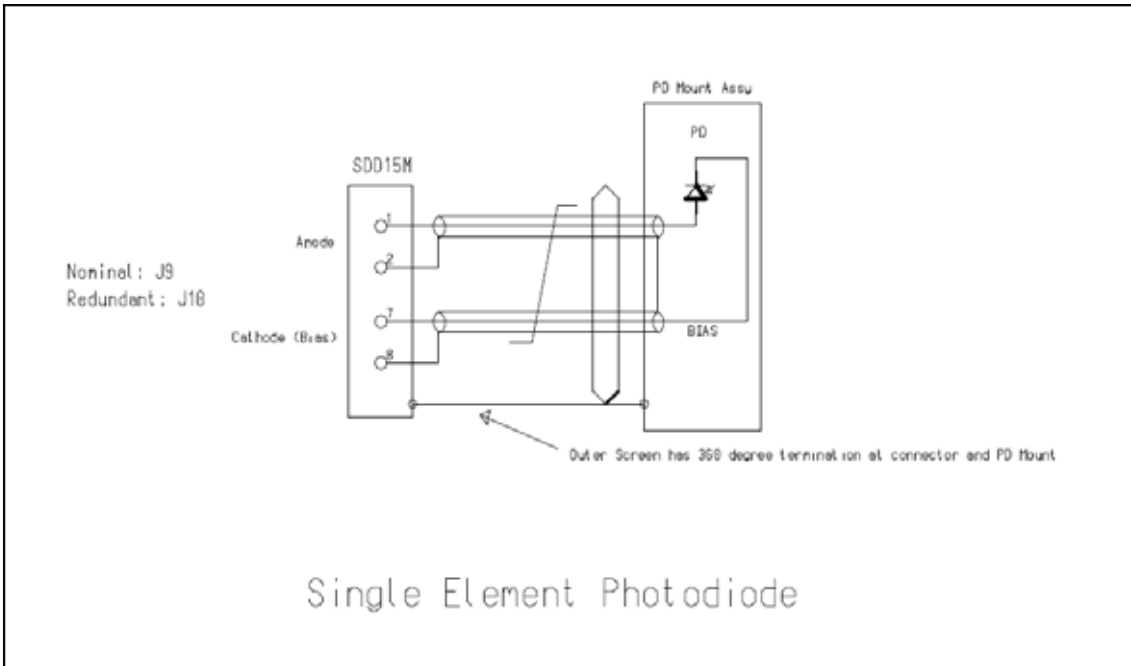


Figure 103: Single Element Photodiode Electrical Schematic

6.5.1.2 Possible "QPD as SEPD" Configurations

There were three distinct ways of using a QPD in the place of a SEPD, namely aiming the beam onto the centre of the QPD, thus using all four of the quadrants, aiming the beam onto only two of the quadrants, and aiming the beam onto only one quadrant.

In the diagrams which follow, the black circle represents the outer edge of the QPD, the blue circle the size of the SEPD, and the red circle, the estimated diameter of the beam on the actual optical bench, at a location representative of the photodiodes.

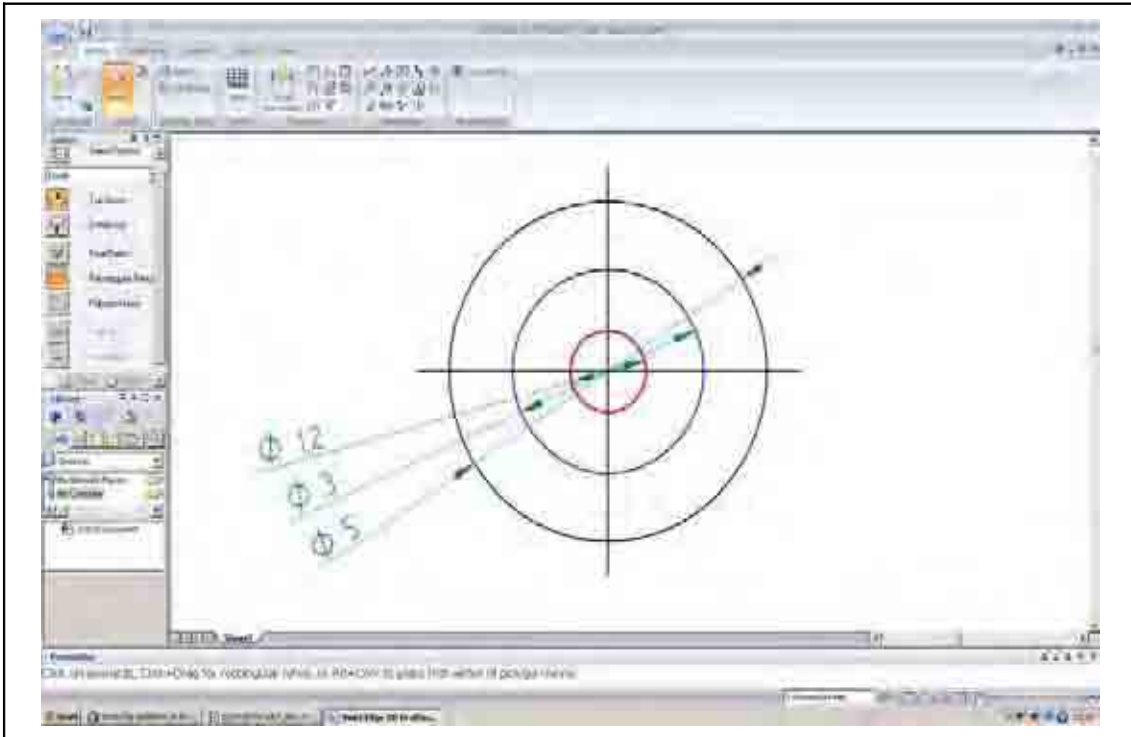


Figure 104: Beam centred on QPD centre

The configuration shown in figure 104 represents the case where the QPD was simply fitted in place of the SEPD without making any other mechanical adjustments. This configuration gave the largest distance between the centre of the beam and the edge of the active area of the QPD of 2.5 mm, but, it did so at the cost of large electrical capacitance.

The zero bias capacitance of the flight QPDs was measured by OSI at 50 °C, each quadrant had a capacitance of approximately 1000 pF compared with the requirement of <1500 pF. Therefore, the effective capacitance of the QPD used as an SEPD in this configuration was approximately 4000 pF, whereas, the SEPD was specified with a capacitance of <1500 pF.

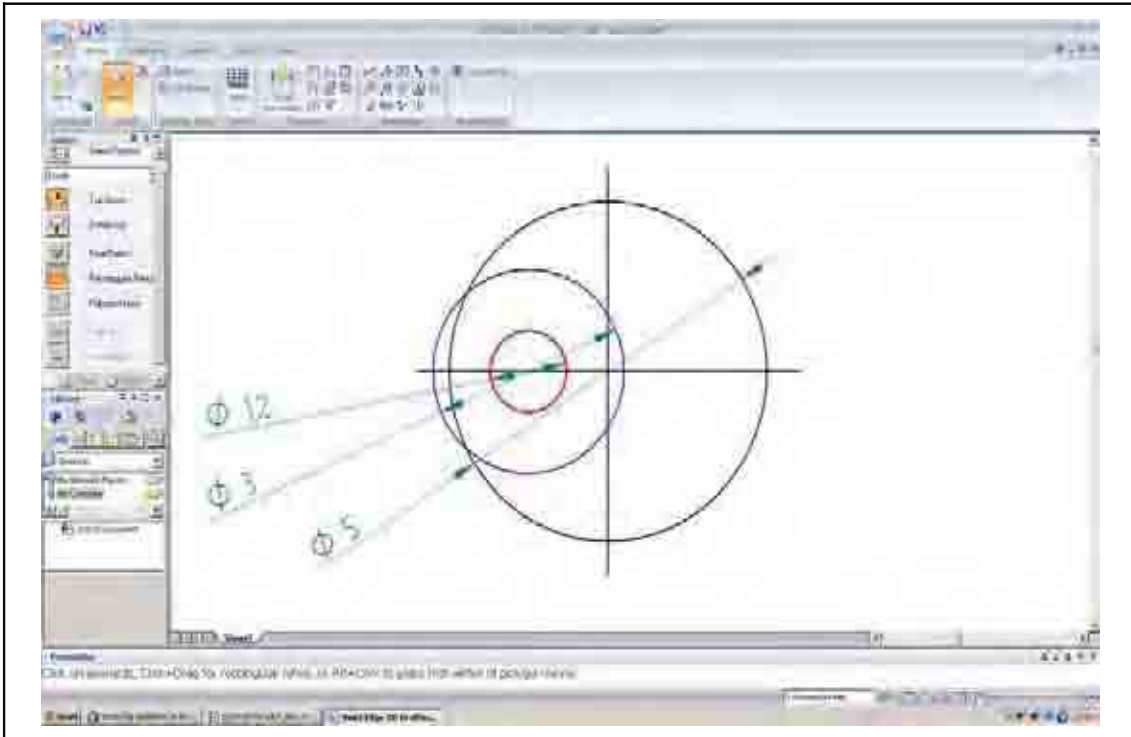


Figure 105: Beam Centred on Two Elements of Laterally Displaced QPD

The configuration shown in figure 105 represents the case where the QPD was fitted in place of the SEPD and was laterally displaced by 1.25 mm, thus aligning the beam centrally on two vertically adjacent QPD segments.

The displacement may be achieved by simply displacing the entire photodiode mount during the bonding process, or, it may also be achieved by installing a modified cassette holder.

The effective capacitance of the QPD used as an SEPD in this configuration was approximately 2000 pF.

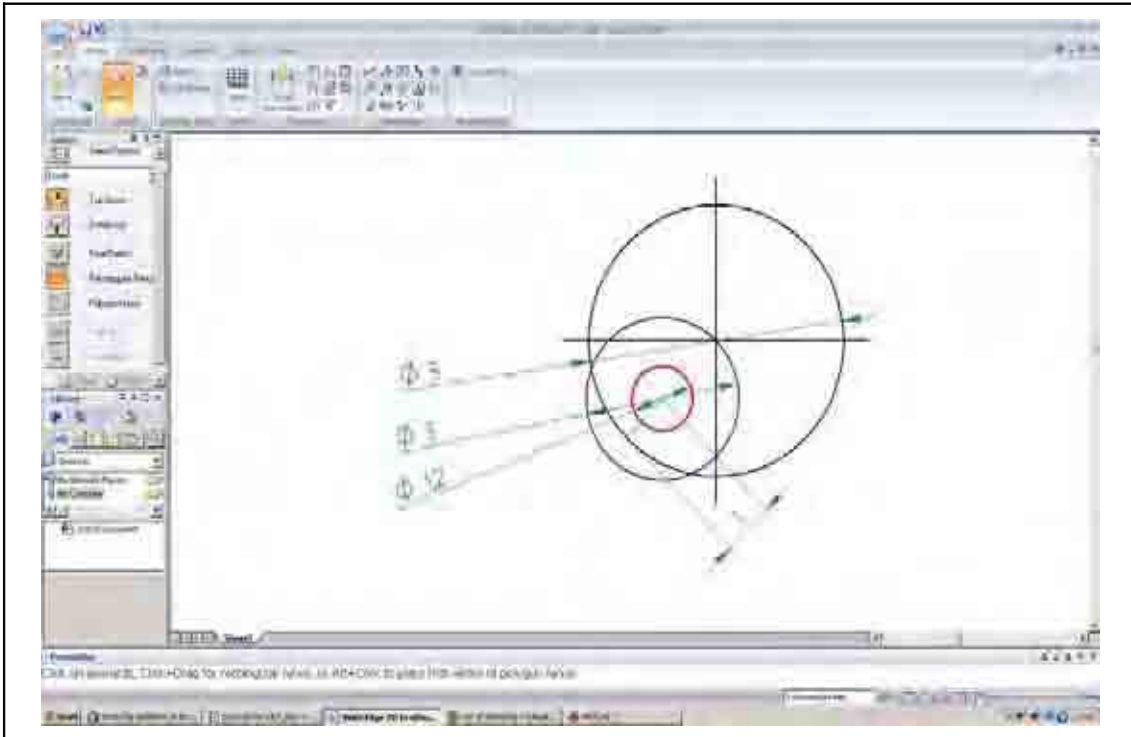


Figure 106: Beam Centred on One Segment of QPD

The configuration shown in figure 106 represents the case where the QPD was fitted in place of the SEPD and was both vertically and laterally displaced by 1.06 mm, $(4r/3\pi)$, thus aligning the beam on with the centroid of one QPD segment.

The lateral displacement may be achieved by simply displacing the entire photodiode mount during the bonding process, or, it may also be achieved by installing a modified cassette holder while the vertical displacement may only be obtained via the use of a modified cassette holder.

The effective capacitance of the QPD used as an SEPD in this configuration was approximately 1000 pF, i.e., less than the original SEPD upper limit. However, this configuration also placed the beam closer to the edge of the QPD than the other configurations, with 1 mm between the beam centre and edge of the QPD.

My suggestion of the use of QPDs as SEPDs was considered during telephone conferences between ESA, ASD, and the UK team. The idea, as per figure 106 was accepted, and the required modified cassettes were designed, built, and bonded to the optical bench. In the re-procurement of photodiodes, the QPD as SEPD principle is being carried forward and used again.

6.6 PHOTODIODE 202 FAILURE INVESTIGATION

After the assembly of the photodiode cassettes into their mount, a basic electrical test was carried out on all photodiodes. During this test, it was found that photodiode 202 had failed.

The test circuit was as shown in figure 107, below; The 20V DC input voltage was supplied via a Farnell laboratory power supply, the voltage and current were measured using Keithley digital meters.

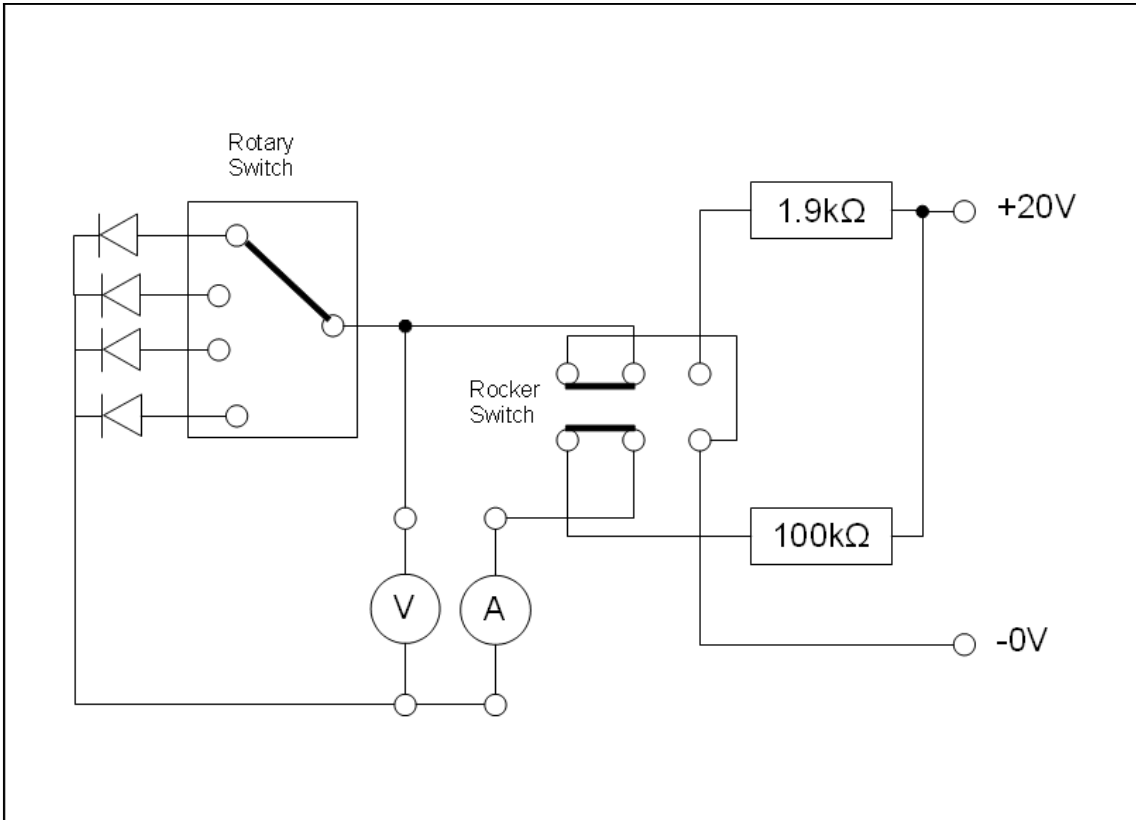


Figure 107: Basic Electrical Test Circuit

The test procedure is listed in table 29, below;

Step N°	Procedure:
	Take appropriate ESD protection precautions when using the quick test box. Care should be taken to prevent the surface of the test box from charging up.
1	Configure a bench power supply to 20.22V 100mA current limit. Connect it to the test box.
2	Configure a DMM to read DC Volts between 1mV and 25V. Attach it to the test box.
3	Configure a DMM to DC Amps between 10nA and 100mA. Connect it to the test box.
4	Short the power supply with a test lead.
5	Remove the shorting connector from the photo-diode and connect it to the test box.
6	Short the power supply with a test lead. Configure the test the test box as required.
7	Remove the shorting lead from the power supply and turn it on.
8	Note down the readings and add them to S2-UGB-TR-3001.
9	Switch off the power supply.
10	Repeat steps 6 to 9 for every quadrant, forward and reverse biased.
11	When complete short the power supply with a test lead.
12	Unplug the photo-diode and replace the shorting connector.
Table 29: Photodiode Quick Test Procedure	

The quick test box specifically tests these two requirements;

- LTP-PFM-PDM-030 The forward voltage, at room temperature, of the photo-diode shall be 1.0 V maximum @ 10mA

- LTP-PFM-PDM-031 The breakdown voltage, at room temperature, shall be 20V minimum @ 10^④A

Which are defined in the photo-diode and mount requirement specification, [94], however, the requirements are also directly comparable with the testing carried out at die level by the photo-diode chip supplier.

Immediately prior to assembling the upper cover of the photo-diode the die was photographed, and this is shown in figure 108, below;

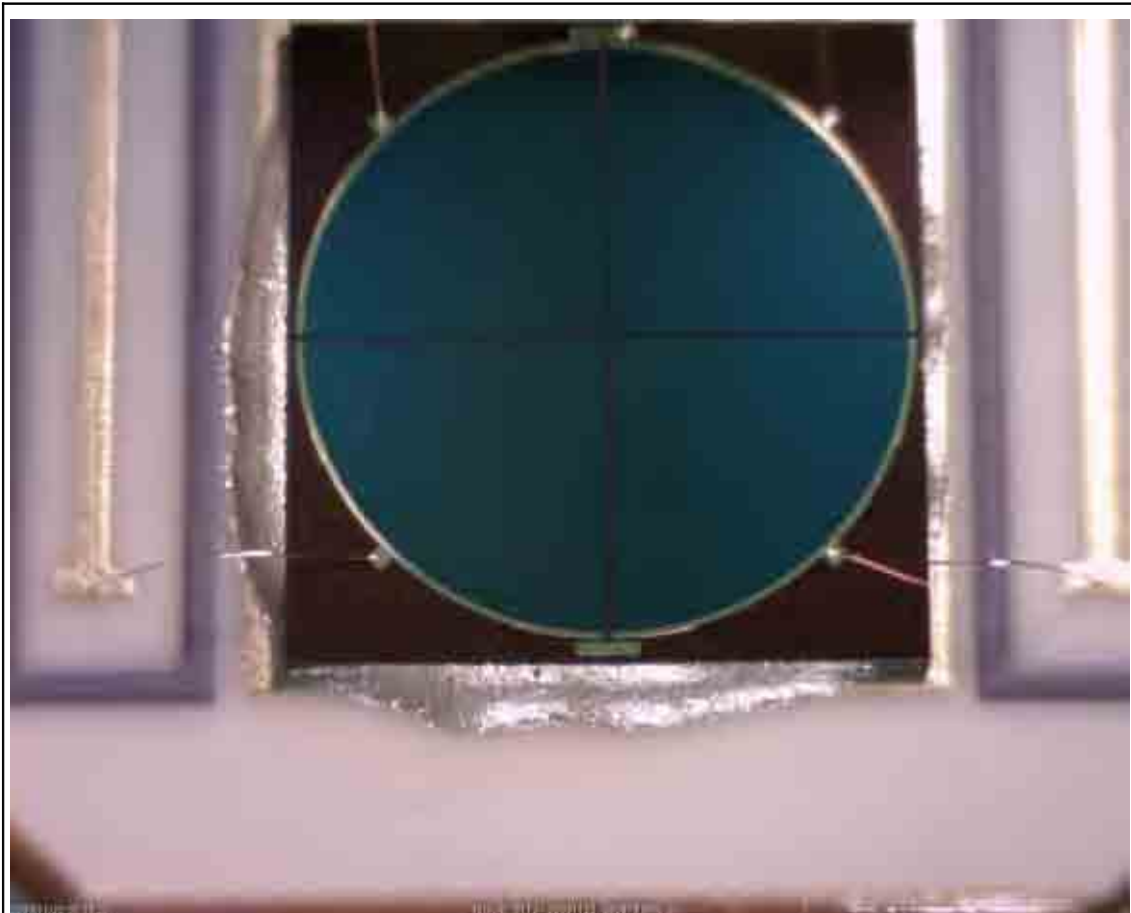







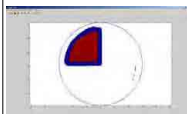
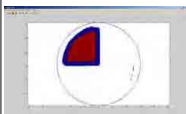
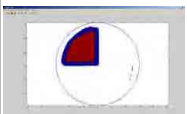
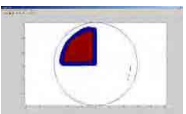
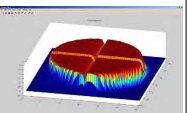
Figure 108: PD202 Prior to cover assembly at UBI

6.6.1 PD 202 Test and Integration History

The test data are shown in table 30, below. All tests listed prior to the delivery to UBI were carried out by the photo-diode supplier. The detail of these tests has not been made available.

<i>Test</i>	<i>Q1</i>	<i>Q2</i>	<i>Q3</i>	<i>Q4</i>	<i>Comments</i>
Pre Temperature Cycling Electrical Test	Dark Current 2.326e-9 A	Dark Current 2.302e-9 A	Dark Current 2.294e-9 A	Dark Current 2.203e-9 A	Pass
	Reverse Voltage 41 V	Reverse Voltage 41 V	Reverse Voltage 41 V	Reverse Voltage 41 V	
	Forward Voltage 0.59 V	Forward Voltage 0.58 V	Forward Voltage 0.58 V	Forward Voltage 0.58 V	
Responsivity	0.769 A/W	0.769 A/W	0.769 A/W	0.769 A/W	Pass Optical Power 2.699e-6 W
Thermal Cycling, 10 cycles					
Pre Burn in Electrical Test	Dark Current 2.44e-9 A	Dark Current 2.41e-9 A	Dark Current 2.39e-9 A	Dark Current 2.40e-9 A	Pass
	Reverse Voltage 41 V	Reverse Voltage 41 V	Reverse Voltage 41 V	Reverse Voltage 41 V	
	Forward Voltage 0.59 V	Forward Voltage 0.58 V	Forward Voltage 0.58 V	Forward Voltage 0.58 V	
Responsivity	0.898 A/W	0.899 A/W	0.900 A/W	0.899 A/W	Pass Optical Power 2.543e-6 W
Burn in 125 °C, 11 V bias, for 240 hours					

<i>Test</i>	<i>Q1</i>	<i>Q2</i>	<i>Q3</i>	<i>Q4</i>	<i>Comments</i>
Post Burn in Electrical Test	Dark Current 2.94e-9 A	Dark Current 2.95e-9 A	Dark Current 2.93e-9 A	Dark Current 2.93e-9 A	Pass
	Reverse Voltage 41 V	Reverse Voltage 41 V	Reverse Voltage 41 V	Reverse Voltage 40 V	
	Forward Voltage 0.6 V	Forward Voltage 0.58 V	Forward Voltage 0.58 V	Forward Voltage 0.58 V	
Capacitance	0.972 nF	0.963 nF	0.970 nF	0.966 nF	Pass
Crosstalk	0.56 %	0.56 %	0.56 %	0.55 %	Pass
Responsivity @ 23 °C	0.90 A/W	0.90 A/W	0.90 A/W	0.90 A/W	Pass Optical Power 2.60e-6 W
Responsivity @ -10 °C	0.91 A/W	0.92 A/W	0.88 A/W	0.87 A/W	Pass Optical Power unknown
Responsivity @ 50 °C	0.93 A/W	0.92 A/W	0.90 A/W	0.91 A/W	Pass Optical Power unknown
Dark Current @ -10 °C	3.80x10 ⁻¹⁰ A	4.00x10 ⁻¹⁰ A	4.00x10 ⁻¹⁰ A	5.20x10 ⁻¹⁰ A	Pass
Dark Current @ 50 °C	8.10x10 ⁻¹⁰ A	7.90x10 ⁻¹⁰ A	7.80x10 ⁻¹⁰ A	8.10x10 ⁻¹⁰ A	Pass
Delivery to UBI					

<i>Test</i>	<i>Q1</i>	<i>Q2</i>	<i>Q3</i>	<i>Q4</i>	<i>Comments</i>
Pre Assembly Scan					
	Good Response	Good Response	Good Response	Good Response	Pass
Assembly of knife edge cover and window					
Post Assembly Scan					
	Good Response 0.2042 mA	Good Response 0.2051 mA	Good Response 0.2048 mA	Good Response 0.2055 mA	Pass
Assembly of photodiode onto mount / cassette holder					
Electrical Test	Reverse Voltage 0.86 V @ 192 μA	Reverse Voltage 20 V @ 2.23 μA	Reverse Voltage 20 V @ 2.26 μA	Reverse Voltage 19.5 V @ 6.45 μA	Fail Requirement >20 V @ 10 μA
	Forward Voltage 0.538 V	Forward Voltage 0.556 V	Forward Voltage 0.558 V	Forward Voltage 0.558 V	Pass Tested at 10.33 mA
Table 30: Photodiode 202 Test and Integration History					

6.6.2 PD 202 Investigation Method

The cassette was removed from the cassette holder to facilitate scanning. The scanning results are shown below.

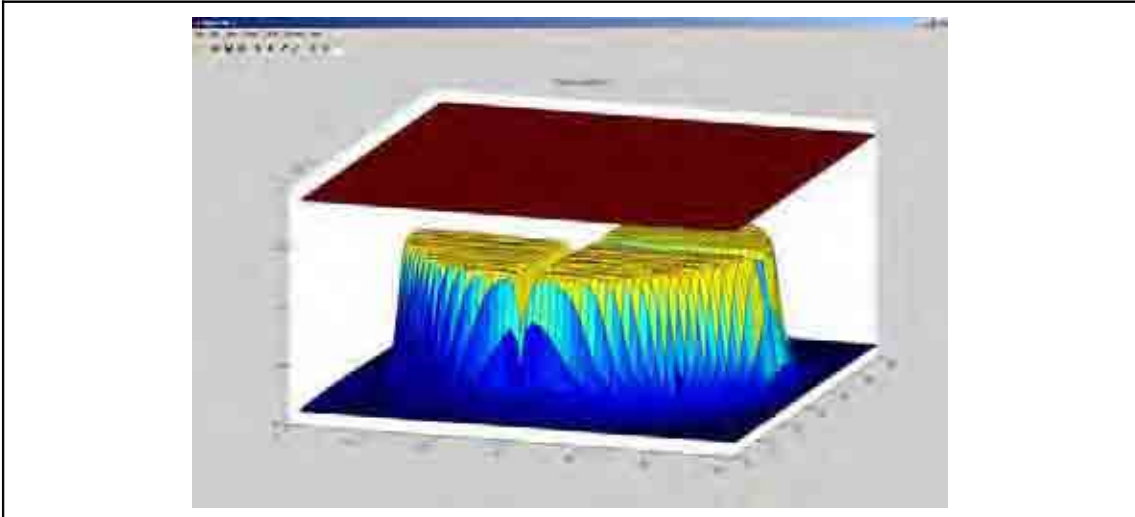


Figure 109: Photodiode 202 Response

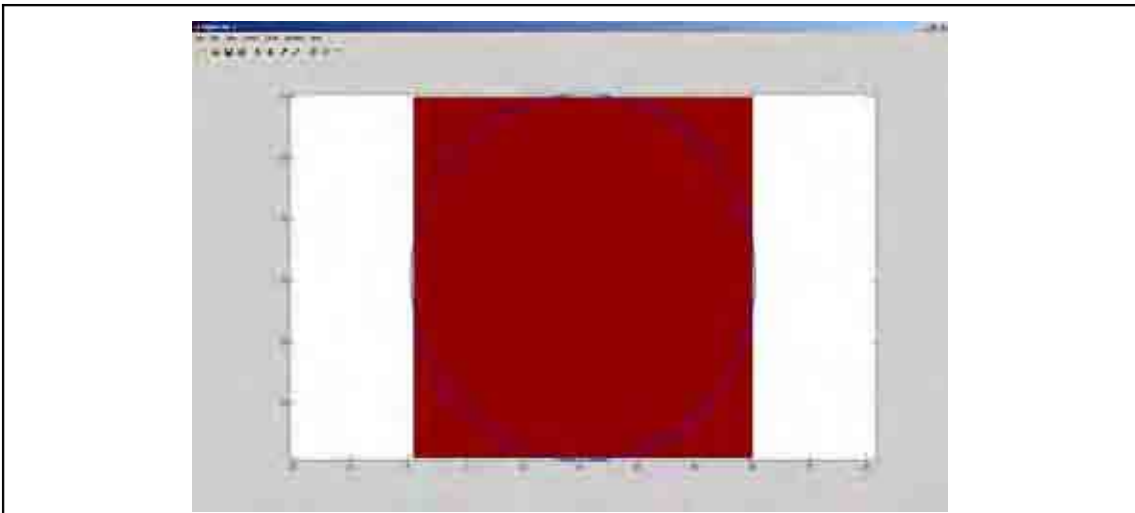


Figure 110: Photodiode 202 Q1 Contours

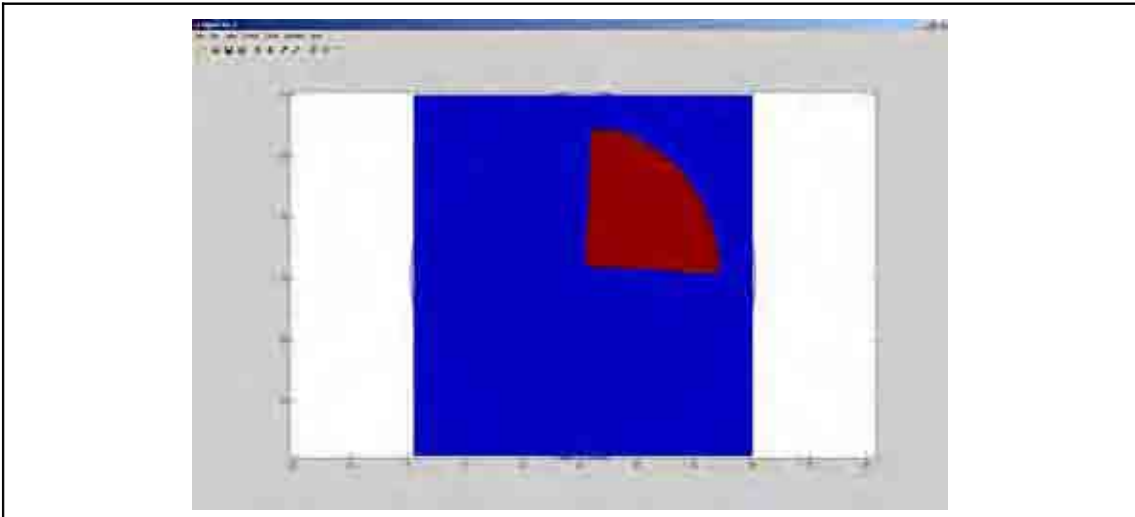


Figure 111: Photodiode 202 Q2 Contours

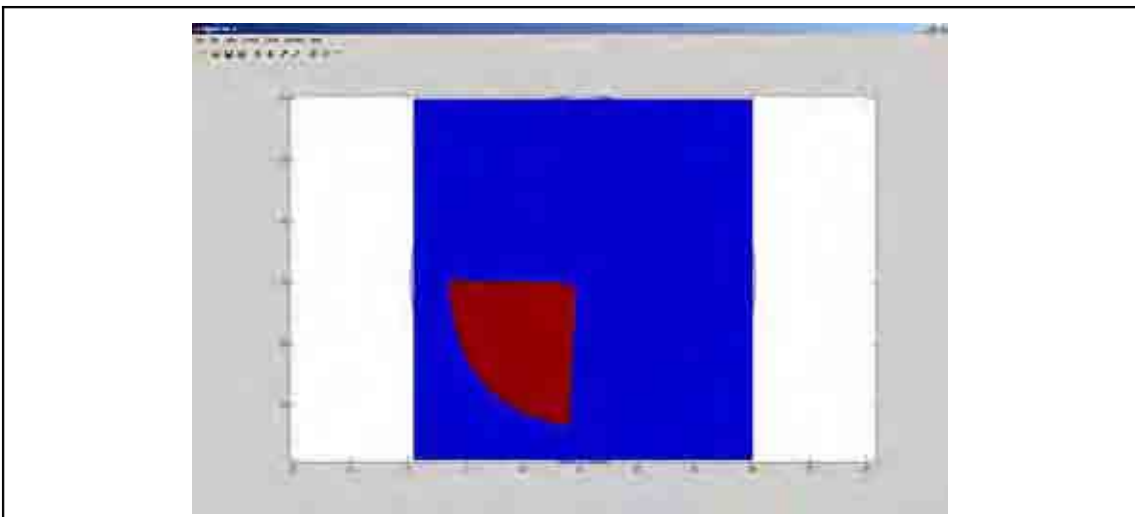


Figure 112: Photodiode 202 Q3 Contours

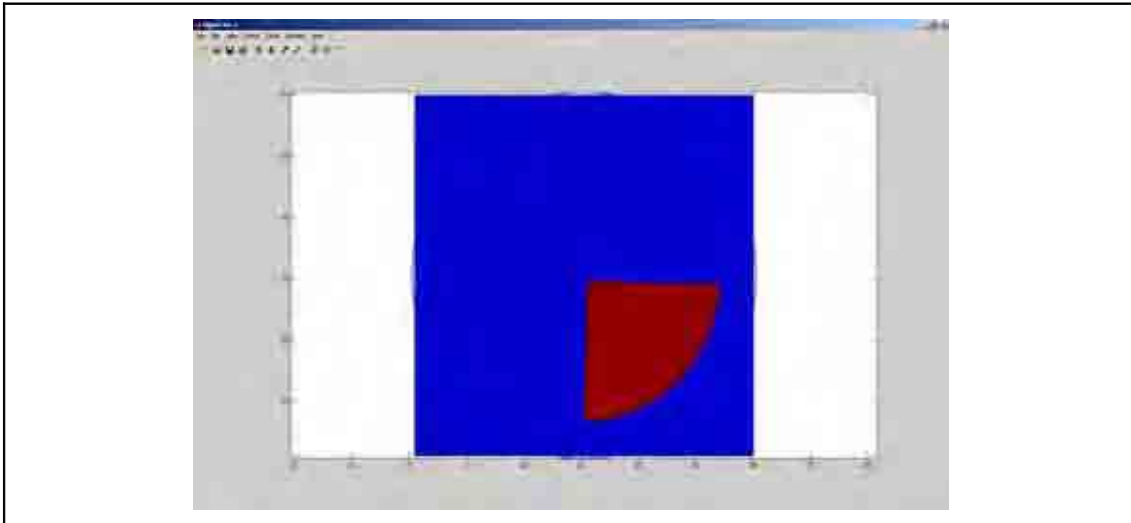


Figure 113: Photodiode 202 Q4 Contours

During the removal of the cassette from the holder, the following items of debris were noted;



Figure 114: Debris Found Between Cassette and Cassette Holder

On visual inspection the debris appeared to be a small piece of epoxy and there was evidence of similar material in the fastener hole immediately adjacent. It was possible that the epoxy was ejected underneath the cassette into the space between the cassette and the cassette holder when the fastener was inserted into the hole.

While unaided visual inspection did not find any stray epoxy, an inspection under magnification, concentrating on the holes in the cassette holder and any gapping between the cassette and cassette holder enabled this issue to be cleared.

It was thought that die cracking owing to twist of the cassette was possible. The mechanical configuration of the cassette is shown in figure 115, below.

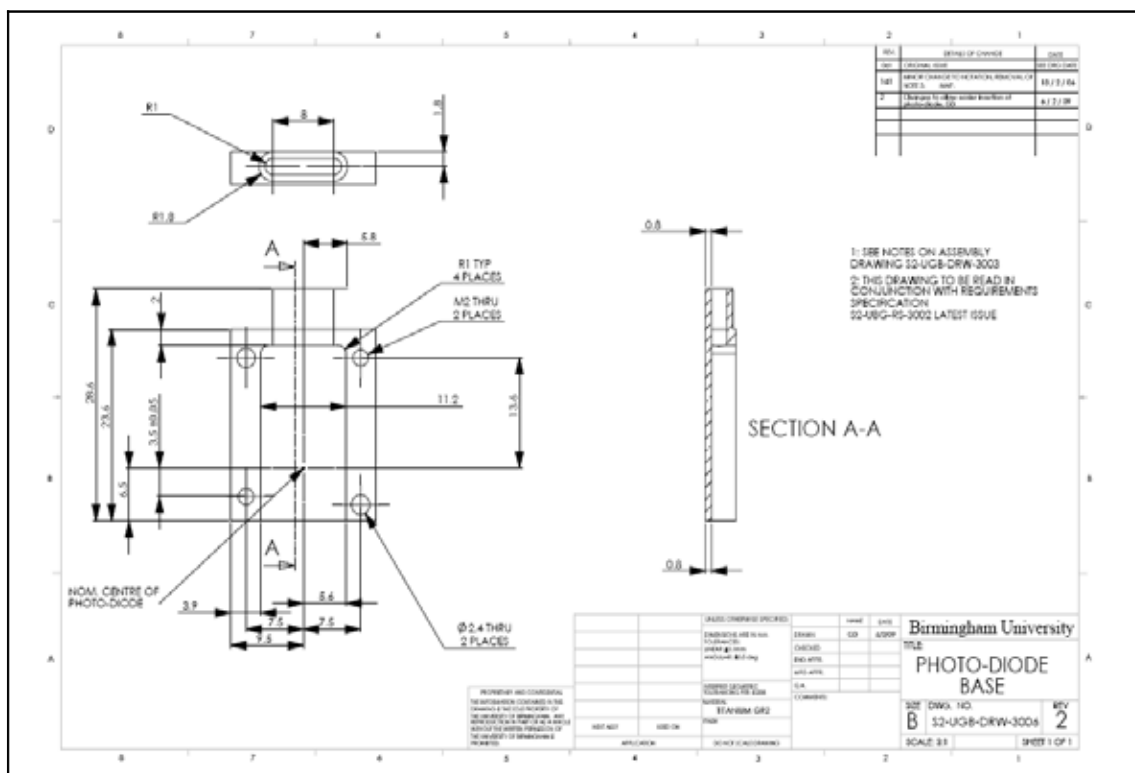


Figure 115: Cassette Drawing

The response of a known cracked die, PD233, may be seen in the pre-assembly scanning report, S2-UGB-RP-3009. The results of the scan of channel 1 of PD 233, showing excessive leakage, are also shown in figure 109, below for comparison

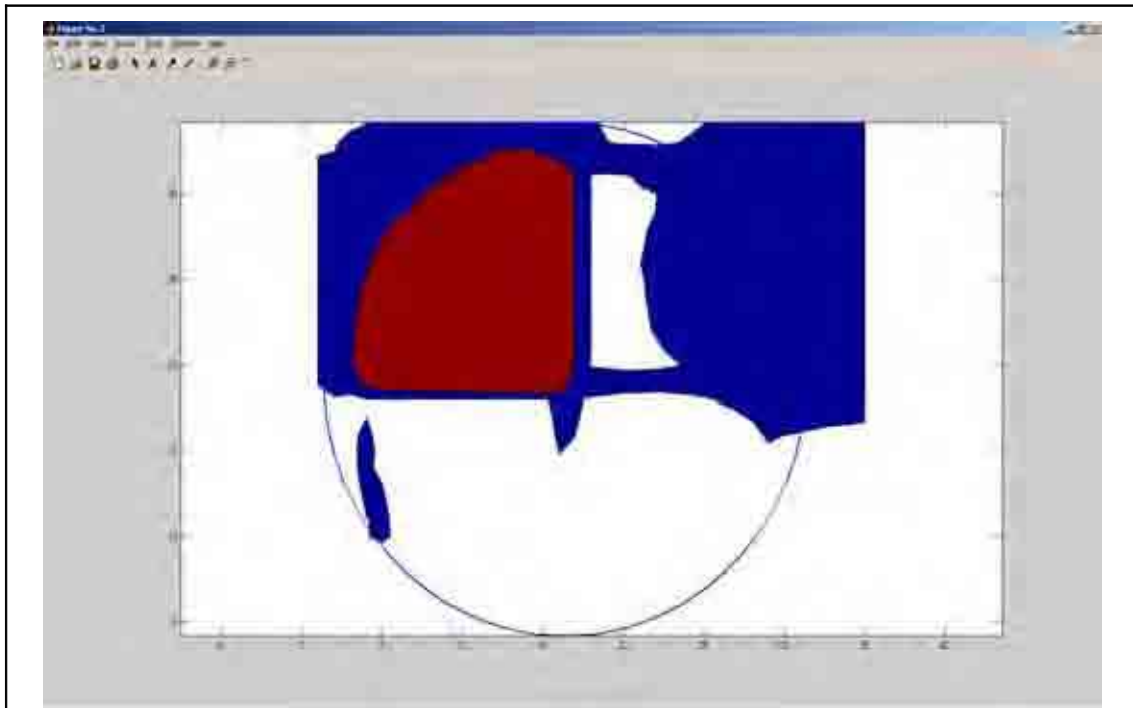


Figure 116: PD 233 Q1 Response

In order to answer the question of whether deformation caused by trapped debris was a possible cause of the cassette twisting during assembly, the bending stiffness of the longer side of the cassette assembly was estimated, and using estimated bolt loads, the maximum possible deflection was estimated. The input data are defined in equations 51, below.

$$\begin{aligned}
b &= 3.9 \text{ mm} \\
d &= 4 \text{ mm} \\
I &= bd^3/12 \\
I &= 2.08\text{e-}11 \text{ m}^4 \\
E &= 105 \text{ GPa} \\
l &= 17.1 \text{ mm} \\
k &= 3EI/l^3 \\
k &= 1.41 \text{ MN/m}
\end{aligned}$$

Equations 51

Where b and d respectively represent the width and depth of the equivalent beam, I is the second moment of area of the beam section, E represents the Young's modulus of elasticity, and k, the stiffness of the cantilevered beam.

Assuming one end of the cassette was built in, and the M2 bolts were torqued to 0.3 Nm, the deflection of the cassette is estimated in equations 52, below;

$$\begin{aligned}
T &= K P D \\
P &= \frac{T}{0.25 D} \\
&= \frac{0.3}{0.25 * 2\text{e-}3} \\
P &= 600 \text{ N} \\
x &= \frac{P}{k} \\
&= \frac{600}{1.31\text{e}6} \\
x &= 458 \text{ } \mu\text{m}
\end{aligned}$$

Equations 52

This calculation demonstrated that if some foreign matter were present beneath the cassette during installation, the cassette could deform by up to 450 μm . Owing to the brittle nature of

InGaAs, it was possible that this deformation might be sufficient to cause damage via brittle fracture. This calculation demonstrated that deflection of the cassette caused by contamination was possible, but the calculation was not proof that the deflection had actually occurred, or that the InGaAs had indeed cracked. During inspections, no evidence for cracking in the InGaAs was observed.

6.6.3 ESTEC Scanning Electron Microscope Inspection

The failed photodiode was sent to ESTEC for further analysis to determine the cause of failure. After repeating the electrical testing which had found the error, the die was examined under an optical microscope, and no defects were seen. The die was prepared as a specimen for use under a scanning electron microscope. Material failures were found in the guard ring area surrounding the photo-sensitive area of the photodiode, as shown in figure 117, below.

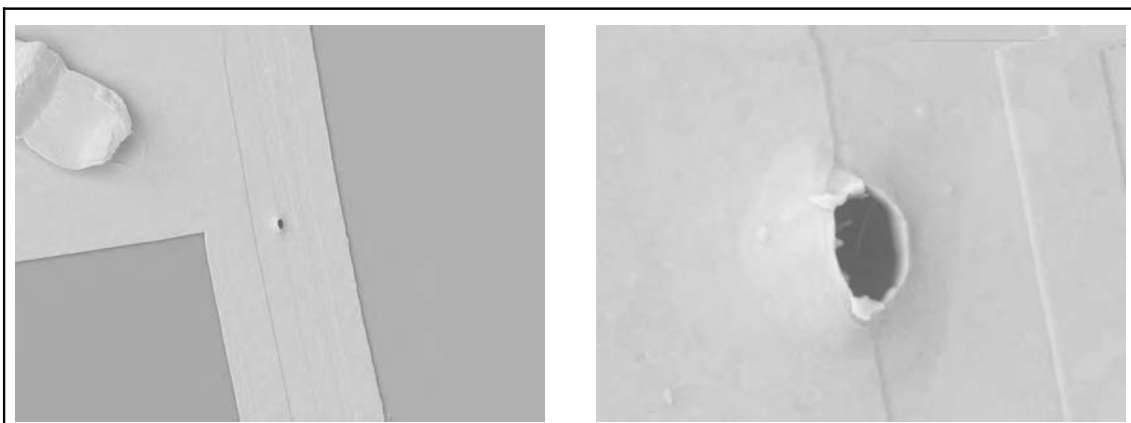


Figure 117: Damage in Guard Ring (Source: ESTEC)

Material failures were also found in the area near the edge of quadrant 1, as shown in figure 118, below;

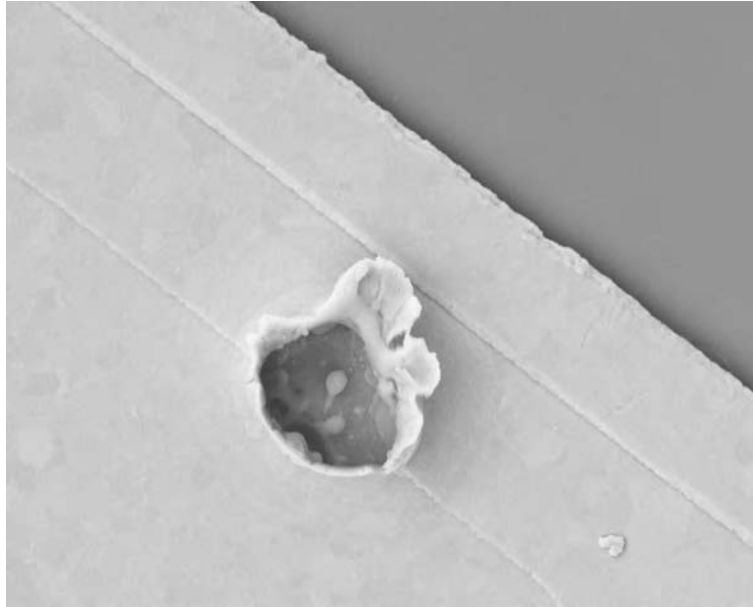


Figure 118: Damage in Quadrant 1 (Source: ESTEC)

To give an idea of the scales in figures 117 and 118, the defects were approximately 10 μm in diameter.

This damage was best explained by the mechanism of electro-static discharge, and as a result of these images been made available, a review was undertaken of all devices which were connected to the photodiodes during the integration procedures. As a result of the review, the grounding provision in the photodiode harness, the transimpedance amplifiers, and in the clean room at UGL were improved.

6.6.4 PD 202 Summary

- PD202 had failed electrical tests,
- The reverse voltage of quadrant 1 was significantly lower than the specification; 0.86 V, versus 20 V, while the forwards voltage was acceptable,
- Under an optical scan quadrant 1 showed no output while there was significant leakage between the remaining channels,
- After last being tested “good”, PD202 had been subject only to assembly onto the cassette holder before this failure was detected during test,
- Prior to the failure, there was no indication of any problem with PD202,
- ESD precautions, including wrist-strap checking were in place during handling of the photodiodes at all stages during the work carried out at Birmingham,
- Debris was found between the cassette and cassette holder,
- Under assembly loads onto uneven surfaces, the cassette distortion of 460 μm is possible,
- Initial, unaided, visual inspection did not detect any further epoxy in the holes in the cassette holder, however, an inspection done under magnification, considering epoxy and gapping provided further confidence,
- Excessive leakage was found on a device with a known cracked die, PD233,
- It was initially thought that the InGaAs die cracked during the assembly of the cassette onto the cassette holder,

- The SEM results obtained by ESTEC suggested that electro-static discharge was the failure mechanism,
- The 8 detectors which were subject to workmanship testing were electrically tested and passed the test,
- The grounding of all equipment connected to the photodiodes was reviewed and updated as required.

As no cracking was found during the visual inspections, even under magnification, and the SEM images provided by ESTEC were indicative of electrical damage, it was likely that the photodiode failure was electrically caused. As a result of this failure analysis, the following steps were taken;

- Cassettes were visually checked for debris prior to assembly onto the cassette holder,
- The test equipment was modified in order to reduce the possibility of stored charges causing damage to the photodiode.

6.7 PHOTODIODE MECHANICAL TESTING

In order to build confidence in the photodiodes prior to acceptance, it was decided to subject them to mechanical loads, similar to those specified in the spacecraft level requirements specification, the GDIR, [91], for ground transportation loads.

Initially, the plan was to carry out shock and vibration testing using a shaker facility, [99], but, owing to facility availability and the time limitations imposed by project schedule pressures, it

was agreed to carry out a reduced testing regime, subjecting the photodiodes to a number of shock loads.

The test fixture was fastened to a heavy aluminium plate at one end. Between the plate and the fixture was a thin shim, which allowed the test fixture to move and flex relative to the heavy plate. In order to measure the acceleration, a Brüel and Kjær model 4505 accelerometer was hard mounted to the test fixture. The charge output of the accelerometer was conditioned and amplified using a Brüel and Kjær model 2635 charge amplifier. The output from the charge amplifier was recorded using an Iotech Wavebook model 512 data acquisition system, sampling at 60 kHz.

Prior to fastening photodiodes to the test fixture, a number of test impacts were made, and the resulting shock measured using a roving accelerometer. The impact parameters, namely the height of the hammer drop, and the impacting material were thus determined. This also allowed the determination of the number of suitable photodiode locations on the test fixture.

The quadrant photodiodes were not connected, or “live” in any way during the test. Instead, the photodiodes were checked prior to the test with their current/voltage characteristics being measured and stored. This characterisation was repeated after the mechanical shocks, and the characteristics examined to check for changes.

Photodiodes and the accelerometer were fastened to the test fixture, The fixture was impacted 10 times in each direction. As the accelerometer was uniaxial, it was re-orientated prior to impacting from a new direction. Cross directional responses were not measured.

In turn each of the 26 photodiodes (10 from the proto-flight model bench, 10 from the FS bench, and 6 from the qualification program) were subjected to this test.

For each axis, a picture of the test set up is shown, as is one sample time history of the 10 taken. The test set up for X axis shock is as shown in figure 119, below.



Figure 119: X Axis Shock

A typical shock test acceleration time history is shown in figure 120, below.

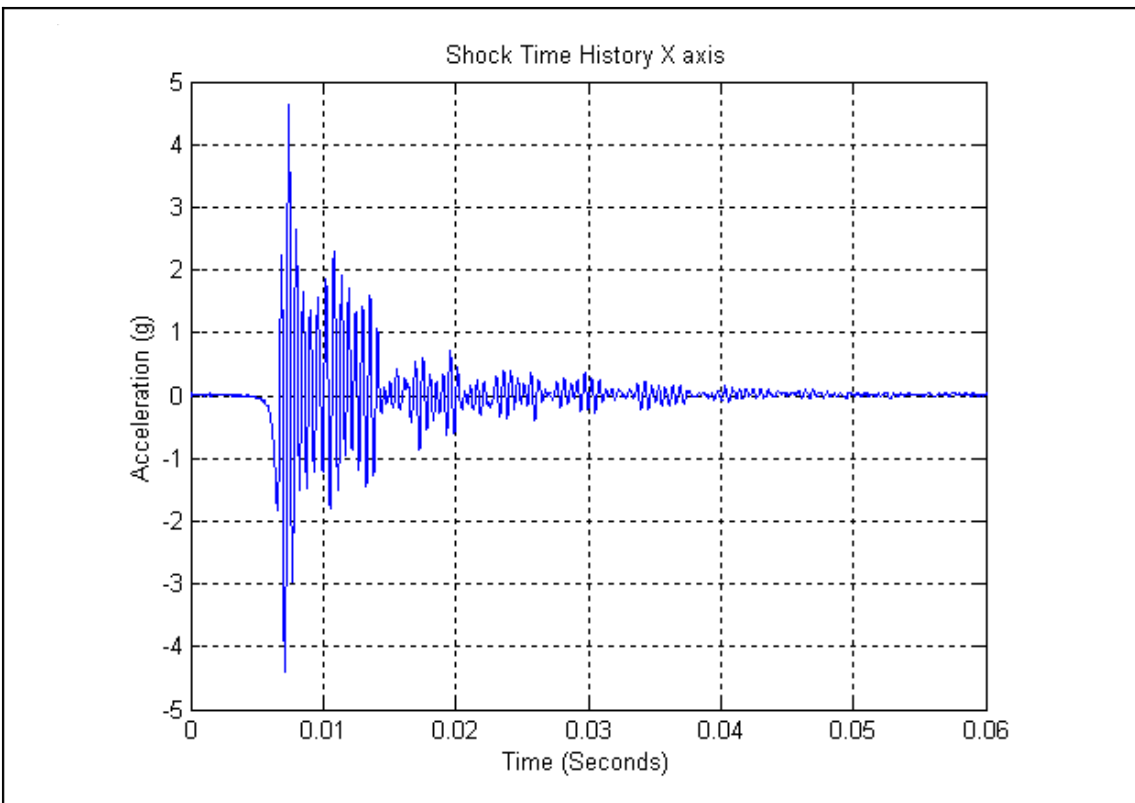


Figure 120: X Axis Shock Time History

The test set up for Y axis shock is shown in figure 121, below.



Figure 121: Y Axis Shock

A typical shock test acceleration time history is shown in figure 122, below.

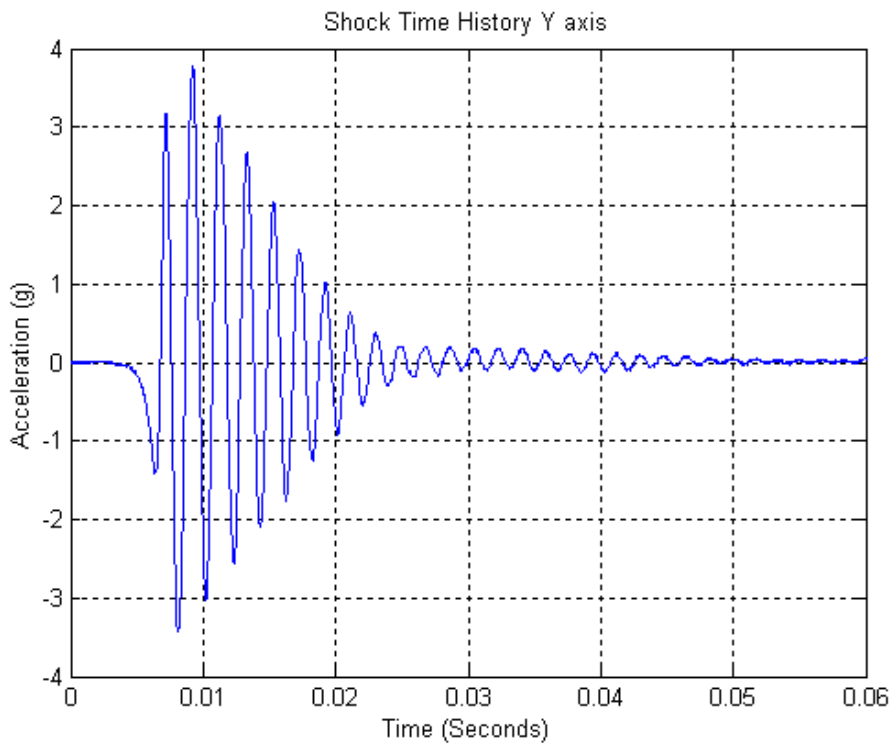


Figure 122: Y Axis Shock Time History

The test set up is as shown in figure 123, below.



Figure 123: Z Axis Shock

A typical shock test acceleration time history is shown in figure 124, below.

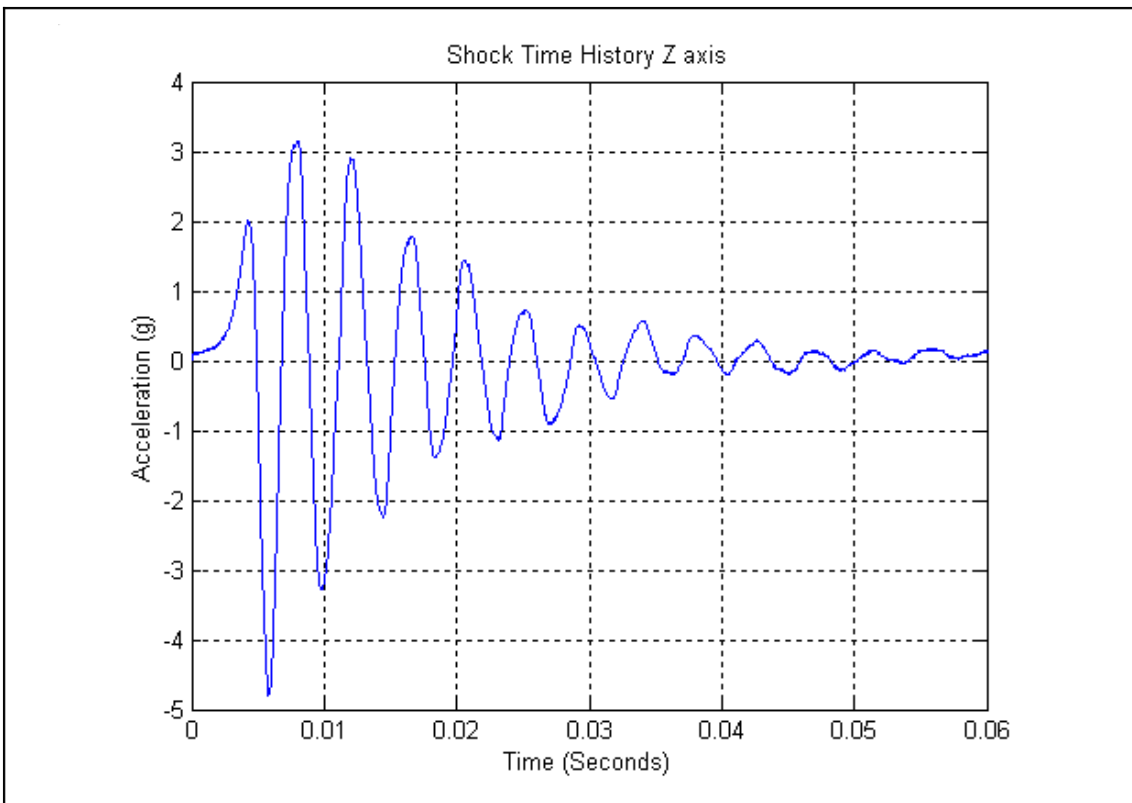
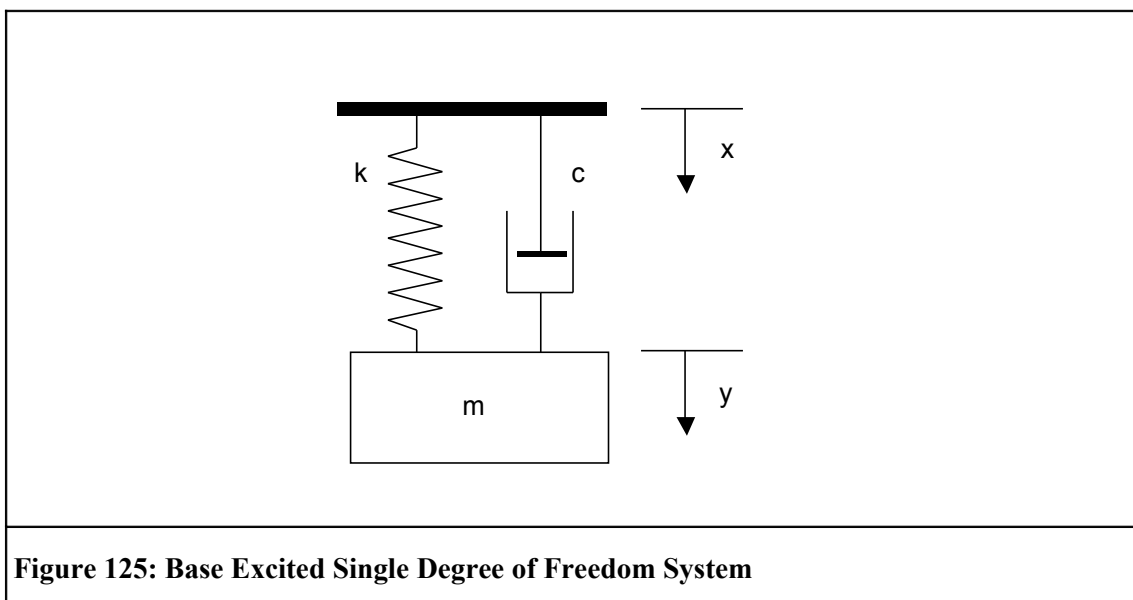


Figure 124: Z Axis Shock Time History

6.7.1 Shock Response Spectrum Analysis

As part of this thesis work, a Simulink model was written in order to post-process the test data. In order to estimate how the mechanical shock might affect different parts of the structure of the photodiode, the time history data was processed in order to produce a shock response spectrum (SRS).

Although the shock response spectrum is a function of frequency, it is not the same as a Fourier Transform of the time history data. Where the Fourier Transform represents the magnitude and phase of a signal as a function of frequency, the level of the SRS at any frequency, f_1 , is equal to an extreme peak value of the response of a base excited single degree of freedom system where the single degree of freedom system has a natural frequency of f_1 , and a specified damping ratio.. In this way, the SRS reduces many time histories into one real function of frequency, and unlike the Fourier Transform, there is no corresponding inversion process as the SRS discards many data. A base excited single degree of freedom system is shown in figure 125, below.



Where;

- x - Displacement of input / base (m)
- y - Displacement of mass (m)
- k - Spring Stiffness (N/m)
- c - Viscous Damping Coefficient (Ns/m)
- m - Mass (kg)
- ξ - Damping Ratio
- ω_n - Natural Frequency (rad/s)

Writing Newton's Second Law for the mass allows the difference between the output acceleration and the input acceleration to be written in equations 53, below;

$$m \frac{d^2 y}{dt^2} = c \left(\frac{dx}{dt} - \frac{dy}{dt} \right) + k(x - y)$$

dividing through by m

$$\frac{d^2 y}{dt^2} = \frac{c}{m} \left(\frac{dx}{dt} - \frac{dy}{dt} \right) + \frac{k}{m}(x - y)$$

Equations 53

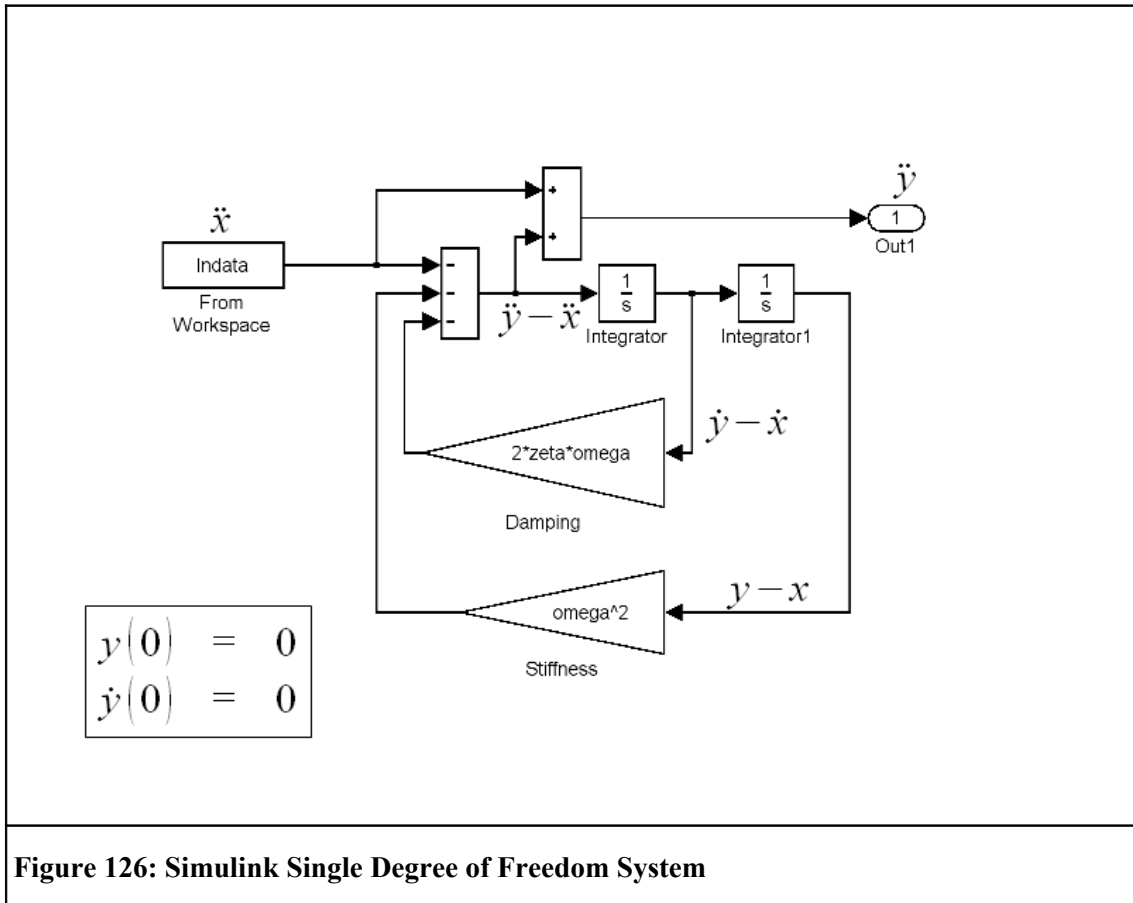
$$\frac{d^2 y}{dt^2} = 2\zeta \omega_n \left(\frac{dx}{dt} - \frac{dy}{dt} \right) + \omega_n^2(x - y)$$

Expressed in terms of the input and output accelerations, equations 53 may be re-written as;

$$\begin{aligned} \frac{d^2 y}{dt^2} &= \frac{d^2 x}{dt^2} + \left(\frac{d^2 y}{dt^2} - \frac{d^2 x}{dt^2} \right) \\ &= \frac{d^2 x}{dt^2} + \left(-2\zeta \omega_n \left(\frac{dy}{dt} - \frac{dx}{dt} \right) - \omega_n^2(y - x) - \frac{d^2 x}{dt^2} \right) \end{aligned}$$

Equations 54

In order to calculate the SRS, a single degree of freedom system was built using Simulink, the sub-model which implements the second of equations 54, and carries out a time stepping integration of the resulting ordinary differential equation is shown in figure 126, below.



Where, Indata represents the acceleration of the base, \ddot{x} , which was read in from the MATLAB workspace, and the output acceleration, \ddot{y} , was passed back to the workspace via the “Out1” block. The sub-model shown in figure 126, was called from a MATLAB script, the pseudo-code for which is given below;

Define damping ratio

Define frequency range

Read in input acceleration time history, e.g., figure 124

Loop in steps of frequency

define frequency, f_i , and store in a vector

set natural frequency of mass spring system to f_i

simulate response of mass spring system to input

acceleration using sub-model as per figure 126

extract maximum and minimum output acceleration values

and store in vectors

End loop

Plot SRS data against natural frequency

An example of a resulting shock response spectrum is shown in figure 127, below.

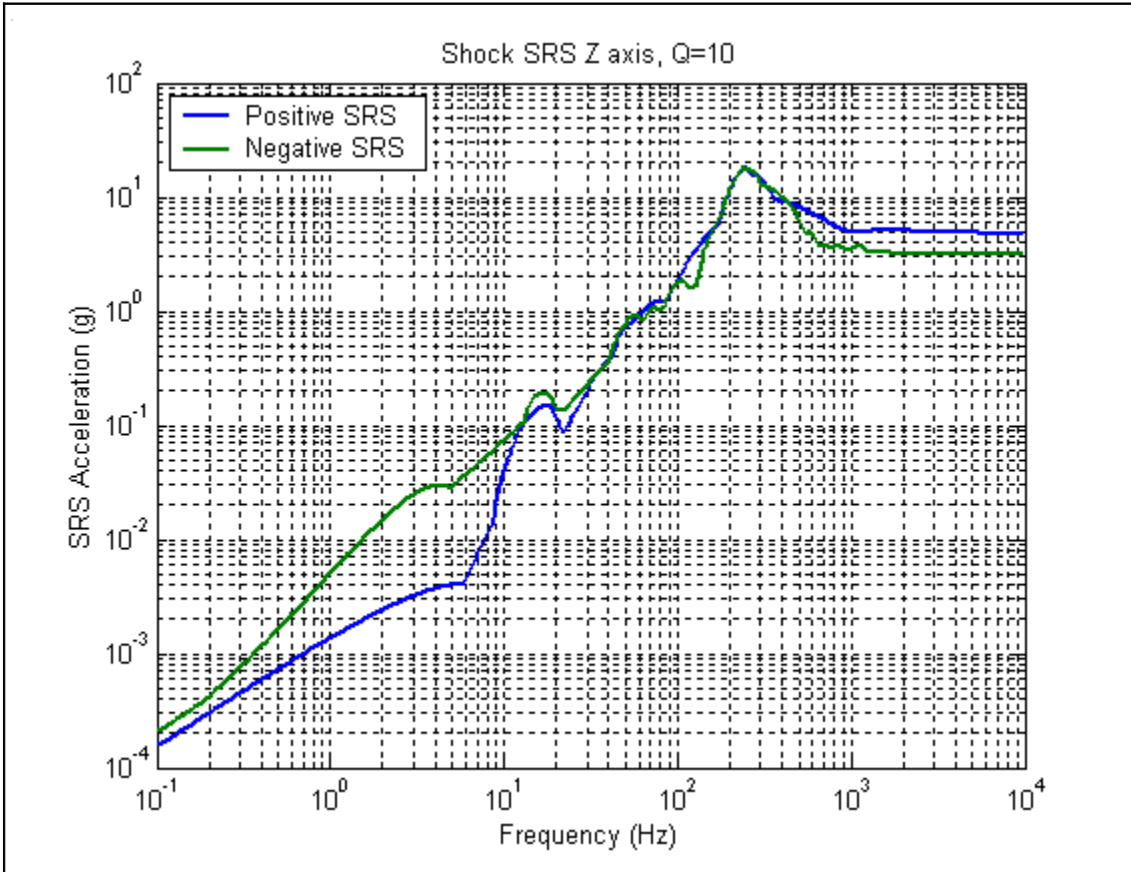


Figure 127: Shock Response Spectrum Plot, Z Axis

The shock response spectrum shows that only parts of the photodiode with a resonant frequency greater than approximately 100 Hz were effectively excited by these impacts. However, the photodiode cassettes as tested were both small rigid components, and hard mounted to the fixture plate. This test was successfully used to give the project confidence in the mechanical design of the photo-diode mounts.

6.7.2 Mechanical Testing Summary

All the photodiodes were electrically tested prior to mechanical testing, and passed electrical testing again after the mechanical shocks were administered. This test added further evidence to support the view that the photodiodes were mechanically strong.

6.8 PHOTODIODE INSTALLATION

6.8.1 Photodiode Installation

In order to meet the science requirements of the optical bench, the photodiodes were placed within the following positional tolerances;

- The required alignment of the centre of the quadrant photodiode and the beam was within a lateral tolerance of 50 μm for quadrant photodiodes, and 500 μm for single element photodiodes.
- The position of the photodiode along the axis of the beam was open tolerance, and may be chosen to maximise adjacent space, or to optimise cable routing.
- In order to minimise any thermal stresses on the optical bench, the clearance between photodiode and optical bench was checked and adjusted to be between 150 μm and 250 μm , with a maximum relative angle of 0.1 $^\circ$.
- For quadrant photodiodes, the “clock face” rotation of the elements was adjusted parallel/orthogonal to the optical bench surface within 0.5 $^\circ$.

In order to comply with these requirements, a positioning system was designed using a combination of bought in translation stages and in-house designed hardware. The photodiodes were placed using the equipment shown in figure 128, below.

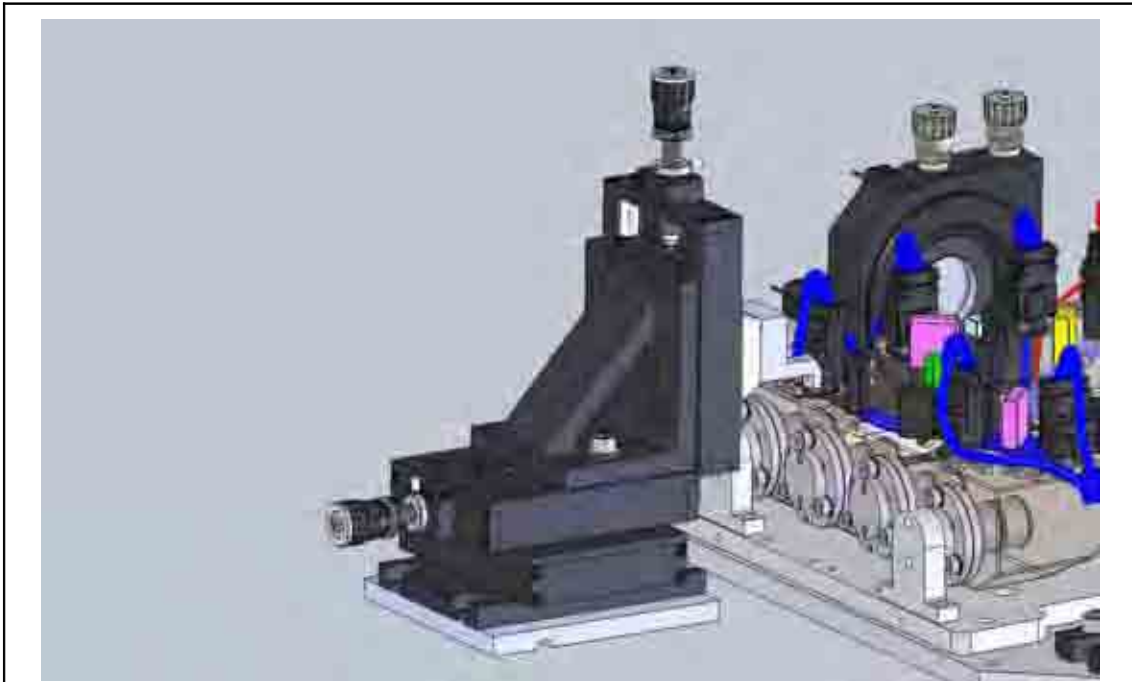


Figure 128: CAD Model of Photodiode Placement

The translation stages were supported using three ball ended screws in a Kelvin Clamp configuration. The three axes of the translation stages and the availability of adjustment in the height of the three ball ended screws gave adjustment in six degrees of freedom required to correctly position the photodiodes. In particular the angular adjustment was important in ensuring the base of the photodiode mount was adequately parallel to the optical bench upper surface.

The following constraints applied to the bonding sequence and procedure;

- While PD1A was bonded, the beam from PD1B was monitored by the calibrated quadrant photodiode to ensure correct test-mass mirror alignment. (or, vice versa, if PD1B were bonded first, PD1A would be monitored.
- While PD12A was bonded, the beam from PD12B was monitored by the calibrated quadrant photodiode to ensure correct test-mass mirror alignment. (or, vice versa, if PD12B were bonded first, PD12A would be monitored.
- While PD1A and PD1B were being bonded, the beam from the optical bench to test mass mirror 1 could not be obscured.
- While PD12A and PD12B were being bonded, the beams from the optical bench to both test mass mirrors could not be obscured.
- Owing to the necessary size of the photodiode positioning equipment, and the need to monitor other beam outputs during bonding, the number of photodiodes which could be placed down in any one session is limited.
- After placement, the EA9361 epoxy must cure for at least 36 hours before the clamps were removed.

During the bonding of a test non-flight photodiode onto a non-flight optical bench, the photodiode bonding procedure, [92], was derived, as shown in table 31, below.

<i>Procedure Step</i>	<i>Procedure</i>
1.	Take appropriate ESD precautions to BSEN61340-5-1-2007 at all times – the shorting plug is to be kept in place whenever possible.
2.	Remove photodiode from bagging and foil wrap. Ensure shorting plug is fitted.

<i>Procedure Step</i>	<i>Procedure</i>
3.	Note photodiode serial number and location. Check identification tag at connector end of harness.
4.	Perform basic electrical test on photodiode, and visually inspect the device.
5.	Temporarily place optical bench onto fixture plate and, using CMM obtain first estimate of optical bench co-ordinate system for coarse adjustment and confirmation of placer location. Configure placer to appropriate layout – end or side mounting of the photodiode, appropriate to the location on the bench and access restrictions.
6.	Fit photodiode to placer, engaging the dowel.
7.	Using the pre-saved CMM program, measure dimensional relationship between photodiode base and features on the placer end effector.
8.	Adjust the placer to give maximum clearance between photodiode and bench – typically, this will mean simply moving the Z stage to give maximum height.
9.	Place photodiode and placer on 3 ball ended screws adjacent to the bench – engage rear first and rock forwards. Stabilize the placer using hand pressure, as the offset load of the photodiode may allow uncontrolled movement of the photodiode and placer.
10.	With one person steadying the photodiode and placer assembly, the three ball ended screws shall be adjusted by another to give correct angular alignment – verified by CMM. Ensure the locknuts are correctly tightened.
11.	Release the clamps, and remove photodiode and placer from 3 ball ended screws adjacent to the bench – rock backwards, and dis-engage rear last. Stabilize the placer using hand pressure, as the offset load of the photodiode may allow uncontrolled movement of the photodiode and placer.
12.	Carry out the above steps for all photodiodes which are intended to be bonded in this session before continuing.
13.	Fit the Zerodur® optical bench in place on the CMM. Use a cleaned acetate sheet to protect the area underneath the photodiode to be placed until the bond is to be finalised.
14.	Place photodiode and placer on 3 ball ended screws adjacent to the bench – engage rear first and rock forwards. Stabilize the placer using hand pressure, as the offset load of the photodiode may allow uncontrolled movement of the photodiode and placer.
15.	Apply clamps to hold placer onto ball ended screws – tighten the clamps lightly in order to avoid causing any undue deformation.

<i>Procedure Step</i>	<i>Procedure</i>
16.	After checking that ESD wrist straps are securely connected, remove shorting plug. Connect transimpedance amplifier and computer alignment system. The photodiode is configured to use ROTATION ZERO on the alignment system. Switch on transimpedance amplifier.
17.	Using coarse adjustment, drive the photodiode towards being centred on the beam. When the photodiode becomes close to the correct alignment, or when assessing clearances visually becomes difficult, take frequent CMM confirmations to give an estimate of the clearance between photodiode and the bench surface.
18.	Centre photodiode onto beam within 10µm.
19.	If beam centre cannot be obtained with >200µm clearance; <ul style="list-style-type: none"> • switch off the transimpedance amplifier and disconnect the photodiode • Re-fit the shorting plug • Drive the placer to give maximum clearance between the photodiode and the optical bench • Remove the placer and photodiode from 3 ball ended screws • Adjust the vertical position of the cassette, using a square and granite surface, to maintain rotational alignment. • Place photodiode and placer on 3 ball ended screws adjacent to the bench. • Go back to step 11.
20.	Once the photodiode is adequately centred on the beam, perform a calibration by moving the photodiode a known amount and monitoring the 4 quadrant signals.
21.	Re-centre the photodiode back onto the beam, within 10µm.
22.	Fit a dial gauge under the vertical stage and zero it.
23.	Release the clamps, and remove photodiode and placer from 3 ball ended screws adjacent to the bench – rock backwards, and dis-engage rear last. Stabilize the placer using hand pressure, as the offset load of the photodiode may allow uncontrolled movement of the photodiode and placer.
24.	Move the vertical adjustment stage to the uppermost extent of its travel
25.	Check torque and lock all M2 fasteners – torquing and locking document to be filled in. Stake all fasteners with Scotch Weld 2216.
26.	Apply the epoxy to the underside of the photodiode mount as per S2-UGB-PR-3001.

<i>Procedure Step</i>	<i>Procedure</i>
27.	Place photodiode and placer on 3 ball ended screws adjacent to the bench – engage rear first and rock forwards. Stabilize the placer using hand pressure, as the offset load of the photodiode may allow uncontrolled movement of the photodiode and placer.
28.	Remove the acetate protective sheet. Drive the vertical stage downwards, initially using the coarse adjuster, onto the beam monitoring both QPD output and the dial gauge.
29.	With the beam re-centred on the photodiode, within 10µm, remove the dial gauge, check position with CMM, and leave the bond to cure. Switch off the transimpedance amplifier, disconnect the photodiode, and re-fit the shorting plug. Secure the wiring harness.
30.	After curing, (36 hours minimum) remove clamp and remove placer.
31.	Recheck position with CMM.
Table 31: Flight Photodiode Bonding Procedure	

The photodiodes were bonded onto optical bench serial number 3 in the clean room at UGL. The placement of photodiodes using the inline configuration of the positioning equipment is shown in figure 129, below.

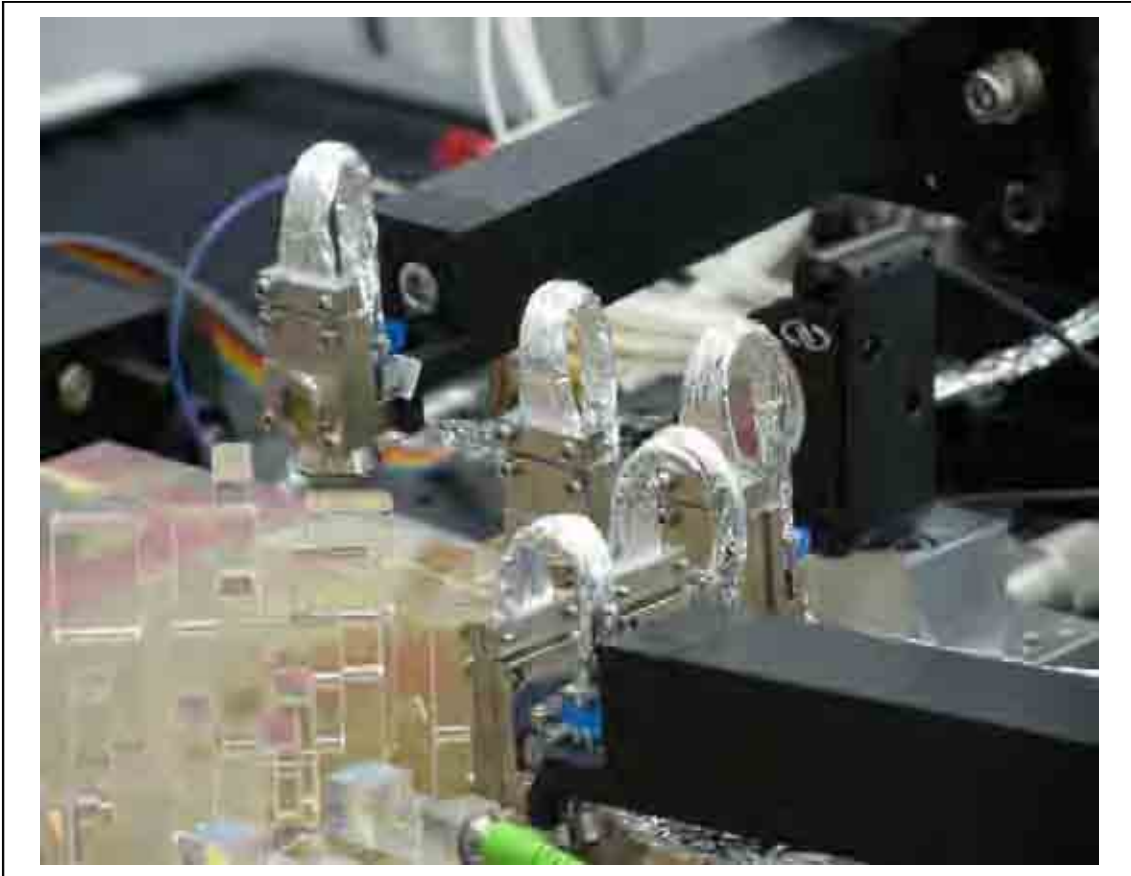


Figure 129: Photodiodes PDRB and PD12A Positioned In-line

In order to clear existing equipment, the positioner was used with a side arm attachment, as shown in figure 130, below.



Figure 130: Photodiode PDFB Positioned from Side

The quadrant photodiodes were positioned with the levels of accuracy defined in the optical bench requirements specification, [36], and recorded in the traveller document, [100] shown in table 32, below;

<i>Photodiode / Location</i>	<i>Lateral Error (μm)</i>			<i>Vertical Error (μm)</i>			<i>Total Error (μm) of mean beam error</i>
	Beam1	Beam 2	Mean	Beam1	Beam 2	Mean	
217 / PDRA	4.5	-4	0.25	6	5	5.5	5.5
238 / PD1B	0 *	-0.8	-0.8	0 *	4.2	4.2	4.3
213 / PDFA	-0.2	1.1	0.45	-3.3	-0.5	-1.9	3.8
206 / PDRB	-6.5	0.9	-2.8	8.7	-0.5	4.1	5.0
203 / PD12A	2.7	-0.8	0.95	3	4.2	3.6	3.7
219 / PDFB	2.3	2	2.15	11	12	11.5	11.7
221 / PD1A	0 *	-5.6	-5.6	0 *	14.5	14.5	15.5
208 / PD12B	0 *	-2.6	-2.6	0 *	-1.1	-1.1	2.8

Table 32: Flight Photodiode Positional Accuracy

In the cases marked with an asterisk, beam 1 was not available – therefore, the total error was derived using only beam 2 data.

Table 32 shows that photodiodes were positioned within 15.5 μm of the beam centre, while the tolerance in the requirement was 50 μm . This demonstrated that the design of the installation equipment, and the development of the photodiode bonding procedures were more than adequate for the task.

6.9 PHOTODIODE SUMMARY

The photodiodes were designed to overcome difficulties encountered using the previous design of photodiode as used on the engineering model optical bench.

The area of the bond between the photodiode and the optical bench warranted particular attention in order to ensure adequate mechanical stability, but, also to ensure that the stresses applied to the optical bench remained within tolerable limits. The photodiode was analysed using hand calculations and finite element analysis. The photodiode bond, and the photodiode as a whole were subjected to mechanical testing in order to verify the adequacy of the design.

The photodiodes were subject to an agreed agenda of electrical and optical testing before and after exposure to onerous thermal environments as part of the qualification plan which was negotiated and agreed with ESA.

After unexpected failures of devices, a failure analysis program was undertaken, centring attention onto photodiode PD202. This analysis indicated that the likely cause of failure was electrical stress. As a result of this work, the configuration of all equipment connecting to photodiodes was reviewed, and modifications made.

In order to check the photodiodes for adequacy of their response, and the uniformity of this response, a scanning test facility was designed, built, and operated. The test facility allowed the grading of the photodiodes in order of the uniformity and quality of their response.

Owing to a number of failures of the single element photodiode, the possibility of using quadrant photodiodes as single element photodiodes was raised, analysed, considered, and finally accepted by all parties. This approach is now being used during the re-procurement of photodiodes.

Equipment and procedures were designed and developed to allow the bonding of the photodiodes onto the optical bench in accurately known positions and orientations. The equipment was used to form a test bond, and the photodiode thus bonded was checked for position changes using a co-ordinate measuring machine. The installation equipment and procedures were used to bond a set of photodiodes onto optical bench serial number 02, with the largest position error being much smaller than the allowable tolerance.

7 THESIS SUMMARY

This thesis has presented a review of gravitational waves in only sufficient depth for the rationale which informs gravitational wave instrument mechanical design to become clear, i.e., to justify the need for very accurate positioning of the photodiodes, for minimising the thermal expansion of any component in the mechanical measurement chain, and for compliance with good space engineering practice, particularly with respect to vacuum compatibility and outgassing.

The potential sources of gravitational waves were reviewed, along with the corresponding instrument designs which are engineered to detect the waves. As an outcome from the consideration of noise sources, the desirability of space borne gravitational wave detectors was justified, and thus, the LISA mission was introduced. Owing to the extreme technological challenges raised by LISA, the need for LISA Pathfinder was introduced.

The LISA Pathfinder mission was described, and in particular, the charge management system, the phasemeter, the optical bench interferometer, and the photodiodes; all parts of the optical metrology system; were described.

I described my work in document preparation and control, and in the preparation and submission to the preliminary design review and the critical design review, my work in maintaining the schedule and in presenting material at oversight committee and progress meetings.

The thesis describes my work in the avoidance of fracture of the optical bench and of other brittle materials used in the interferometer's construction. I carried out detailed mechanical analysis, using both classical methods and finite element analysis whereby the stress levels and

deformations undergone by the optical bench were found. Particularly challenging and detailed finite element analysis was carried out where the thin layer of epoxy immediately surrounding an insert was modelled, allowing better understanding of inter-insert load transfer.

With the help of my supervisor, a rationale based upon Weibull statistics for applying a factor of safety to the stress levels borne by the optical bench was derived.

The optical bench inspection facility was designed jointly by myself and Dr. Andreas Freise; Andreas being responsible for the procurement of the translation stages and the digital camera. I built and commissioned the test facility, and I prepared a theoretical example of a birefringence measurement to provide some confidence in the interpretation of the fringe patterns observed.

I carried out two inspections of the optical bench;

- the first was a scanning operation followed by a numerical post-processing of the image data to reduce the data to a manageable amount for final visual image checking,
- the second was a detailed visual inspection of the volume of material surrounding the more highly loaded inserts.

Using sample pieces of Zerodur[®], a verification of the method was attempted, but, owing to an insufficient number of samples, and the limited load range of the test equipment, it was not possible to be definite.

Photodiodes and mounts were designed using titanium to avoid thermal expansion issues, and using a removable cassette design to enable the removal and replacement of a photodiode in-situ on the optical bench. For this, I designed a kinematic mount which was pre-tensioned by vertical bolts, thus allowing access even though the photodiodes were mounted very close to the side walls of the LCA structure.

I carried out careful design work on the bond between the photodiode and the optical bench, as I was concerned that loads from this component might be sufficient to cause fracture of the optical bench itself. I prepared hand calculations and finite element analysis, both to determine the most onerous loading condition, and then to inform the design to mitigate its effects. In conjunction with my supervisor and staff from UGL, I defined a mechanical test scheme for the photodiode mounts, and I carried this out, with the result that the mount and bond design were both fully acceptable.

Working with engineers from ESTEC, I negotiated and agreed a photodiode qualification plan which was followed by the photodiode supplier.

During the failure analysis of photodiode PD202, I chaired non-conformance review board telephone conferences, and I carried out supporting work, namely mechanical testing of photodiodes at cassette level.

I designed, built, commissioned and operated a photodiode response scanning facility. Using this facility enabled me, in collaboration with staff at UGL, to rank the photodiodes, and to enable the determination of the final installation location of each flight photodiode.

In order to maintain progress when it became clear that there were insufficient single element photodiodes to form a meaningful flight batch, I proposed the use of quadrant photodiodes as single element detectors. In collaboration with staff from Albert Einstein Institute and UGL, we determined that the approach would be adequate mechanically, electrically, and optically. The proposal was accepted for use on the project, and I designed the modified cassette holders with appropriate offsets to centre the beam on the centroid of a quadrant. This approach is now being used during the re-procurement of photodiodes, i.e., in the new procurement, there are no separate single element photodiodes, QPDs are used throughout.

I designed equipment, and helped to develop the procedures whereby photodiodes were bonded to the optical bench in accurately known positions and orientations. After validating the equipment and procedures on a test photodiode which was monitored for position changes using a program of CMM measurements. David Smith and I used the installation equipment and procedures to successfully bond a set of photodiodes onto optical bench serial number 02, with the largest position error being 15 μm as opposed to the requirement which was 50 μm .

8 INDEX OF TABLES

Table 1: Photodiode Allocation.....	28
Table 2: Zerodur® Mechanical Properties.....	53
Table 3: Initial Analysis Results.....	62
Table 4: Stress Levels in Detailed Insert Model.....	69
Table 5: Insert Stiffness.....	71
Table 6: Stress and Deflection Summary.....	82
Table 7: Optical Bench Interferometer Insert Loading.....	85
Table 8: Enveloped Stress Data.....	89
Table 9: Misaligned Insert Stress Data.....	89
Table 10: Crack Geometries.....	97
Table 11: Launch Vehicle Success Statistics (Source [70], including failures to attain correct orbit).....	102
Table 12: Image Processing.....	128
Table 13: Optical Bench Post Inspection I Release.....	130
Table 14: Optical Bench Interferometer Number 03 – Defect Summary.....	135
Table 15: Initial Zerodur® Fracture Test Results.....	138
Table 16: Zerodur® Fracture Test Results.....	144
Table 17: Photodiode Mechanical Parts Thermal Data.....	156
Table 18: Photodiode Bond Stress Summary.....	160

Table 19: Photodiode Bond Test Results.....	165
Table 20: Shock Test Levels.....	166
Table 21: Random Test Levels.....	167
Table 22: Sine Test Levels.....	168
Table 23: Photodiode Allocation.....	171
Table 24: Photodiode Allocation.....	175
Table 25: Photodiode Component Mass.....	177
Table 26: Photodiode 205 Reference Data.....	190
Table 27: Photodiode Scan Data Summary.....	196
Table 28: Photodiode Grouping.....	197
Table 29: Photodiode Quick Test Procedure.....	205
Table 30: Photodiode 202 Test and Integration History.....	209
Table 31: Flight Photodiode Bonding Procedure.....	234
Table 32: Flight Photodiode Positional Accuracy.....	237
Table 33: Photodiode 202 Reference Data.....	287
Table 34: Photodiode 203 Reference Data.....	289
Table 35: Photodiode 205 Reference Data.....	291
Table 36: Photodiode 206 Reference Data.....	293
Table 37: Photodiode 208 Reference Data.....	295
Table 38: Photodiode 209 Reference Data.....	297
Table 39: Photodiode 211 Reference Data.....	299

Table 40: Photodiode 213 Reference Data.....	301
Table 41: Photodiode 217 Reference Data.....	303
Table 42: Photodiode 218 Reference Data.....	305
Table 43: Photodiode 219 Reference Data.....	307
Table 44: Photodiode 221 Reference Data.....	309
Table 45: Photodiode 222 Reference Data.....	311
Table 46: Photodiode 232 Reference Data.....	313
Table 47: Photodiode 236 Reference Data.....	316
Table 48: Photodiode 238 Reference Data.....	318
Table 49: Photodiode 239 Reference Data.....	320
Table 50: Photodiode 241 Reference Data.....	322
Table 51: Photodiode 244 Reference Data.....	325
Table 52: Photodiode 245 Reference Data.....	327
Table 53: Photodiode 246 Reference Data.....	329

9 INDEX OF FIGURES

Figure 1: “Elevator” Initial Conditions.....	3
Figure 2: Uniform and Tidal Gravitational Forces.....	4
Figure 3: Gravitational Wave Motion (Source: [7]).....	6
Figure 4: Gravitational Wave Motion and Interferometer Topology (Source: [22]).....	16
Figure 5: LISA Orbit Schematic (Source: ESA).....	20
Figure 6: Gravitational Wave Sensitivity [26].....	22
Figure 7: Optical Metrology System (OMS) Schematic, (Source: [32]).....	26
Figure 8: Optical Bench Interferometer Optical Layout, Source[36]).....	31
Figure 9: Optical Bench CAD Rendering (Source: [48]).....	51
Figure 10: Photodiode Bond Detail.....	52
Figure 11: Section Through Optical Bench Showing Insert and Interface.....	55
Figure 12: Simply Supported Beam	56
Figure 13: Built in Beam	56
Figure 14: Optical Bench Principal Stress; +256g Z Direction.....	59
Figure 15: Optical Bench Principal Stress; -256g Z Direction.....	60
Figure 16: Representation of Optical Bench Deflection and Photodiode Bond Peel.....	62
Figure 17: LCA, showing optical bench, sideslabs and support struts [54].....	64
Figure 18: Insert Detailed Solid Model Mesh.....	65

Figure 19: Zerodur® Insert Bore – 0.5 mm Radius – 1320 N Axial Load.....	66
Figure 20: Zerodur® Insert Bore - 0.5 mm Radius - 1320 N Axial Load - Detail.....	66
Figure 21: Insert Model – Zerodur® Insert Bore – 3.0 mm Radius – 1320 N Lateral Load.....	67
Figure 22: Insert Model – Zerodur® Insert Bore – 3.0 mm Radius – 1320 N Lateral Load – Insert Suppressed.....	68
Figure 23: 0.5 mm Radius, 30 °C Thermal Load.....	69
Figure 24: Maximum Principal Stress and Deflection –256 g Z Direction Body Load.....	73
Figure 25: Maximum Principal Stress and Deflection –256 g Z Direction Body Load.....	74
Figure 26: Maximum Principal Stress and Deflection +256 g Z Direction Body Load.....	75
Figure 27: Maximum Principal Stress and Deflection +256 g Z Direction Body Load.....	76
Figure 28: Maximum Principal Stress and Deflection –256 g Z Direction Body Load.....	78
Figure 29: Maximum Principal Stress and Deflection –256 g Z Direction Body Load.....	79
Figure 30: Maximum Principal Stress and Deflection +256 g Z Direction Body Load.....	80
Figure 31: Maximum Principal Stress and Deflection +256 g Z Direction Body Load.....	81
Figure 32: Insert Detailed Solid Model Mesh.....	83
Figure 33: Epoxy Detailed Solid Model Mesh.....	84
Figure 34: Assembled Insert, Epoxy and Zerodur® Detailed Solid ¼ Model Mesh.....	84
Figure 35: Optical Bench Model Mesh.....	86
Figure 36: Optical Bench Model Mesh Detail.....	86
Figure 37: Example Model Run Results (+FX -FY +FZ -MX -MY -MZ).....	87
Figure 38: Enveloped Stress Results for Corner Insert.....	88

Figure 39: Enveloped Principal Stress Results for Middle Insert.....	88
Figure 40: Vickers Indentation of Zerodur® (RH Image Zoomed).....	91
Figure 41: Zerodur® Statistical Fracture Mechanics Analysis (5,000 Trials).....	95
Figure 42: Zerodur® Statistical Fracture Mechanics Analysis (10,000,000 Trials).....	96
Figure 43: Edge Crack at Thin Section Between Insert Bore and Baseplate Upper Surface.....	98
Figure 44: Edge Crack Between Insert Bore and Baseplate Upper Surface – Simplified Geometry.....	99
Figure 45: Unfactored Fracture Mechanics Results.....	101
Figure 46: Factored Fracture Mechanics Results.....	104
Figure 47: Crossed Polariser Inspection Apparatus Outline (Source: [80]).....	107
Figure 48: General 2D Stress Field.....	108
Figure 49: Mohr's Circle Construction.....	110
Figure 50: Stress Analysis of a Cracked Plate	114
Figure 51: Isochromatic Fringe Pattern in Cracked Plate	115
Figure 52: Isochromatic Fringe Pattern in Cracked Plate, (Source: [80]).....	116
Figure 53: Inspection Apparatus.....	117
Figure 54: Inspection Rig	118
Figure 55: Damage on Lower Surface of Optical Bench (Serial No 3).....	120
Figure 56: Optical Bench Rotation Fixture.....	131
Figure 57: Insert Anomaly.....	132

Figure 58: Scratch in Optical Bench Surface Adjacent to Insert 3 (False colour used to enhance image).....	133
Figure 59: 60µm Defect in Optical Bench.....	134
Figure 60: Optical Bench Inspection Image.....	134
Figure 61: Tensile Testing Fixture.....	137
Figure 62: Failed Sample, Showing Cracking Along Interface.....	139
Figure 63: Potential Fixture Inadequacy – Exaggerated Deflection in Bending.....	139
Figure 64: Zerodur® Sample Test Fixture Model Detail.....	140
Figure 65: Stress Concentration Results.....	143
Figure 66: Re-designed Tensile Testing Fixture.....	144
Figure 67: Inspection Data – 0.1 mm Defect in Sample LC01.....	145
Figure 68: End View of 0.6mm Hole in Fused Silica with ~0.25mm Crack [False colour to enhance image].....	147
Figure 69: Single Element Ø3mm InGaAs die (Left), and Quadrant Ø5mm InGaAs die (Right)	149
Figure 70: Exploded View of Proto-Flight Model Photodiode Mount Design.....	151
Figure 71: Assembled Proto-Flight Model Photodiode.....	152
Figure 72: OMS Temperature Limits [32].....	155
Figure 73: Photodiode Bond Thermal Stress.....	157
Figure 74: Photodiode Bond Thermal Stress - Detail of Outer Bond Radius.....	158
Figure 75: Through Thickness Averaging.....	159

Figure 76: Thermal Stress with respect to varying Bond Thickness.....	160
Figure 77: Proposed PD Mount Geometry.....	161
Figure 78: Thermal Stress of Proposed Geometry.....	162
Figure 79: Photodiode Bond Test Fixture Design (Tensile - Left, Shear - Right).....	164
Figure 80: Test Item and Z Axis Test Configuration.....	168
Figure 81: X Axis Test Configuration (Left) and Y Axis Configuration (Right).....	169
Figure 82: Optical Bench Schematic Layout, Source: [36]).....	170
Figure 83: Single Element Ø3mm InGaAs die (Left), and Quadrant Ø5mm InGaAs die (Right)	172
Figure 84: Electrically Assembled Quadrant Photodiode.....	172
Figure 85: QPD Die Specification.....	173
Figure 86: Exploded View of Quadrant	174
Figure 87: Photodiode Mount Side View and Salient Dimensions (mm).....	177
Figure 88: Titanium Harness Tie Down (S2-UGB-DRW-3056).....	179
Figure 89: Titanium Harness Tie Down.....	180
Figure 90: Photodiode Qualification Plan.....	182
Figure 91: Laser Enclosure (25mm tapped hole pitch in bench for scale).....	184
Figure 92: Laser Beam Profiling Camera.....	185
Figure 93: Lens System Simulation – all lenses convex with focal length of 100 mm.....	186
Figure 94: Beam Profile.....	187
Figure 95: Transimpedance Schematic.....	188

Figure 96: Scanning Apparatus.....	189
Figure 97: Photodiode 205 Response (QPD is Ø5mm).....	190
Figure 98: Photodiode 205 Q1 Contour.....	191
Figure 99: Photodiode 205 Q2 Contour.....	191
Figure 100: Photodiode 205 Q3 Contour.....	191
Figure 101: Photodiode 205 Q4 Contour.....	192
Figure 102: Quadrant Photodiode Electrical Schematic.....	198
Figure 103: Single Element Photodiode Electrical Schematic.....	199
Figure 104: Beam centred on QPD centre.....	200
Figure 105: Beam Centred on Two Elements of Laterally Displaced QPD.....	201
Figure 106: Beam Centred on One Segment of QPD.....	202
Figure 107: Basic Electrical Test Circuit.....	204
Figure 108: PD202 Prior to cover assembly at UBI.....	206
Figure 109: Photodiode 202 Response.....	210
Figure 110: Photodiode 202 Q1 Contours.....	210
Figure 111: Photodiode 202 Q2 Contours.....	211
Figure 112: Photodiode 202 Q3 Contours.....	211
Figure 113: Photodiode 202 Q4 Contours.....	212
Figure 114: Debris Found Between Cassette and Cassette Holder.....	212
Figure 115: Cassette Drawing.....	213
Figure 116: PD 233 Q1 Response.....	214

Figure 117: Damage in Guard Ring (Source: ESTEC).....	216
Figure 118: Damage in Quadrant 1 (Source: ESTEC).....	217
Figure 119: X Axis Shock.....	221
Figure 120: X Axis Shock Time History.....	221
Figure 121: Y Axis Shock.....	222
Figure 122: Y Axis Shock Time History.....	222
Figure 123: Z Axis Shock.....	223
Figure 124: Z Axis Shock Time History.....	223
Figure 125: Base Excited Single Degree of Freedom System.....	224
Figure 126: Simulink Single Degree of Freedom System.....	226
Figure 127: Shock Response Spectrum Plot, Z Axis.....	228
Figure 128: CAD Model of Photodiode Placement.....	230
Figure 129: Photodiodes PDRB and PD12A Positioned In-line.....	235
Figure 130: Photodiode PDFB Positioned from Side.....	236
Figure 131: 40 μm defect, 3mm away from insert edge.....	268
Figure 132: 45 μm defect, in bulk material.....	268
Figure 133: 60 μm defect, in bulk material.....	269
Figure 134: 65 μm defect, 3.5mm away from insert edge.....	269
Figure 135: 65 μm defect, < 1mm away from insert edge.....	270
Figure 136: 130 μm defect, in bulk material.....	270
Figure 137: Scratch on lower edge of optical bench.....	271

Figure 138: Fibre Injector (Source: UGL).....	272
Figure 139: An acceptable beam profile (Source: UGL).....	273
Figure 140: An unacceptable beam profile (Source: UGL).....	273
Figure 141: Microscope optical image showing damaged fibre (Source: UGL).....	274
Figure 142: Scanning Electron Microscope Backscatter image of the fibre's fracture surface (Source: ESTEC).....	275
Figure 143: Detail image of the possible fracture initiation site (Source: ESTEC).....	276
Figure 144: Extensive cracking after torsional stressing of a fibre sample (Source: UGL).....	277
Figure 145: Linear Superposition of solutions.....	280
Figure 146: Axial Stress Distribution.....	280
Figure 147: Axial Stress Distribution on fibre surface.....	281
Figure 148: Photodiode 202 Response.....	286
Figure 149: Photodiode 202 Q1, Q2, Q3, and Q4 Contours.....	287
Figure 150: Photodiode 203 Response.....	288
Figure 151: Photodiode 203 Q1, Q2, Q3, and Q4 Contours.....	289
Figure 152: Photodiode 205 Response.....	290
Figure 153: Photodiode 205 Q1, Q2, Q3, and Q4 Contours.....	291
Figure 154: Photodiode 206 Response.....	292
Figure 155: Photodiode 206 Q1, Q2, Q3, and Q4 Contours.....	293
Figure 156: Photodiode 208 Response.....	294
Figure 157: Photodiode 208 Q1, Q2, Q3, and Q4 Contours.....	295

Figure 158: Photodiode 209 Response.....	296
Figure 159: Photodiode 209 Q1, Q2, Q3, and Q4 Contours.....	297
Figure 160: Photodiode 211 Response.....	298
Figure 161: Photodiode 211 Q1, Q2, Q3, and Q4 Contours.....	299
Figure 162: Photodiode 213 Response.....	300
Figure 163: Photodiode 213 Q1, Q2, Q3, and Q4 Contours.....	301
Figure 164: Photodiode 217 Response.....	302
Figure 165: Photodiode 217 Q1, Q2, Q3, and Q4 Contours.....	303
Figure 166: Photodiode 218 Response.....	304
Figure 167: Photodiode 218 Q1, Q2, Q3, and Q4 Contours.....	305
Figure 168: Photodiode 219 Response.....	306
Figure 169: Photodiode 219 Q1, Q2, Q3, and Q4 Contours.....	307
Figure 170: Photodiode 221 Response.....	308
Figure 171: Photodiode 221 Q1, Q2, Q3, and Q4 Contours.....	309
Figure 172: Photodiode 222 Response.....	310
Figure 173: Photodiode 222 Q1, Q2, Q3, and Q4 Contours.....	311
Figure 174: Photodiode 232 Response.....	312
Figure 175: Photodiode 232 Q1, Q2, Q3, and Q4 Contours.....	313
Figure 176: Photodiode 236 Response.....	315
Figure 177: Photodiode 236 Q1, Q2, Q3, and Q4 Contours.....	316
Figure 178: Photodiode 238 Response.....	317

Figure 179: Photodiode 238 Q1, Q2, Q3, and Q4 Contours.....	318
Figure 180: Photodiode 239 Response.....	319
Figure 181: Photodiode 239 Q1, Q2, Q3, and Q4 Contours.....	320
Figure 182: Photodiode 241 Response.....	321
Figure 183: Photodiode 241 Q1, Q2, Q3, and Q4 Contours.....	322
Figure 184: Photodiode 244 Response.....	324
Figure 185: Photodiode 244 Q1, Q2, Q3, and Q4 Contours.....	325
Figure 186: Photodiode 245 Response.....	326
Figure 187: Photodiode 245 Q1, Q2, Q3, and Q4 Contours.....	327
Figure 188: Photodiode 246 Response.....	328
Figure 189: Photodiode 246 Q1, Q2, Q3, and Q4 Contours.....	329

10 REFERENCES

1. I. Newton, The Principia, Prometheus Books, First American (Chittenden 1846) Edition, 1995
2. Kaye and Laby (NPL), Kaye and Laby Online, Last accessed from URL:
http://www.kayelaby.npl.co.uk/general_physics/2_7/2_7_2.html
3. S. Carroll, Spacetime and Geometry: An Introduction to General Relativity, Addison-Wesley, First Edition, 2004
4. I.R. Kenyon, General Relativity, Oxford, First Edition, 1990
5. B. Schutz, Gravity from the Ground Up, Cambridge University Press, First Edition, 2003
6. G Gamow, Gravity, Dover, 1962 Edition, 2002
7. L. Ju, D. G. Blair, C. Zhao, Detection of gravitational waves, Rep. Prog. Phys., Volume 63, Pages 1317 - 1427, 2000
8. R. d'Inverno, Introducing Einstein's Relativity, Oxford University Press, First Edition, 1992
9. L. Cremer, M. Heckl, E.E. Ungar, Structure-Borne Sound, Springer-Verlag, Second Edition, 1988
10. P.M. Morse, K.U. Ingard, Theoretical Acoustics, Princeton University Press, First Edition, 1968
11. J.R. Reitz, F.J. Milford, R.W. Christy, Foundations of Electromagnetic Theory, Addison Wesley, Fourth Edition, 1992
12. P.R. Saulson, Fundamentals of Interferometric Gravitational Wave Detectors, World Scientific, First Edition, 1994

13. P.C.W. Davis, *The Search for Gravity Waves*, Cambridge University Press, First Edition, 1980
14. R.V. Southwell, *Theory of Elasticity*, Oxford University Press, First Edition, 1936
15. R. A. Hulse, J. H. Taylor, Discovery of a pulsar in a binary system, *ApJ*, Volume 195, Pages L51 - L53, 1975
16. J.H. Taylor, R.A. Hulse, L.A. Fowler, G.E. Gullahorn, J.M. Rankin, Further observations of the binary pulsar PSR 1913+16, *ApJ*, Volume 206, Pages L53 - L58, 1976
17. J.H. Taylor, J.M. Weisberg, A new Test of General Relativity. Gravitational Radiation and the binary pulsar PSR 1913+16, *ApJ*, Volume 253, Pages 908 - 920, 1982
18. J.H. Taylor, J.M. Weisberg, Further experimental test of relativistic gravity using the binary pulsar PSR 1913+16, *ApJ*, Volume 345, Pages 434 - 450, 1989
19. C. Cutler, K.S. Thorne et al, An Overview of Gravitational Wave Sources (Submitted - 30 April 2002, Last Accessed - 9 April 2011), Last accessed from URL: <http://arxiv.org/abs/gr-qc/0204090>
20. N.A. Robertson, *Laser Interferometric Gravitational Wave Detectors*, *Classical and Quantum Gravity*, Volume 20, Pages R19 - R40, 2000
21. J. Weber, *Detection and Generation of Gravitational Waves*, *Phys. Rev.*, Volume 117, Pages 306 - 313, 1960
22. K. McKenzie, Thesis: Experimental Demonstration of a Gravitational Wave Detector Configuration Below the Shot Noise Limit, Australian National University, 2002
23. F. K. Richtmyer and E.H. Kennard, *Introduction to Modern Physics*, McGraw-Hill, Fourth Edition, 1947

24. J. Shamir, Optical Systems and Processes, SPIE Optical Engineering Press, First Edition, 1999
25. ESA, LISA Mission Homepage, Last accessed from URL: <http://sci.esa.int/science-e/www/area/index.cfm>
26. P. Bender et al (LISA Study Team), Laser Interferometer Space Antenna for the detection and observation of gravitational waves: A Cornerstone Project in ESA's long term space science programme "Horizon 2000 Plus", Pre-Phase A Report, Document Number: MPQ-208, and updated MPQ-233, 1995 and updated July 1998
27. M. Armano et al., LISA Pathfinder: the experiment and the route to LISA, Classical and Quantum Gravity, Volume 26, Pages 1 - 18, 2009
28. S. Anza et al., The LTP experiment on the LISA Pathfinder mission, Classical and Quantum Gravity, Volume 22, Pages S125 - S138, 2005
29. D. Bortoluzzi, C.D. Hoyle, S. Vitale, G. Heinzel, K. Danzmann,, Science Requirements and Top-level Architecture Definition for the Lisa Test-flight Package (LTP) on Board LISA Path Finder (SMART-2), Document Number: LTPA-UTN-ScRD-Iss002-Rev1, 2004
30. LISA Pathfinder Science Working Team, LISA Pathfinder: Einstein's Geodesic Explorer (The Science Case for LISA Pathfinder), Document Number: ESA-SCI(2007)1, 2007
31. D.N.A. Shaul, H.M. Araujo, G.K. Rochester, M. Schulte, T.J. Sumner, C. Trenkel, P. Wass, Charge Management for LISA and LISA Pathfinder, International Journal of Modern Physics D, Volume 17, Pages 993 - 1003, 2008
32. Markus Bode, OMS Requirements Specification, Document Number: S2-ASD-RS-3010, 7/12/2007

33. ASD LTP Team, LTP System Requirements Specification, Document Number: S2-ASD-RS-3001, 23/02/2006
34. D. Robertson, OBI FMECA, Document Number: S2-UGL-DDD-3008, 2005
35. EJ Elliffe, J Bogenstahl, A Deshpande, J Hough, C Killow, S Reid, D Robertson, S Rowan, H Ward, and G Cagnoli, Hydroxide-catalysis bonding for stable optical systems for space, Classical and Quantum Gravity, Volume 22, Pages S257 - S267, 26th April 2005
36. D Robertson, OBI Requirement Specification, Document Number: S2-UGL-RS-3001, 5th July 2007
37. S.T. Smith, D.G. Chetwynd, Foundations of Ultraprecision Mechanism Design, Taylor & Francis, First Edition, 1992
38. G. F. Franklin, J. D. Powell, A. Emami-Naeini, Feedback Control of Dynamic Systems, Addison-Wesley, Third Edition, 1994
39. A.M. Cruise, J.A. Bowles, T.J. Patrick, C.V. Goodall, Principles of Space Instrument Design, Cambridge University Press, First Edition, 1998
40. SM-2 Team, Project References, Document Number: S2-EST-PR-1001, 23 September 2004
41. ESA, Project Reporting Integrated System for Management and Administration, Last accessed from URL: <https://prisma.esa.int/admin/logon.jsp>
42. H.U. Maier, PA Requirements for LTP Suppliers, Document Number: S2-ASD-RS-3006, 12 August 2004
43. J.E. Shigley, Mechanical Engineering Design, McGraw-Hill, First Metric Edition, 1986
44. Schott, Design Strength of Optical Glass and Zerodur, Document Number: TIE 33, 2004
45. D.S. Steinberg, Vibration Analysis for Electronic Equipment, Wiley, Second Edition, 1988

46. R.T. Fenner, Finite Element Methods for Engineers, Imperial College Press, First Edition, 1996
47. O.C. Zienkiewicz, R.L. Taylor, The Finite Element Method for Solid and Structural Mechanics, Elsevier, Sixth Edition, 2005
48. M. Perreux-Lloyd, OBI Assembly Drawing, Document Number: S2-UGL-DRW-3013, 2005
49. G. Dixon, Photo-Diode Mount to Zerodur Bond Design, Document Number: S2-UGB-TN-3003, 2006
50. G. Dixon, Optical Bench - Mechanical Modelling, Document Number: S2-UGB-RP-3002, 31/10/2005
51. P.P. Benham, R.J. Crawford, Mechanics of Engineering Materials, Longman, First Edition, 1987
52. R.J. Roark, W.C. Young, Formulas for Stress and Strain, McGraw-Hill, Fifth (International) Edition, 1976
53. MSC Software, MSC Nastran for Windows, MSC, Edition, 2002
54. K. Eckert, LISA Technology Package Progress Meeting #4, Document Number: N/A, 2006
55. I Zeid, CAD / CAM, McGraw-Hill, International Edition, 1991
56. B. Lawn, Fracture of Brittle Solids, Cambridge University Press, Second Edition, 1993
57. R.W. Davidge, Mechanical Behaviour of Ceramics, Cambridge, First Edition, 1979
58. D.M. Miannay, Fracture Mechanics, Springer, First Edition, 1998
59. M.F. Ashby, D.R.H. Jones, Engineering Materials, Pergamon, First Edition, 1980

60. D. Broek, The Practical Use of Fracture Mechanics, Kluwer Academic Publishers, First Edition, 1989
61. G. Pluvinage, Fracture and Fatigue Emanating from Stress Concentrators, Kluwer, First Edition, 2003
62. G.W. McLellan, E.B. Shand, Glass Engineering Handbook, McGraw-Hill, Third Revised Edition, 1985
63. A. Knight, Basics of MATLAB and Beyond, Chapman and Hall, First Edition, 1999
64. A. Biran, M. Breiner, MATLAB 5 for Engineers, Prentice Hall, Second Edition, 1999
65. N.P. Buslenko, D.I. Golenko, Yu.A. Shreider, I.M. Sobol, V.G. Sragovich, The Monte Carlo Method, Pergamon, First English Edition, 1966
66. P. Papoulis, S.U. Pillai, Probability, Random Variables, and Stochastic Processes, McGraw Hill, Fourth Edition, 2002
67. P. Fortescue, J. Stark, G. Swinerd, Spacecraft Systems Engineering, Wiley, Edition, 2003
68. H. Tada, P.C. Paris, G.R. Irwin, The Stress Analysis of Cracks Handbook, Professional Engineering Publishing, Third Edition, 2000
69. D. Hanselman, B Littlefield, The Student Edition of MATLAB, Prentice Hall, First Edition, 1995
70. E. Kyle, Space Launch Report, Last accessed from URL:
<http://www.spacelaunchreport.com/logsum.html>
71. NASA, Kennedy Space Centre Next Gen Site, Last accessed from URL:
science.ksc.nasa.gov/shuttle/nexgen/rlvhp.htm
72. A Hammesfar, Product Tree, Document Number: S2-ASD-PT-3001, 23/11/2005

73. H.T. Jessop, F.C. Harris, Photoelasticity, principles and methods, Cleaver-Hume, First Edition, 1949
74. F.A. Jenkins, H.E. White, Fundamentals of Optics, McGraw-Hill, Third Edition, 1957
75. Schott, Lightweighting of Zerodur, Document Number: TIE-38, October 2005
76. S. Timoshenko, Theory of Elasticity, McGraw-Hill, Second Edition, 1951
77. A. Yariv, P. Yeh, Optical Waves in Crystals, Wiley, First Edition, 1984
78. D. Brewster, On the communication of the structure of doubly-refracting crystals to glass, murite of soda, flour spar, and other substances by mechanical compression and dilation, Philosophical Transactions of the Royal Society of London, Volume , Pages 156 - 178, 1816
79. R.S. Figliola, D.E. Beasley, Theory and Design for Mechanical Measurements, Wiley, Second Edition, 1995
80. A Asundi, Recent Advances in Photoelastic Applications, Last accessed from URL:
http://www3.ntu.edu.sg/mae/research/programmes/sensors/sensors/photoelasticity/Recent_advances.html
81. J.M. Gere, S.P. Timoshenko, Mechanics of Materials, Chapman & Hall, Third SI Edition, 1991
82. I.N. Sneddon, Fourier Transforms, Dover, McGraw-Hill 1951 Edition, 1995
83. R. Jain, R. Kasturi, B.G. Schunk, Machine Vision, McGraw-Hill, International Edition, 1995
84. G Dixon, Optical Bench - Calibration Samples Test Procedure, Document Number: S2-UGB-TP-3001, 2006
85. Henkel, Henkel Hysol EA 9361 Epoxy Paste Adhesive Data Sheet, Document Number: Hysol EA 9361, Undated

86. Anon., Laser Crystal Home Page, Last accessed from URL: <http://www.lasercrystal.co.uk/>
87. M. Hetényi, Beams on elastic foundation : theory with applications in the fields of civil and mechanical engineering., Oxford, First Edition, 1946
88. I. Gilmour, SMART-2 Analysis of Bondline Strength for Photodiode Mount KE-0159-407, Document Number: OB-TN-3320-01 Issue 1, 20/05/2003
89. 3M, 3M Scotch Weld Epoxy Adhesive 2214 Regular Data Sheet, Document Number: 78-6900-9680-1, March 2005
90. 3M, 3M Scotch Weld Epoxy Adhesive 2216 B/A Gray Data Sheet, Document Number: 78-6900-9583-7, March 2002
91. The LISA Pathfinder Team, General Design and Interface Requirements, Document Number: S2-ASU-RS-2031, 16th February 2006
92. G Dixon, Flight Photo-diodes - Bonding Procedure, Document Number: S2-UGB-PR-3010, 15th February 2010
93. S.H. Crandall, W.D. Mark, Random Vibration, Academic Press, First Edition, 1963
94. G Dixon, Photo-diode and Mount Requirement Specification, Document Number: S2-UGB-RS-3002, 18 Feb 2009
95. M Perreur-Lloyd, OBI Assembly and ICD Drawing, Document Number: S2-UGL-DRW-3013, 11th November 2009
96. D. Hoyland, Part Approval Document - Quadrant Photo-diode, Document Number: S2-UBI-PAD-3001, 10/2/06
97. D. Hoyland, Part Approval Document - Single Element Photo-diode, Document Number: S2-UBI-PAD-3002, 120/2/06

98. G. Dixon, SEPD and QPD Qualification Flow Issue 4, Document Number: S2-UGB-PL-3006, 25/3/2009
99. G Dixon, LPF Photo-Diode Vibration & Shock Screening Test Procedure, Document Number: S2-UGB-TP-3010, 24 May 2010
100. D Robertson, E Fitzsimons, C Killow, 3OB Build Traveller, Document Number: S2-UGL-TRV-3103, 21 March 2010
101. R.C Bradt, R.E. Tressler, Fractography of Glass, Plenum, First Edition, 1994
102. C. J. Tranter, Integral Transforms in Mathematical Physics, Methuen, Third Edition, 1966
103. L.C. Andrews, Special Functions of Mathematics for Engineers, Oxford, Second Edition, 1998
104. H. Jeffreys, B. Swirles, Methods of Mathematical Physics, Cambridge, Third Edition, 1956
105. I.S. Sokolnikoff, Mathematical Theory of Elasticity, McGraw-Hill, First Edition, 1946

11 APPENDICES

APPENDIX A STRAIN AS APPLIED TO GRAVITATIONAL WAVES

12 The details of the derivation of the gravitational wave solution to Einstein's equations of General Relativity are beyond the scope of this thesis. However, the factor of two which appears in equation 2 was in contrast to the usual mechanical engineering definition of a strain, which is simply a change in length divided by the original length. Therefore, a brief discussion of the source of the factor of two based upon the presentation given in [4], is included in these appendices.

Beginning with the metric tensor;

$$g_{ij} = \begin{bmatrix} 0 & 0 & 0 & 0 \\ 0 & 1+h\cos(\omega t) & 0 & 0 \\ 0 & 0 & 1-h\cos(\omega t) & 0 \\ 0 & 0 & 0 & 0 \end{bmatrix} \quad \text{Equation 55}$$

The measured separation, L , of objects separated by co-ordinate differences $dx^{0,1,2,3}$ is given by;

$$dL^2 = g_{ij} dx^i dx^j \quad \text{Equation 56}$$

Where summation is implied. Consider the x axis only;

$$\begin{aligned} dL^2 &= (1+h\cos(\omega t)) L^2 \\ dL &= (1+h\cos(\omega t))^{\frac{1}{2}} L \end{aligned} \quad \text{Equation 57}$$

As h is very small, it is appropriate to use the binomial expansion to simplify the square root;

$$(1 + \alpha)^{\frac{1}{2}} \approx \left(1 + \frac{1}{2}\alpha\right) \quad \text{Equation 58}$$

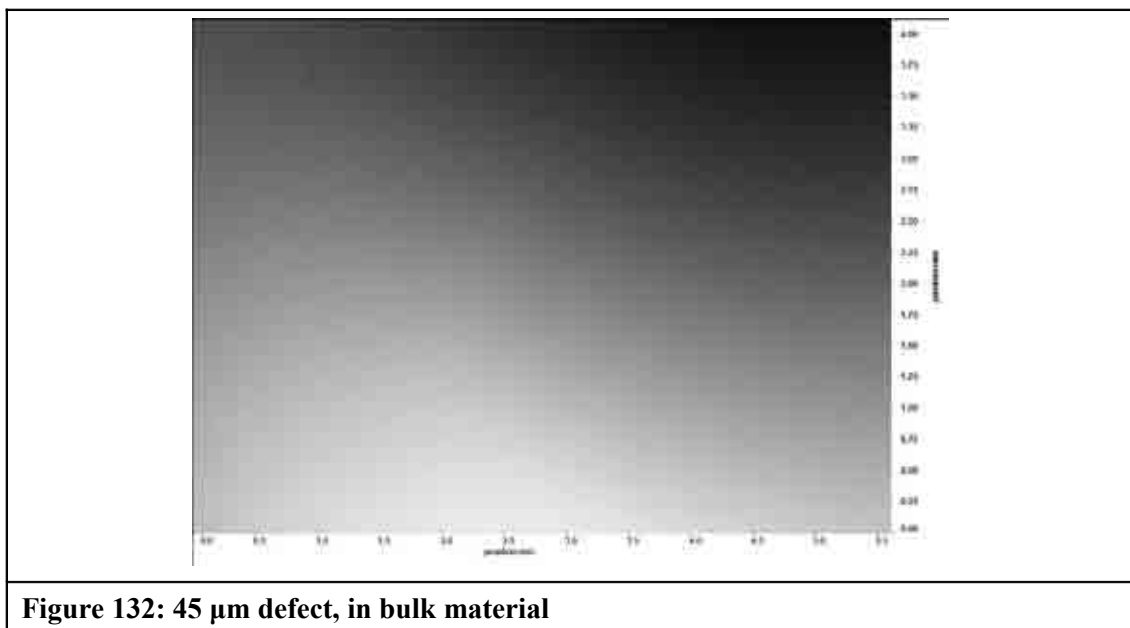
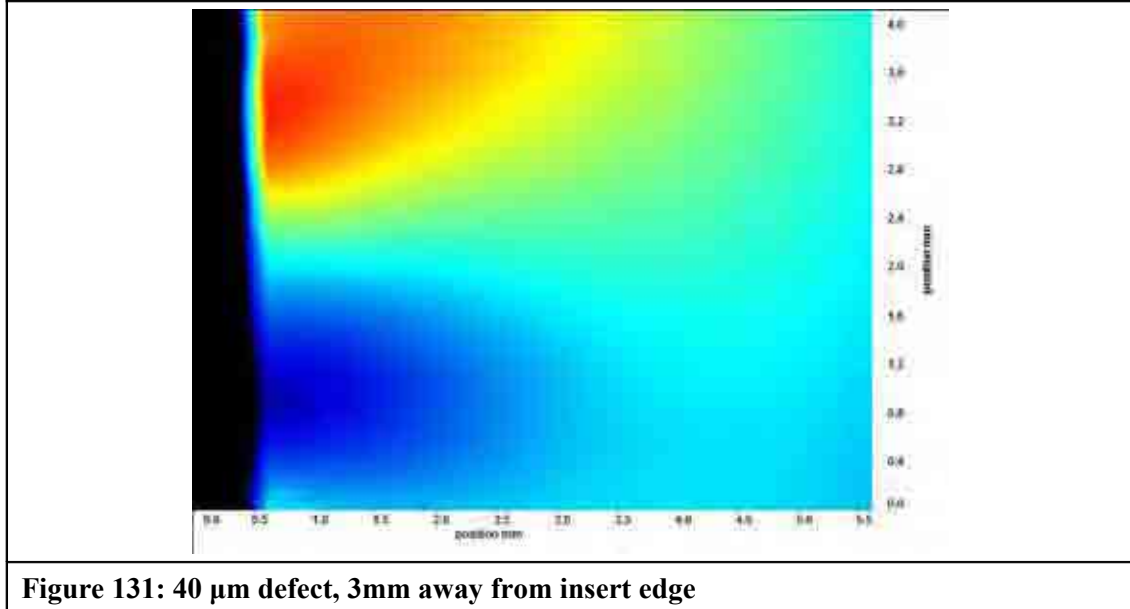
If dL is the change in the the separation L caused by the gravitational wave,

$$\begin{aligned} dL &\approx \frac{1}{2}h\cos(\omega t)L \\ h\cos(\omega t) &= 2\frac{dL}{L} \end{aligned} \quad \text{Equation 59}$$

Therefore it is the use of the binomial expansion to approximate the square root which is the source of the factor of 2 in the derivation.

APPENDIX B OPTICAL BENCH SERIAL NUMBER 03, INSPECTION II IMAGES

The images referenced in table 14 are appended in figures 131 to 137, below.



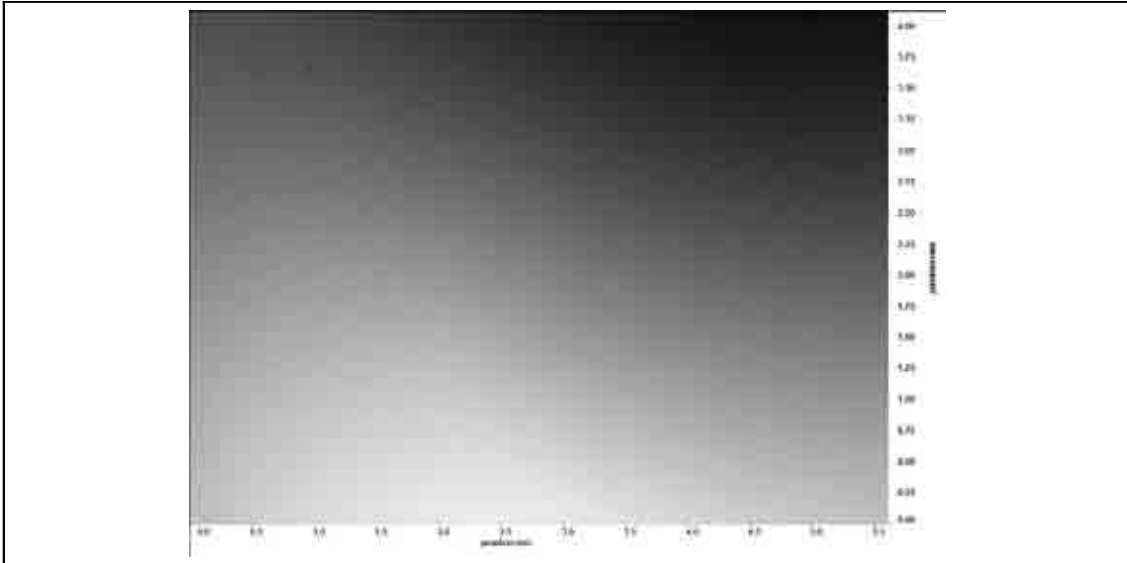


Figure 133: 60 μm defect, in bulk material

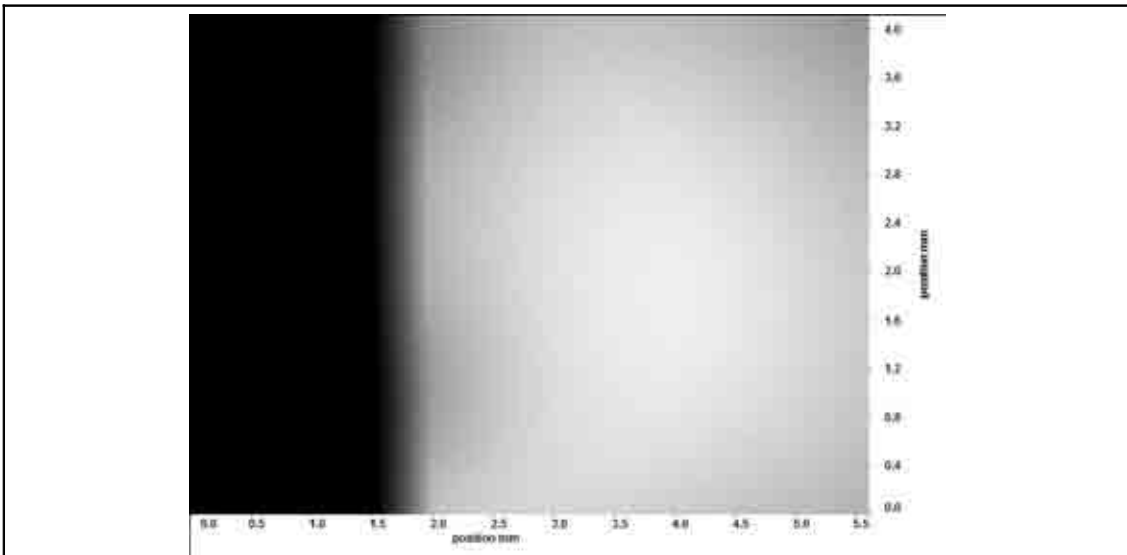


Figure 134: 65 μm defect, 3.5mm away from insert edge

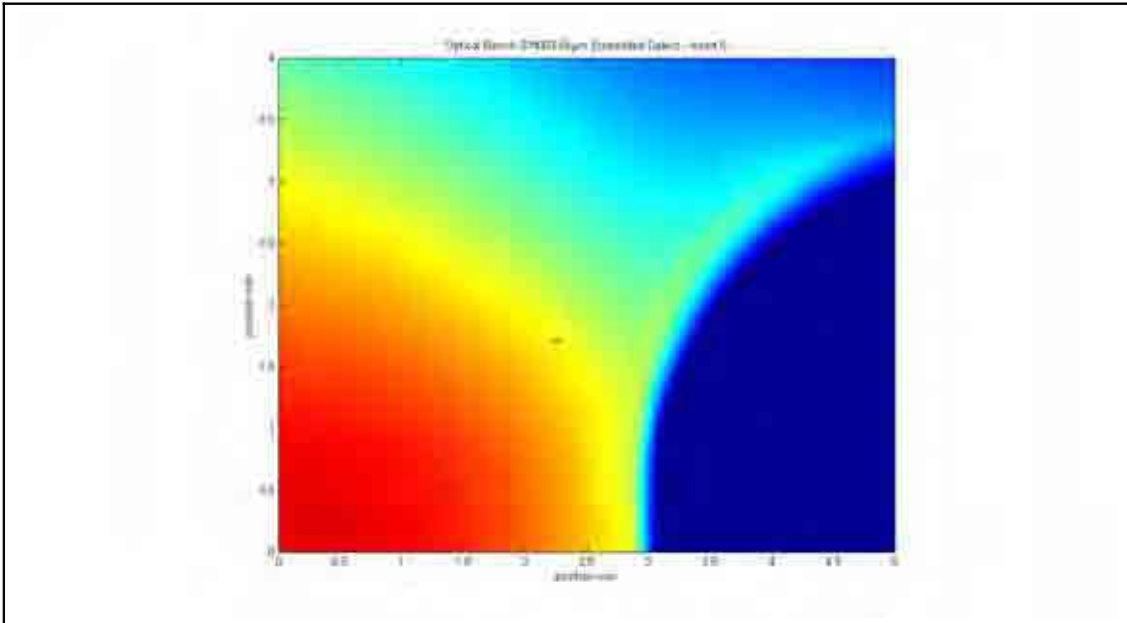


Figure 135: 65 μm defect, < 1mm away from insert edge

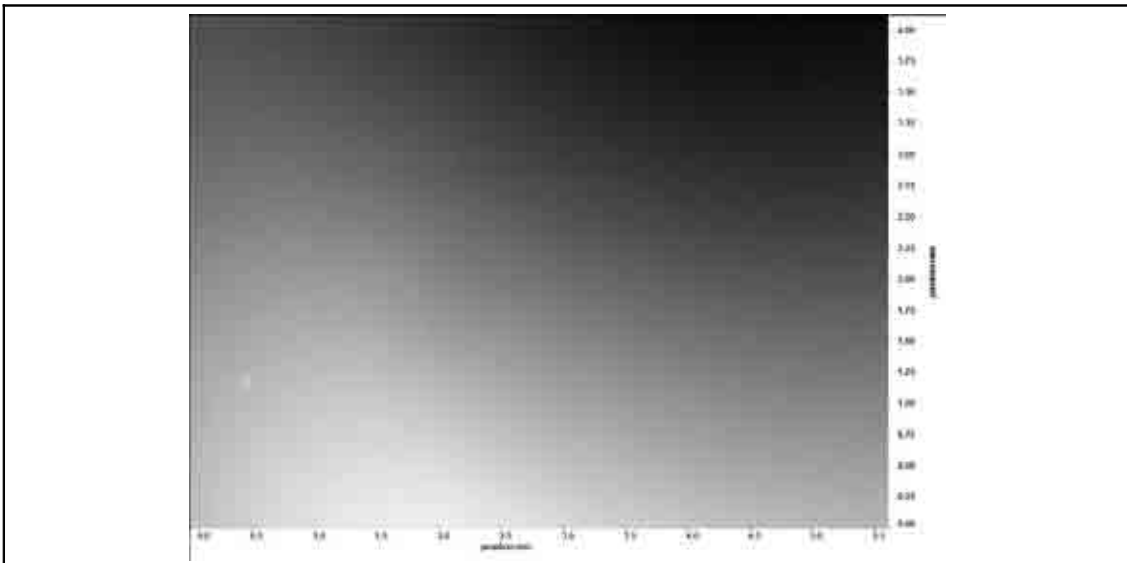


Figure 136: 130 μm defect, in bulk material

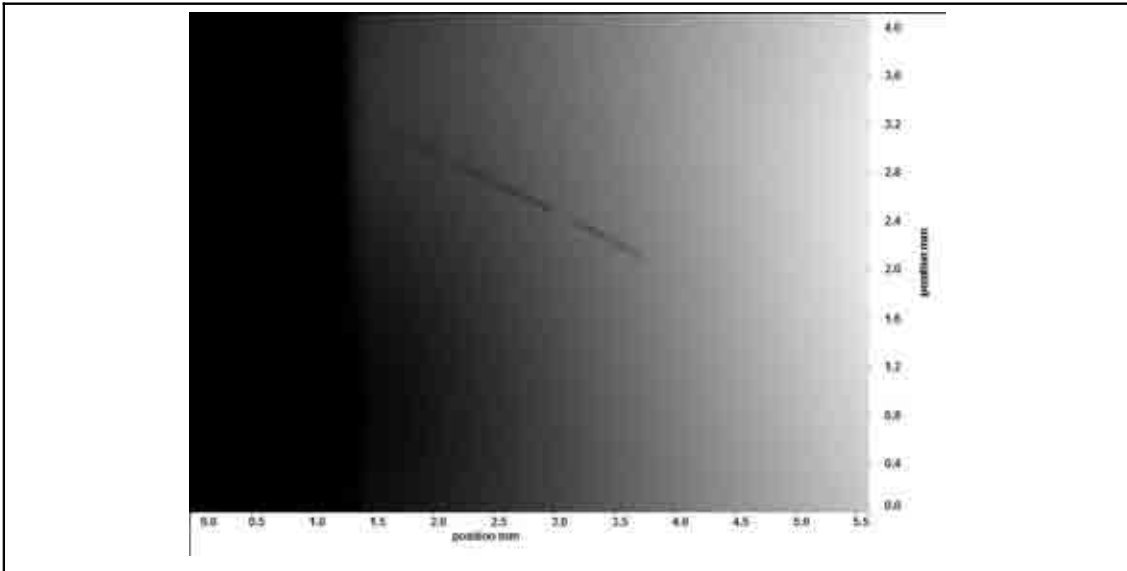
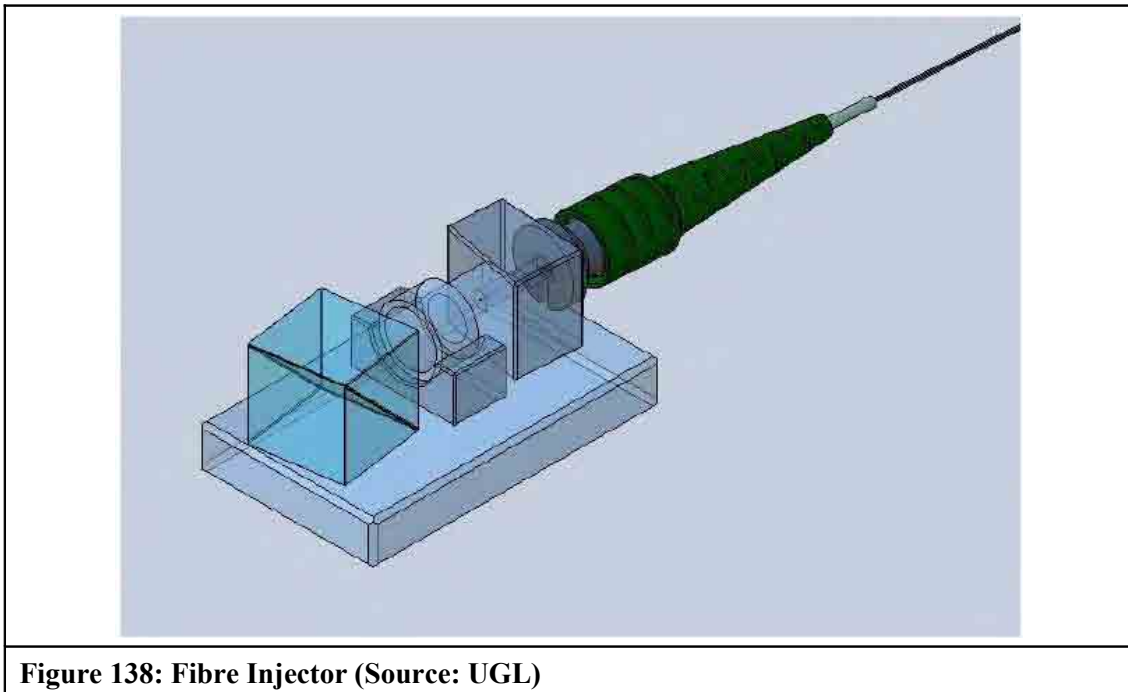


Figure 137: Scratch on lower edge of optical bench

APPENDIX C FIBRE INJECTOR FAILURE

As an example of the handling of a non-conformance, during manufacture, and of the sudden and problematic nature of brittle fracture, a reduction in the beam quality was noticed by UGL. A CAD model of a fibre injector is shown in figure 138, below.



The latest adequate beam profile is shown in figure 139, below. The beam profile was measured as part of routine work at UGL prior to the polishing of the fibre injector cube output face.

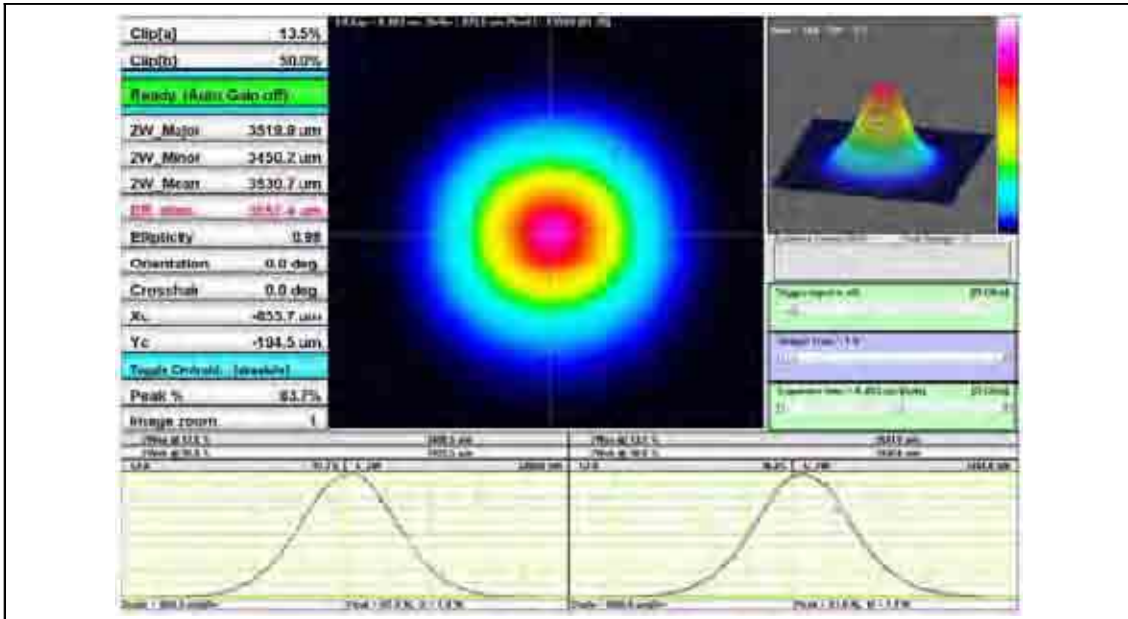


Figure 139: An acceptable beam profile (Source: UGL)

Upon receipt of the fibre injector after polishing, the beam profile was re-measured, and the beam profile as shown in figure 140, below.

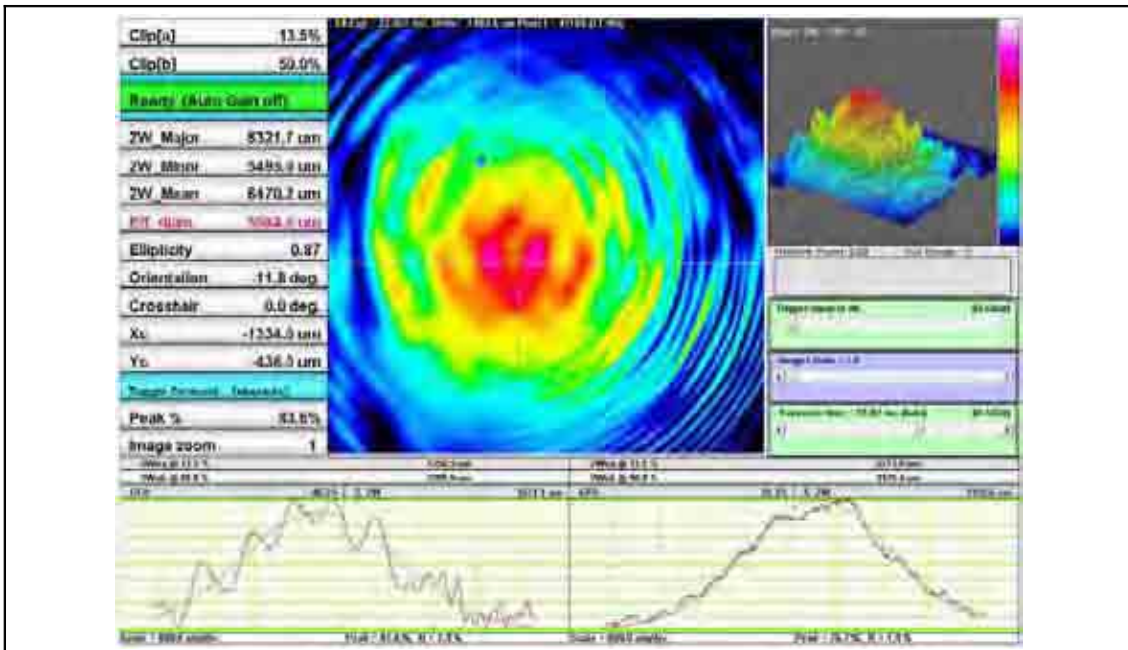


Figure 140: An unacceptable beam profile (Source: UGL)

Upon the measurement of the unacceptable beam profile, UGL contacted their PA support engineers at UBI. Together, the teams compiled the information which would enable external scrutiny, and uploaded the information to the ESA non-conformance tracking system, [41].

The suspect fibre injector was inspected using a microscope, and an image showing the damage is shown in figure 141, below.

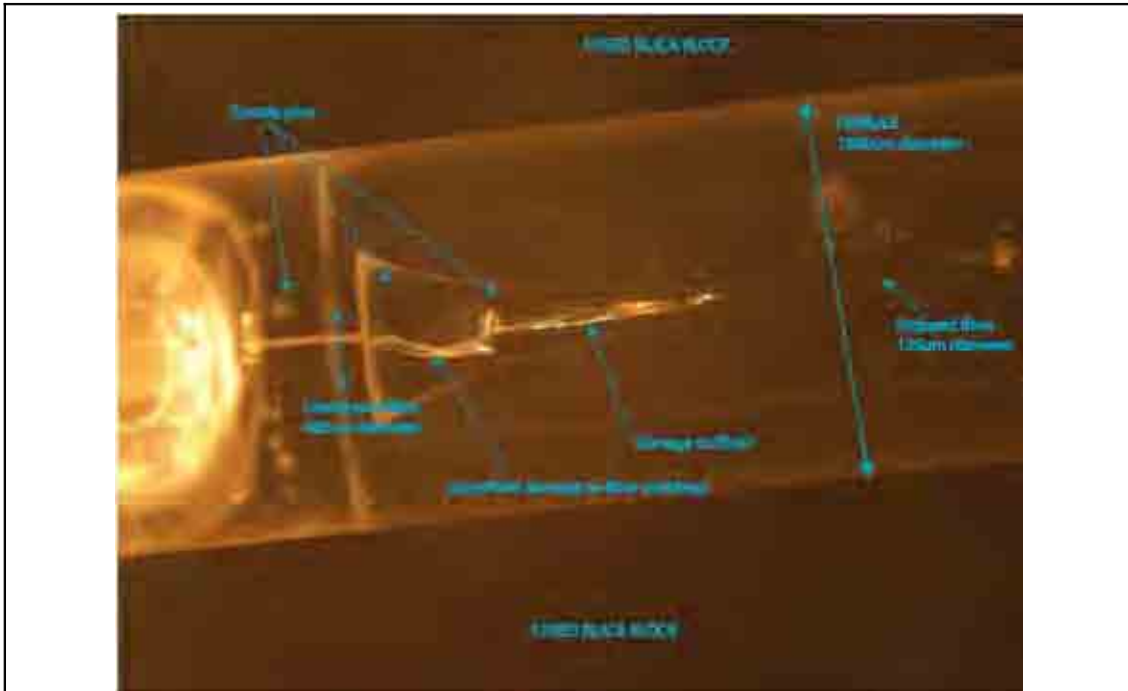


Figure 141: Microscope optical image showing damaged fibre (Source: UGL)

The investigation into the cause of the failure was conducted by a non-conformance review board (NRB) via telephone conference with the participation of UGL, UBI, ASD, and ESTEC. The focus of the NRB was to find the root cause of the failure, and to assess the suitability of the remaining fibre injectors, which were made using the same processes, using material from the same batches for flight use.

As a result of the first NRB, the damaged fibre injector was sent to ESTEC for more detailed examination. The scanning electron images obtained by ESTEC are shown in figures 142 and 143, below.

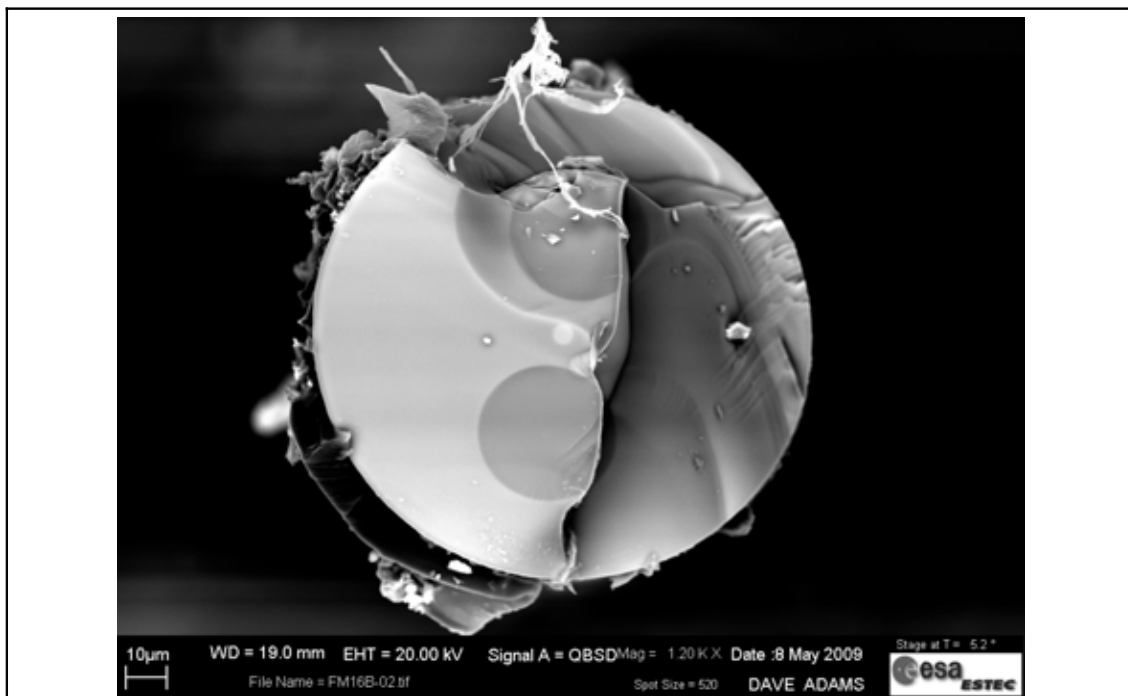


Figure 142: Scanning Electron Microscope Backscatter image of the fibre's fracture surface (Source: ESTEC)

The two darker circles within the fibre face visible in figure 142 are reinforcing fibres with a boron doping, while the two smaller light coloured circles are the light guiding cores of the fibre, responsible for maintaining the polarisation of the beam.

The fracture was found coincident with the point along the fibre where the cladding was stripped off prior to assembly. While this sudden step change in the properties of the fibre represented a stress concentrating feature, it also suggested the possibility that the stripping process was the cause of the fracture.

The striations visible on the fracture surface towards the upper right hand side of the image are where it was reported by ESTEC that the fracture was initiated. A more detailed view of this area is shown in figure 143, below.

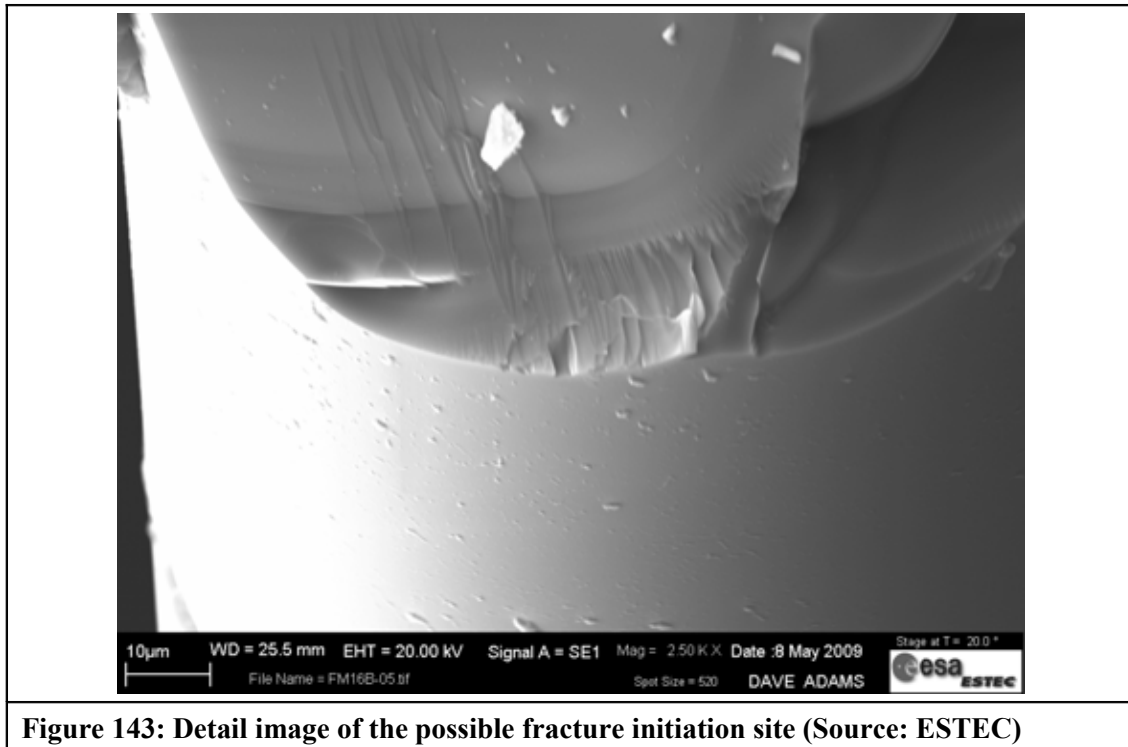


Figure 143: Detail image of the possible fracture initiation site (Source: ESTEC)

The inspection by ESTEC initially suggested that owing to the helical appearance of the fracture, the failure may have had a torsional origin, [81], [56], and the fracture was thought to have been initiated towards the lower edge of the fracture surface as shown in figure 143.

However, it may be possible that this was not the site of fracture initiation, but where the fracture ended. The irregular, long, thin, lines are known as hackle, and generally, the hackle is initially fine, and becomes more irregular as the crack progresses, [101], while the broader curved lines are known as Wallner lines, [82], and are usually concave towards the initiation site.

Owing to the possibility of torsion being the responsible stress which drove the fracture, the NRB recommended that UGL should conduct some torsional testing of various fibre samples, kept under varying environmental conditions after the cladding was stripped. One result of such testing is shown in figure 144, below, where among the shattered fragments, the dominant torsional failure may be seen. UGL tested a number of fibres, and none of them produced a fracture at all like the original flight fibre injector failure.

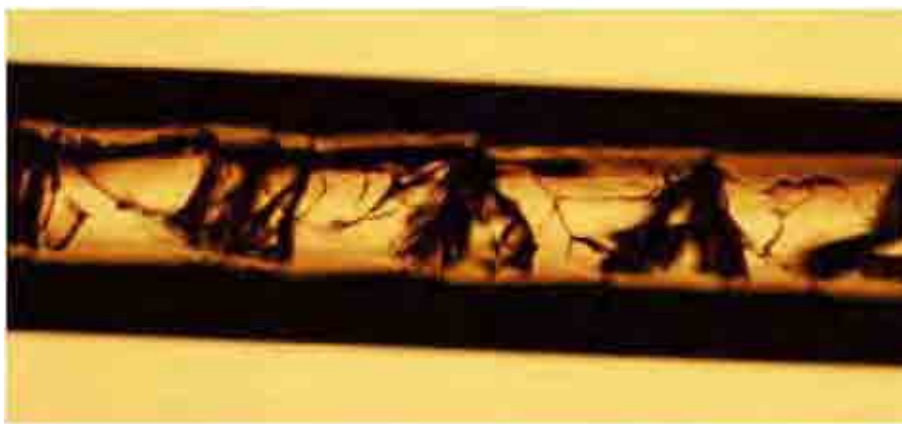


Figure 144: Extensive cracking after torsional stressing of a fibre sample (Source: UGL)

As fibre stripping was discussed during the NRB as a potential process which might have caused damage to the fibre, a number of stripped fibres were submitted to ESTEC for inspection. No damage was found on any of these submitted parts.

The stripping process at UGL comprises two parts. First, the clad fibre is centred in the stripping tool, and a pair of semi-circular blades cut into the cladding. The cladding is of diameter 400µm, the fibre, 125µm, and the closed hemi-spherical blades form a circle of diameter 250µm. In order to protect against the possibility of scratching the fibre, the stripping

tool is removed, and the cladding is pulled away by hand, splitting naturally at the circumferential cut made by the stripping tool.

It was not known whether the localised squeezing of the fibre during the incision of the cladding would produce significant tensile stress on the fibre surface. The radial component of stress would certainly be compressive, but, the state of axial stress was not clear.

In order to investigate this further a previous result of a cylinder subjected to a discontinuous stress was considered. The solution, [102],[82], evaluated the problem of a cylinder with a surface $r = a$ deformed by the application of unit pressure to the semi-infinite length $z > 0$, while $z < 0$ remained unloaded. The solution was obtained via the use of Fourier Transforms, and is expressed as integrals over modified Bessel functions, [103], [104], as shown in equations 60 and 61, below.

$$\begin{aligned}\sigma_r &= \frac{-1}{2} + \frac{a}{r\pi} \int_0^{\infty} A(\eta) \frac{\sin(\eta \frac{z}{a})}{\eta D(\eta)} d\eta \\ \sigma_\theta &= \frac{-1}{2} + \frac{a}{r\pi} \int_0^{\infty} B(\eta) \frac{\sin(\eta \frac{z}{a})}{\eta D(\eta)} d\eta \\ \sigma_z &= \frac{1}{\pi} \int_0^{\infty} C(\eta) \frac{\sin(\eta \frac{z}{a})}{D(\eta)} d\eta\end{aligned}\tag{Equations 60}$$

Where;

$$\begin{aligned}
A(\eta) &= \frac{r\eta^2}{a} I_0(\eta) I_0\left(\frac{\eta r}{a}\right) + \frac{r\eta}{a} I_0\left(\frac{\eta r}{a}\right) I_1(\eta) - I_0(\eta) I_1\left(\frac{\eta r}{a}\right) \\
&\quad - \left[\left(\frac{r^2 \eta^2}{a^2} \right) + 2(1-\nu) \right] I_1(\eta) I_1\left(\frac{\eta r}{a}\right) \\
B(\eta) &= \eta I_0(\eta) I_1\left(\frac{\eta r}{a}\right) + 2(1-\nu) I_1(\eta) I_1\left(\frac{\eta r}{a}\right) \\
&\quad + (2\nu-1) \frac{r}{a} \eta I_1(\eta) I_0\left(\frac{\eta r}{a}\right) \\
C(\eta) &= 2 I_0\left(\frac{\eta r}{a}\right) I_1(\eta) + \left(\frac{\eta r}{a}\right) I_1(\eta) I_1\left(\frac{\eta r}{a}\right) - \eta I_0(\eta) I_0\left(\frac{\eta r}{a}\right) \\
D(\eta) &= [\eta^2 + 2(1-\nu)] I_1^2(\eta) - \eta^2 I_0^2(\eta)
\end{aligned}
\tag{Equations 61}$$

Where I_α is the modified Bessel function of the first kind, order α . The material Poisson's ratio is represented by ν .

By calculating these stresses, [64], [68], at an array of points in z and in r , the stress field can be obtained as an array. If the array is shifted, the stress distribution may be shifted in the axial direction. If the array is flipped, the stress distribution for the application of pressure to the semi-infinite length of fibre $z < 0$ may be obtained. As the stress was calculated using linear assumptions, namely the generalised form of Hooke's law, linear superposition of the results is permissible, [14], [105].

The array of results may be manipulated and summed to find the stress distribution due to a concentrated band of load either side of $z=0$. The combination of solutions superposed is shown graphically in figure 145, below.

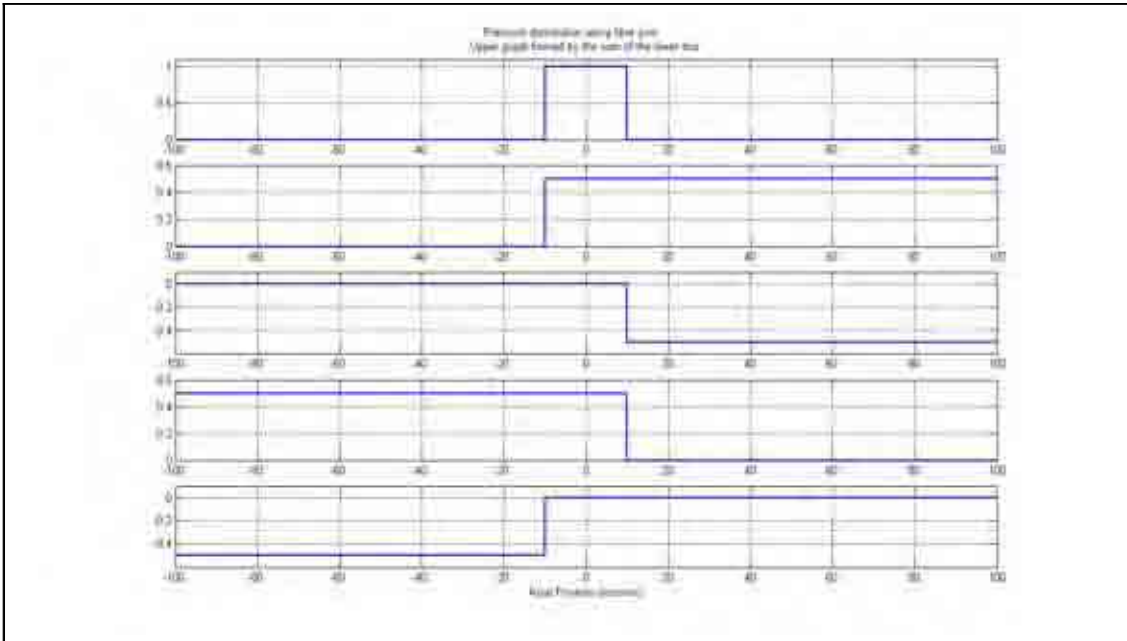


Figure 145: Linear Superposition of solutions

The axial stress distribution for a fibre of diameter 125 μm with a concentrated pressure over an axial length of 10 μm , is shown in figure 146, below.

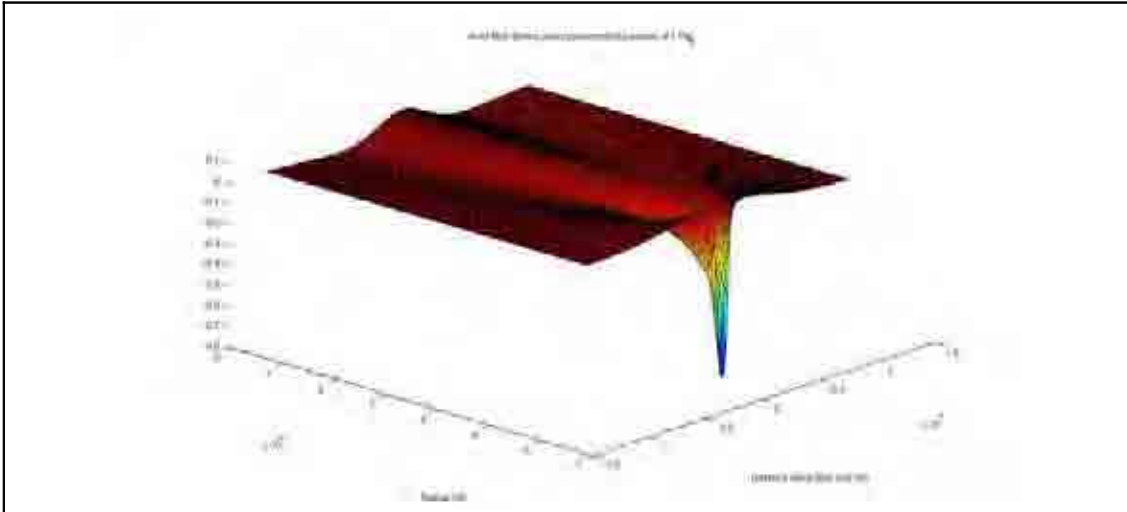


Figure 146: Axial Stress Distribution

The most important location is the fibre surface, the stress distribution on the fibre surface is shown in figure 147, below.

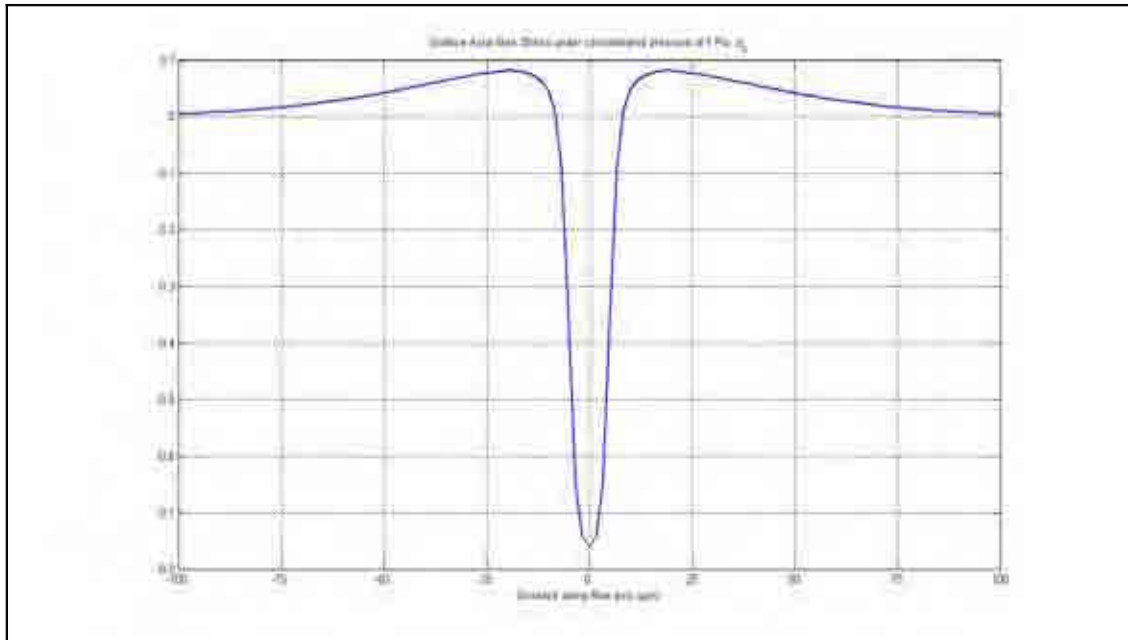


Figure 147: Axial Stress Distribution on fibre surface

The concentrated pressure, of 1 Pa, was applied between axial positions, minus 5 μm and plus 5 μm . The largest stress on the surface of the fibre was compressive (~ 0.75 Pa) - this meant that the application of pressure during the cladding stripping process was not likely to cause cracks to grow, as compression tends to close cracks rather than opening them, [61]. There were, however, areas of tensile stress on each side of the negative peak, although these were much lower in magnitude (< 0.1 Pa). As the material had been assumed linearly elastic, these stresses remain scalable if, for example, the magnitude of the concentrated pressure were determined.

While this demonstrates that clamping the cladding to enable stripping was not likely was not likely to produce large tensile stresses, the act of puling the cladding away from the fibre might remain the cause of the fibre failure.

Despite this work, the root cause of the failure was not established beyond doubt.

The likely fracture history was traced using the patterns on the fracture surface as a guide. It was decided that the likely failure mode was bending, however, owing to the complicated structure of the fibre, it was difficult to be definitive. The marks on the fracture surface indicate that the crack had started and stopped a number of times. Owing to the brittle nature of glass, this indicates a strain limited event rather than one which was stress driven. Such possible strain sources include thermal cycling, coiling and uncoiling fibre, and repetitive forces during polishing.

Tests attempting to replicate the most likely loading scenarios had been carried out, but, they did not cause failure. The NCR board accepted that, the root cause had not be established, and within project time and cost constraints probably could not be established.

In order to reduce the risk for the remaining, critical, stock of fibre two operators were mandated when any handling of the fibre attached to the optical bench interferometer was carried out. Owing to limited space in the clean room at Glasgow, the possibility of a third person was dismissed, however, where possible, digital webcams should be used to record the activity on the bench.

The methods by which any similar failure in the future might be detected at all levels of integration were discussed and defined, requiring the availability of lasers, modulators and a photodiode readout system.

APPENDIX D THEORY - BEAM ON AN ELASTIC FOUNDATION

The small curvature bending of prismatic beams is governed by the Euler-Bernoulli beam theory, [81], and may be written as per equation 62, below;

$$EI \frac{d^4 w}{dx^4} - q = 0 \quad \text{Equation 62}$$

Where E represents the Young's modulus of elasticity of the beam material, I, the second moment of area about the neutral axis, q the force per unit length, w,, the deflection of the beam, and x is the dimension along the length of the beam.

The elastic support requires a modification to the usual Euler-Bernoulli beam theory, via the inclusion of a term describing the elastic restoring force per unit length of the beam, kw, as shown in equations 63, below.

$$\begin{aligned} EI \frac{d^4 w}{dx^4} + kw &= 0 \\ \frac{d^4 w}{dx^4} + 4 \beta^4 w &= 0 \\ \beta^4 &= \frac{k}{4EI} \end{aligned} \quad \text{Equations 63}$$

Where k is the so-called Winkler constant, and is equal to the Young's modulus of elasticity multiplied by the width of the epoxy layer divided by its depth. The deflection of the beam, w, can be written as shown in equations 64, below.

$$\begin{aligned} w(x) &= Ae^{\beta x} e^{i\beta x} + Be^{\beta x} e^{-i\beta x} + Ce^{-\beta x} e^{i\beta x} + De^{-\beta x} e^{-i\beta x} \\ w(x) &= Ae^{(1+i)\beta x} + Be^{(1-i)\beta x} + Ce^{(-1+i)\beta x} + De^{(-1-i)\beta x} \end{aligned} \quad \text{Equations 64}$$

The successive spatial differentials of this solution are shown in equations 65, 66, 67, and 68, where the solution is demonstrated as a valid solution of the original differential equation of equations 63.

$$\frac{dw}{dx} = \beta \begin{pmatrix} (1+i)Ae^{(1+i)\beta x} \\ +(1-i)Be^{(1-i)\beta x} \\ +(-1+i)Ce^{(-1+i)\beta x} \\ +(-1-i)De^{(-1-i)\beta x} \end{pmatrix} \quad \text{Equations 65}$$

$$\frac{d^2w}{dx^2} = \beta^2 \begin{pmatrix} (1+i)(1+i)Ae^{(1+i)\beta x} \\ +(1-i)(1-i)Be^{(1-i)\beta x} \\ +(-1+i)(-1+i)Ce^{(-1+i)\beta x} \\ +(-1-i)(-1-i)De^{(-1-i)\beta x} \end{pmatrix} \quad \text{Equations 66}$$

$$\frac{d^2w}{dx^2} = \beta^2 \begin{pmatrix} (2i)Ae^{(1+i)\beta x} \\ +(-2i)Be^{(1-i)\beta x} \\ +(-2i)Ce^{(-1+i)\beta x} \\ +(2i)De^{(-1-i)\beta x} \end{pmatrix}$$

$$\frac{d^3w}{dx^3} = \beta^3 \begin{pmatrix} (1+i)(2i)Ae^{(1+i)\beta x} \\ +(1-i)(-2i)Be^{(1-i)\beta x} \\ +(-1+i)(-2i)Ce^{(-1+i)\beta x} \\ +(-1-i)(2i)De^{(-1-i)\beta x} \end{pmatrix} \quad \text{Equations 67}$$

$$\frac{d^3w}{dx^3} = \beta^3 \begin{pmatrix} (2i-2)Ae^{(1+i)\beta x} \\ +(-2i-2)Be^{(1-i)\beta x} \\ +(2i+2)Ce^{(-1+i)\beta x} \\ +(2-2i)De^{(-1-i)\beta x} \end{pmatrix}$$

$$\frac{d^4 w}{d x^4} = \beta^4 \left(\begin{array}{l} (1+i)(2i-2) A e^{(1+i)\beta x} \\ +(1-i)(2i-2) B e^{(1-i)\beta x} \\ +(-1+i)(2+2i) C e^{(-1+i)\beta x} \\ +(-1-i)(2-2i) D e^{(-1-i)\beta x} \end{array} \right)$$

$$\frac{d^4 w}{d x^4} = \beta^4 \left(\begin{array}{l} (-4) A e^{(1+i)\beta x} \\ +(-4) B e^{(1-i)\beta x} \\ +(-4) C e^{(-1+i)\beta x} \\ +(-4) D e^{(-1-i)\beta x} \end{array} \right)$$

$$\frac{d^4 w}{d x^4} + 4 \beta^4 w = 0$$

Equations 68

APPENDIX E PHOTODIODE 202 INSPECTION RESULTS

The response of the photodiode is shown below

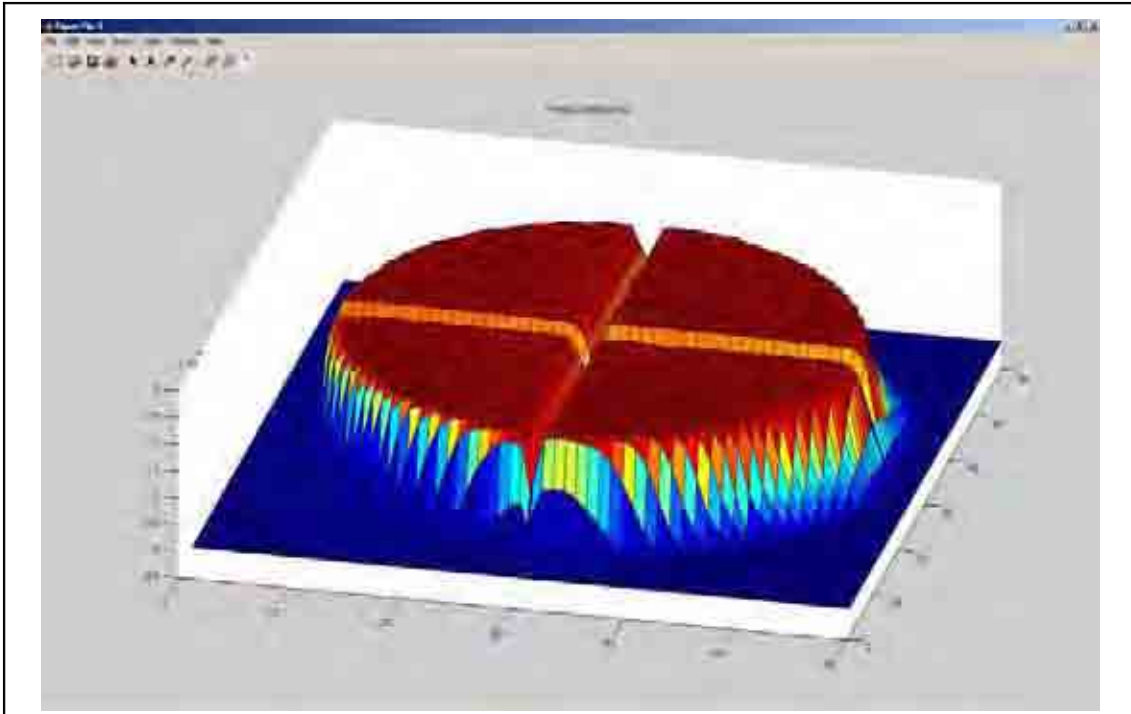


Figure 148: Photodiode 202 Response

The maximum photo-current was 0.2098 mA, the contour plots of the individual quadrants, shown below, show the 3%, 97%, and 103% response contours. The reference data for each quadrant is shown in table 33, below.

<i>Quadrant</i>	<i>Reference Photo-current (mA)</i>	<i>Relative Reference levels (%)</i>
<i>1</i>	0.2042	-0.61
<i>2</i>	0.2051	-0.16
<i>3</i>	0.2048	-0.32
<i>4</i>	0.2055	0.00

Table 33: Photodiode 202 Reference Data

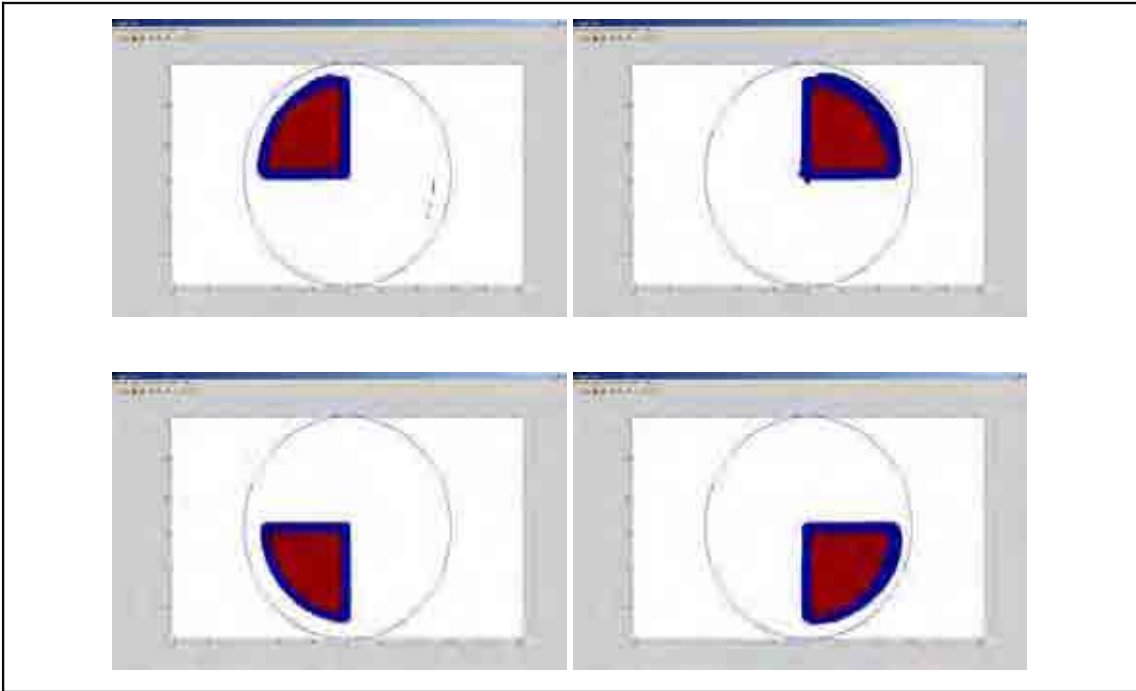


Figure 149: Photodiode 202 Q1, Q2, Q3, and Q4 Contours

APPENDIX F PHOTODIODE 203 INSPECTION RESULTS

The response of the photodiode is shown below

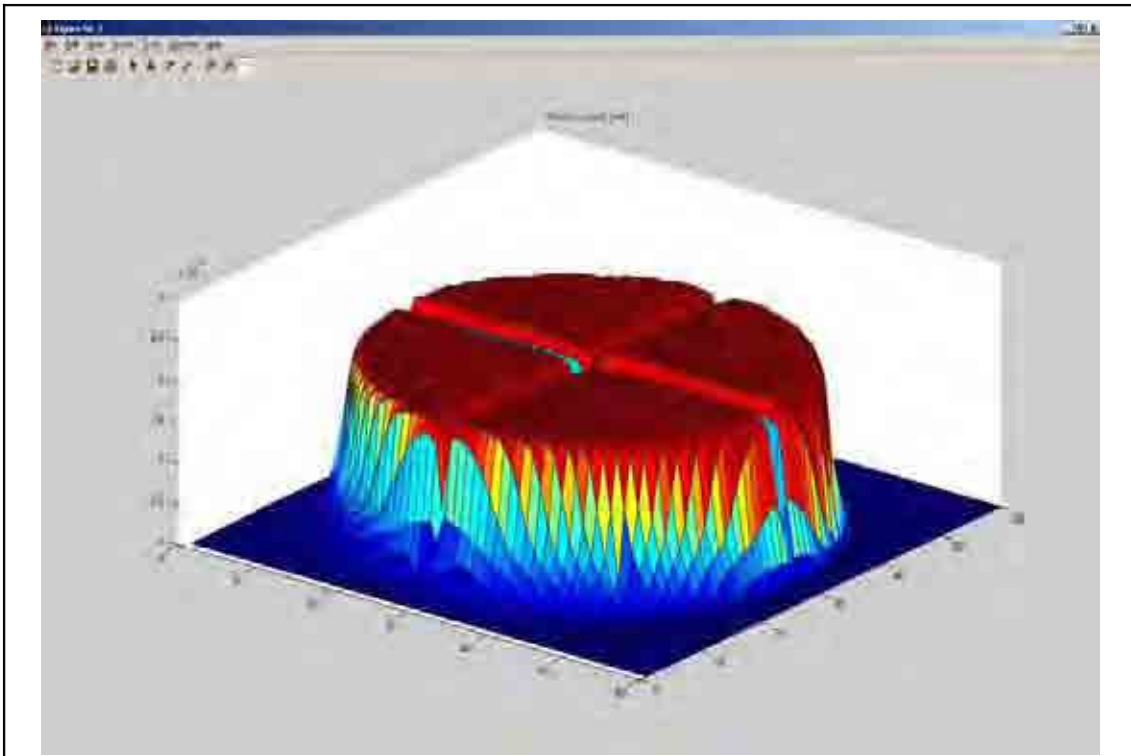


Figure 150: Photodiode 203 Response

The maximum photo-current was 0.2066 mA, the contour plots of the individual quadrants, shown below, show the 3%, 97%, and 103% response contours. The reference data for each quadrant is shown in table 34, below.

<i>Quadrant</i>	<i>Reference Photo-current (mA)</i>	<i>Relative Reference levels (%)</i>
<i>1</i>	0.2030	0.00
<i>2</i>	0.2026	-0.2
<i>3</i>	0.2021	-0.47
<i>4</i>	0.2024	-0.31

Table 34: Photodiode 203 Reference Data

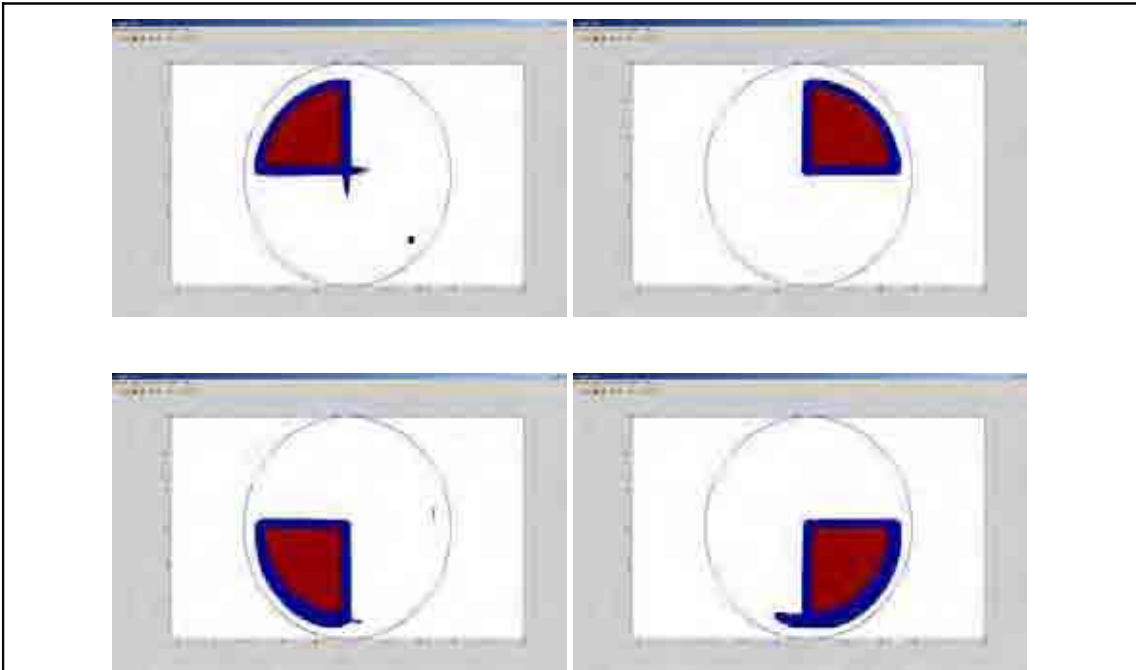


Figure 151: Photodiode 203 Q1, Q2, Q3, and Q4 Contours

APPENDIX G PHOTODIODE 205 INSPECTION RESULTS

The response of the photodiode is shown below

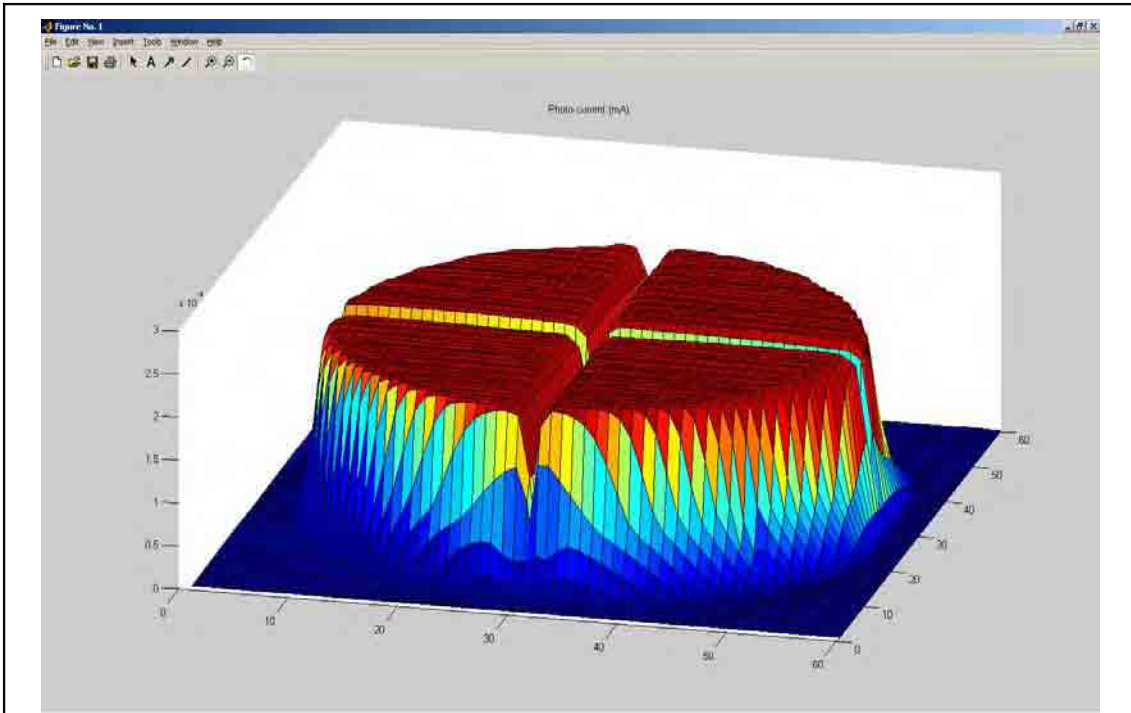


Figure 152: Photodiode 205 Response

The maximum photo-current was 0.2094 mA, the contour plots of the individual quadrants, shown below, show the 3%, 97%, and 103% response contours. The reference data for each quadrant is shown in table 35, below.

<i>Quadrant</i>	<i>Reference Photo-current (mA)</i>	<i>Relative Reference levels (%)</i>
<i>1</i>	0.2047	0.00
<i>2</i>	0.2042	-0.26
<i>3</i>	0.2044	-0.15
<i>4</i>	0.2047	0.00

Table 35: Photodiode 205 Reference Data

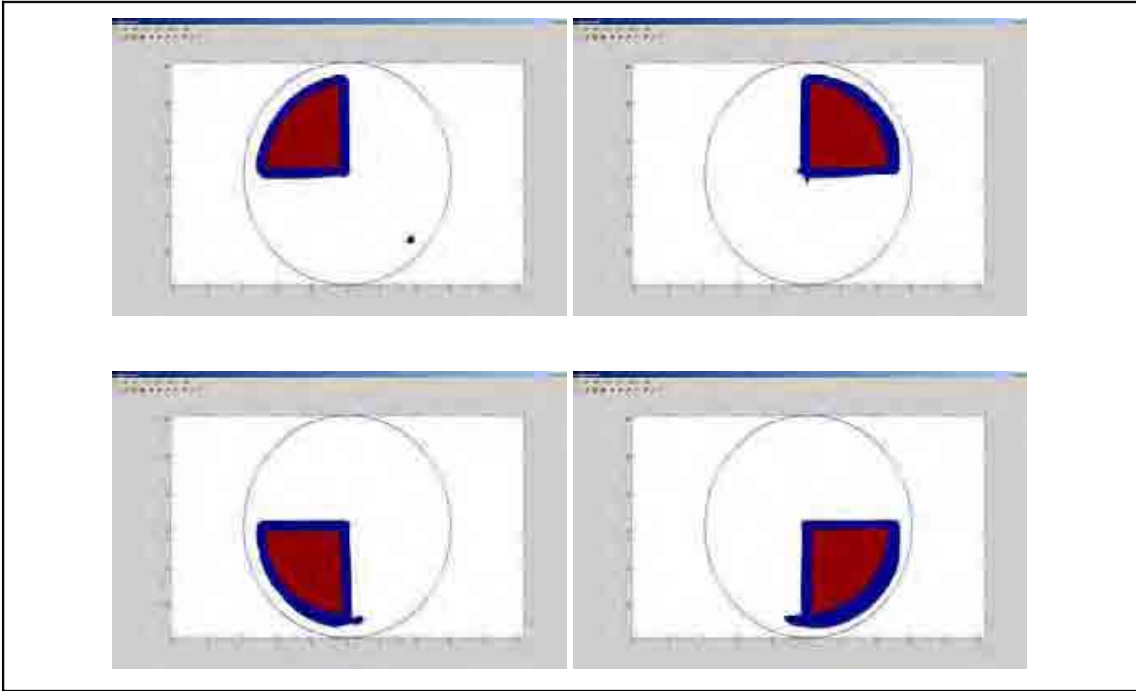


Figure 153: Photodiode 205 Q1, Q2, Q3, and Q4 Contours

APPENDIX H PHOTODIODE 206 INSPECTION RESULTS

The response of the photodiode is shown below

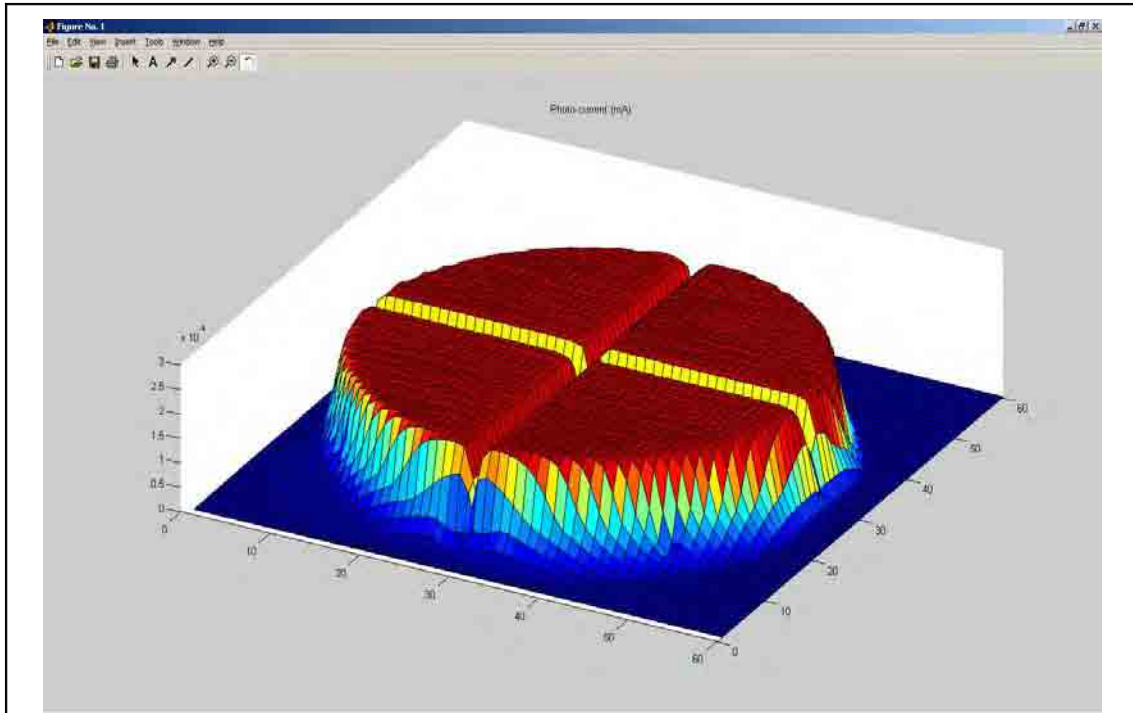


Figure 154: Photodiode 206 Response

The maximum photo-current was 0.2084 mA, the contour plots of the individual quadrants, shown below, show the 3%, 97%, and 103% response contours. The reference data for each quadrant is shown in table 36, below.

<i>Quadrant</i>	<i>Reference Photo-current (mA)</i>	<i>Relative Reference levels (%)</i>
<i>1</i>	0.2035	-0.49
<i>2</i>	0.2036	-0.42
<i>3</i>	0.2033	-0.56
<i>4</i>	0.2045	0.00

Table 36: Photodiode 206 Reference Data

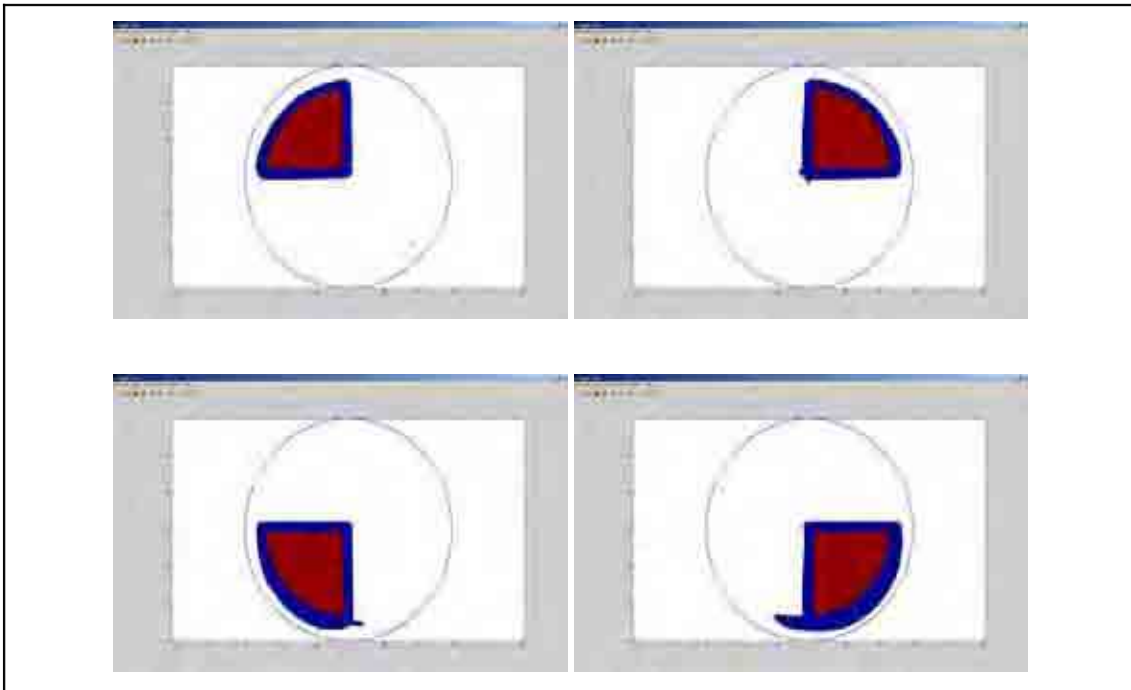


Figure 155: Photodiode 206 Q1, Q2, Q3, and Q4 Contours

APPENDIX I PHOTODIODE 208 INSPECTION RESULTS

The response of the photodiode is shown below

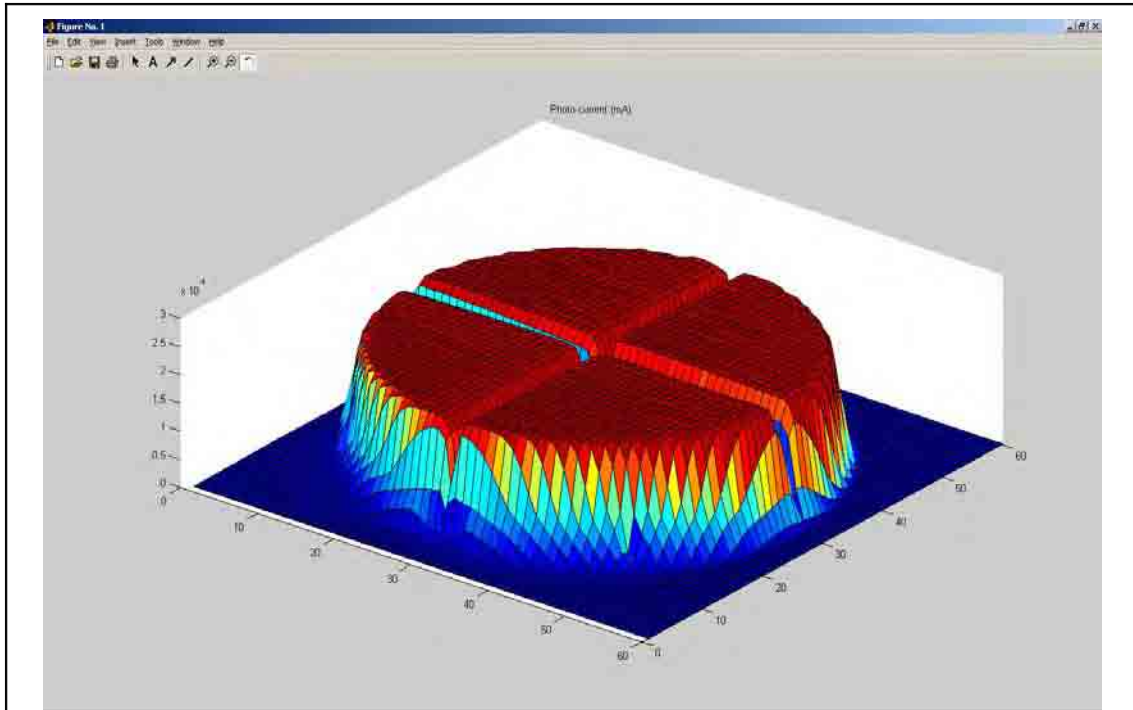


Figure 156: Photodiode 208 Response

The maximum photo-current was 0.2116 mA, the contour plots of the individual quadrants, shown below, show the 3%, 97%, and 103% response contours. The reference data for each quadrant is shown in table 37, below.

<i>Quadrant</i>	<i>Reference Photo-current (mA)</i>	<i>Relative Reference levels (%)</i>
<i>1</i>	0.2068	-0.41
<i>2</i>	0.2069	-0.35
<i>3</i>	0.2068	-0.39
<i>4</i>	0.2076	0.00

Table 37: Photodiode 208 Reference Data

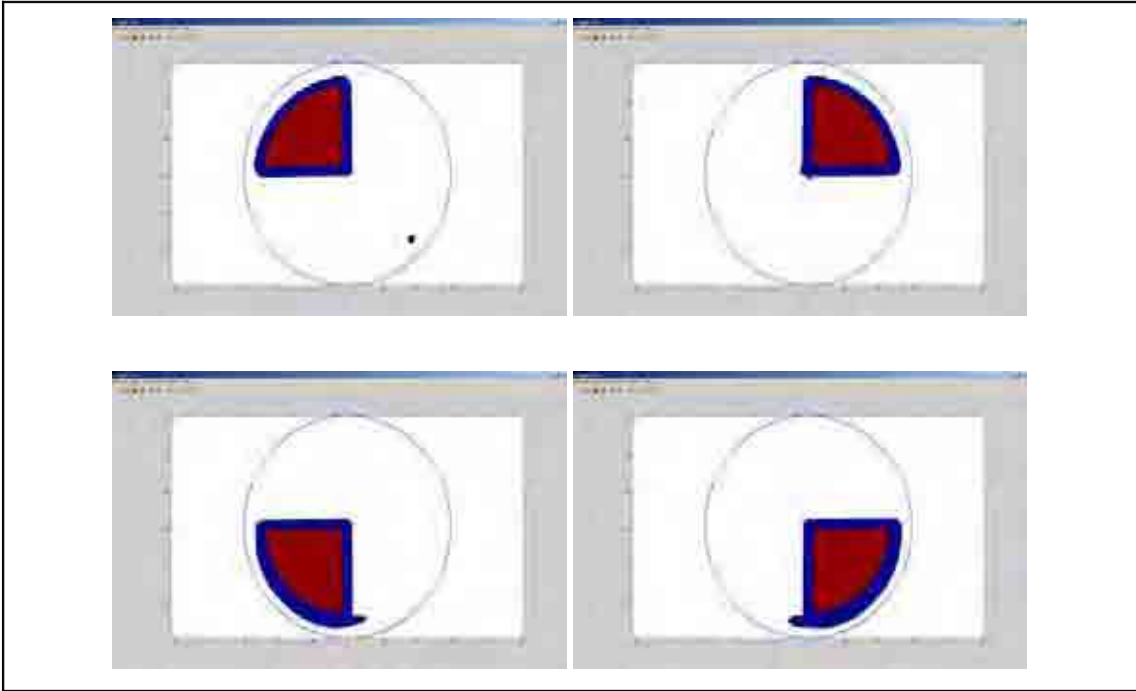


Figure 157: Photodiode 208 Q1, Q2, Q3, and Q4 Contours

APPENDIX J PHOTODIODE 209 INSPECTION RESULTS

The response of the photodiode is shown below

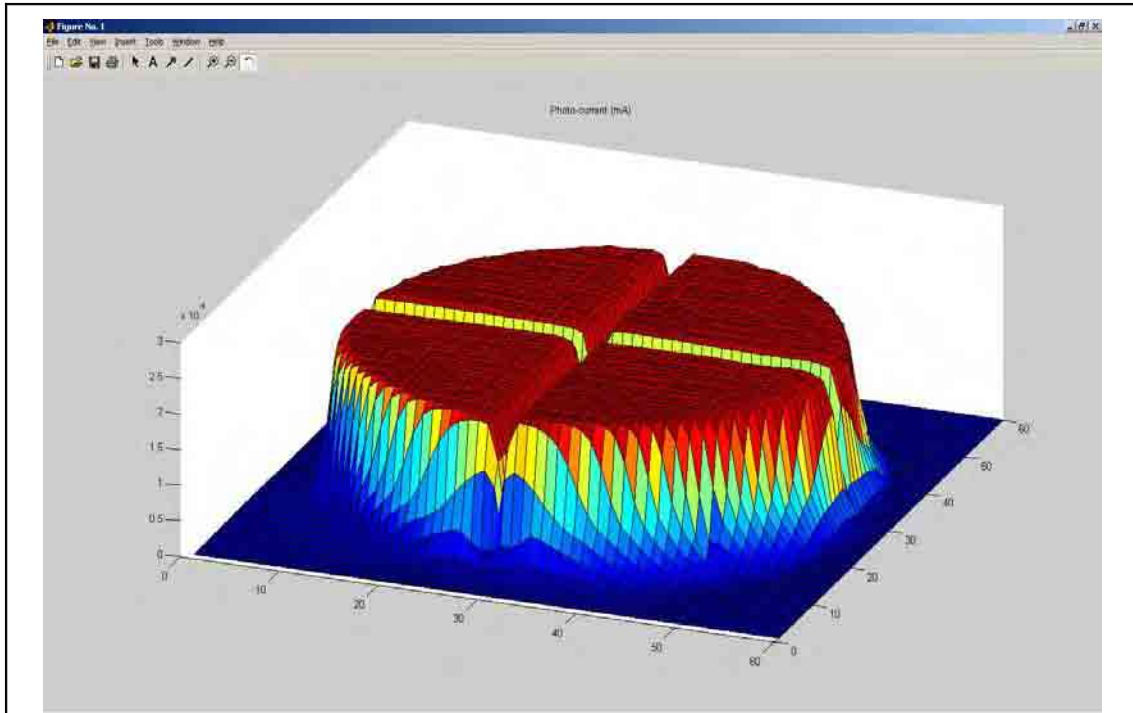


Figure 158: Photodiode 209 Response

The maximum photo-current was 0.2129 mA, the contour plots of the individual quadrants, shown below, show the 3%, 97%, and 103% response contours. The reference data for each quadrant is shown in table 38, below.

<i>Quadrant</i>	<i>Reference Photo-current (mA)</i>	<i>Relative Reference levels (%)</i>
<i>1</i>	0.2076	-0.25
<i>2</i>	0.2075	-0.3
<i>3</i>	0.2071	-0.47
<i>4</i>	0.2081	0.00

Table 38: Photodiode 209 Reference Data

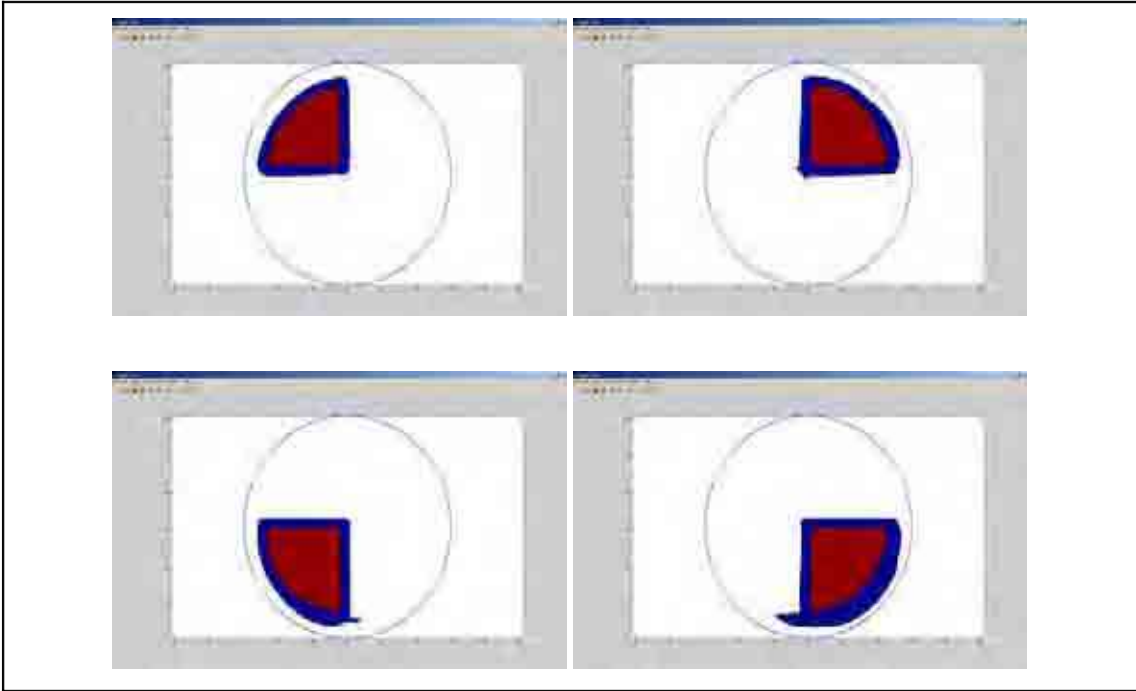


Figure 159: Photodiode 209 Q1, Q2, Q3, and Q4 Contours

APPENDIX K PHOTODIODE 211 INSPECTION RESULTS

The response of the photodiode is shown below

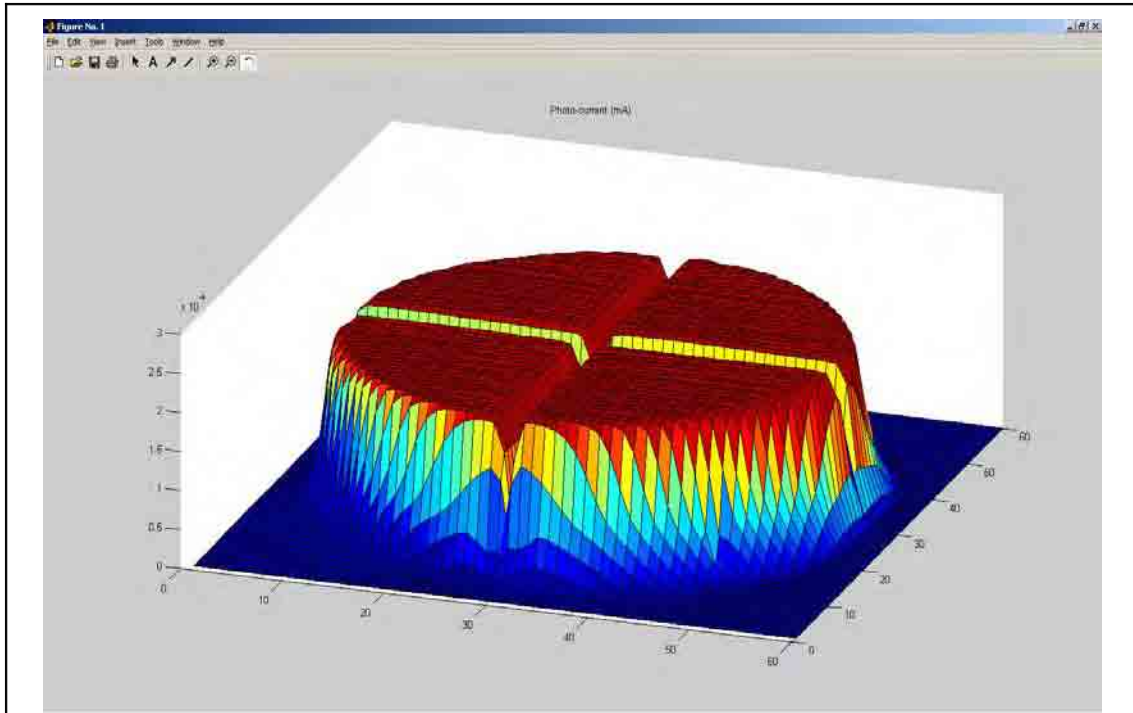


Figure 160: Photodiode 211 Response

The maximum photo-current was 0.2033 mA, the contour plots of the individual quadrants, shown below, show the 3%, 97%, and 103% response contours. The reference data for each quadrant is shown in table 39, below.

<i>Quadrant</i>	<i>Reference Photo-current (mA)</i>	<i>Relative Reference levels (%)</i>
<i>1</i>	0.1997	-0.22
<i>2</i>	0.1994	-0.38
<i>3</i>	0.1996	-0.29
<i>4</i>	0.2002	0.00

Table 39: Photodiode 211 Reference Data

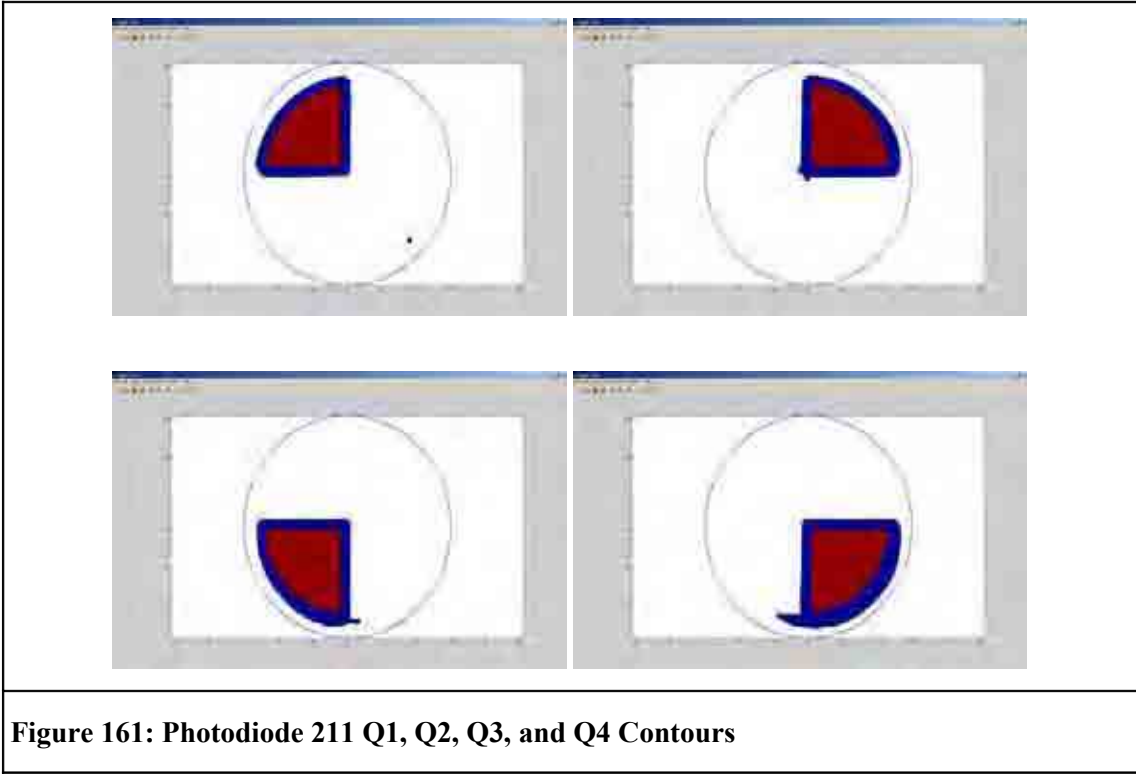


Figure 161: Photodiode 211 Q1, Q2, Q3, and Q4 Contours

APPENDIX L PHOTODIODE 213 INSPECTION RESULTS

In order to check the operation of the inspection rig, this detector was scanned using increased resolution. The response of the photodiode is shown below

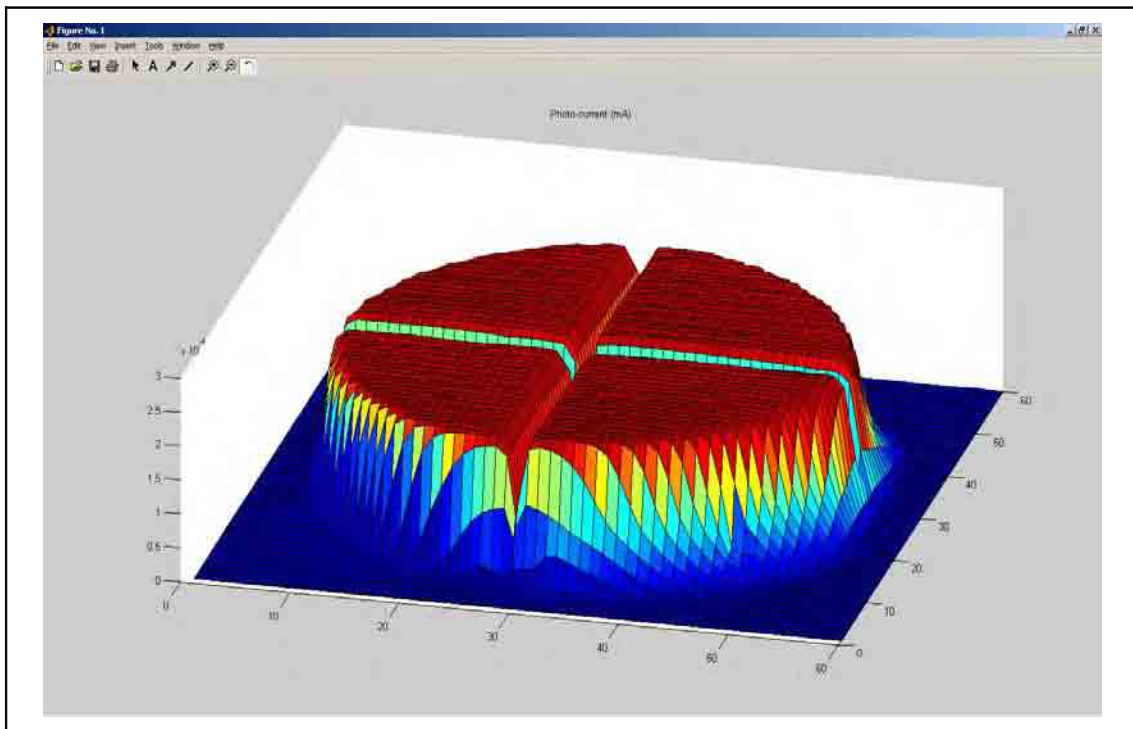


Figure 162: Photodiode 213 Response

The maximum photo-current was 0.2102 mA, the contour plots of the individual quadrants, shown below, show the 3%, 97%, and 103% response contours. The reference data for each quadrant is shown in table 40, below.

<i>Quadrant</i>	<i>Reference Photo-current (mA)</i>	<i>Relative Reference levels (%)</i>
<i>1</i>	0.2045	-0.39
<i>2</i>	0.2042	-0.54
<i>3</i>	0.2046	-0.37
<i>4</i>	0.2053	0.00

Table 40: Photodiode 213 Reference Data

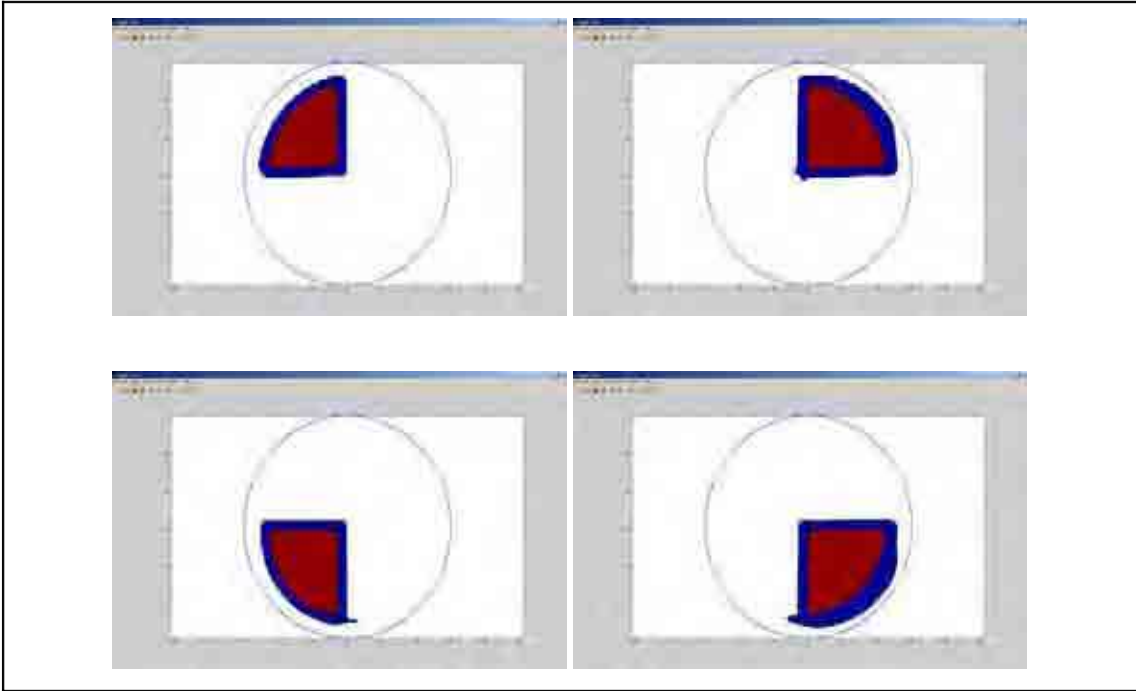


Figure 163: Photodiode 213 Q1, Q2, Q3, and Q4 Contours

APPENDIX M PHOTODIODE 217 INSPECTION RESULTS

The response of the photodiode is shown below

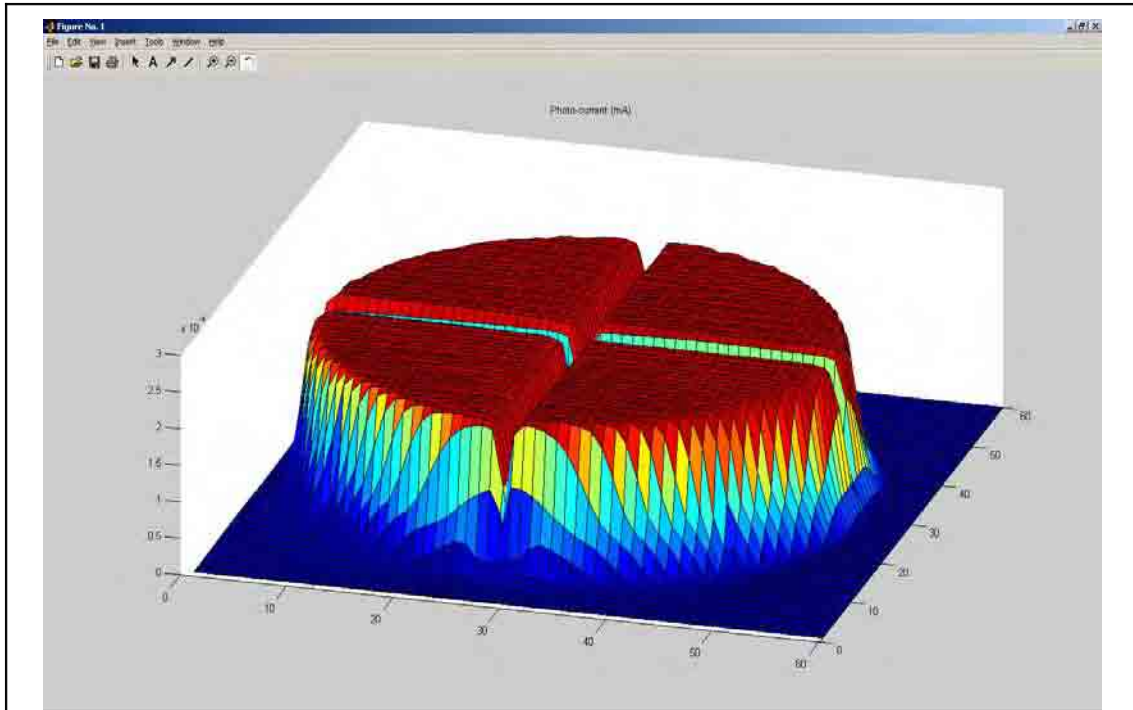


Figure 164: Photodiode 217 Response

The maximum photo-current was 0.2120 mA, the contour plots of the individual quadrants, shown below, show the 3%, 97%, and 103% response contours. The reference data for each quadrant is shown in table 41, below.

<i>Quadrant</i>	<i>Reference Photo-current (mA)</i>	<i>Relative Reference levels (%)</i>
<i>1</i>	0.2066	-0.27
<i>2</i>	0.2069	-0.14
<i>3</i>	0.2067	-0.24
<i>4</i>	0.2072	0.00

Table 41: Photodiode 217 Reference Data

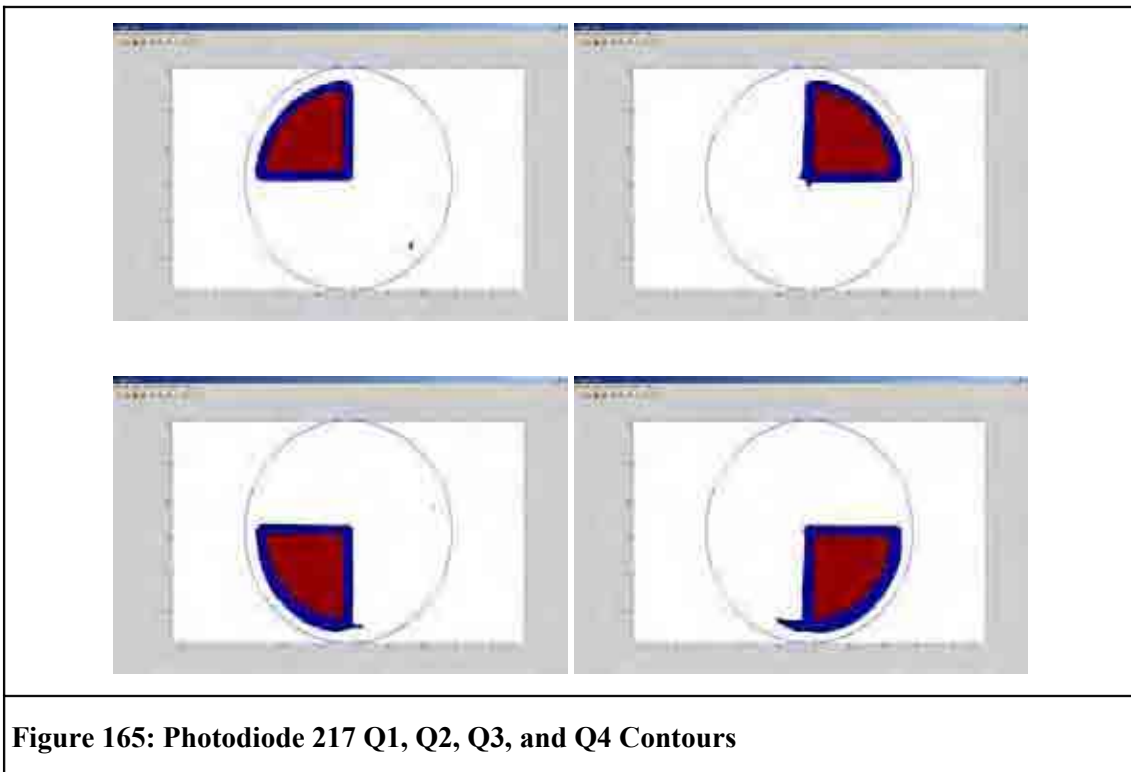


Figure 165: Photodiode 217 Q1, Q2, Q3, and Q4 Contours

APPENDIX N PHOTODIODE 218 INSPECTION RESULTS

The response of the photodiode is shown below

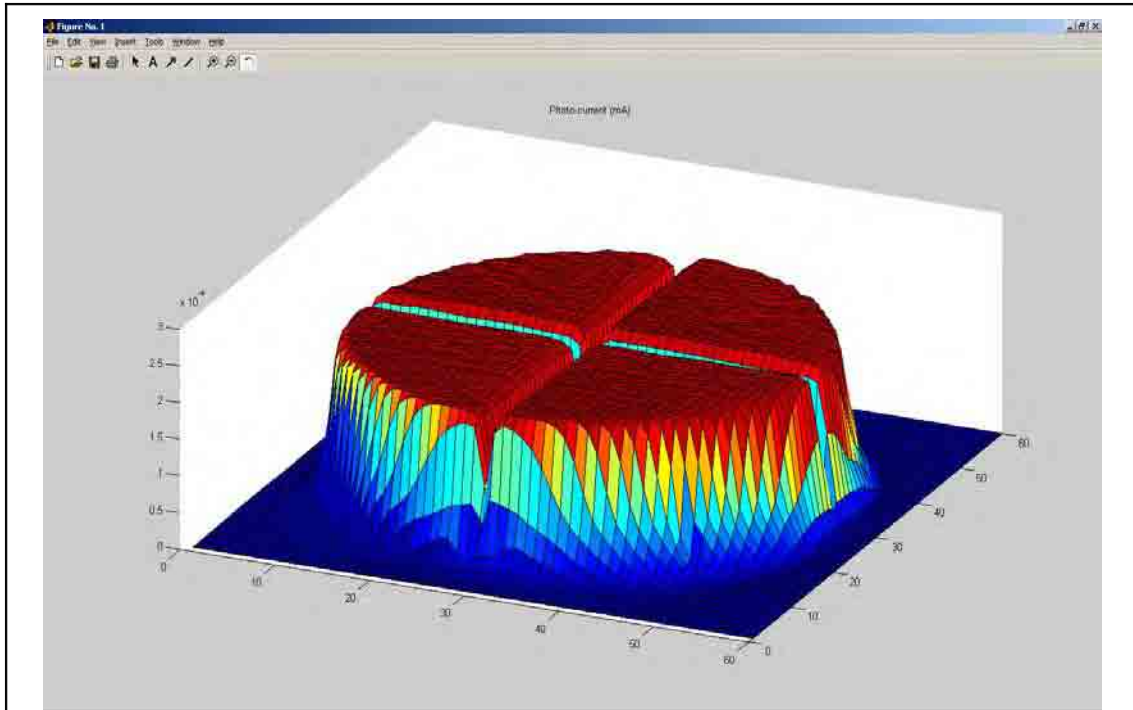


Figure 166: Photodiode 218 Response

The maximum photo-current was 0.2130 mA, the contour plots of the individual quadrants, shown below, show the 3%, 97%, and 103% response contours. The reference data for each quadrant is shown in table 42, below.

<i>Quadrant</i>	<i>Reference Photo-current (mA)</i>	<i>Relative Reference levels (%)</i>
<i>1</i>	0.2072	-0.44
<i>2</i>	0.2070	-0.54
<i>3</i>	0.2077	-0.21
<i>4</i>	0.2081	0.00

Table 42: Photodiode 218 Reference Data

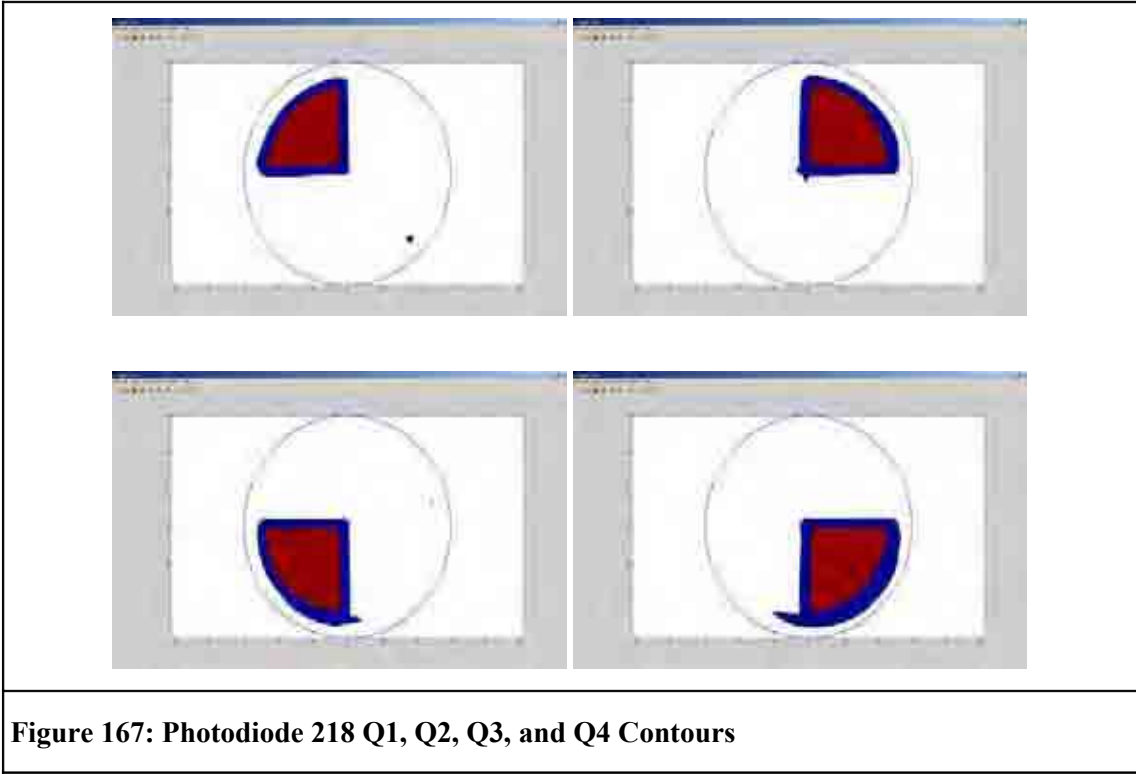


Figure 167: Photodiode 218 Q1, Q2, Q3, and Q4 Contours

APPENDIX O PHOTODIODE 219 INSPECTION RESULTS

The response of the photodiode is shown below

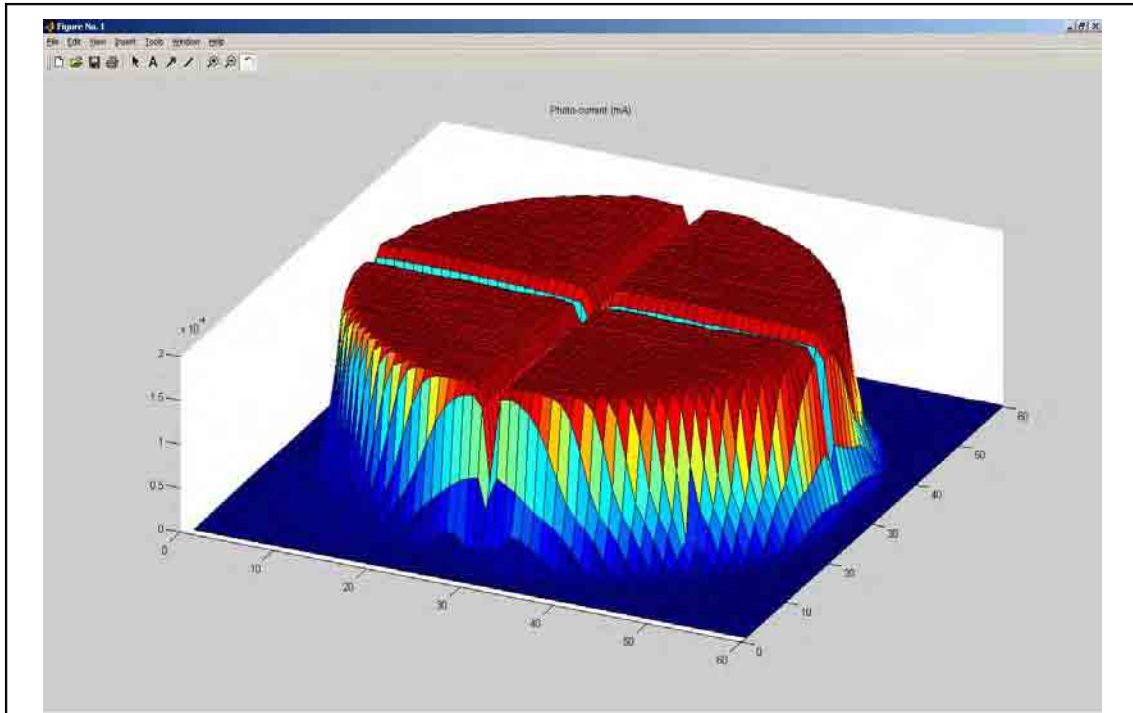


Figure 168: Photodiode 219 Response

The maximum photo-current was 0.1958 mA, the contour plots of the individual quadrants, shown below, show the 3%, 97%, and 103% response contours. The reference data for each quadrant is shown in table 43, below.

<i>Quadrant</i>	<i>Reference Photo-current (mA)</i>	<i>Relative Reference levels (%)</i>
<i>1</i>	0.1929	-0.23
<i>2</i>	0.1927	-0.34
<i>3</i>	0.1927	-0.36
<i>4</i>	0.1934	0.00

Table 43: Photodiode 219 Reference Data

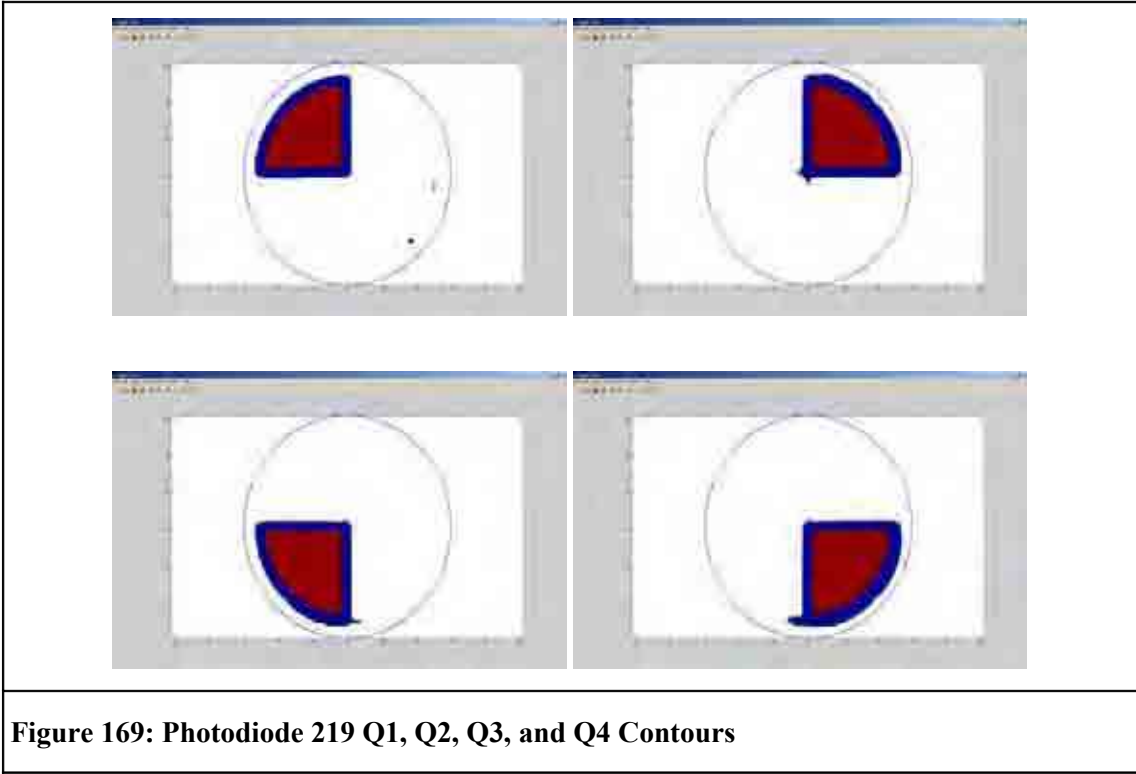


Figure 169: Photodiode 219 Q1, Q2, Q3, and Q4 Contours

APPENDIX P PHOTODIODE 221 INSPECTION RESULTS

The response of the photodiode is shown below

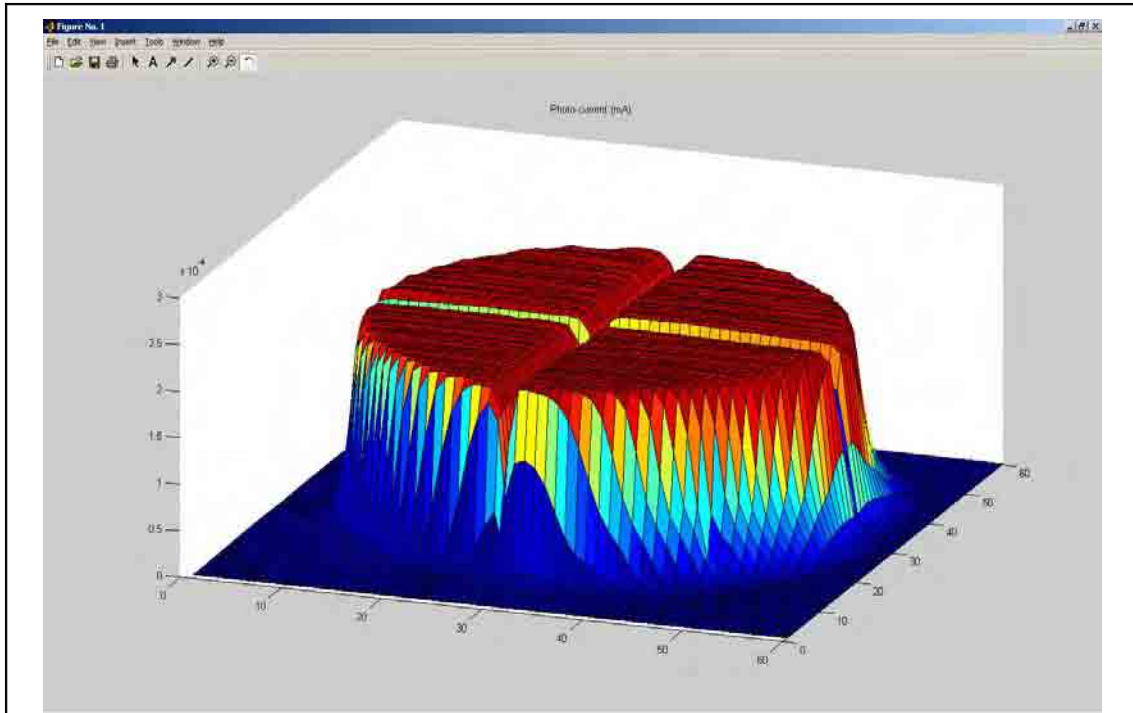


Figure 170: Photodiode 221 Response

The maximum photo-current was 0.2075 mA, the contour plots of the individual quadrants, shown below, show the 3%, 97%, and 103% response contours. The reference data for each quadrant is shown in table 44, below.

<i>Quadrant</i>	<i>Reference Photo-current (mA)</i>	<i>Relative Reference levels (%)</i>
<i>1</i>	0.2024	-0.55
<i>2</i>	0.2025	-0.48
<i>3</i>	0.2029	-0.26
<i>4</i>	0.2035	0.00

Table 44: Photodiode 221 Reference Data

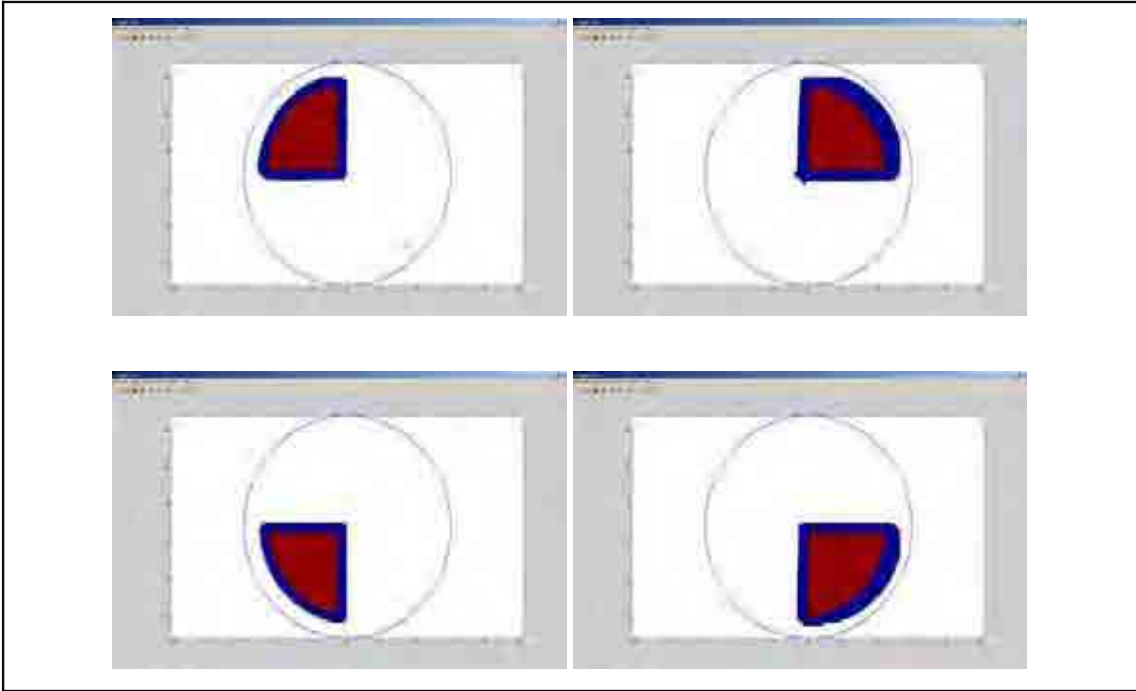


Figure 171: Photodiode 221 Q1, Q2, Q3, and Q4 Contours

APPENDIX Q PHOTODIODE 222 INSPECTION RESULTS

The response of the photodiode is shown below

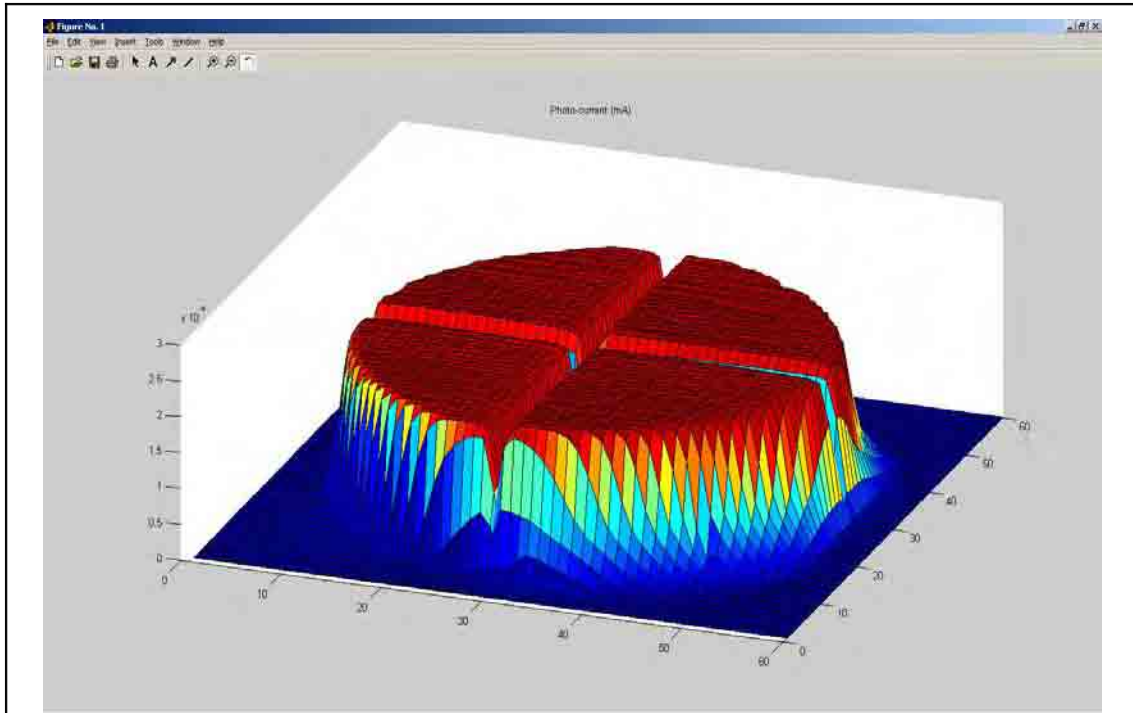


Figure 172: Photodiode 222 Response

The maximum photo-current was 0.2121 mA, the contour plots of the individual quadrants, shown below, show the 3%, 97%, and 103% response contours. The reference data for each quadrant is shown in table 45, below.

<i>Quadrant</i>	<i>Reference Photo-current (mA)</i>	<i>Relative Reference levels (%)</i>
<i>1</i>	0.2071	-0.33
<i>2</i>	0.2068	-0.48
<i>3</i>	0.2067	-0.50
<i>4</i>	0.2077	0.00

Table 45: Photodiode 222 Reference Data

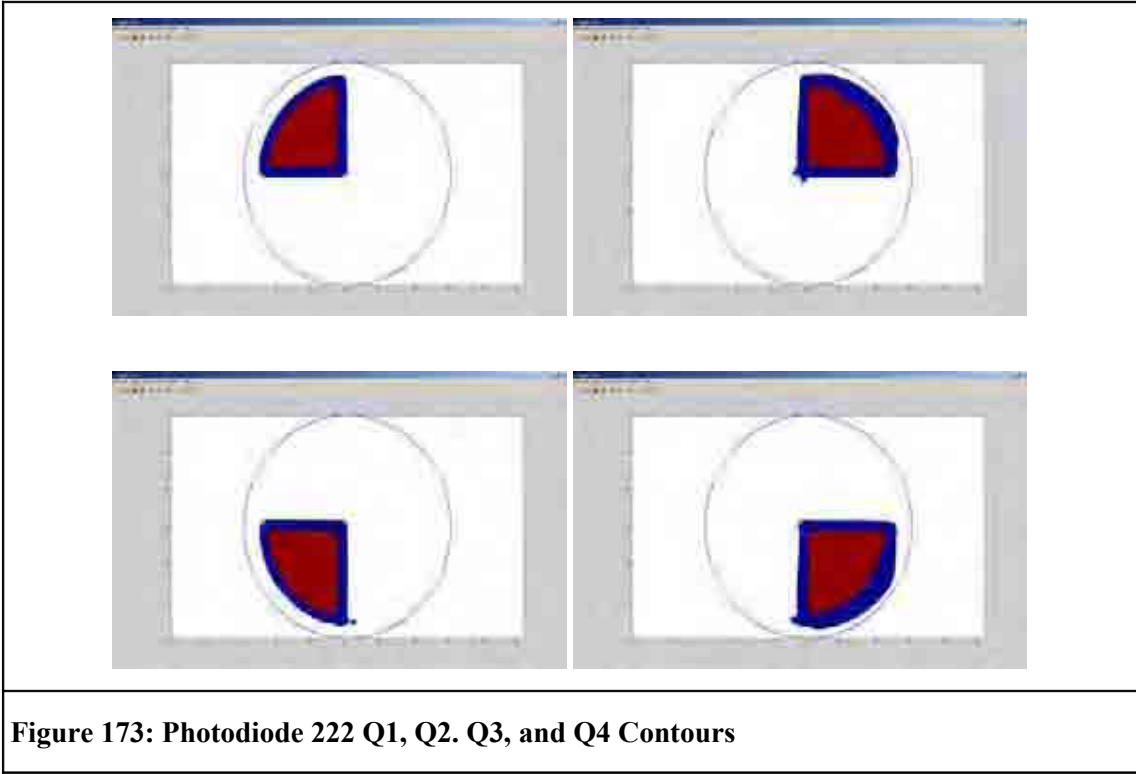


Figure 173: Photodiode 222 Q1, Q2, Q3, and Q4 Contours

APPENDIX R PHOTODIODE 232 INSPECTION RESULTS

The response of the photodiode is shown below

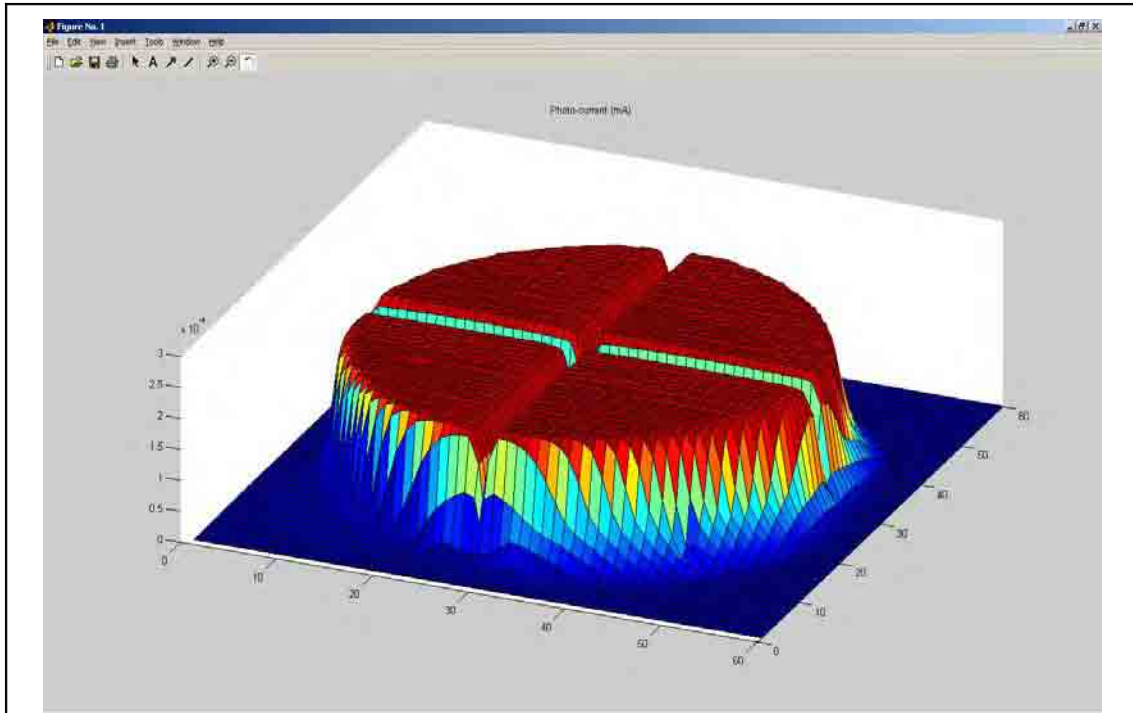


Figure 174: Photodiode 232 Response

The maximum photo-current was 0.2116 mA, the contour plots of the individual quadrants, shown below, show the 3%, 97%, and 103% response contours. The reference data for each quadrant is shown in table 46, below.

<i>Quadrant</i>	<i>Reference Photo-current (mA)</i>	<i>Relative Reference levels (%)</i>
<i>1</i>	0.2063	-0.50
<i>2</i>	0.2064	-0.46
<i>3</i>	0.2066	-0.38
<i>4</i>	0.2074	0.00

Table 46: Photodiode 232 Reference Data

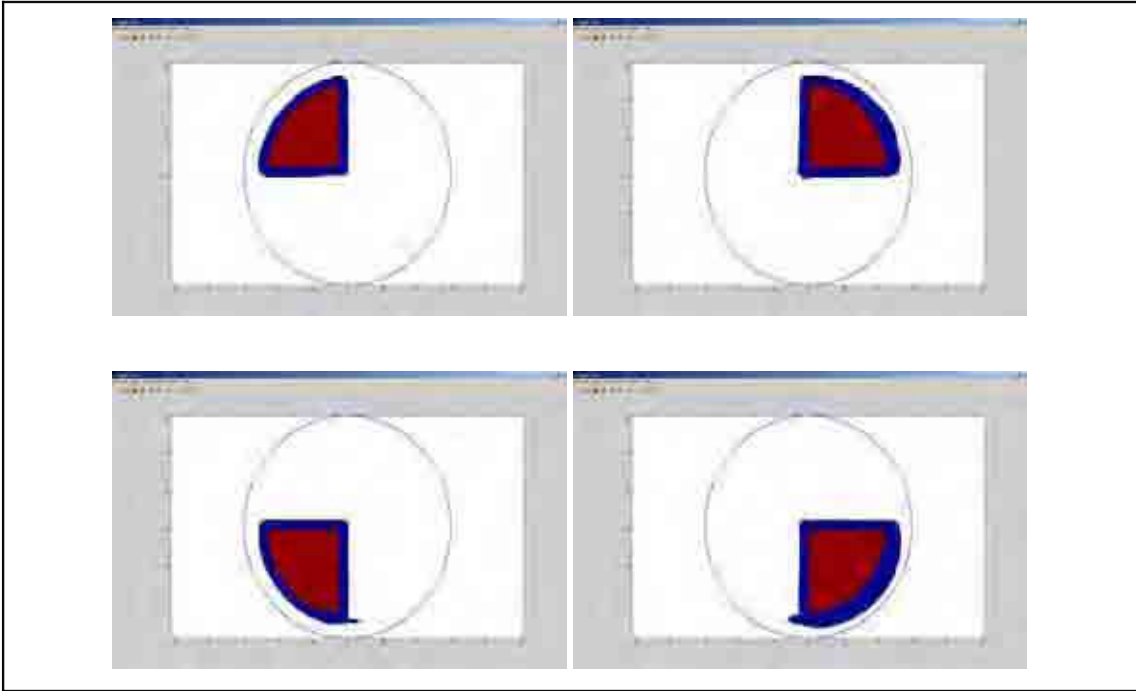


Figure 175: Photodiode 232 Q1, Q2, Q3, and Q4 Contours

APPENDIX S PHOTODIODE 233 INSPECTION RESULTS

Owing to the poor response of photodiode 233, as measured during the pre-assembly testing, this photodiode was not mechanically assembled, and therefore was not re-scanned.

APPENDIX T PHOTODIODE 236 INSPECTION RESULTS

The response of the photodiode is shown below

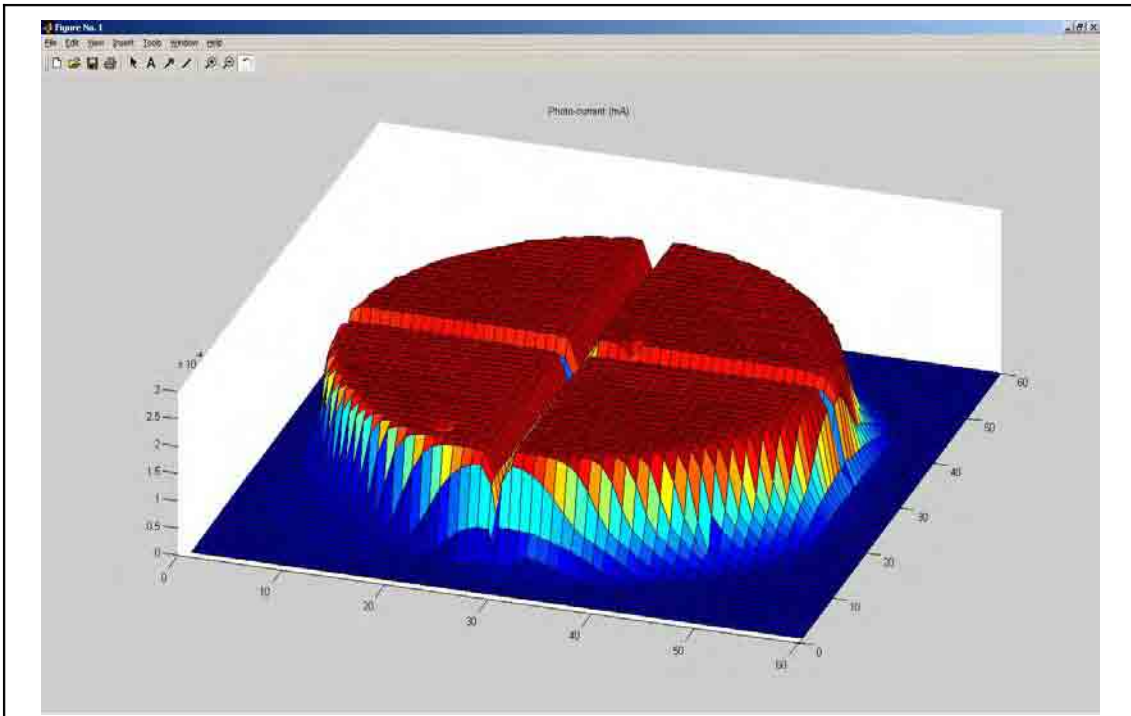


Figure 176: Photodiode 236 Response

The maximum photo-current was 0.2066 mA, the contour plots of the individual quadrants, shown below, show the 3%, 97%, and 103% response contours. The reference data for each quadrant is shown in table 47, below.

<i>Quadrant</i>	<i>Reference Photo-current (mA)</i>	<i>Relative Reference levels (%)</i>
<i>1</i>	0.2029	-0.12
<i>2</i>	0.2029	-0.15
<i>3</i>	0.2019	-0.61
<i>4</i>	0.2032	0.00

Table 47: Photodiode 236 Reference Data

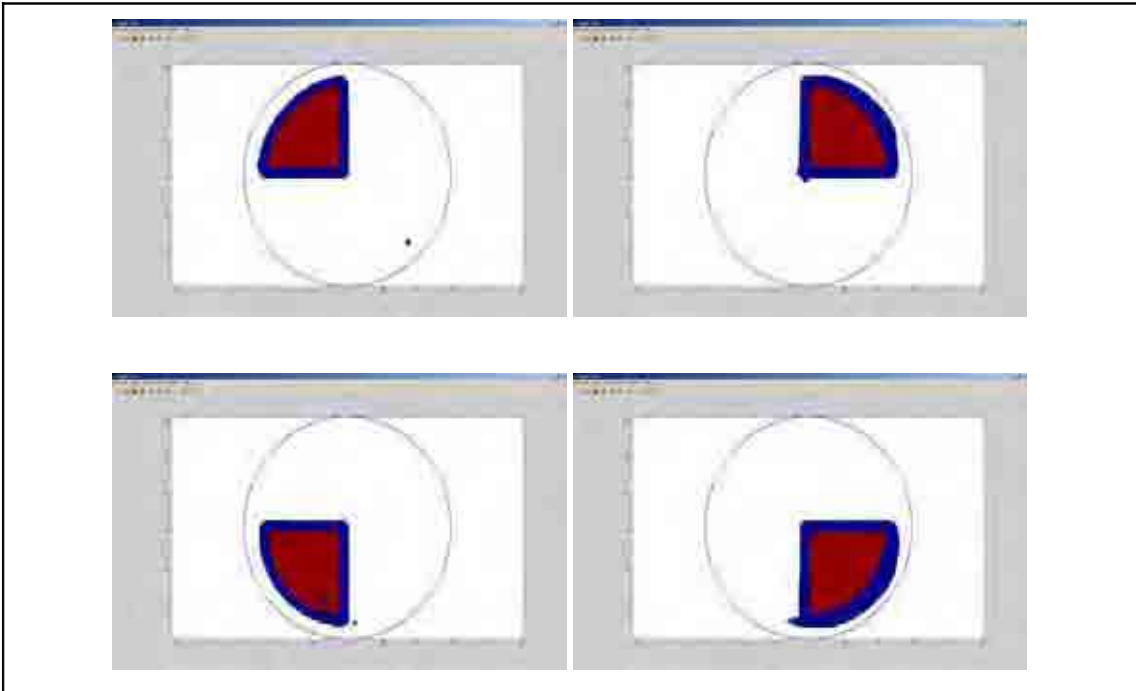


Figure 177: Photodiode 236 Q1, Q2, Q3, and Q4 Contours

APPENDIX U PHOTODIODE 238 INSPECTION RESULTS

The response of the photodiode is shown below

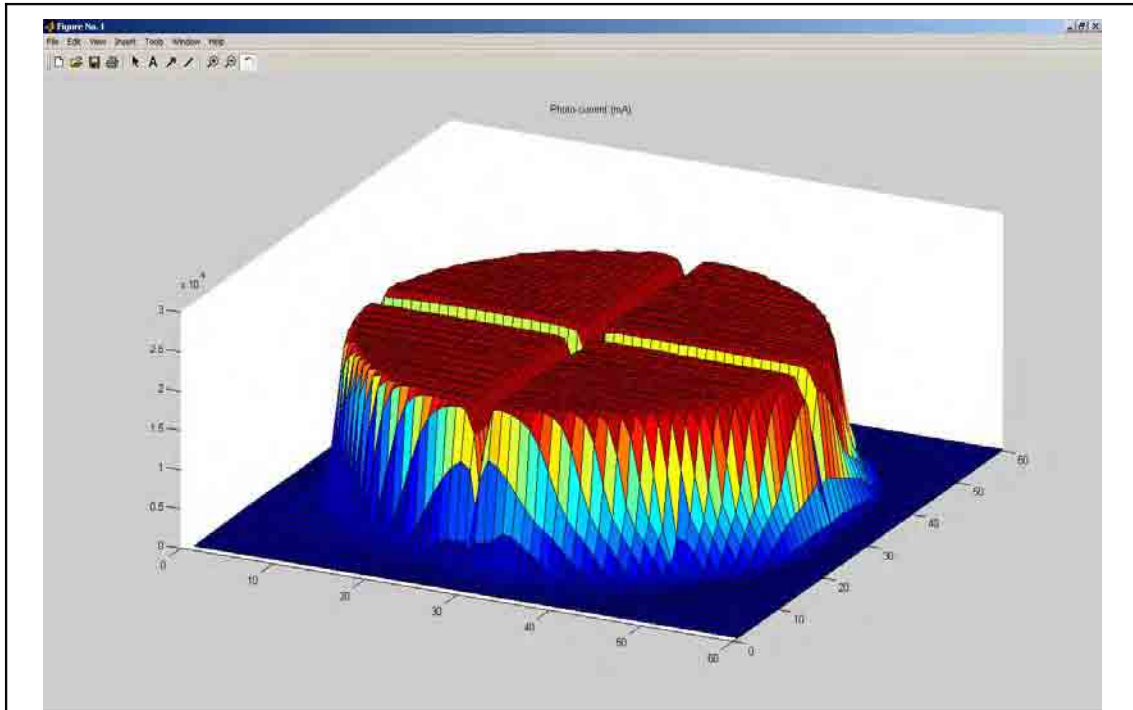


Figure 178: Photodiode 238 Response

The maximum photo-current was 0.2064 mA, the contour plots of the individual quadrants, shown below, show the 3%, 97%, and 103% response contours. The reference data for each quadrant is shown in table 48, below.

<i>Quadrant</i>	<i>Reference Photo-current (mA)</i>	<i>Relative Reference levels (%)</i>
<i>1</i>	0.2025	-0.31
<i>2</i>	0.2023	-0.39
<i>3</i>	0.2023	-0.39
<i>4</i>	0.2031	0.00

Table 48: Photodiode 238 Reference Data

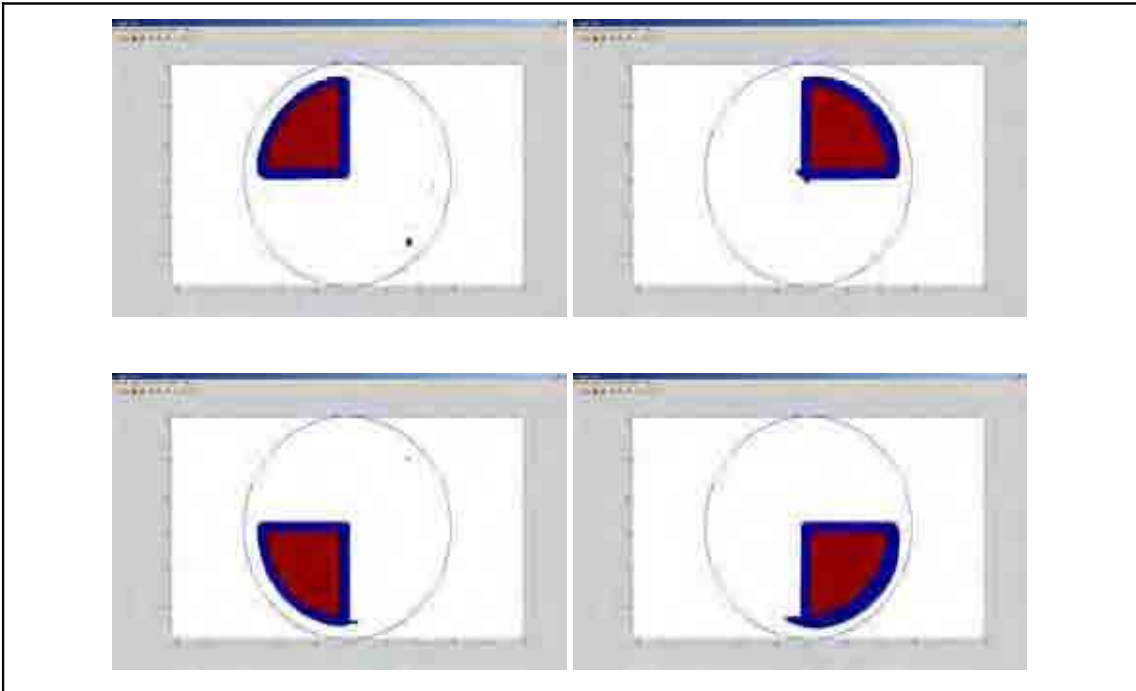


Figure 179: Photodiode 238 Q1, Q2, Q3, and Q4 Contours

APPENDIX V PHOTODIODE 239 INSPECTION RESULTS

The response of the photodiode is shown below

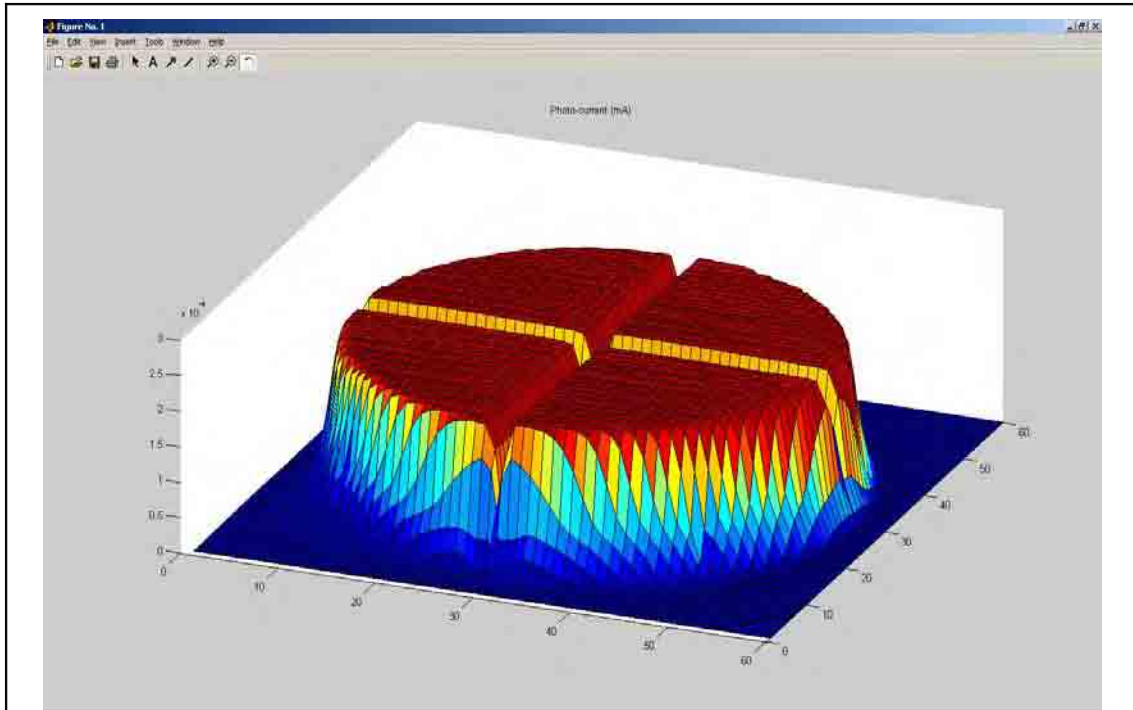


Figure 180: Photodiode 239 Response

The maximum photo-current was 0.2067 mA, the contour plots of the individual quadrants, shown below, show the 3%, 97%, and 103% response contours. The reference data for each quadrant is shown in the table 49, below.

<i>Quadrant</i>	<i>Reference Photo-current (mA)</i>	<i>Relative Reference levels (%)</i>
<i>1</i>	0.2029	-0.06
<i>2</i>	0.2021	-0.48
<i>3</i>	0.2026	-0.19
<i>4</i>	0.2030	0.00

Table 49: Photodiode 239 Reference Data

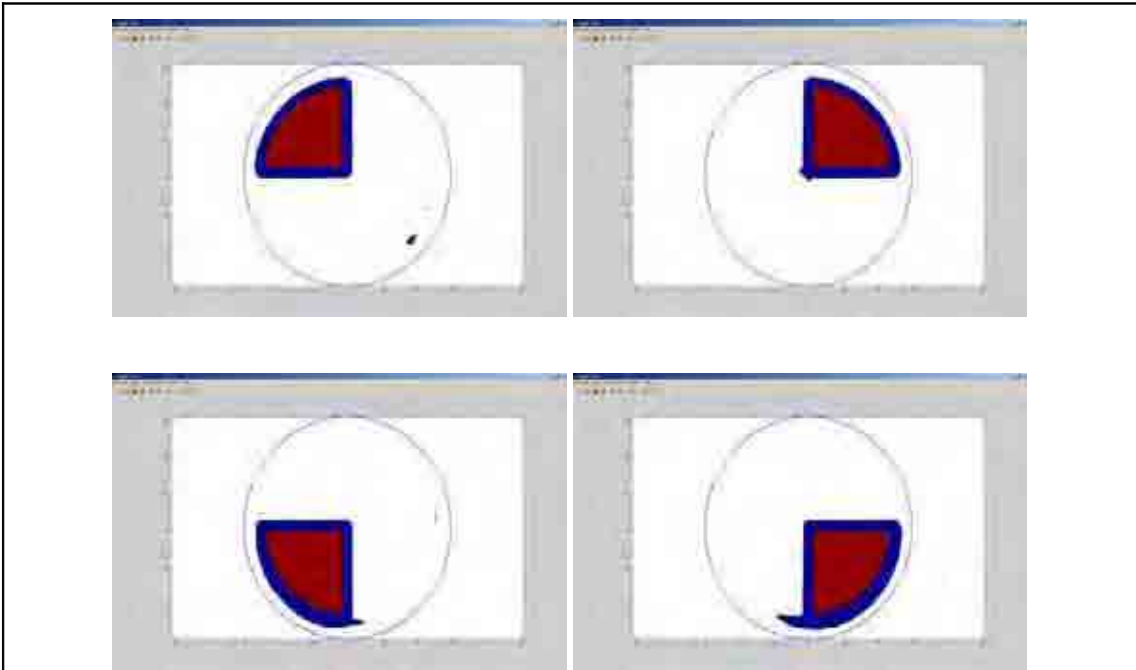


Figure 181: Photodiode 239 Q1, Q2, Q3, and Q4 Contours

APPENDIX W PHOTODIODE 241 INSPECTION RESULTS

The response of the photodiode is shown below

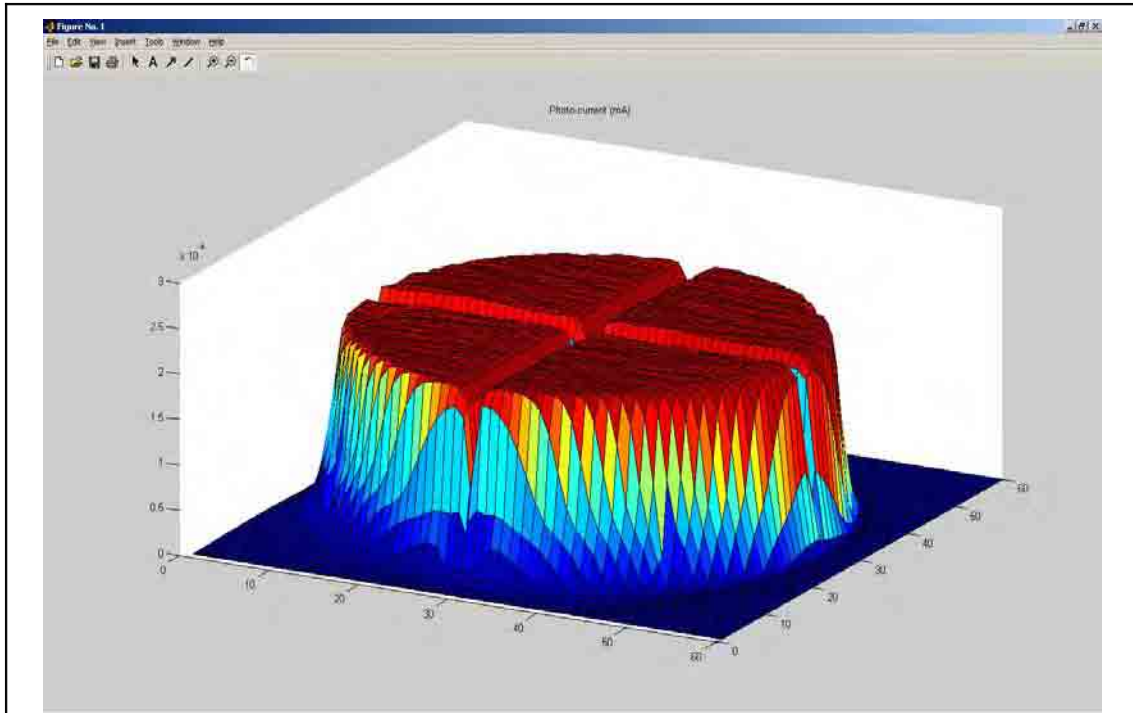


Figure 182: Photodiode 241 Response

The maximum photo-current was 0.2117 mA, the contour plots of the individual quadrants, shown below, show the 3%, 97%, and 103% response contours. The reference data for each quadrant is shown in table 50, below.

<i>Quadrant</i>	<i>Reference Photo-current (mA)</i>	<i>Relative Reference levels (%)</i>
<i>1</i>	0.2076	-0.03
<i>2</i>	0.2065	-0.57
<i>3</i>	0.2065	-0.54
<i>4</i>	0.2077	0.00

Table 50: Photodiode 241 Reference Data

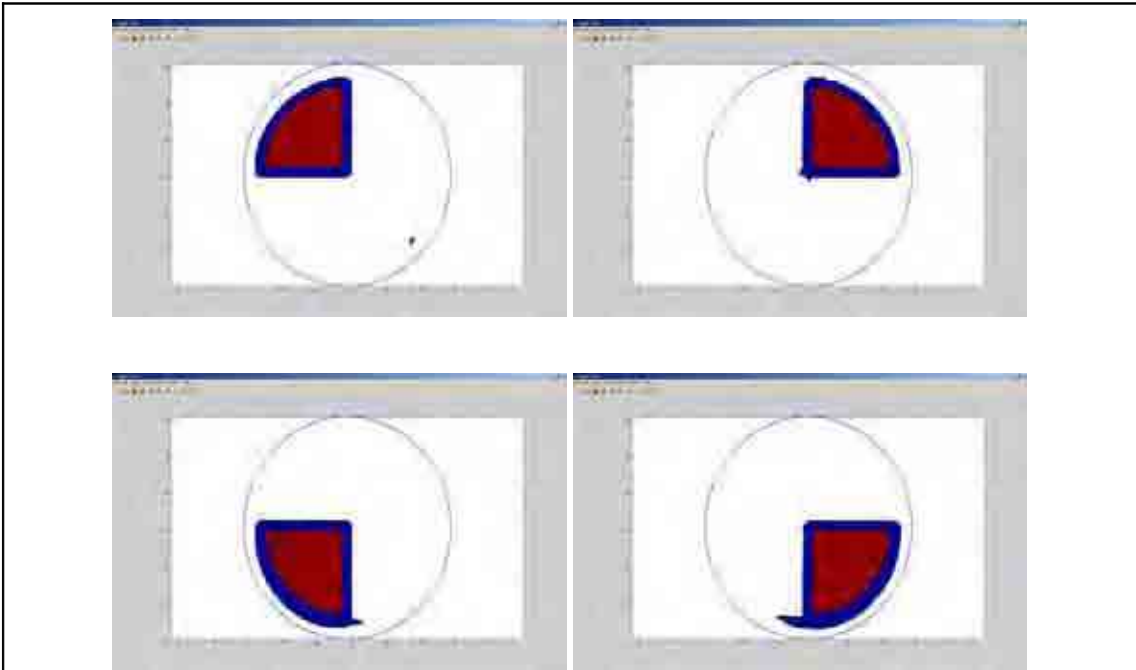


Figure 183: Photodiode 241 Q1, Q2, Q3, and Q4 Contours

APPENDIX X PHOTODIODE 242 INSPECTION RESULTS

Owing to the poor response of photodiode 242, as measured during the pre-assembly testing, this photodiode was not mechanically assembled, and therefore was not re-scanned.

APPENDIX Y PHOTODIODE 244 INSPECTION RESULTS

The response of the photodiode is shown below

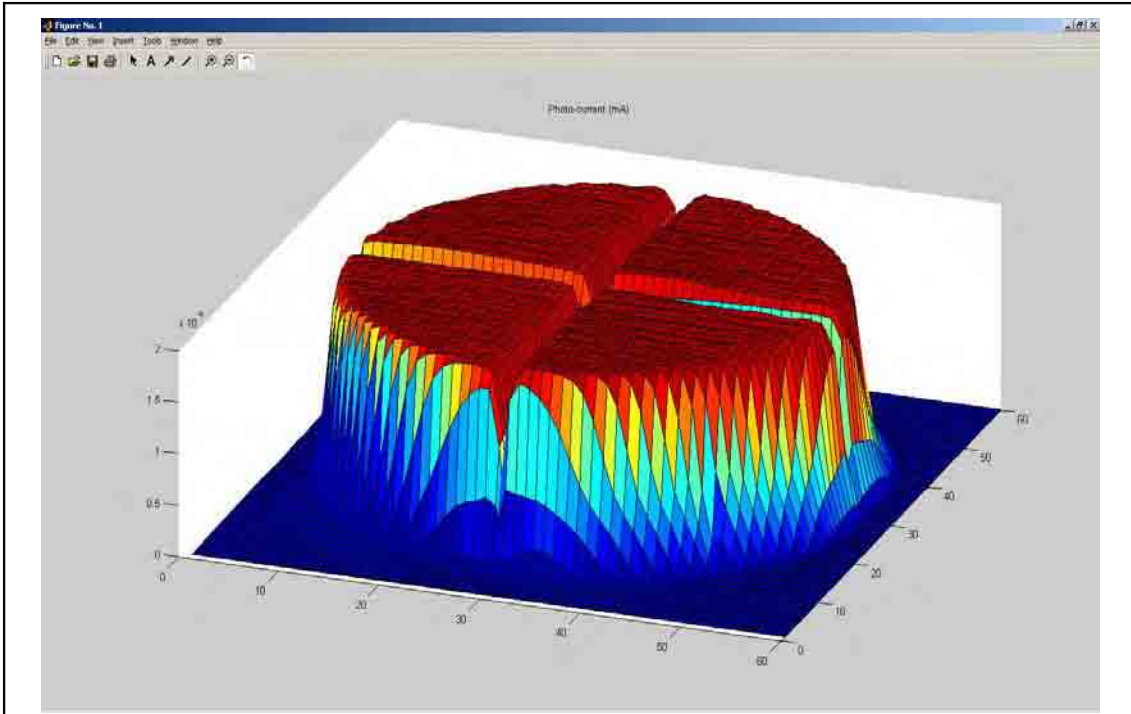


Figure 184: Photodiode 244 Response

The maximum photo-current was 0.1941 mA, the contour plots of the individual quadrants, shown below, show the 3%, 97%, and 103% response contours. The reference data for each quadrant is shown in table 51, below.

<i>Quadrant</i>	<i>Reference Photo-current (mA)</i>	<i>Relative Reference levels (%)</i>
<i>1</i>	0.1920	-0.19
<i>2</i>	0.1922	-0.08
<i>3</i>	0.1920	-0.18
<i>4</i>	0.1923	0.00

Table 51: Photodiode 244 Reference Data

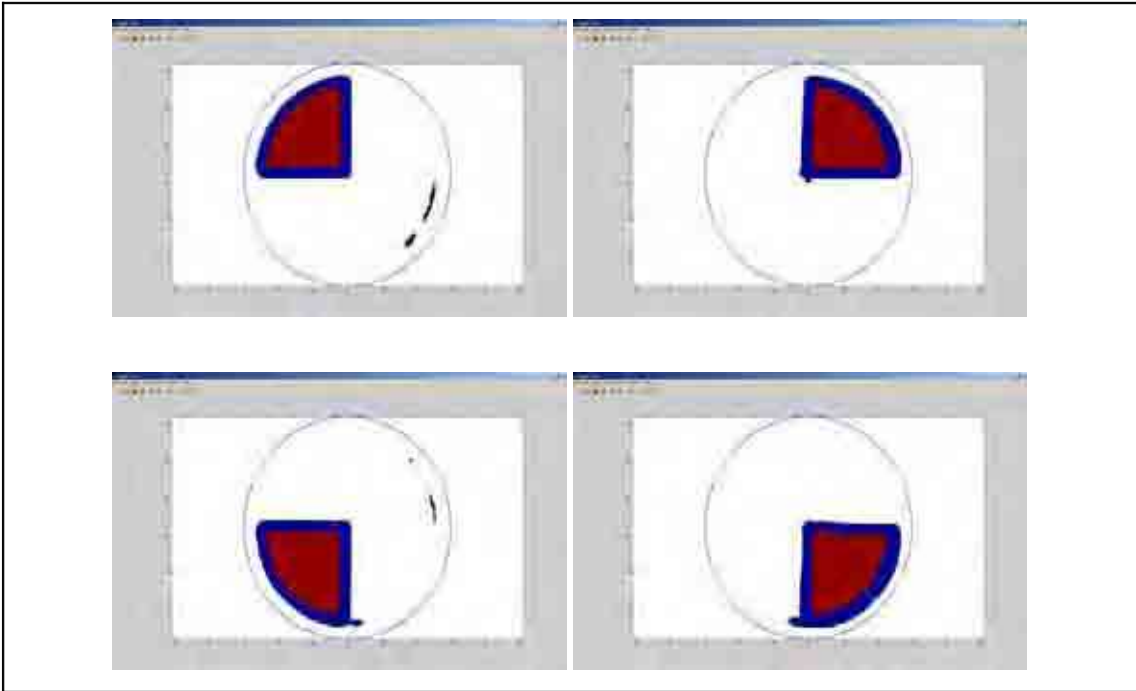


Figure 185: Photodiode 244 Q1, Q2, Q3, and Q4 Contours

APPENDIX Z PHOTODIODE 245 INSPECTION RESULTS

The response of the photodiode is shown below

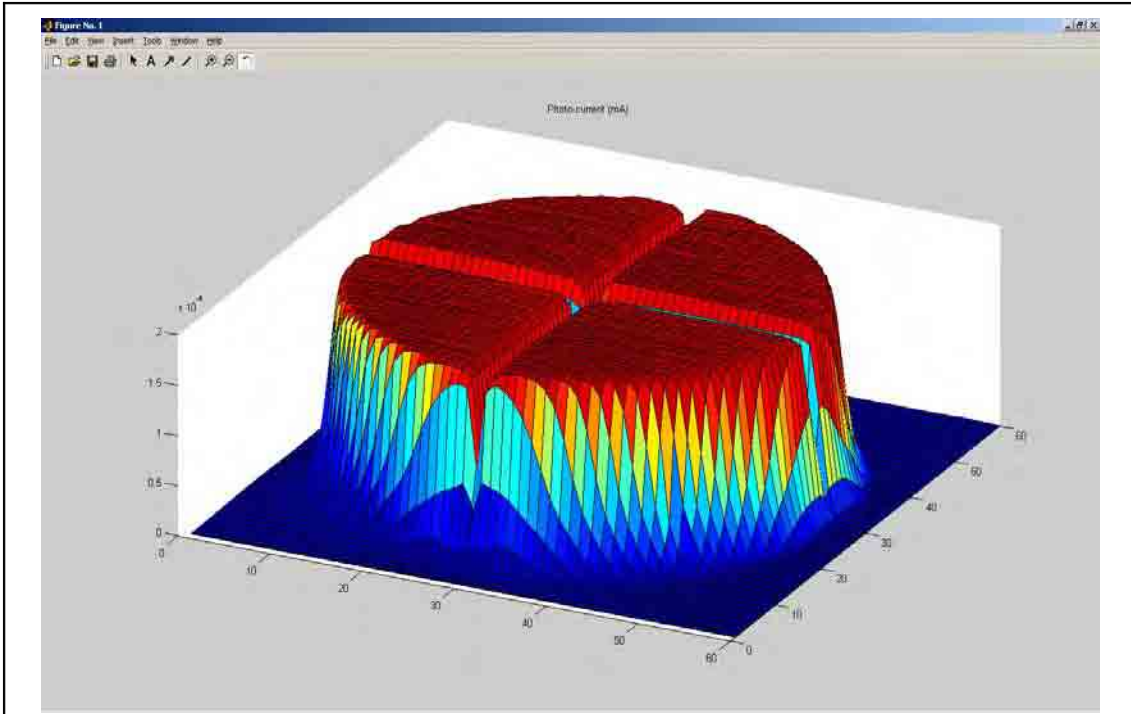


Figure 186: Photodiode 245 Response

The maximum photo-current was 0.1916 mA, the contour plots of the individual quadrants, shown below, show the 3%, 97%, and 103% response contours. The reference data for each quadrant is shown in table 52, below.

<i>Quadrant</i>	<i>Reference Photo-current (mA)</i>	<i>Relative Reference levels (%)</i>
<i>1</i>	0.1911	-0.06
<i>2</i>	0.1911	-0.08
<i>3</i>	0.1911	-0.08
<i>4</i>	0.1913	0.00

Table 52: Photodiode 245 Reference Data

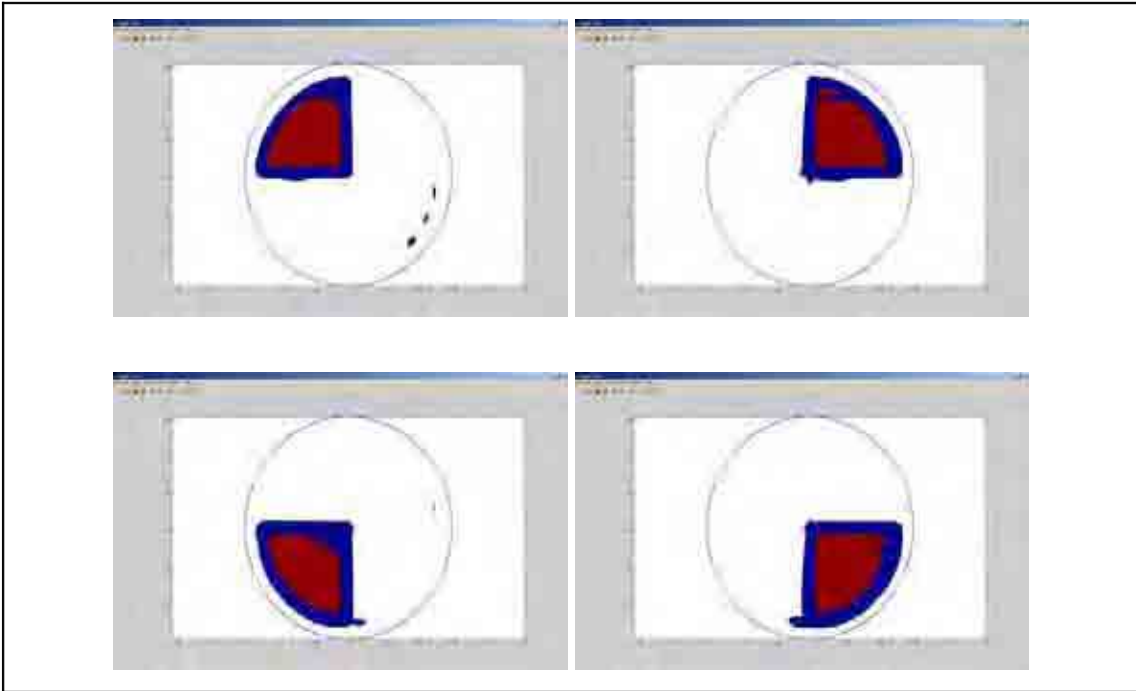


Figure 187: Photodiode 245 Q1, Q2, Q3, and Q4 Contours

APPENDIX AA PHOTODIODE 246 INSPECTION RESULTS

The response of the photodiode is shown below

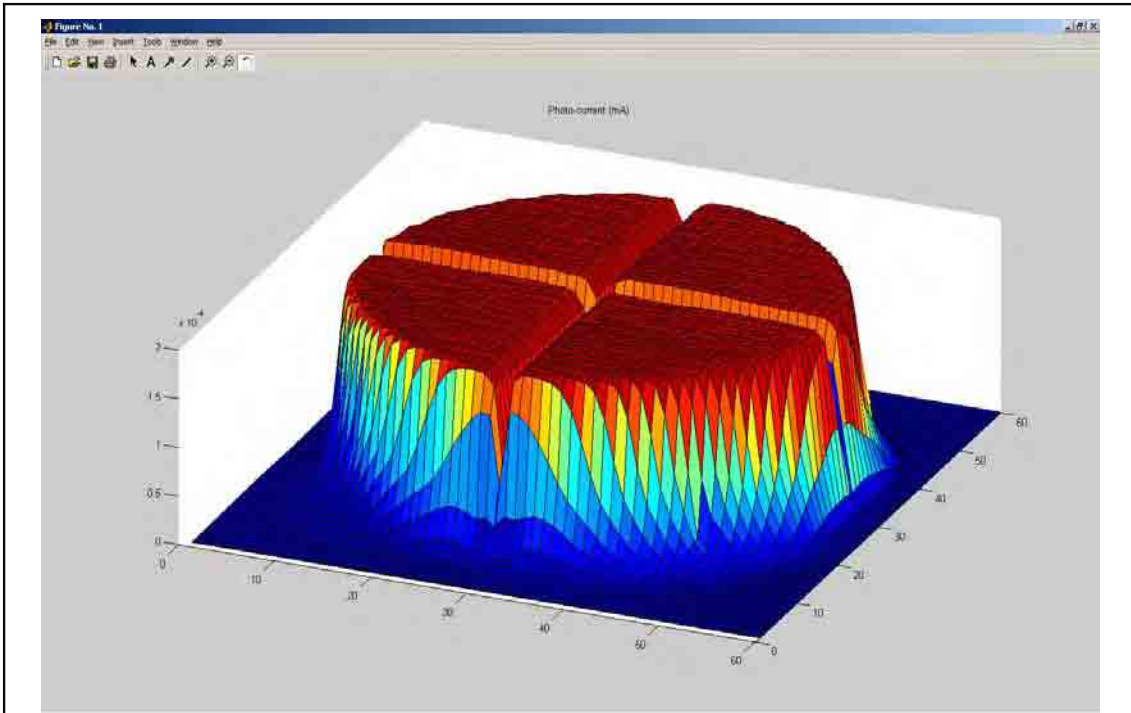


Figure 188: Photodiode 246 Response

The maximum photo-current was 0.1951 mA, the contour plots of the individual quadrants, shown below, show the 3%, 97%, and 103% response contours. The reference data for each quadrant is shown in table 53, below.

<i>Quadrant</i>	<i>Reference Photo-current (mA)</i>	<i>Relative Reference levels (%)</i>
<i>1</i>	0.1925	-0.23
<i>2</i>	0.1927	-0.12
<i>3</i>	0.1925	-0.24
<i>4</i>	0.1930	0.00

Table 53: Photodiode 246 Reference Data

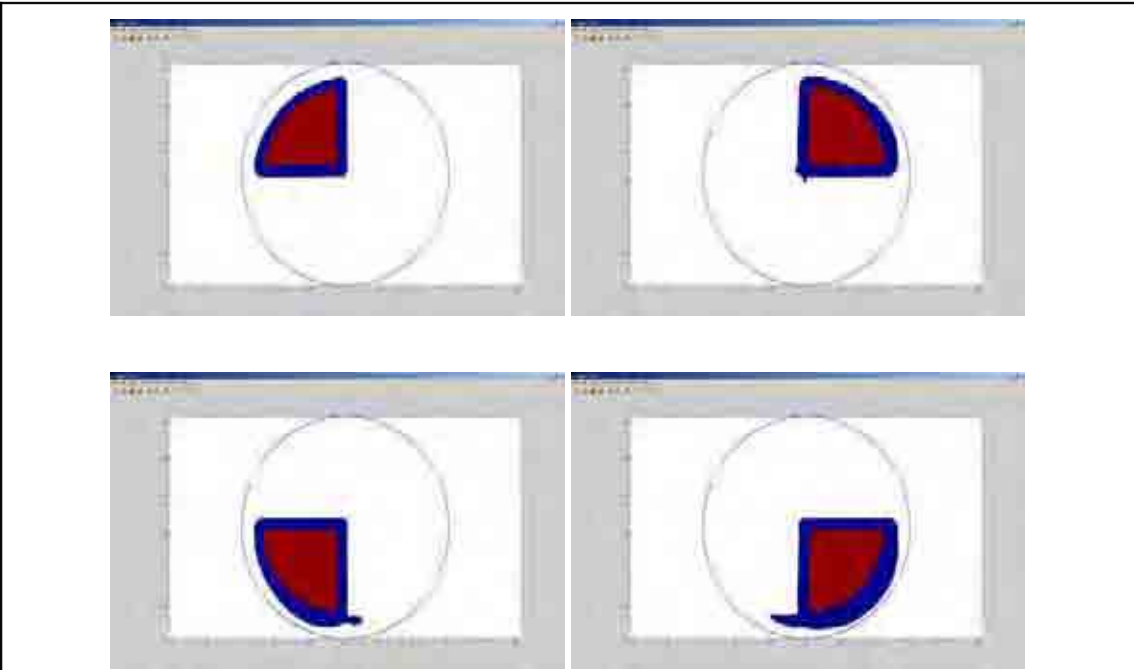


Figure 189: Photodiode 246 Q1, Q2, Q3, and Q4 Contours